Dynamics of Swirling Flows Induced by Twisted Tapes in Circular Pipes

A Thesis
Presented to
The Academic Faculty

By

Radu Cazan

In Partial Fulfillment
Of the Requirements for the Degree
Doctor of Philosophy in Mechanical Engineering

School of Mechanical Engineering
Georgia Institute of Technology
May 2010

Dynamics of Swirling Flows Induced by Twisted Tapes in Circular Pipes

Approved by:

Dr. Cyrus Aidun, Advisor
School of Mechanical Engineering
Georgia Institute of Technology

Dr. Minami Yoda
School of Mechanical Engineering
Georgia Institute of Technology

Dr. Ari Glezer
School of Mechanical Engineering
Georgia Institute of Technology

Dr. Mostafa Ghiaasiaan
School of Mechanical Engineering
Georgia Institute of Technology

Dr. Donald Webster
School of Civil and Environmental Engineering
Georgia Institute of Technology

Dr. Jerry Seitzman
School of Aerospace Engineering
Georgia Institute of Technology

Date Approved:
17 August 2009

Acknowledgments

First I would like to express my sincere gratitude to my advisor Dr. Cyrus Aidun for his guidance and patience throughout the time I spent in the School of Mechanical Engineering at Georgia Tech. I would like to thank him first for offering me this great learning opportunity but also for allowing me the freedom to work at my own pace.

In addition, I would like to extend my thanks to the rest of my reading committee Dr. Minami Yoda, Dr. Donald Webster, Dr. Ari Glezer, Dr. Mostafa Ghiaasiaan and Dr. Jerry Seitzman for their time and valuable suggestions. I would especially like to thank Dr. Jerry Seitzman who helped me through this project and through some of my previous projects at Georgia Tech as well.

I would like to thank Dr. Tudor Bodea, Dr. Camil Ghiu, Dr. Ionut Porumbel, Dr. Tudor Palaghita, Dr. Dragos Viieru and Dr. Radu Iliescu, to name just a few of my friends who helped me in my studies and made my stay in Atlanta enjoyable. I also thank my friends at home and my family for supporting me during the time of my studies.

The financial support of IPST which made this study possible is also gratefully acknowledged.

TABLE OF CONTENTS

ACKNOWLEDGMENTS……………………………………………………………... iii

LIST OF TABLES ………………………...………...………………………… vi

LIST OF FIGURES ………………………...………...………………………… vii

NOMENCLATURE …………………………………………………………….... xvi

SUMMARY…………………………………………………………………..… xxii

CHAPTER 1: INTRODUCTION…………………………………………….… 1

1.1 Motivation……………………………………………….……………… 1

1.2 Objectives ………………………………………………….…………… 6

CHAPTER 2: LITERATURE REVIEW………………………………………….. 10

2.1 Turbulent swirling flows ………………………………..................… 10

2.2 Vortex identification…………………………………………….…... 21

2.3 Flows in pipes with twisted tape inserts……………………………….. 24

2.4 Related studies: flows through curved and helical pipes………………. 30

2.5 Flows with helical vortices……………………………………………... 34

CHAPTER 3: EXPERIMENTAL SETUP……………………………………..… 43

3.1 General setup……………………………………..…………..… 43

3.2 Setup for LDV measurements…………………………..……….…… 47

CHAPTER 4: EXPERIMENTAL RESULTS AND COMMENTS…………...… 53

4.1 Results of LDV measurements………………………..…………..… 53

4.2 Air bubbles visualization……………………….…..……….….… 60

4.3 Velocity field reconstruction……………………..…..……….….… 68

4.4 Secondary flow recovery……………………………………………… 70

4.5 Vortex Inception and Development……..…………………………..… 74

CHAPTER 5: NUMERICAL SIMULATIONS: MODELS…………………...… 76

5.1 Background………………………………………………...…...… 76

5.2 Governing equations……………………………………………………. 77

5.3 Computational domain…………………………………………………. 79

5.4 Numerical solver……………………………………………………….. 82

5.5 Boundary conditions…………………………………………………… 85

CHAPTER 6: NUMERICAL SIMULATIONS: RESULTS AND ANALYSIS… 87

6.1 Numerical model validation……………………………………………. 87

6.2 Vortex identification……………………………………………………. 97

6.3 Flow field analysis……………………………………………………… 101

6.4 Comparison with counter-rotating flow in previous studies.………… 114

6.5 Vortex inception and development…………………………………….. 118

6.6 Multiple twists…………………………………………………………. 132

6.7 Secondary motion at low Re…………………………………………... 138

6.8 Multiple vortices…………………………………………………..... 145

CHAPTER 7: CONCLUSIONS AND RECOMMENDATIONS………………. 148

7.1 Conclusions………………………………………............................ 148

7.2 Recommendations for future work..……………………….............. 152

REFERENCES…………………………………………………………………. 154

APPENDIX 1: Tangential Velocity Corrections ...……………………………..… 163

LIST OF TABLES

Table A1 Tangential Velocity Corrections 163

LIST OF FIGURES

Figure 1.1 Beloit Converflo hydraulic headbox [Smook 1992]: (a) components schematic, (b) perspective flow schematic. **2**

Figure 1.2 Twisted tape parameters **3**

Figure 1.3 Average tangential velocity profiles downstream of a 60 mm long, 180^o twisted tape swirler at different axial positions. Some of the profiles display counter-rotating flow near the core [Aidun and Parsheh 2007]. **4**

Figure 1.4 Average tangential velocity profiles across the core of a swirling jet induced by rotating pipes at Re = 24000, S=0.5[Facciolo et al 2007]: a) complete profiles, b) core close-up. **5**

Figure 2.1.1 Axial and tangential average velocity profiles for turbulent swirling flows [Baker and Sayre 1974]. **13**

Figure 2.1.2 Rankine vortex [Loiseleux et al 1998]. **14**

Figure 2.1.3 Batchelor vortex [Lessen et al 1974]. **15**

Figure 2.1.4 Radial distribution of the components of the Reynolds stress tensor along the pipe axis [Parchen and Steenbergen 1998]. **18**

Figure 2.1.5 The shear stresses in a turbulent swirling flow at different axial locations [Kitoh 1991]. **19**

Figure 2.3.1 Swirling flow induced by twisted tapes [Kreith and Sonju 1965]: (a) twisted tape inserts and rotating blade devices for 1 and 2 inch diameter pipes, (b) swirl decay at Re = $6.1x10^4$ in a 1 inch diameter pipe. **26**

Figure 2.3.2 Characteristics of the flow in the cross section of a 3 inch diameter pipe with a twisted tape insert at Re 100,000 [Seymour 1966]: (a) velocity field, (b) axial velocity contours**.** **27**

Figure 2.3.3 Axial velocity contours calculated at Re = 1,200 for tapes with different twist ratios [Date 1974] **27**

Figure 2.3.4 Comparison between smoke visualizations and computed flow fields in a 2 inch (50.8 mm) diameter pipe with twisted tape inserts (direction of tape twist from left to right): a), b) [Manglik and Ranganathan 1997], c) [Yerra et al 2007]. **28**

Figure 2.3.5 Transition of secondary flow for y_r = 10, Re = 2,000 [Kazuhisa et al 2004]. **29**

Figure 2.3.6 Numerical simulation of the flow through a pipe with a static mixer insert [Rahmani 2004]: (a) static mixer schematics, (b) cross section velocity vectors, (c) particles location after the 4th element at Re = 1,000. **30**

Figure 2.4.1 Smoke visualization of secondary flow patterns in curved semicircular tubes [Cheng et al 1987]: (a) Re = 530, Dn = 87, (b) Re = 1070, Dn = 175. **31**

Figure 2.4.2 Dean vortices in U-shaped and helical pipes: (a) schematic [Tiwari et al 2006], (b) smoke visualization in U-shaped pipe [Cheng et al 1987], (c) smoke visualization in helical pipes [Yamamoto et al 2002]. **33**

Figure 2.5.1 Vortex breakdown over a delta wing displaying both the helical and the bubble modes [original in Lambourne and Bryer 1961 - reproduced from Leibovich 1978]; **36**

Figure 2.5.2 Visualization of vortex breakdown [Sarpkaya 1971]: (a) bubble mode with helical tail (the flow outside the bubble is unaffected), (b) double helix breakdown mode. **37**

Figure 2.5.3 Double helical mode breakdown in swirling flows induced by tangential injection: (a) dye visualization at Re = 220, (b) cavitating flow at Re = $9x10^4$ [Escudier and Zehnder1982]. **38**

Figure 2.5.4 Vortex breakdown bubble at Re = 2560: (a) dye visualization (b) tangential velocity measurements (S marks stagnation points) [Faler and Leibovich 1978]. **39**

Figure 2.5.5 Helical vortices in a swirling jet at Re = 606 and S = 1.41: (a) vertical and cross-section jet structure, (b) vortex development along the jet axis (locations in diameters) [Billant et al 1998] **40**

Figure 2.5.6 Particle paths in a numerical simulation of a swirling jet show a double helix structure downstream of a breakdown bubble at Re = 150 [Ruith et al 2003]. **41**

Figure 2.5.7 Helical vortices in the swirling flow induced by centrifugal injection into a rectangular container [Alekseenko et al 1999]: (a) setup top view, (b) setup side view with a sketch of the helical vortices, (c) air bubble visualization. **42**

Figure 3.1.1 Setup Schematic **44**

Figure 3.1.2 General view of the experimental setup **44**

Figure 3.1.3 Twisted tape swirler: pitch = 60 mm, diameter = 25.4 mm, pitch to diameter ratio y_r = 2.36 **45**

Figure 3.1.4 Air bubbles injector: a) general view, b)close-up of the perforated needle. **46**

Figure 3.2.1 Light refraction through the different media surrounding the test section for the tangential velocity component (not to scale) **48**

Figure 4.1.1 Variation of the average tangential velocity V_θ along the pipe axis from $z = 150$ mm (5.91d) to $z = 230$ mm (9.06d) for the flow induced by a twisted tape with $H = 60$ mm pitch (y_r = 2.36) at $\mathrm{Re} = 7.7\times10^4$. **54**

Figure 4.1.2 Variation of the normalized angular velocity ω_n along the pipe axis from 0 to 350 mm (13.78d) from swirler exit for flows induced by twisted tapes with H = 45, 60 and 90 mm pitch (1.77, 2.36 and 3.54 twist ratio) at $\mathrm{Re} = 7.7\times10^4$. **54**

Figure 4.1.3 Variation of the normalized angular velocity ω_n with Reynolds number for the swirler with pitch H = 90 mm (y_r = 3.54) on axial locations from 50 mm (2d) to 350 mm (13.78d) from swirler exit. **56**

Figure 4.1.4 Measurements of the normalized average axial velocity V_z / U_b (top) and the normalized rms fluctuations of the axial velocity v'_z / U_b (bottom) in the flow induced by a 60 mm long twisted tape (y_r = 2.36) at Re = 7.7×10^4 (U_b = 3m/s) at three axial locations z = 150, 185 and 230 mm (5.9d, 7.28d and 9.06d) downstream of the swirler. **57**

Figure 4.1.5 Measurements of the normalized average tangential velocity V_θ / U_b (top) and the normalized rms fluctuations of the tangential velocity v'_θ / U_b (bottom) in the flow induced by a 60 mm long twisted tape (y_r = 2.36) at Re = 7.7×10^4 (U_b = 3m/s) at three axial locations z = 150, 185 and 230 mm (5.9d, 7.28d and 9.06d) downstream of the swirler. **57**

Figure 4.1.6 Power spectra analysis of the axial velocity V_z inside the helical vortex core at z = 185 mm (7.28d) and r = -5 mm (-0.2d) for the flow induced by a twisted tape with 60 mm (y_r = 2.36) pitch at Re $= 7.7\times10^4$. **58**

Figure 4.1.7 Normalized average axial velocity V_z / U_b (top) and normalized rms fluctuations of the axial velocity v'_z / U_b (bottom) at $\mathrm{Re} = 7.7\times10^4$ (U_b =3m/s) in the absence of the swirler at two axial locations, $z = 40$ mm (1.57d) and $z = 300$ mm (11.81d) downstream of the contraction end. **59**

Figure 4.2.1 Side and top views of the air bubble streams showing their helical nature and corresponding centerline angular velocities calculated from LDV measurements for the flow induced by a twisted tape with pitch H = 60 mm (y_r = 2.36) at Re = 7.7x10^4 (U_b=3m/s). **61**

Figure 4.2.2 Air bubble visualizations of the helical vortices for the flow induced by the tape with pitch $H = 60$ mm (y_r = 2.36) at Re = 7.7x10^4 (the flow is from right to left): (a) general view, (b) high speed camera close-up at the straight pipe entrance, (c) high speed camera side view, d) high speed camera side view at Re = 2.5x10^4. **63**

Figure 4.2.3 The air bubble stream drifts away from the twisted tape toward the center of the channel (right) and continues smoothly inside the straight pipe (left) (flow induced by the tape with pitch $H = 60$ mm (y_r = 2.36) at Re = 7.7x10^4). **63**

Figure 4.2.4 Helical vortices variation with Re in the range 100,000 to 10,000 **65**

Figure 4.2.5 Vortex development in the flow induced by a 60 mm (2.36d) long twisted tape at Re = 7.7x10^4 in a 1.3 m (51.18d) pipe. **67**

Figure 4.2.6 Cooper twisted tape swirler with 110 mm pitch (y_r = 4.33): (a) inlet view, (b) inside the straight pipe. **68**

Figure 4.2.7 High-speed camera view of the formation of the helical vortices inside the 110 mm (y_r = 4.33) long twisted tape swirler at Re = 7.7x10^4. **68**

Figure 4.3.1 Reconstructed average tangential velocity field of the swirling flow induced by a twisted tape with pitch $H = 60$ mm (y_r =2.36) at Re = 7.7x10^4 (U_b = 3m/s). **69**

Figure 4.4.1 The actual tangential velocity profile of the lower secondary vortex is highlighted in the plot of $\Delta V_\theta = V_\theta(z_1) - V_\theta(z_2)$ where $V_\theta(z_1 = 180mm)$ are the measurements through the center of the lower vortex and $V_\theta(z_2 = 225mm)$ is the main vortex velocity distribution **71**

Figure 4.4.2 Average tangential velocity contours of the secondary vortices after removing the main vortex background at Re = 7.7x10^4 (U_b = 3m/s). The circles show the boundaries of the vortices while the arrows show their rotation. **72**

Figure 4.4.3 Average tangential velocity profiles of the three vortices present in the flow induced by a twisted tape wit pitch H = 60 mm (y_r = 2.36) at Re = 7.7x10^4 (U_b = 3m/s). **73**

Figure 5.3.1 Computational domain for the twisted tape with y_r = 2.36: (a) inlet cross section, (b) cross section showing the inlet of the twisted tape swirler, (c) full 17.72d long computational domain. **81**

Figure 6.1.1 Experimental and numerical visualizations of the development of the helical vortices for the twisted tape with y_r = 2.36 at Re = 7.7x10^4: (a) side view photo of air bubbles streams, (b) side view plot of isobar surfaces (p = 1) and pathlines calculated with a laminar simulation at steady state. **88**

Figure 6.1.2 Relative position in the pipe cross-section of the helical vortices induced by the twisted tape with y_r = 2.36 at Re = 7.7x10^4: (a) experimental photo, (b) laminar numerical simulation. **88**

Figure 6.1.3 Helical vortices generated by a twisted tape with twist ratio y_r = 1.77 (45 mm pitch) at Re = 7.7x10^4: (a) high speed camera visualization, (b) numerical results. **89**

Figure 6.1.4 Helical vortices generated by a twisted tape with twist ratio y_r = 2.36 (60 mm pitch) at Re = 7.7x10^4: (a) high speed camera visualization, (b) numerical results. **89**

Figure 6.1.5 Helical vortices generated by a twisted tape with twist ratio y_r = 3.54 (90 mm pitch) at Re = 7.7x10^4: (a) high speed camera visualization, (b) numerical results. **89**

Figure 6.1.6 Helical vortices induced by a swirler with y_r = 1.77 at Re = 7.7x10^4: (a) isobar surfaces of p = 0.99 for the laminar simulation, (b) isobar surfaces of p =1.01 for the turbulent simulation. **90**

Figure 6.1.7 Helical vortices induced by a swirler with $y_r = 2.36$ at Re = 7.7×10^4: (a) isobar surfaces of p = 1 for the laminar simulation, (b) isobar surfaces of p = 1.02 for the turbulent simulation. **90**

Figure 6.1.8 Cross-section velocity vectors at the end of the swirler (z = 0) for the tapes with $y_r = 1.77$, 2.36 and 3.54 at Re = 7.7×10^4: (top row) laminar simulation, (bottom row) turbulent simulation. **92**

Figure 6.1.9 Comparison between experimental average tangential velocity profiles and calculated tangential velocity profiles from the steady state numerical simulation for the tape with $y_r = 2.36$ at Re = 7.7×10^4 (U_b = 3 m/s): (a) between the helical vortices, (b) through the helical vortices. **93**

Figure 6.1.10 Variation of the normalized tangential velocity with Re: (a) Experimental profiles at z/d = 7.48, (b) Numerical results at z/d = 8.03 (the profiles collected through the secondary co-rotating helical vortices display counter-rotating flow). **95**

Figure 6.1.11 Velocity vectors calculated with an inviscid numerical simulation for the tape with $y_r = 2.36$ at Re = 7.7×10^4 at two axial locations: (a) z/d = 0, (b) z/d = 10. **97**

Figure 6.2.1 Visualizations of the velocity field in the cross-section plane at z/d = 6.57 in the flow induced by a twisted tape with $y_r = 2.36$ at Re = 7.7×10^4 (a) velocity vectors, (b) stream lines. **99**

Figure 6.2.2 Normalized vorticity magnitude contours at z/d = 6.57 in the flow induced by a twisted tape with $y_r = 2.36$ at Re = 7.7×10^4 **100**

Figure 6.2.3 Comparison between vortex identification with isobar surfaces and λ_2 lines: (a) full domain, (b) close-up view of the swirler. **101**

Figure 6.3.1 Isobar surfaces, pathlines and velocity vectors identify helical vortices in the flow field induced by a twisted tape with $y_r = 2.36$ at Re = 7.7×10^4 calculated with a steady state laminar simulation (perspective view). **102**

Figure 6.3.2 Variation of the flow parameters between and through the helical vortices (along the horizontal and vertical diameter, respectively) for the flow induced by a twisted tape with $y_r = 2.36$ at Re = 7.7×10^4 (U_b = 3m/s) in the cross-section plane at z/d = 6.57 downstream of the swirler: (a) velocity vectors, (b) tangential velocity, (c) pressure, (d) axial velocity. **103**

Figure 6.3.3 2D distribution of the flow parameters for the flow induced by a twisted tape with $y_r = 2.36$ at Re = $7.7x10^4$ (U_b = 3 m/s) in the cross-section plane at z/d = 6.57 downstream of the swirler: (a) normalized pressure p/P_0, (b) normalized tangential velocity V_θ/U_b, (c) normalized axial velocity V_a/U_b, (d) normalized radial velocity V_r/U_b. **105**

Figure 6.3.4 Helical vortices for the three cases investigated experimentally at Re = $7.7x10^4$: (a) y_r = 1.77 tape, (b) y_r = 2.36 tape, (c) y_r = 3.54 tape. **108**

Figure 6.3.5 The flow field at the swirler exit described by velocity vectors (top row) and streamlines (bottom row) at Re = $7.7x10^4$: a) y_r = 1.77 tape, b) y_r = 2.36 tape, c) y_r = 3.54 tape. **109**

Figure 6.3.6 Pressure contours at axial positions where the helical vortices are in vertical and horizontal positions. The flow is induced by a tape with y_r = 2.36 at Re = $7.7x10^4$). **109**

Figure 6.3.7 Vorticity distribution for the flow induced by a twisted tape with twist ratio y_r = 2.36 at Re = $7.7x10^4$ (U_b = 3 m/s) in the cross section plane at z/d = 7.28: (a) normalized vorticity magnitude, (b) normalized axial vorticity component **110**

Figure 6.3.8 Swirl decay along the pipe axis as quantified by the variation of the swirl number S for the three swirlers with twist ratios 1.77, 2.36 and 3.54 at Re = $7.7x10^4$ **112**

Figure 6.3.9 Swirl number variation with Re. The swirl number S is calculated at z/d = 1 downstream of the swirler with twist ratio y_r = 2.36 (60 mm pitch in the experiments). **113**

Figure 6.3.10 Swirl decay along the pipe axis as quantified by the variation of the swirl number S for the 180^o, 60 mm pitch swirler at Re in the range 10^2 to 10^5. **113**

Figure 6.4.1 Flow structures in the swirling jet induced by a rotating pipe [Meciel et al. 2008] (in these plots x is the jet axis): (a) snapshots of instantaneous vortical structures identified with λ_2 iso-surfaces, (b) side-view close-up at the pipe exit, (c) instantaneous velocity field. **115**

Figure 6.4.2 Helical vortices identified by isobar surfaces of p/P_0 = 1.03 and vortex cores identified with λ_2 method in the swirling flow induced by a swirler with d = 25.4mm and y_r = 2.36 at Re = $7.7x10^4$ **116**

Figure 6.4.3 Velocity vectors at several axial locations following a 40% increase in the pipe diameter downstream from the swirler with y_r =2.36 at Re = 7.7x10^4 **117**

Figure 6.5.1 Swirler inlet: (a) photo of the swirler, (b) velocity vectors at the inlet (at the far end in figure 6.5.1a) **119**

Figure 6.5.2 Flow field inside the swirler after 5^o twist (~2mm): a) static pressure contours after 5^o twist, b) Wall shear stress contours [Pa] and cross-section velocity vectors, c) normalized tangential vorticity, d) normalized radial vorticity **120**

Figure 6.5.3 Secondary vortex development: (a) wall shear stress and velocity vectors after 30^o twist (10 mm), (b) normalized axial vorticity and velocity vectors after 60^o twist (20mm). **123**

Figure 6.5.4 Flow field inside the swirler after 75^o twist (25mm):a) streamlines b) normalized axial vorticity and velocity vectors, c) normalized tangential vorticity and velocity vectors, d) normalized radial vorticity and velocity vectors. **124**

Figure 6.5.5 Vortex formation for a twisted tape with y_r = 2.36 (60 mm pitch) at Re = 7.7x10^4. **126**

Figure 6.5.6 Variation of the normalized axial vorticity in the center of the secondary vortex along the twisted tape for the flow through an 180^o twisted tape with y_r = 2.36 at Re = 7.7x10^4. **127**

Figure 6.5.7 Formation of the secondary vortices inside the swirler. The plots show isobar surfaces of p/P_0 = 1 and cross-section planes with tangential velocity vectors for the tape with y_r = 2.36 (60 mm pitch) at Re = 7.7x10^4: (a) side view, (b) front view, (c) actual swirler. **128**

Figure 6.5.8 Axial velocity contours (a) and velocity vectors (b) at the exit of the twisted tape swirler with y_r = 2.36 at Re = 7.7x10^4. **130**

Figure 6.5.9 Change of position for the secondary vortices inside the swirler: (a) the vortices appear first after 60^o twist; (b) secondary vortices at the swirler exit, after 180^o twist. The red lines highlight the fact that the angle between the lines through the secondary vortices in the two plots is approximately 90^o. **131**

Figure 6.6.1 Effect of multiples twists on the secondary vortices: (a) 180^o twist, (b) 360^o twist, (c) 720^o twist, (d) 1080^o twist. **132**

Figure 6.6.2 Helical vortices induced by a 360^o twisted tape with 60 mm pitch (y_r = 2.36) at Re = $7.7x10^4$: a) high speed camera visualization, b) numerical simulation. **133**

Figure 6.6.3 Cross-section planes on a tape with 1080^o twist: (a) full domain, (b) close-up of the last twists (between 540^o and 1080^o) with isobar surfaces of $p/P_0 = 0$.
. **133**

Figure 6.6.4 Development of the secondary vortices **134**

Figure 6.6.5 Normalized axial vorticity inside a twisted tape swirler with y_r =2.36 and multiple twist at Re = $7.7x10^4$: a) variation along the swirler, b) cross-section velocity vectors and normalized axial vorticity after 1080^o twist. **137**

Figure 6.7.1 Secondary motion at low Re: (a) velocity vectors at the swirler exit, (b) side views of the swirler with secondary vortices identified by λ_2 method (the flow is from right to left). **139**

Figure 6.7.2 Squared circulation distribution at the swirler exit for Re = 500 (U_b = 0.02 m/s): (a) colored velocity vectors, (b) radial profiles along the radii (R = 0.0127 m) at 45^o and 135^o shown in plot (a). **141**

Figure 6.7.3 Flow characteristics at the swirler exit for Re 100, 250 and 500 (bulk velocities 4, 10 and 20 mm/s): (a) tangential velocity, (b) centrifugal force density, (c) total pressure, (d) circulation squared, e) axial vorticity; (red indicates maxima). **143**

Figure 6.7.4 Streamlines at the swirler exit at different Re **144**

Figure 6.8.1 Complex 180^o swirlers: (a) three chambers, (b) four chambers. **145**

Figure 6.8.2 Secondary vortices in 180^o, 60 mm long swirlers (y_r = 2.36) at Re = $7.7x10^4$ identified by isobar surfaces $p/P_0 = 1$: (a) three chambers swirler, (b) four chambers swirler. **146**

Figure 6.8.3 Streamlines for multiple vortices: a), b), c) 3 vortices; d), e), f) 4 vortices **147**

NOMENCLATURE

Latin symbols

Symbol	Units	Description
a	mm	seeding particles diameter
A	m^2	area
A_d	-	coefficient for exponential tangential velocity profile
BX	mm	glass tank half thickness
d	mm	pipe inner diameter
$d2$	mm	pipe inner diameter after step
d_{fr}	μm	fringe spacing
Dn	-	Dean number
err	-	relative error for actual position calculations
f	mm	focal length
f_d	Hz	Doppler frequency
F_{cf}	N/m^3	centrifugal force density
g	m/s^2	gravitational acceleration
G_θ	m^2/s^2	axial flux of tangential momentum
G_x	m/s^2	axial flux of axial momentum
G_{x_avg}	m/s^2	average axial flux of axial momentum

Symbol	**Units**	**Description**
H	mm	twisted tape 180° pitch
H_{ω}	mm	helical vortex 180° pitch
n	m	normal vector
n_a	-	index of refraction for air (= 1)
n_{g1}	-	index of refraction for the glass container wall (= 1.51)
n_{g2}	-	index of refraction for the glass pipe wall (= 1.47)
n_m	-	index of refraction for glycerin (= 1.47)
n_x	-	number of grid points in x direction (width)
n_y	-	number of grid points in y direction (height)
n_z	-	number of grid points in z direction (axial)
n_w	-	index of refraction for water (= 1.33)
N_c	-	number of cells intersected by a cross-section plane
M	-	number of measurements used for velocity field reconstruction
P	Pa	pressure
P_0	Pa	atmospheric pressure 101,325 Pa
P_u	Hz	first invariant of the characteristic equation
Q	-	non-dimensional circulation
Q_u	Hz^2	second invariant of the characteristic equation
r	mm	radial position
r_0	m	radial position of maximum tangential velocity
R	mm	inner radius of the test pipe

Symbol	**Units**	**Description**
R_c	mm	radius of curvature of the path of the U-bend pipe
R_o	mm	outer radius of the test pipe
R_u	Hz^3	third invariant of the characteristic equation
Re	-	Reynolds number
S	m	unit length
S	-	swirl number
S_0	-	swirl number at reference position x_0
S_u	tensor	rate of strain
SW	-	non-dimensional number characterizing twisted tapes swirling flow
t_{g1}	mm	glass container wall thickness
u_i	m/s	average velocity component in vector notation (Cartesian coordinates)
u_i'	m/s	fluctuating velocity component in vector notation (Cartesian coordinates)
u_τ	m/s	friction velocity
U	-	non-dimensional axial velocity
U_b	m/s	bulk velocity (average velocity corresponding to Re number)
v_r'	m/s	fluctuation of radial velocity
v_θ'	m/s	fluctuation of tangential velocity
v_z'	m/s	fluctuation of axial velocity
V	m/s	velocity vector

Symbol	**Units**	**Description**
V_0	m/s	maximum tangential velocity
$\tilde{V}_i$	m/s	instantaneous velocity in *i* direction
$\overline{V}_i$	m/s	average velocity in *i* direction
V_r	m/s	average radial velocity
V_s	m/s	settling velocity of seeding particles
V_w	m/s	tangential velocity of rotating pipe
V_z	m/s	average axial velocity
V_θ	m/s	average tangential velocity
x_i	m	spatial coordinate in vector notation
$x_{t\arg et}$	mm	desired radial location for LDV measurements
$x_{calculated}$	mm	calculated radial location for LDV measurements
Δx	m	spatial resolution in x direction for numerical simulation
X	mm	apparent LDV measurement location
X'	mm	actual LDV measurement location
y_r	-	twist ratio ($= H / d$)
Δy	m	spatial resolution in y direction for numerical simulation
y_w	mm	distance from the wall
y^+	-	non-dimensional distance from the wall measured in wall units
W	-	non-dimensional tangential velocity

Symbol	Units	Description
Z	mm	axial position
z_0	mm	reference axial location for swirl measurements
Δz	m	spatial resolution in z direction for numerical simulation

Greek symbols

Symbol	Units	Description
β	-	swirl decay coefficient
Γ	m^2/s	circulation
δ	mm	tape thickness
δ_ν	mm	wall unit (viscous length)
Δ	Hz^6	discriminant of the characteristic equation
ε	-	relative error
θ	degree	angle between diameters for reconstruction
θ_i	degree	diffraction angles of light for LDV ($i = 1 \div 6$)
κ	degree	beam half angle $3.97°$
κ'	degree	distorted beam half angle inside the pipe
λ	Hz	eigenvalue of the velocity gradient
λ_{ci}	Hz	complex part of the eigenvalue of the velocity gradient
λ_{cr}	Hz	real part of the eigenvalue of the velocity gradient
λ_n	nm	light wavelength

Symbol	**Units**	**Description**
μ_g	kg/m s	dynamic viscosity of water
ν	m^2/s	kinematic viscosity of water
ξ	-	normalized turn angle for a twisted tape simulation
ρ	kg/m^3	density of flow medium (water)
$\Delta\rho$	kg/m^3	difference between the density of the medium and the density of the particles for seeding
σ_v	m/s	standard deviation of LDV velocity measurements
τ	N/m^2	shear stress
τ_b	s	total burst time
τ_w	N/m^2	wall shear stress
Φ	-	generic variable for integration
ω	Hz	angular velocity
ω_0	Hz	centerline angular velocity
ω_n	-	normalized angular velocity at the centerline
Ω	Hz	vorticity
Ω_r	Hz	radial vorticity
Ω_z	Hz	axial vorticity
Ω_θ	Hz	tangential vorticity

SUMMARY

The present study describes the flow characteristics of swirling flows induced by twisted tape inserts in circular pipes. The study is focused on the secondary flow which is investigated experimentally and with numerical models. The results are expected to improve the paper manufacturing process by identifying and removing the detrimental secondary flow.

Experimental tests show for the first time the existence of two co-rotating helical vortices superimposed over the main swirling flow, downstream of twisted tapes. The close proximity of the two co-rotating vortices creates a local counter-rotating flow at the pipe centerline. The flow is analyzed using LDV measurements and high speed camera visualization with fine air bubbles seeding which confirm that the helical vortices are stable. After extracting the characteristic tangential velocity profiles of the main vortex and of the two secondary vortices, it was observed that the maximum tangential velocity of all three vortices is the same, approximately half of the bulk velocity. The winding of the helical vortices is in the swirl direction and the pitch of the helical vortices is found to be independent of the inlet velocity.

The experimental findings are confirmed by numerical simulations. The numerical results show that the helical vortices originate inside the swirler and evolve from single co-rotating vortices on each side of the tape. The flow characteristics are analyzed in detail. Swirlers with multiple twists and multiple chambers are shown to have less stable secondary motion and could be employed in applications were the secondary motion is detrimental.

CHAPTER 1

INTRODUCTION

This study investigates the characteristics of swirling flows induced by 180^o twisted tapes in circular pipes. The main goal of the study is to elucidate the secondary motion. The results of this investigation are expected to improve technology associated primarily with the paper manufacturing industry, however swirling flows have numerous other applications including homogenizing mixtures for casting or production of chemicals, enhancing heat transfer in heat exchangers and stabilizing flames and breaking fuel droplets in combustion.

Swirling flows are flows combining rectilinear motion and rotation around the flow axis. The average motion is characterized by spiral streamlines, increasing the path traveled by the fluid compared to a flow without rotation. The most common swirl generation systems are angled vanes, eccentric fluid injection, rotating pipes and twisted tape inserts.

The secondary flow presented in this study consisting of helical vortices downstream of twisted tapes swirlers has never been documented before. These new findings are expected to benefit both the paper industry and swirling flow research in general, particularly heat transfer applications where twisted tapes are used.

1.1 Motivation

In the paper manufacturing industry a mixture of wood fibers, water and chemicals named pulp is spread on a forming wire mesh and dried to form a paper sheet. The aspect and strength of the final paper depend on the isotropy of the fiber distribution.

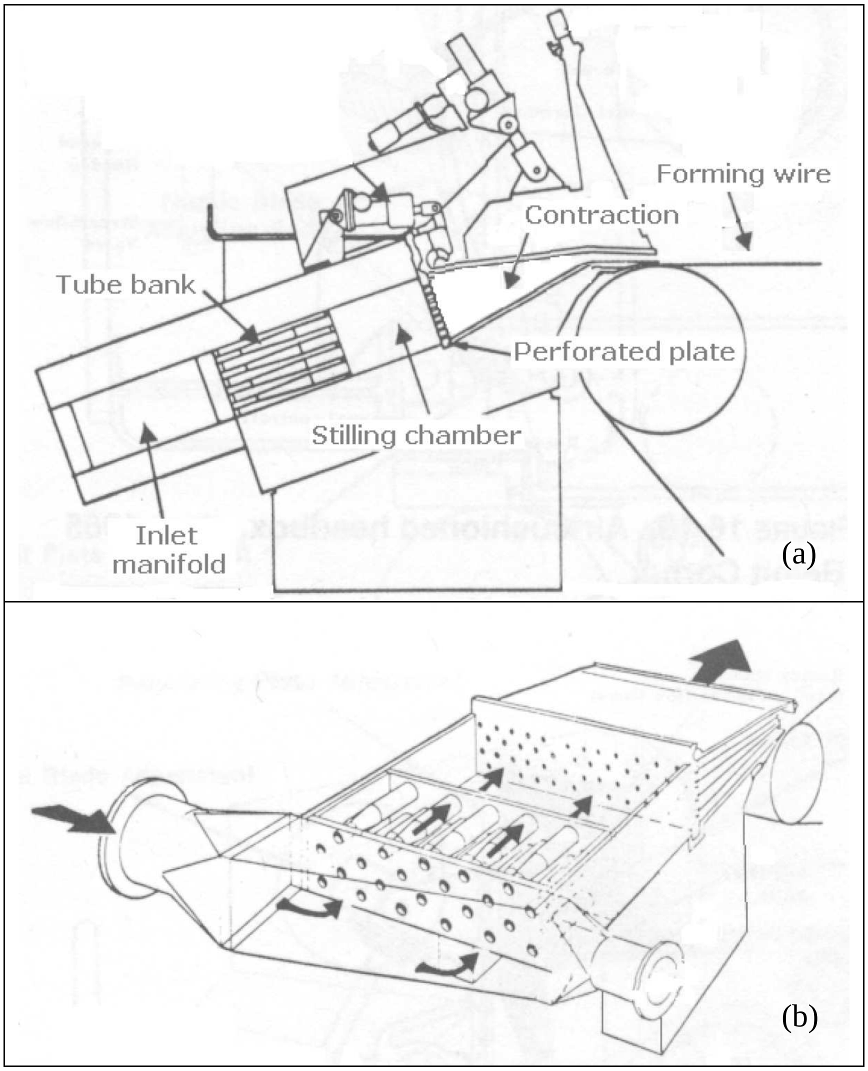

Figure 1.1 Beloit Converflo hydraulic headbox [Smook 1992]: (a) components schematic, (b) perspective flow schematic.

A schematic of the paper forming process is shown in figure 1.1. In order to spread the pulp into a thin sheet, the pulp is first passed through a tube bank which provides a fast transition from a circular cross-section to a wide rectangular cross section.

The average flow speed in the forming section is approximately 3 m/s. As fibers tend to align preferentially in the flow direction, inducing swirl and fine turbulence in the tubes was shown to be beneficial for the quality of the pulp jet [Aidun 1995]. The fiber distribution isotropy is improved, producing stronger paper with less wood consumption [Aidun 1998, 1999, 2000, 2002]. One of the systems used to generate swirl is to insert 180^o twisted tapes in the tubes of the tube bank shown in figure 1.1. However, preliminary tests showed the presence of secondary motion in the flow downstream of the tube bank containing twisted tapes, which creates streaks and non-uniformities in paper, compromising its quality.

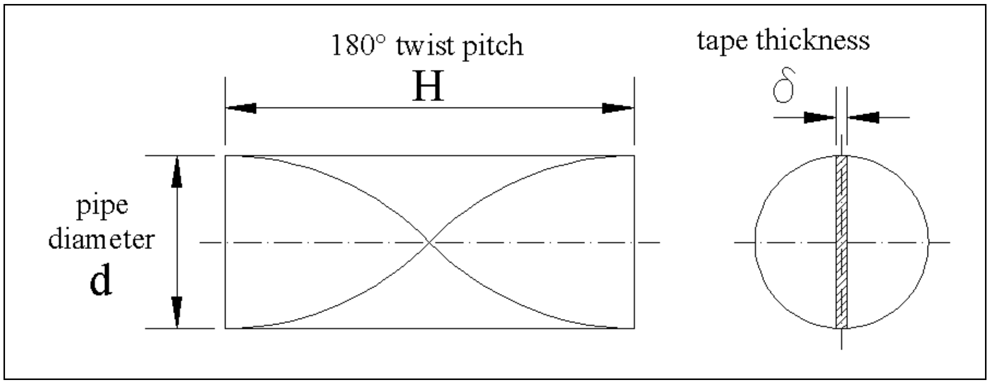

Figure 1.2: Twisted tape parameters.

Traditionally, twisted tapes have been used both for heat transfer improvement and mixing of chemical products. The main characteristics of twisted tapes are presented in figure 1.2. The defining parameters are the $180°$ pitch H, the pipe diameter d and the tape thickness δ. The relevant non-dimensional parameters are the Reynolds number $\mathrm{Re} = d \cdot U_b / \nu$ and the twist ratio $y_r = H / d$ where U_b is the bulk velocity and ν is the kinematic viscosity. Low values of the ratio y_r correspond to strong twist and high swirl numbers.

Prior to this investigation, the presence of secondary motion in the swirling flow downstream of a twisted tape swirler was indicated by a periodic change of the velocity profiles near the pipe centerline observed in Laser Doppler Velocimetry (LDV) measurements of the tangential velocity [Islek 2004, Aidun and Parsheh 2007]. The flow appeared to periodically counter-rotate and then revert to a normal swirling flow (figure 1.3). No explanation was found in published literature as the only similar reports are documenting a non-periodic, low amplitude counter-rotating flow in a swirling jet induced by a rotating pipe (figure 1.4).

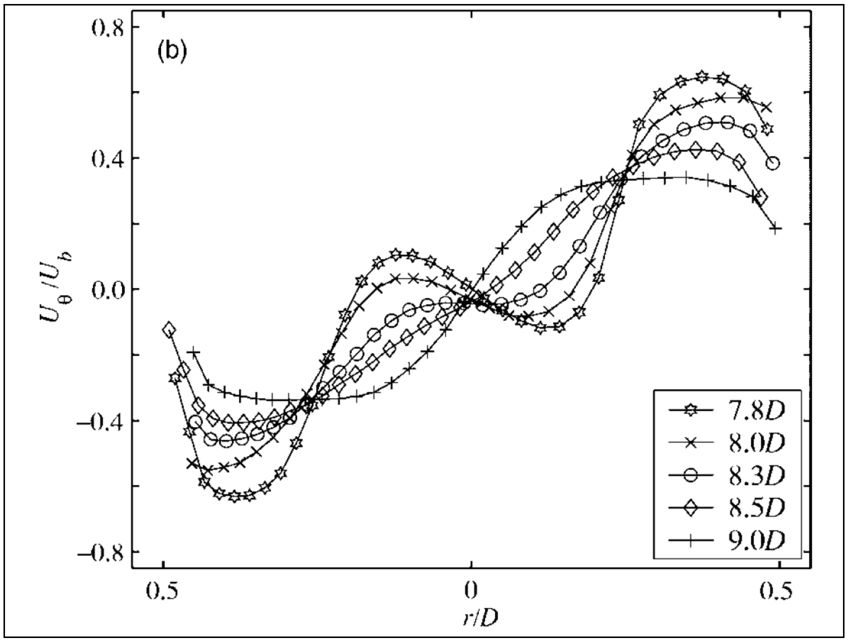

Figure 1.3: Average tangential velocity profiles downstream of a 60 mm long, 180° twisted tape swirler at different axial positions. Some of the profiles display counter-rotating flow near the core [Aidun and Parsheh 2007].

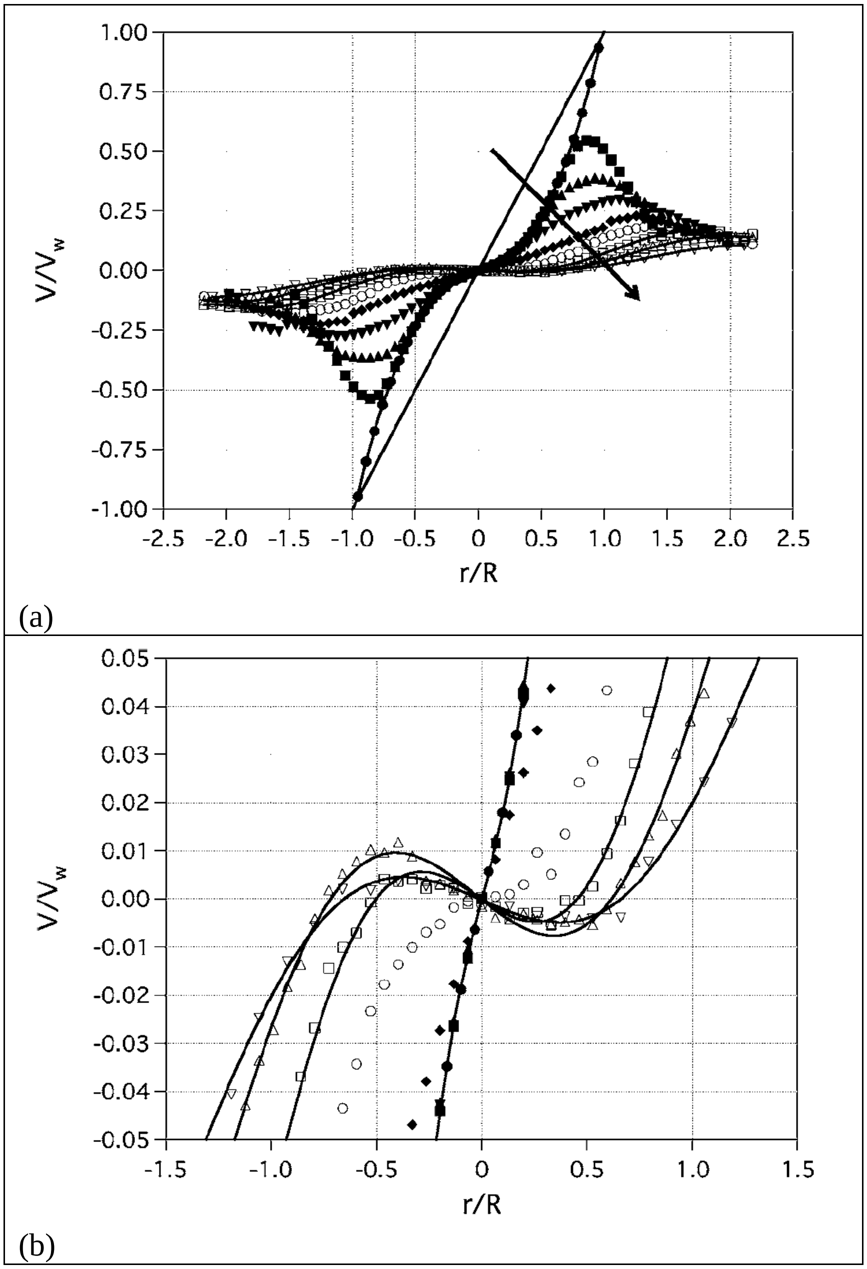

Figure 1.4: Average tangential velocity profiles across the core of a swirling jet induced by rotating pipes at Re = 2.4x10^4, S=0.5 [Facciolo et al. 2007]: a) complete profiles, b) core close-up. *x* represents axial distance from pipe exit and the symbols are:
(•) $x/D=0$, (■) $x/D=1$ (▲) $x/D=2$, (▼) $x/D=3$, (◆) $x/D=4$,
(∘) $x/D=5$, (□) $x/D=6$, (△) $x/D=7$, (▽) $x/D=8$

The authors of the rotating pipe jet experiments [Facciolo and Alfredsson 2004, Facciolo et al. 2007, Maciel et al. 2008] attributed the counter-rotating flow to the influence of the cross flow Reynolds stress. Using a simplified form of the conservation of tangential momentum developed for fully developed axially rotating pipe flow (assuming no axial or tangential gradients) they showed that the mean tangential velocity depends on the cross flow Reynolds stress as:

$$V_\theta(r) = V_w \frac{r}{R} - \frac{r}{\nu} \int_r^R \overline{v_\theta v_r} \frac{dr}{r} \qquad (1.1)$$

where V_w is the tangential velocity of the rotating pipe, R is the inner radius of the pipe and $\overline{v_\theta v_r}$ is the cross flow Reynolds stress. Based on equation (1.1) the authors suggested that a large, positive $\overline{v_\theta v_r}$ could produce a deviation from the solid-body rotation large enough to create a counter-rotating core. However, the counter rotating flow in jets was not spatially periodic as the flow observed in the flow in pipes with twisted tape inserts [Aidun and Parsheh 2007].

The main objective of the present investigation is to identify the cause of the secondary flow in swirling flows induced by short twisted tape inserts in circular pipes in order to eliminate it. Eliminating the secondary flow will improve the isotropy of the fiber distribution in paper, which would allow achieving a specific strength with less wood consumption. Also, improving the overall quality of the paper would reduce the losses resulting from discarded substandard paper (with streaks or holes) and the production time losses caused by sheet breaks. Due to the large scale of the industry, small efficiency improvements result in significant financial savings.

The paper industry is a multibillion dollars industry covering a large range of products from tissues to packaging. There are numerous paper production centers throughout the world with a considerable environmental and economical impact associated with their large consumption of wood and energy. The present study is part of the larger effort to improve the efficiency of the industry, improving its economic output while reducing its environmental impact [Islek 2004].

1.2 Objectives

The investigation presented here has two main parts associated with its two complementary objectives. The first part identifies the cause of the secondary flow downstream of short twisted tapes using experimental techniques. The second part investigates how the secondary flow appears and how to eliminate it using numerical modeling. This exploratory study evolved sequentially and the steps in the second part were determined by the results of the first part. The following section is an outline of the steps followed to meet each objective and also a short summary of the main findings corresponding to each step, which led to the current structure of the study.

Objective I: *Identify the Cause of the Secondary Flow*

- The existing literature is reviewed in order to find similar flow reports
    - Counter-rotating flow was never observed before downstream of twisted tapes
    - The only previous case of counter–rotating flow was observed in jets induced by rotating pipes but it was not periodic
- Laser Doppler Velocimetry (LDV) measurements are collected in the swirling flow induced by a twisted tape with a 60 mm pitch to confirm the previous results [Aidun and Parsheh 2007]
    - The previous results are confirmed by the LDV measurements
    - The LDV measurements are collected along the entire 350mm (14d) long test section with a 5 mm (0.2d) axial resolution

- New measurements are performed for twisted tapes with 45 and 90 mm pitch to identify pitch dependency
    - The flow behavior is similar to that observed downstream of the 60 mm pitch twisted tape
- Direct visualization of the secondary motion is performed to determine its structure and the results are correlated with the LDV measurements
    - An air bubbles injection system was designed and installed in the flow circuit
    - The air bubble distribution shows the presence of a stable pair of helical vortices
- The results are processed in order to determine the characteristics of the secondary flow
    - The tangential velocity field is reconstructed from LDV measurements
        - The helical vortices are co-rotating with the primary vortex
        - The helical vortices are responsible for the counter-rotating flow region near the centerline which is not axi-symmetric

Objective II: ***Identify Methods to Eliminate the Secondary Flow***

- A numerical model is developed
    - The test section is modeled at its actual size using the commercial software FLUENT
- The model is validated with experimental results
    - All flow features are qualitatively recovered with a laminar formulation
- The flow is investigated inside the twisted tape swirler
    - The secondary motion originates inside the swirler
    - The characteristics of the swirler determine the characteristics of the helical vortices

- The secondary motion formation mechanism is identified
    - The vortices are a result of pressure and centrifugal imbalances created by the swirler geometry
- The flow is modeled numerically for different swirler configurations
    - Tests are performed for twisted tapes with multiple twists
    - Tests are performed for twisted tapes with multiple chambers
- Configurations which have the potential to create swirl without secondary motion are identified
    - Multiple chambers could create swirl without secondary motion within a short distance from the swirler

As a result of this investigation several phenomena were observed for the first time. To the knowledge of the author, the following findings are original contributions of the present study:

- First observation and characterization of co-rotating helical vortices downstream of the twisted tape.
- First explanation of the counter-rotating core of the primary vortex based on co-rotating helical vortices.
- First numerical modeling of the formation of helical vortices downstream of twisted tapes swirlers.
- First indications that the secondary motion inside twisted tape swirlers consists of single co-rotating vortices each side of the tape, as all previous studies report two counter-rotating vortices.
- First accurate, non-intrusive, LDV velocity measurements through helical vortices
- First detailed high speed camera visualizations of helical vortices showing the 3D motion.

Some of the experimental results presented in this study were published in Cazan and Aidun [2009].

CHAPTER 2

LITERATURE REVIEW

2.1 Turbulent swirling flows

Many industrial devices with rotating parts (turbines, compressors) operate with high Reynolds number flows where swirl and turbulence interact. In laboratories, due to size constrains, swirling flows are reproduced either using static devices (angled vanes, twisted tapes, eccentric injection) or dynamic devices like rotating pipes. Since counter-rotating flow has been previously attributed to turbulence, as explained in the previous chapter, the following section presents a summary of turbulence/swirl interactions.

Swirling flows are a result of the superposition of axial flow and vortex motion. The equations governing the swirling flow are the definition of vorticity $\Omega = \nabla \times V$ (also equal to twice the rate of rotation for a fluid rotating as a solid body), mass conservation $\nabla \cdot V = 0$ and the vorticity equation. For incompressible flows the vorticity equation states that the rate of change of vorticity is given by:

$$\frac{D\Omega}{Dt} = (\Omega \cdot \nabla)V + \nu \cdot \nabla^2 \Omega \qquad (2.1.1)$$

The first term on the right side is called the vortex stretching term. If the strain rate produced by the velocity gradients act to stretch the material line aligned with Ω, then the magnitude of Ω increases correspondingly. The second term on the right side is a viscous diffusion term describing the rate of change of Ω due to molecular diffusion of vorticity.

One convenient way to quantify the vortex motion is using the circulation defined as the line integral of the tangential component of the velocity taken around a closed curve in the flow field. The circulation is related to the vorticity through Stokes theorem:

$$\Gamma = \oint V \cdot ds = \iint \Omega \cdot n \cdot dA \qquad (2.1.2)$$

If the flow is inviscid, the circulation is governed by the Kelvin theorem, which states that no circulation is produced or destroyed in the absence of viscous shear:

$$\frac{D\Gamma}{Dt} = 0 \qquad (2.1.3)$$

The tangential velocity induced by a vortex is related to the circulation through the equation:

$$V_\theta(r) = -\frac{1}{4\pi} \iiint \frac{r_1 \times \Omega}{\left|r - r_1\right|^3} dv \qquad (2.1.4)$$

which reduces to the Biot-Savart law if the vorticity is concentrated to a single line filament of circulation Γ [Widnall 1975]:

$$V_\theta(r) = -\frac{\Gamma}{4\pi} \int \frac{r_1 \times dr_1}{\left|r - r_1\right|^3} \qquad (2.1.5)$$

The amount of swirl present in the flow is usually described by a non-dimensional swirl number [Gupta et al. 1984]. The swirl number (or swirl intensity) is defined as the ratio of the angular momentum flux to the axial momentum flux:

$$S = \frac{\text{axial flux of tangential momentum}}{(\text{radius}) \cdot (\text{axial flux of axial momentum})} = \frac{G_\theta}{R \cdot G_x} \qquad (2.1.6) \quad \text{where}$$

$$G_\theta = \int \rho \cdot r \cdot V_\theta \cdot V_x \cdot dA \qquad (2.1.7)$$

$$G_x = \int \rho \cdot V_x^2 \cdot dA \qquad (2.1.8)$$

This formula can be further simplified if an average axial momentum G_{x_avg} is used instead of G_x such that:

$$R \cdot G_{x\_avg} = \pi \cdot R^3 \cdot \rho \cdot U_b^2 \qquad (2.1.9)$$

in which case S represents the non-dimensional angular momentum flux:

$$S = \frac{G_\theta}{\pi \cdot R^3 \cdot \rho \cdot U_b^2} \qquad (2.1.10)$$

Since S represents a ratio of two integrated quantities, two swirling flows with different velocity distributions may have the same swirl number. The swirl number does not differentiate between swirling flows with or without secondary motion. For swirling flows induced by rotating pipes the swirl number is expressed as the ratio of the tangential velocity of the pipe V_w and the bulk velocity U_b [Facciolo et al. 2007]:

$$S = \frac{V_w}{U_b} \qquad (2.1.11)$$

It is usually assumed that the radial pressure gradient and the mean tangential velocity component are related by:

$$\frac{dP}{dr} \approx \frac{\rho \cdot V_\theta^{\,2}}{r} \qquad (2.1.12)$$

where V_θ^2 / r is the centripetal acceleration [Baker and Sayre 1974]. This simplified form of the radial momentum equation in cylindrical coordinates shows that there are strong pressure gradients in the radial direction and also that as the swirl decays the pressure becomes more uniform. When the swirl decays the resulting adverse pressure gradients in the axial direction can produce flow reversal [Kitoh 1991, Pashtrapanska et al. 2006].

The decay of the swirl follows an exponential distribution in the axial direction [Smithberg and Landis 1964]:

$$S = S_0 \cdot \exp(-\beta \cdot (z - z_0)/d) \qquad (2.1.13)$$

where S_0 is the swirl intensity at a reference position z_0 and z is the axial location were the swirl intensity S is calculated. Experimental measurements [Baker and Sayre 1974, Kitoh 1991] revealed that the decay coefficient β is dependent on Re, increasing as the Re decreases (the decay is faster at low Re). Kitoh [1991] showed that there is no universal formula fitting all swirling flows as the decay depends on the geometry generating the swirl and initial swirl intensity.

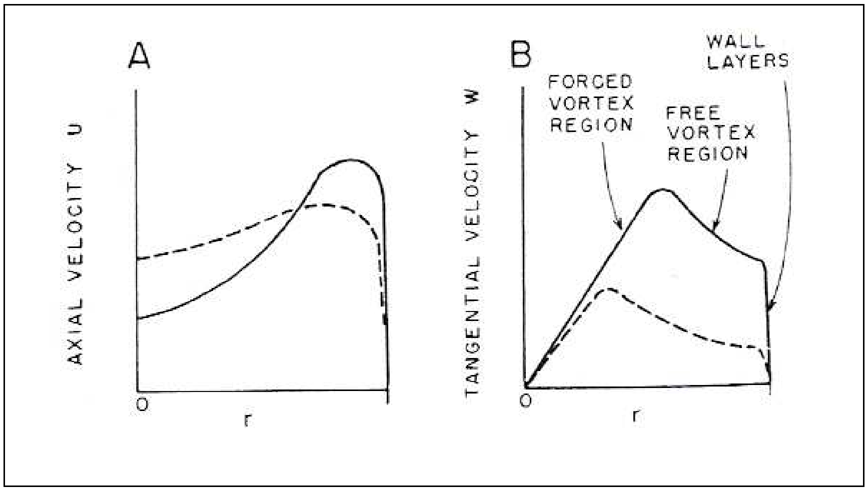

Figure 2.1.1: Axial and tangential average velocity profiles for turbulent swirling flows: ── upstream, - - - downstream [Baker and Sayre 1974].

Most studies [Algifri et al. 1987, Baker and Sayre 1974, Kitoh 1991] show that there are three flow regions in the turbulent swirling flow inside a pipe, regions characterized by the average tangential velocity distribution (figure 2.1.1). These regions are a forced vortex region near the pipe axis where the flow rotates at a constant angular velocity $\omega = V_\theta / r = constant$ followed by a free vortex region where the angular momentum is constant $\omega = V_\theta \cdot r = constant$ and a wall region where viscosity dissipates the angular momentum and tangential velocity decreases sharply.

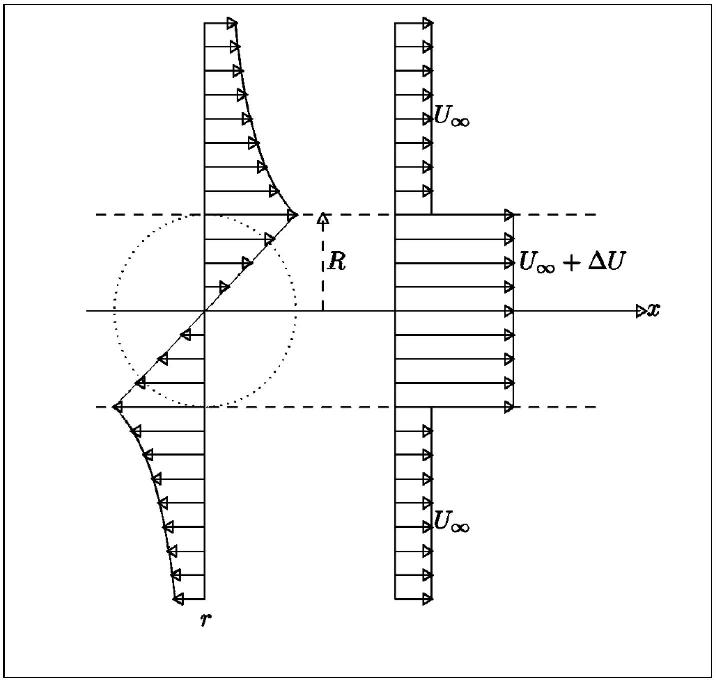

Figure 2.1.2 : Rankine vortex [Loiseleux et al 1998].

The combined vortex structure is common to both confined swirling flows in pipes and swirling jets. The combined vortex was described first by Rankine [1888] and is usually called a “Rankine vortex”. The mathematical formulation of the variation of the tangential velocity V_θ with the radial distance r from the vortex axis is:

$$V_\theta(r) = \begin{cases} V_0 \cdot \dfrac{r}{r_0} & for\ r \le r_0 \\ V_0 \cdot \dfrac{r_0}{r} & for\ \ r > r_0 \end{cases} \qquad (2.1.14)$$

where $V_0 = \omega \cdot r_0$ is the maximum tangential velocity, r_0 is the radial location of V_0 and ω is the constant angular velocity in the core region corresponding to a solid body rotation. The tangential and axial velocity profiles for a swirling jet with Rankine velocity distribution are shown in figure 2.1.2.

Most experiments show a smooth transition between the core and the free vortex region as opposed to the singularity in the Rankine model, which neglects the shear layer. A more realistic description of the tangential velocity distribution for the combined vortex is an exponential distribution sometimes called Gaussian due to its mathematical similarity with the Gaussian distribution in statistics. The model is also called a "Batchelor vortex" after the author of a paper which described the trailing vortices behind a wing [Batchelor 1964], but a similar solution was described previously by Burgers [1948] while investigating turbulent flows.

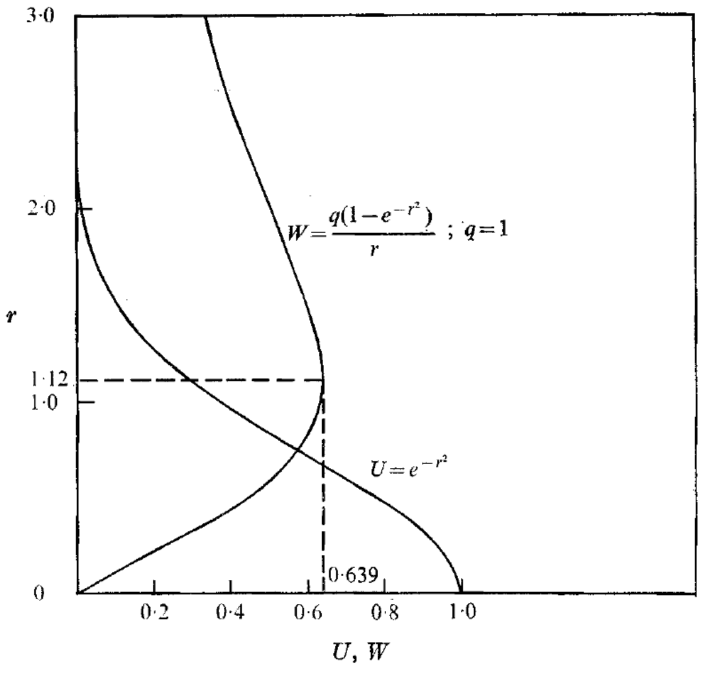

Figure 2.1.3 : Batchelor vortex [Lessen et al. 1974].

The mean tangential velocity distribution is given by:

$$V_\theta(r) = \Gamma \frac{1 - e^{-A_d \cdot r^2}}{r} \qquad (2.1.15)$$

where Γ is the circulation and A_d is a constant [Burgers 1948, Batchelor 1964, Lessen et al. 1974]. Figure 2.1.3 shows the non-dimensional velocity distribution of a swirling jet where W is the non-dimensional mean tangential velocity, U is the non-dimensional axial velocity, q is the non-dimensional circulation and r is a non-dimensional radius [Lessen et al 1974]. In the non-dimensional form the tangential velocity distribution has a maximum of 0.639 at r = 1.12 so the dimensional form can be recovered if the results are adjusted accordingly.

In the wall region where viscous effects are dominant the mean axial velocity follows approximately the classic “log law” near the wall [Kitoh 1991, Klepper 1972]:

$$V_z / u_\tau = 2.5 \cdot \ln y^+ + 5.5 \qquad (2.1.16)$$

where $u_\tau = \sqrt{\tau_w / \rho}$ is the friction velocity, τ_w is the wall shear stress and $y^+ = y_w / \delta_v$ is the distance from the wall measured in wall units (or viscous lengths) $\delta_v = \nu / u_\tau$. Inside the boundary layer the mean tangential velocity is much smaller than the mean axial velocity and follows a linear distribution [Smithberg and Landis 1964].

In the axial direction, as the swirl decays, the flow tends toward regular axial flow. The tangential velocity decreases while the axial velocity increases near the centerline and decreases near the wall (figure 2.1.1). As a result, in the axial direction the static pressure strongly decreases near the wall and slightly increases near the centerline. However, the static pressure gradients are stronger in the radial direction than in the axial direction. Several studies observed a recirculation zone near the inlet created by the axial adverse pressure gradient, the existence and size of the recirculation zone depending on the geometry of the swirler and increasing with the Re number [Kitoh 1991, Parchen and Steenbergen 1998]. The recirculation zone created by swirling jets is used to stabilize flames in combustors [Dewan et al. 2004].

As the swirl decays, the rotating motion also loses its symmetry. Several investigations showed that after the swirl decays to a certain level the vortex axis does not coincide with the pipe axis, the asymmetry being as large as 10% of the pipe radius [Baker and Sayre 1974, Parchen and Steenbergen 1998, Pashtrapanska et al. 2006].

The swirl/turbulence interaction is the subject of numerous studies as part of the effort to model swirling flows at high Reynolds numbers. Analyzing the flow structure Kitoh [1991] pointed out that the turbulent structures in the flow are subject to centrifugal forces due to the helical streamline and also to flow skewness due to the non-uniform spiral pitch. Consequently the shear stress direction in the annular region does not coincide with the velocity gradient direction as assumed by the "eddy viscosity model" which models the turbulent stresses similarly to the viscous stresses.

Most studies agree on the anisotropic character of the turbulence in swirling flows [Parchen and Steenbergen 1998, Pashtrapanska et al. 2006]. As the swirl decays downstream, the decay affects first the annular region. Immediately after exiting the swirler the turbulent kinetic energy decreases and then increases again as the solid-body rotation core shrinks and disappears [Pashtrapanska et al. 2006].

For swirling flows induced by vanes normal Reynolds stresses show a significant increase near the centerline as the swirl decays (figure 2.1.4). The levels of the fluctuations of the tangential velocity $\overline{v_\theta^2}$ ($\overline{v^2}$ in figure 2.1.4) and radial velocity $\overline{v_r^2}$ ($\overline{w^2}$

in figure 2.1.4) are approximately equal and much larger than the fluctuations of the axial velocity $\overline{v_z^2}$ ($\overline{u^2}$ in figure 2.1.4). The velocity fluctuations show a return to isotropy as the swirl decays farther downstream [Parchen and Steenbergen 1998].

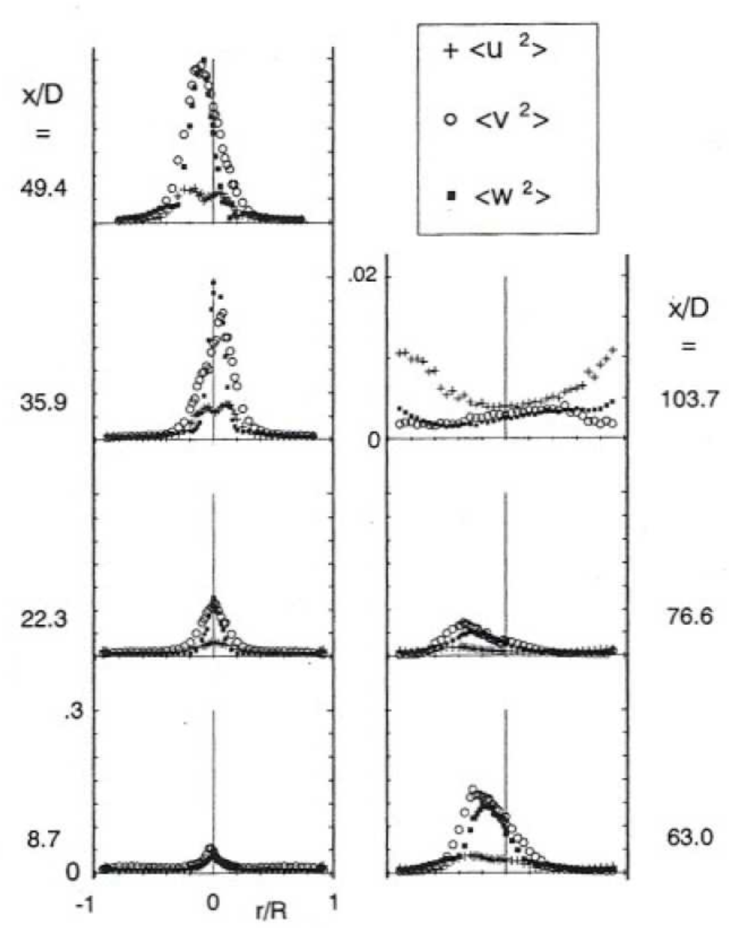

Figure 2.1.4: Radial distribution of the components of the Reynolds stress tensor along the pipe axis [Parchen and Steenbergen 1998].

The Reynolds shear stresses are shown in figure 2.1.5 for a swirling flow induced by vanes [Kitoh 1991]. In figure 2.1.5 u, v and w correspond to axial, tangential and radial velocity fluctuations (v_z', v_θ', v_r'). The arrows in the $\overline{uv}$ profile show locations where $\frac{\partial U}{\partial r} = 0$ but the sign changes of $\overline{uv}$ do not coincide with those locations as eddy viscosity models would predict.

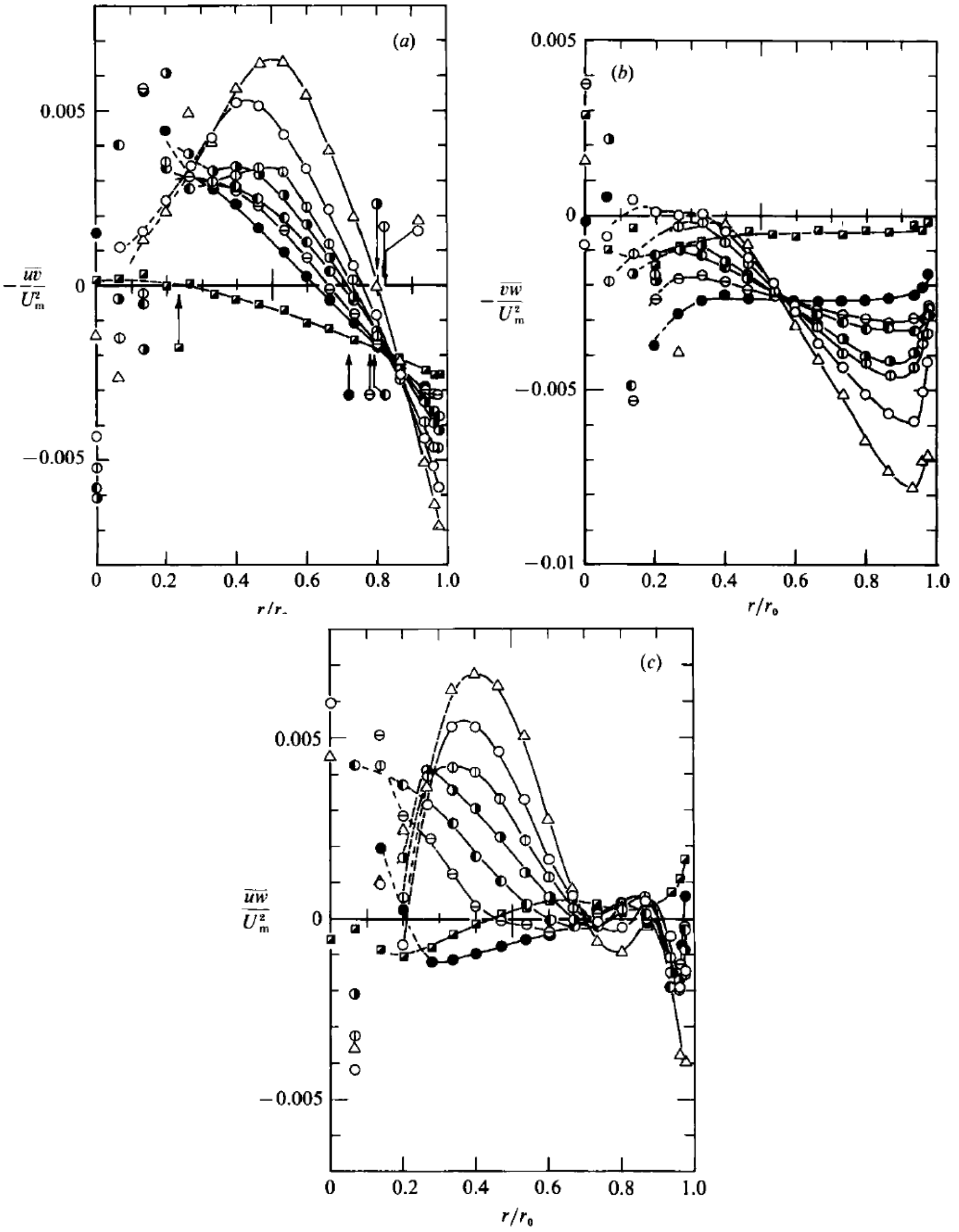

Figure 2.1.5: The shear stresses in a turbulent swirling flow at different axial locations [Kitoh 1991]. Arrows in (a) indicate radial positions of $\frac{\partial U}{\partial r} = 0$.

There are a number of studies investigating the turbulent swirling flow inside a rotating pipe. In the case of a rotating pipe, the wall shear actually induces the swirl instead of reducing it as in the studies of stationary pipes. The velocity fluctuations are larger near the wall with the axial velocity fluctuations being the largest while the radial and tangential fluctuations are almost equal [Imao et al. 1996]. These characteristics are similar to the non-rotating case and opposite from the swirling flows generated by vanes. The same characteristics persist even in swirling flows inside stationary pipes if the swirl is generated by rotating pipes [Anwer and So 1989, Rocklage-Marliani et al. 2003].

Inside a rotating pipe the turbulent flow becomes laminar near the inlet but then returns to turbulence [Nishibori et al. 1987]. For the same rotation rate, the laminarization of the flow occurs as the axial Reynolds number is increasing. Most studies agree that the swirl has a stabilizing effect on turbulent flows while destabilizing the laminar flows [Anwer and So 1989, Kitoh 1991, Nishibori et al. 1987]. Increased rotation reduces the turbulent fluctuations and the overall friction loss while the axial velocity profile becomes parabolic.

There have been numerous attempts of modeling swirling flows unfortunately with limited success. Early simulations [Kobayashi and Yoda 1987, Parchen and Steenbergen 1998] used $k-\varepsilon$ models based on “scalar eddy-viscosity” but the results did not match the experiments and they concluded that this was a result of the velocity fluctuations anisotropy in the swirling flow.

To simulate turbulent swirling flows models have to capture the anisotropic effects of rotation on the Reynolds shear stresses which determine the turbulence decay [Kitoh 1991, Pashtrapanska et al. 2006, Rocklage-Marliani et al. 2003]. Accurate simulations of turbulent swirling flows should employ Reynolds Stress Models (RSM) [Kitoh 1991, Pope 2000] which calculate each component of the turbulent stress tensor, unfortunately with an increase in the computational cost. Other alternatives are Direct Numerical Simulations (DNS) or Large Eddy Simulations (LES), but the computational cost of these methods is even larger.

Orlandi and Fatica [1997] performed a DNS simulation of the turbulent flow in a rotating pipe which showed a large logarithmic region spanning from the wall up to half of the radius. While most studies agree with a logarithmic variation near the wall, the size of the region is much larger than that reported by experimental studies.

2.2 Vortex identification

One of the biggest challenges encountered in the study of swirling and vortex flow is to consistently identify vortices. Many methods have been suggested but most of them failed to receive a wide acceptance. These methods associate specific flow features with the presence of vortices in order to identify them.

Some of these features are intuitive like closed stream lines [Lugt 1979, Robinson et al. 1989], large vorticity magnitude [Hussain and Hayakawa 1987] and regions of low pressure balancing the centrifugal forces [Robinson 1991]. However, these methods have limitations in specific cases: the streamlines depend on the reference system, the vorticity magnitude has maxima near the walls and pressure minima are generated by unsteady strain [Jeong and Hussain 1995]. Most researchers favor quantitative methods to identify vortices which are independent of the reference system used (Galilean invariant).

Several advanced methods have been proposed based on the invariants of the characteristic equation of the velocity gradient tensor ∇u. A short description of these methods is presented below while in depth analysis and comparison of these methods are described by Jeong and Hussain [1995] and Chakraborty et al. [2005].

The eigenvalues λ of the velocity gradient tensor ∇u satisfy the characteristic equation:

$$\lambda^3 + P_u \lambda^2 + Q_u \lambda + R_u = 0 \qquad (2.2.1)$$

where P_u (the first invariant) is given by $P_u = -\nabla \cdot u$, Q_u (the second invariant) is given by $Q_u = \left((\nabla \cdot u)^2 - tr\left((\nabla u)^2\right)\right)/2$ and R_u (the third invariant) is given by $R_u = -Det(\nabla u)$. For incompressible flows $P_u = 0$ and the discriminant Δ of the equation is given by $\Delta = (Q_u/3)^3 + (R_u/2)^2$.

Hunt et al. [1988] proposed using $Q_u > 0$ to identify vortices (the Q criterion). Q_u can also be written as $Q_u = \left(\|\Omega\|^2 - \|S_u\|^2\right)/2$ where $\|\Omega\| = \left(tr\left(\Omega\Omega^t\right)\right)^{1/2}$ is the Euclidean norm of the vorticity tensor $\Omega = \left(\nabla u - (\nabla u)^t\right)/2$ (the anti-symmetric part of ∇u) and $\|S_u\| = \left(tr\left(S_u S_u{}^t\right)\right)^{1/2}$ is the Euclidean norm of the rate of strain tensor $S_u = \left(\nabla u + (\nabla u)^t\right)/2$ (the symmetric part of ∇u). In an incompressible flow, Q_u is a measure of the excess of rotation rate relative to the strain rate.

Another method to identify vortices is the Δ criterion proposed by Chong et al. [1990]. This method considers a vortex core a region where the streamlines are closed or spiraling which translates in ∇u having a pair of two complex conjugate eigenvalues

$\lambda_{cr} \pm i\lambda_{ci}$. This condition is satisfied when the discriminant Δ of the characteristic equation is positive $\Delta > 0$.

A variant of the Δ criterion method named the "Swirling Strength" criterion was later proposed by Zhou et al. [1999]. The method associates the complex part of the complex pair of eigenvalues λ_{ci} to the strength of the vortex, as the time period for completing one revolution of the streamline is $2\pi / \lambda_{ci}$. Thresholds values of λ_{ci} are used to obtain vortices which correspond in size with vortices obtained with the other criteria. Chakraborty et al. [2005] added an extra condition of "Spiraling Compactness" to account for differences in vortex size between the "Swirling Strength" method and other methods when applied to swirling jets. They relate the ratio $\lambda_{cr} / \lambda_{ci}$ to the radius of the spiral streamlines. A point is considered to be inside a vortex core if this ratio is smaller than a threshold value in addition to the previous condition that λ_{ci} is larger than a threshold value.

One of the most widely accepted methods to identify vortices to this date is the λ_2 criterion introduced by Jeong and Hussain [1995]. This method identifies the location of minimum pressure regions which indicate the presence of a vortex core while neglecting misleading effects such as unsteady straining which could create a pressure minimum without a vortical motion and viscous effects which could eliminate the pressure minimum in a flow with vortical motion. After applying the gradient operator to the Navier-Stokes equations and neglecting the unsteady and viscous terms, the pressure can be written as:

$$S_u{}^2 + \Omega^2 = -\frac{1}{\rho}\nabla(\nabla p) \qquad (2.2.2)$$

A local pressure minimum requires two positive eigenvalues of the pressure Hessian, so using the previous equation the authors define a vortex core as a connected region with two negative eigenvalues of $S_u{}^2 + \Omega^2$. As $S_u{}^2 + \Omega^{\ 2}$ is symmetric, all its eigenvalues are real. Ordering the three eigenvalues λ in a sequence such that $\lambda_1 \le \lambda_2 \le \lambda_3$, the definition is equivalent to the requirement that $\lambda_2 < 0$ within the vortex core (which is why the method was named the λ_2 criterion).

Comparing the vortex identification methods presented above on multiple test cases Jeong and Hussain [1995] observed different results. However, Chakraborty et al. [2005] concluded that in intense swirling regions the vortex structures identified using these methods were almost identical for kinematic and dynamic interpretation. In the present study, vortices are identified by the λ_2 criterion and also elongated low pressure regions, closed streamlines and vorticity magnitude.

2.3 Flows in pipes with twisted tape inserts

Swirling flows are widely used in industries where enhanced mixing is required. This investigation is focused on swirling flows induced by twisted tapes and this chapter summarizes the studies published previously. The main characteristics of twisted tapes were presented in Chapter 1.

There are numerous studies dedicated to flows through twisted tape swirlers but most of them investigate only the variations of the heat transfer and of the friction coefficient [Abu-Khader 2006], with few attempts to elucidate the mechanisms behind these changes. A comprehensive list of articles regarding twisted tape inserts is summarized in the review article of Dewan et al. [2004].

While the twisted tapes used in this study are twisted 180^o and the flows investigated are in the range Re 10^4 to 10^5, in previous investigations researchers studied mostly flows induced by tapes with multiple twists (twist angle larger than 180^o) and a large number of the published reports focused on low Re flows in the laminar regime. However, the numerical part of the present study reproduces both the experiments at high Re using 180^o twisted tapes and also tapes with multiple twists and flows in the laminar regime, allowing a better comparison with the previous studies.

One of the first investigations [Kreith and Sonju 1965] studied theoretically and experimentally the decay of turbulent swirling water flow in a 1 inch (25.4 mm) diameter pipe with twisted tape inserts for Re between 10^4 and 10^5 (figure 2.3.1a). The authors used long twisted tapes (30d) and considered the flow fully developed. The swirl measured at different axial locations using a rotating blade in the center of the pipe decayed to 10-20 % of the initial swirl intensity in approximately 50 diameters (figure 2.3.1b). The swirl decay was faster at low Reynolds numbers and independent of the pitch. However, the swirl measurements made using the rotating blade actually measured an average angular velocity which does not capture the presence of secondary flow.

Another early work [Seymour 1966] investigated high Reynolds number swirling flows in pipes with 1, 2 and 3 inch diameters. The experiments showed the presence of two asymmetric vortices in the flow field at Re $=10^5$ in a 3 inch (76.2 mm) diameter pipe (figure 2.3.2a).

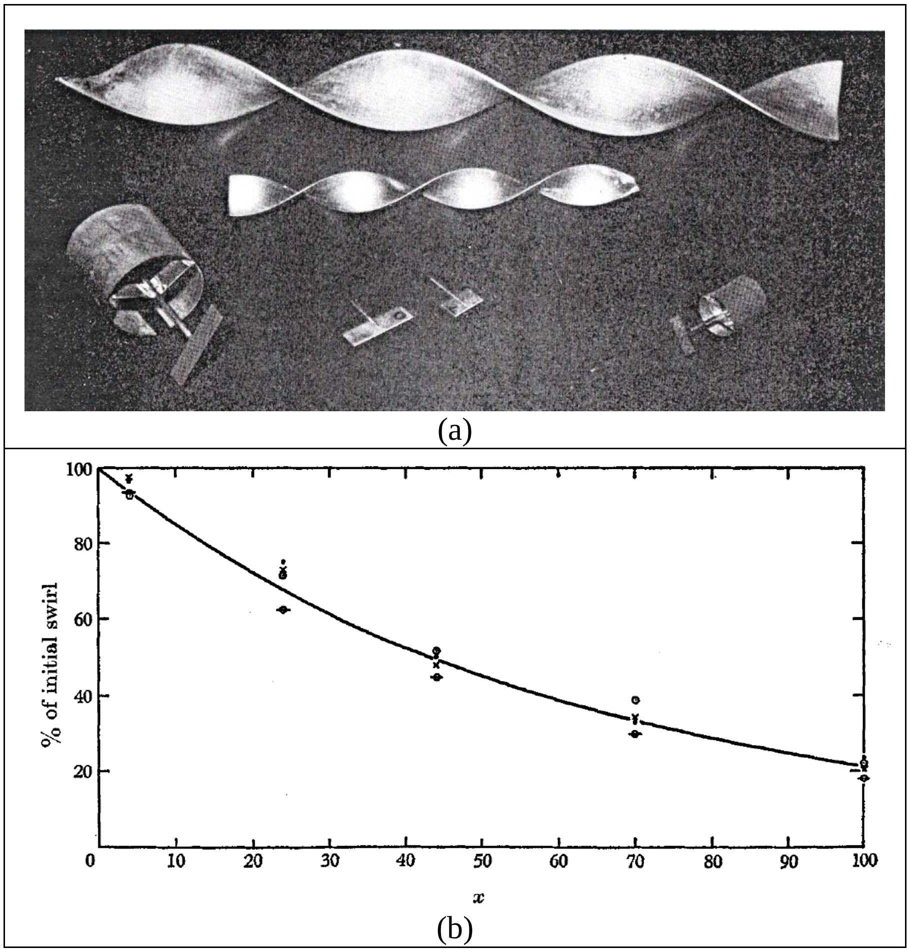

(a)

(b)

Figure 2.3.1 Swirling flow induced by twisted tapes [Kreith and Sonju 1965]: (a) twisted tape inserts and rotating blade devices for 1 and 2 inch diameter pipes, (b) swirl decay at Re = 6.1×10^4 in a 1 inch diameter pipe. The twisted tape characteristics for the data in plot (b) are:
●, Pitch 15, length 30 in.; ×, pitch 9, length 30 in.; ⊙, pitch 9, length 18 in.
⊖, pitch 15, length 18 in.; ———, theory.

The pressure profiles near the walls of the pipe and near the twisted tape revealed a pressure gradient in the direction of the twist and the experiments also showed two maxima in the axial velocity contours (figure 2.3.2b). A study on twisted tape inserts conducted by Smithberg and Landis [1964] showed similar features as Seymour's investigation for axial velocities, but no secondary flow patterns for tangential velocities.

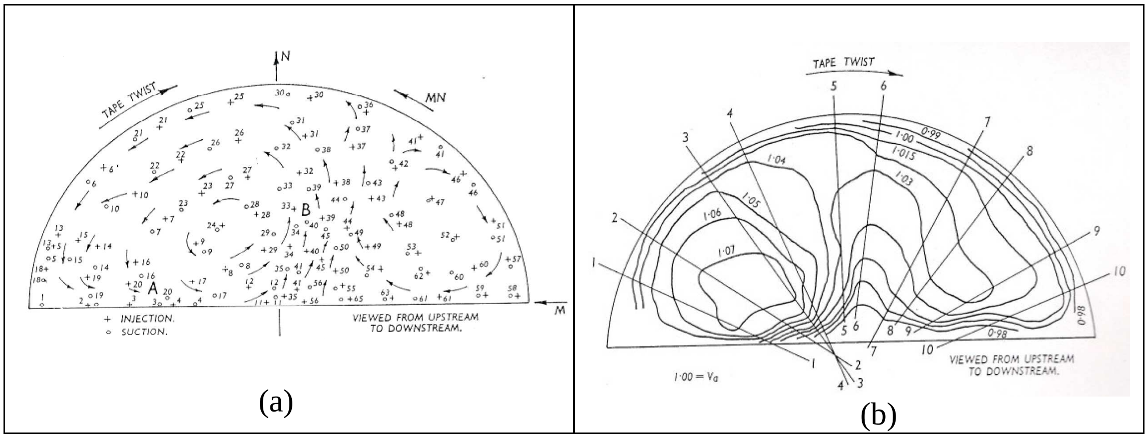

(a)

(b)

Figure 2.3.2: Characteristics of the flow in the cross section of a 3 inch diameter pipe with a twisted tape insert at Re = 10^5 [Seymour 1966]: (a) cross section velocity field, (b) axial velocity contours

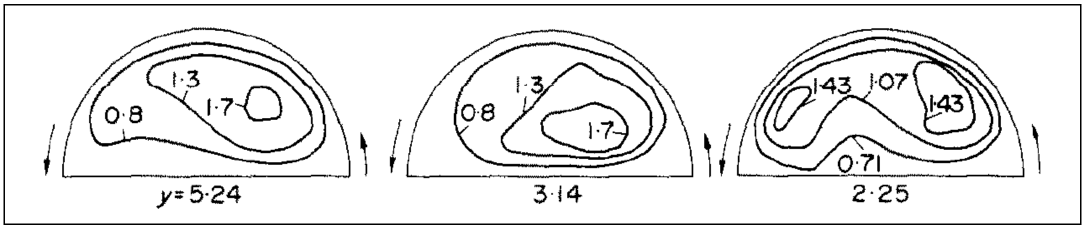

Figure 2.3.3 Axial velocity contours calculated at Re = 1,200 for tapes with different twist ratios [Date 1974]

Date [1974] investigated the flow induced by twisted tapes using a numerical model. The model assumed fully developed flow with no axial gradients and it was based on a vorticity-stream function formulation solved with finite differences. The axial velocity profiles of flows induced by tapes with larger twist ratios showed single maxima peaks near the wall, in the opposite direction relative to the twist of the tape. At lower twist ratios, the velocity profiles showed two peaks (figure 2.3.3).

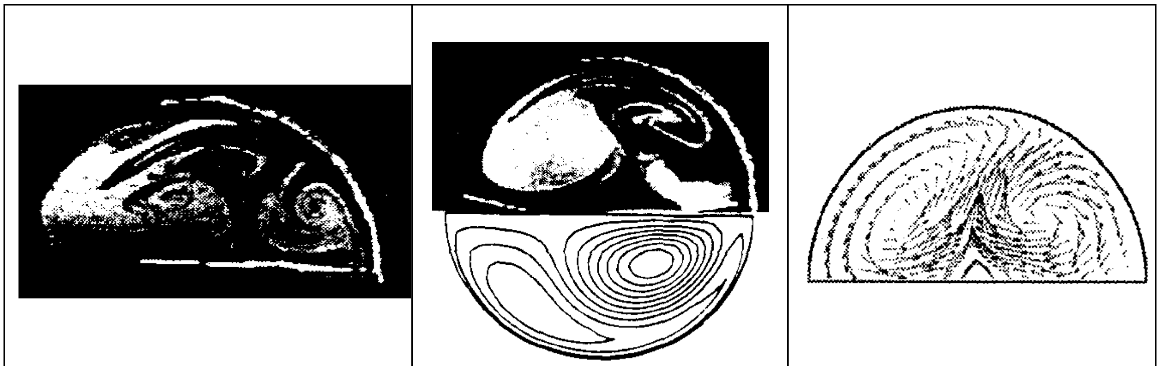

(a) $y_r = 4.32$, Re = 668
1.52 m long tape
(~7 x 180^o twists)

(b) $y_r = 3.53$, Re = 554
1.52 m long tape
(~8.5 x 180^o twists)

(c) $y_r = 3.0$, Re = 1000

Figure 2.3.4: Comparison between smoke visualizations and computed flow fields in a 2 inch (50.8 mm) diameter pipe with twisted tape inserts (direction of tape twist from left to right): a), b) [Manglik and Ranganathan 1997], c) [Yerra et al. 2007].

More recent studies [Manglik et al. 1993, 1997, 2001, Yerra et al. 2007] identified the secondary flow as one of the important causes of the heat transfer enhancement. Smoke visualizations in air flows at low Reynolds numbers were compared to finite difference numerical simulations using a vorticity-stream function formulation. Their images show the presence of two structures in the semicircular cross section which they identified as counter-rotating vortices (Fig. 2.3.4). The two vortex cell pattern emerged as either the Reynolds number was increased or the twist ratio was decreased. Consequently the authors introduced a swirl number defined as $SW = \mathrm{Re}/\sqrt{y_r}$ to characterize the flow changes in pipes with twisted tapes.

Kazuhisa et al. [2004] described another numerical investigation of the laminar swirling flow generated by a twisted-tape insert in a cylindrical pipe. Their model employed a non-orthogonal coordinate system rotating with the tape, while the equations were solved using the SIMPLEC algorithm [Patankar 1980]. The simulation captured the inception and evolution of the secondary flow showing that a counter-rotating vortex appears immediately downstream of the inlet in a central position and than drifts to the corner of the semicircular domain, against the twist direction (Fig. 2.3.5). The drifting was explained as an effect of the centrifugal forces, but the exact mechanism was not detailed. The authors assumed that the effect of buoyancy is important only for the laminar regime subject to high heat flux and not for turbulent flows. They concluded that in cases where the buoyancy is neglected, the flow patterns depend only on the swirl number and not on the Reynolds number.

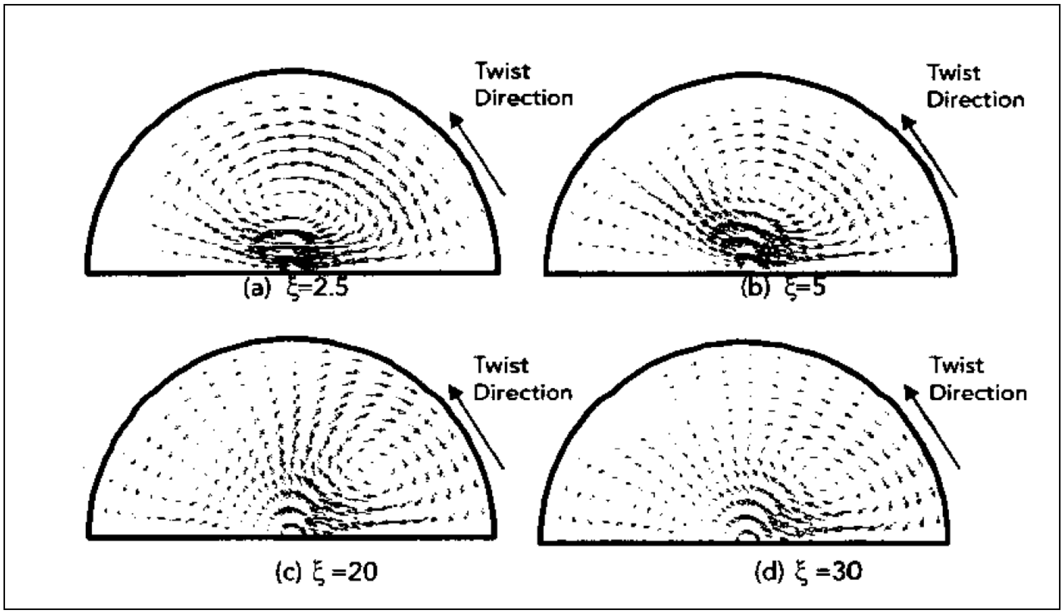

Figure 2.3.5: Transition of secondary flow for $y_r = 10$, Re = 2,000 where ξ represents the normalized turn angle of the twisted tape [Kazuhisa et al 2004].

Some researchers [Klepper 1972, Saha et al 2001] pointed out that more efficient heat transfer can be achieved using multiple short twisted tapes. These devices produce less pressure drop compared to full length twisted tapes and they can be optimized using different distances between tapes and tapes with different pitch [Dewan et al 2004].

Rahmani et al [2004, 2005] simulated a similar problem: the flow through a helical static mixer which consists of a series of left and right twisting helical elements at right angles to each other. Each element is twisted 180° (figure 2.3.6a). The two-phase flow was modeled using the commercial software FLUENT [Fluent Inc. 2006]. The plots of the velocity vectors and the particle locations showed very similar profiles to those in the regular twisted tape flows with two distinct regions and a vortex near the wall in the direction of the rotation (figure 2.3.6 b and c).

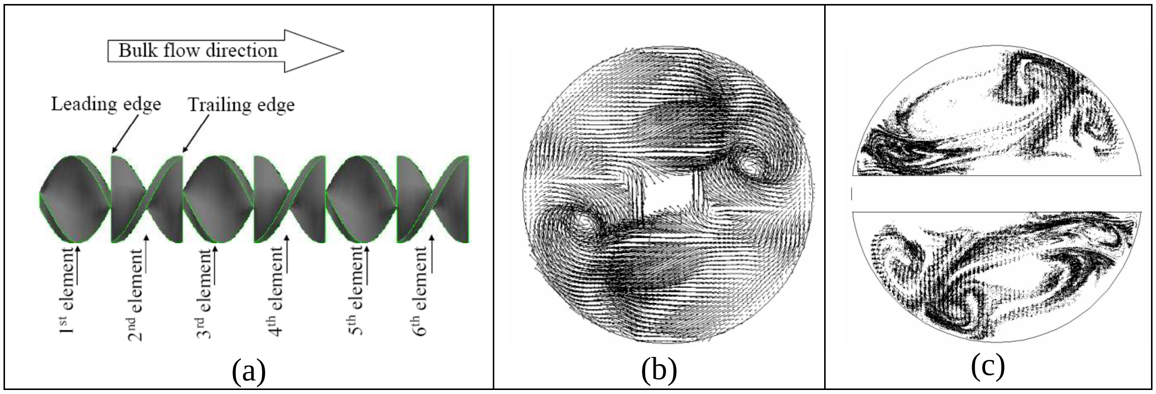

(a) (b) (c)

Figure 2.3.6: Numerical simulation of the flow through a pipe with a static mixer insert [Rahmani 2004]: (a) static mixer schematics, (b) cross section velocity vectors, (c) particles location after the 4th element at Re = 1000.

2.4 Related studies: flows through curved and helical pipes

Some researchers suggested that the secondary vortices presented in the previous section have similar characteristics to another type of centrifugally driven secondary motion, usually known as Dean vortices [Ujhidy et al. 2003]. The next section is dedicated to Dean vortices which are pairs of counter-rotating vortices formed in U-curved and helical pipes.

The centrifugal effect of a U-bend on the flow through a cylindrical pipe was first observed by Eustice [1911] using dye injection. Dean [1927, 1928] developed the first analytic solution for the U-shaped pipe problem, assuming small perturbations and that the pipe curvature is much larger than the pipe diameter ($R_c >> d$). He demonstrated that the centrifugal forces induced by the pipe radius were larger in the center of the pipe where the velocity was higher than near the walls, creating an unstable stratification. As a result, the fluid moved toward the exterior wall creating two counter-rotating vortices. These types of vortices were consequently named “Dean vortices” and the non-dimensional parameter introduced by him to characterize flow stability $Dn = \mathrm{Re} \cdot \left[d / (2 \cdot R_c) \right]^{1/2}$ was named the “Dean number” where d is the pipe inner diameter, Re is the Reynolds number based on d and R_c is the radius of the pipe curvature.

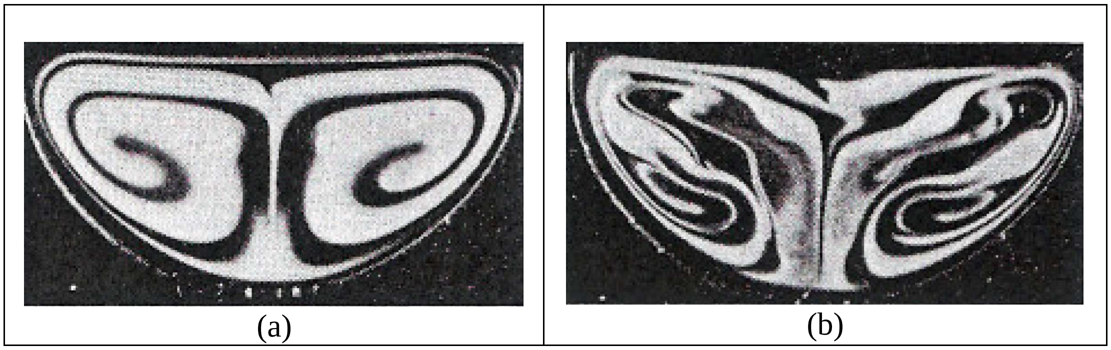
(a) (b)

Figure 2.4.1: Smoke visualization of secondary flow patterns in curved semicircular tubes [Cheng et al 1987]: (a) Re = 530, Dn = 87, (b) Re = 1070, Dn = 175.

There are numerous theoretical studies and visualizations of the flows through curved pipes with circular, semicircular and squared sections. Cheng et al [1987] recorded images of the flow patterns in U-shaped ducts with semicircular sections using smoke in air at low Reynolds numbers. The photos show the Dean vortices clearly (figure 2.4.1).

Another class of flows with similar characteristics to the twisted tape flows are the flows through helical pipes. Kao [1987] demonstrated that increasing the torsion magnitude at low Dean numbers might reduce the two cell secondary flow to a single vortex. His numerical simulations using the orthogonal coordinate transformation developed earlier by Germano [1982] showed that small changes in torsion caused significant changes in the flow pattern. The changes were more dramatic as the Dean number increased. He found that the flow patterns were influenced by the ratio torsion/curvature, rather then the absolute values of the two parameters. Testing the effect of the ratio, he found that for a ratio of 3 the lower vortex is so dominant that the upper one is squeezed in a very narrow region with a poorly defined core.

Liu and Masliyah [1993] who also studied numerically the laminar flow in helical pipes with circular cross section confirmed these findings. For constant Reynolds and Dean numbers the two-cell vortex pattern changed to one vortex as a result of increased torsion. As torsion increased, the maximum axial velocity location moved spirally from the outer wall toward the center while the pressure plots showed a low-pressure zone near the inner wall.

In a more recent study Tiwari et al. [2006] demonstrated numerically that the formation of Dean vortices in helical pipes reduces the near wall concentration buildup for two-phase flows by increasing the shear rates at the wall. They explained the complex flow field as a result of the combination of Coriolis force effects (due to the torsion of the tube centerline) and centrifugal force effects (due to the curvature). Their simulations also showed that the flow reaches a fully developed state after a 238° rotation. The presence of a straight pipe at the end changed the flow field in the last 20° of the helical pipe as a result of the changes in the pressure field.

These findings are illustrated in the cross-section flow schematic for a helical pipe (figure 2.4.2a) which shows non-symmetric vortices with the upper vortex smaller than the lower one. Simulations with and without gravity showed that it has little effect on vortex position. A two-phase flow simulation with 1-micron diameter particles also showed that for Dean numbers larger than 1,000 centrifugal forces balanced the gravity and reduced the peak concentrations of the particles.

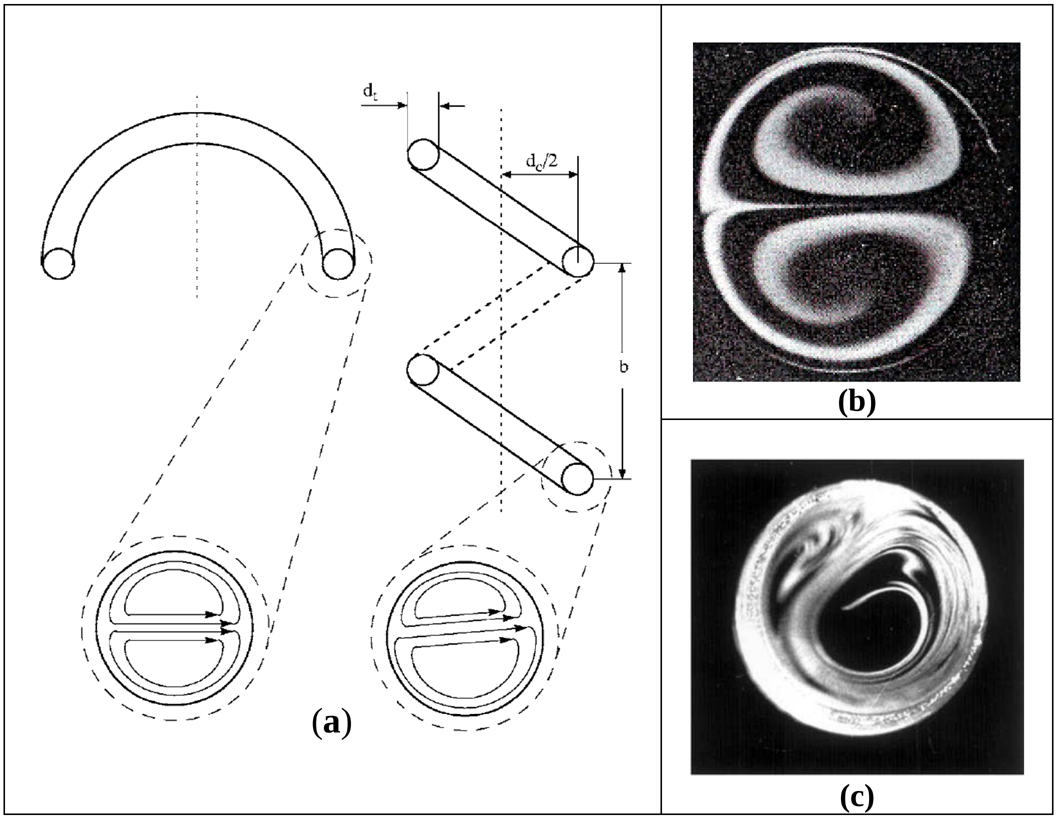

Figure 2.4.2: Dean vortices in U-shaped and helical pipes: (a) schematic [Tiwari et al 2006], (b) smoke visualization in U-shaped pipe [Cheng et al 1987], (c) smoke visualization in helical pipes [Yamamoto et al 2002].

Smoke visualizations confirm the sketches of the secondary motion in U-shaped and helical pipes shown in Figure 2.4.2a. Figure 2.4.2b shows a visualization of air flow through U-shaped pipes [Cheng et al 1987] while figure 2.4.2c shows a flow visualization of the secondary motion in helical pipes [Yamamoto et al 2002].

2.5 Flows with helical vortices

As will be shown in the following chapters, the flow in this study contains a pair of co-rotating helical vortices. Similar helical vortices have been observed in different rotating flows, most of the reports coming from investigations of vortex breakdown either in confined swirling flows, swirling jets or on highly swept delta wings. The presence of helical vortices was also reported in the swirling flow created by tangential injection inside a chamber with a closed end [Alekseenko et al. 1999].

In vortex breakdown helical vortices appear either as a single helix or double helix. These structures can be present with or without a vortex breakdown bubble. The helical structures are generally unstable and the single helix sometimes rotates around the flow axis. The focus of most of the vortex breakdown studies are the bubble mode and the single helix mode. These modes create an axial recirculation flow region in swirling jets which is used to stabilize flames in combustion. While the bubble mode has a stagnation point on the axis and the helical mode has a stagnation point off-axis, the double helical mode does not have a stagnation point or axial flow recirculation so it does not provide a stabilizing effect like the bubble and single helix modes. Comprehensive reviews of vortex breakdown are presented by Lucca-Negro and O’Doherty [2000], Escudier [1988] and Leibovich [1984, 1978].

A vortex breakdown is “an abrupt change in the structure of the core of a swirling flow” [Althaus et al. 1995, Sarpkaya 1971]. The first observations of vortex breakdown are attributed to Peckham and Atkinson [1957] in an investigation of the vortices formed by flow separation over the leading edge of delta wings at high angle of incidence. After the initial observation of vortex breakdown on wings, most investigations focused on vortex breakdown in pipes, as the axial and tangential components of the flow can be controlled independently. Unfortunately, despite over 50 years of research, there is still no general agreement on how the breakdown forms [Snyder and Spall 2000]. In fact, as Billant et al. [1998] point out, the theories are contradictory and even the features observed experimentally are different. Some researchers observed a dominant bubble mode and a secondary helical mode [Escudier 1988, Ruith et al. 2003] while others consider the helical mode the basic mode and the bubble secondary [Leibovich 1978, Sarpkaya 1971]. At the same time, there are reports of both helical vortices winding in the direction of the flow rotation [Leibovich 1978, Sarpkaya 1971] and vortices winding against the flow rotation [Escudier 1988, Lambourne and Bryer 1961, Ruith et al. 2003]. These differences are generally attributed to the different swirl generation methods as the swirl can be generated with adjustable vanes [Sarpkaya 1971, Faler and Leibovich 1978], rotating walls [Escudier 1984], tangential injection [Escudier and Zehnder 1982] or rotating pipe sections [Billant et al. 1998]. The vortex breakdown was found to be very sensitive to the swirl generation method making generalization difficult.

Vortex breakdown occurs when the swirl number exceeds a critical value or when swirling flows are exposed to an adverse pressure gradient (sudden expansion, divergent pipes). The breakdown mode selection is dependent on Re and swirl level. However, several regimes are bi-stable and the mode changes suddenly from one mode to the other. This unpredictable behavior was best captured by the classic photo of Lambourne and Bryer [1961] which shows both the bubble and the helical breakdown modes occurring in the same conditions, at the same time on each side of a delta wing (figure 2.5.1.).

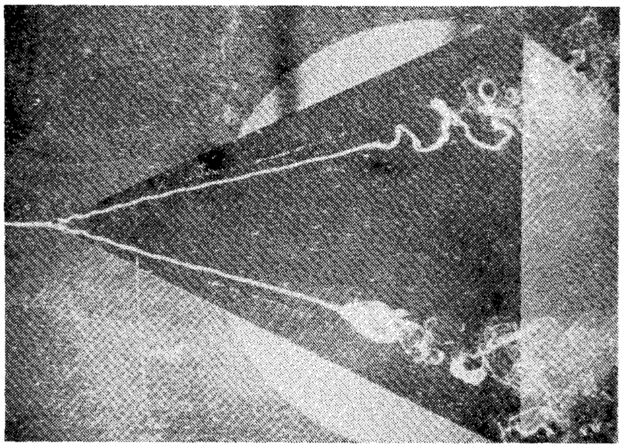

Figure 2.5.1 Vortex breakdown over a delta wing displaying both the helical and the bubble modes [original in Lambourne and Bryer 1961 - reproduced from Leibovich 1978];

The vortex breakdown appears as the swirling flow undergoes a transition from a supercritical state (which does not allow the presence of waves) to a subcritical state (which allows the presence of standing waves) [Leibovich 1978, Escudier 1988]. All authors agree that the presence of helical vortices in vortex breakdown is a result of instabilities amplified by the centrifugal forces in the rotating flow [Sarpkaya 1971, Escudier 1988, Leibovich 1978]. However, the authors do not agree on the relevance of the helical mode which is considered fundamental for breakdown by Leibovich [1978] and just a particular case by Escudier [1982, 1988] and Ruith et al. [2003]. Axisymmetric vortex breakdown has been achieved in well controlled experiments with no helical disturbances suggesting that the vortex breakdown is an axisymmetric phenomenon [Escudier 1988].

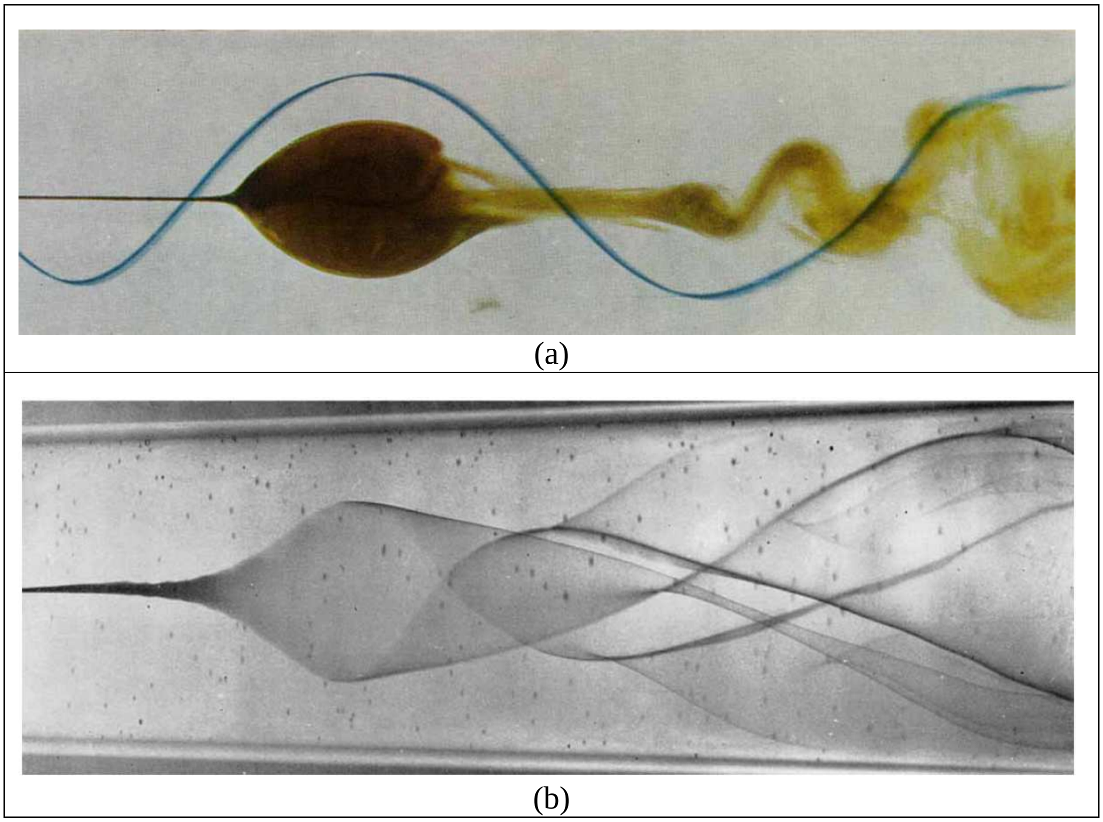

Figure 2.5.2 Visualization of vortex breakdown [Sarpkaya 1971]: (a) bubble mode with helical tail (the flow outside the bubble is unaffected), (b) double helix breakdown mode.

The double helical mode was observed for the first time by Sarpkaya [1971] who presented numerous dye visualizations of vortex breakdown in water (figure 2.5.2). The double helical mode appeared at Re < 2000 and high circulation. The dye stream injected on the centerline evolved into a curved sheet and each side of the sheet wrapped around the other in a double helix which eventually broke into turbulence. The helical vortices were co-rotating and the helix winding was in the direction of the flow. The author attributed the appearance of this mode to the amplification of helical instabilities.

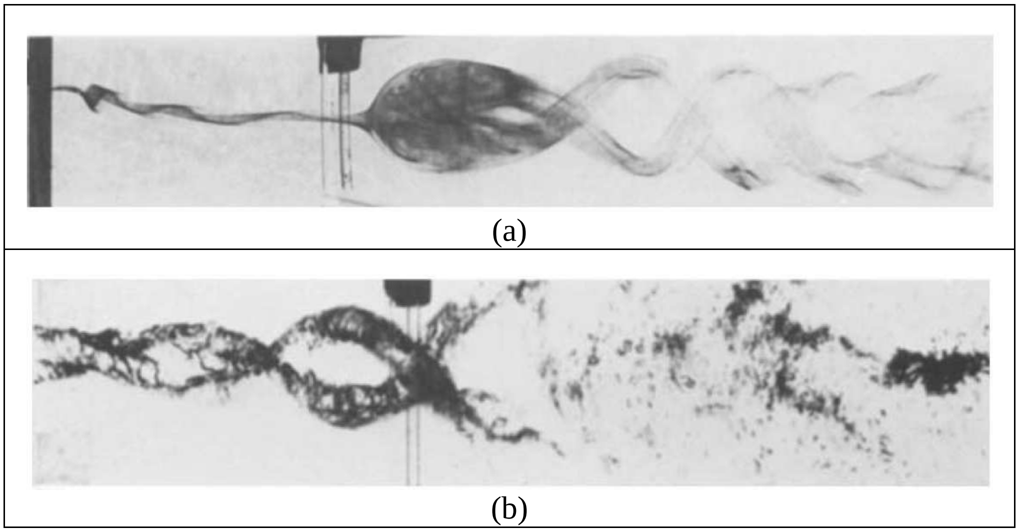

Figure 2.5.3 Double helical mode breakdown in swirling flows induced by tangential injection: (a) dye visualization at Re = 220, (b) cavitating flow at Re = $9x10^4$ [Escudier and Zehnder1982].

Later, the helical modes were also observed by Escudier and Zehnder [1982] (figure 2.5.3) but the helix winding was in the opposite sense compared to the rotation of the outer flow. In figure 2.5.3a, dye injection in water shows a breakdown bubble followed by a double helix at Re = 220 while figure 2.5.3b shows a similar behavior at Re = $9x10^4$ for cavitating flows.

Several articles report tangential velocity measurements but none of these reports have showed the velocity distribution corresponding to the double helical mode or identified counter-rotating flow. Faller and Leibovich [1978] report velocity measurements with Laser Doppler Velocimetry in a vortex bubble with a helical tail (figure 2.5.4a). Their plots show that tangential velocity profiles have two inflection points at the end of the bubble (figure 2.5.4b), similar to the velocity profiles investigated in the present study, but the flow did not become counter-rotating. The swirl was produced with swirl vanes while the vortex breakdown bubble was created in an expanding pipe.

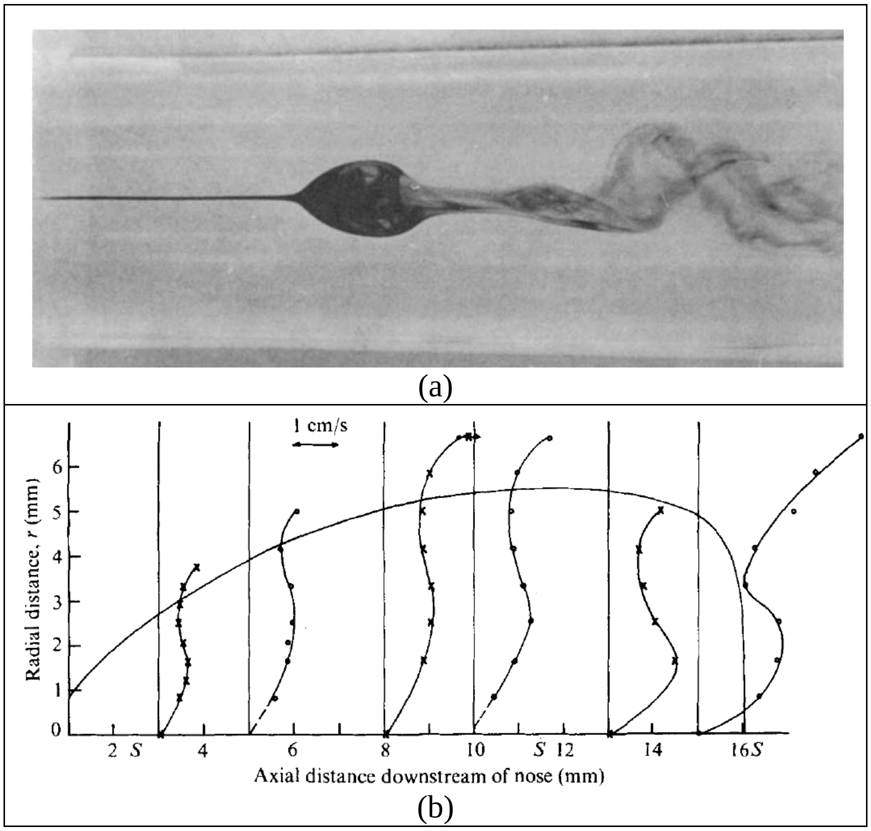

Figure 2.5.4 Vortex breakdown bubble at Re = 2560: (a) dye visualization (b) tangential velocity measurements (S marks stagnation points) [Faler and Leibovich 1978].

The previous studies confirmed the presence of helical vortices in vortex breakdown in pipes. Helical vortices are also present in vortex breakdown in unconfined jets. The presence of two helical vortices in swirling jets was visualized by Billant et al. [1998] with fluorescent dye in water and two laser light sheets. Figure 2.5.5a shows axial and cross-sectional visualizations of the jet structure while figure 2.5.5b shows the jet development along the axis. The swirl was created using a rotating honeycomb and the helical vortices were present in flows with Re < 2000 and S < 1.4. For S > 1.4 the vortex breakdown evolves into the bubble mode independent of Re. At higher Re but under the critical swirl number S = 1.4 the jet structure evolved from a double helix to three helical vortices.

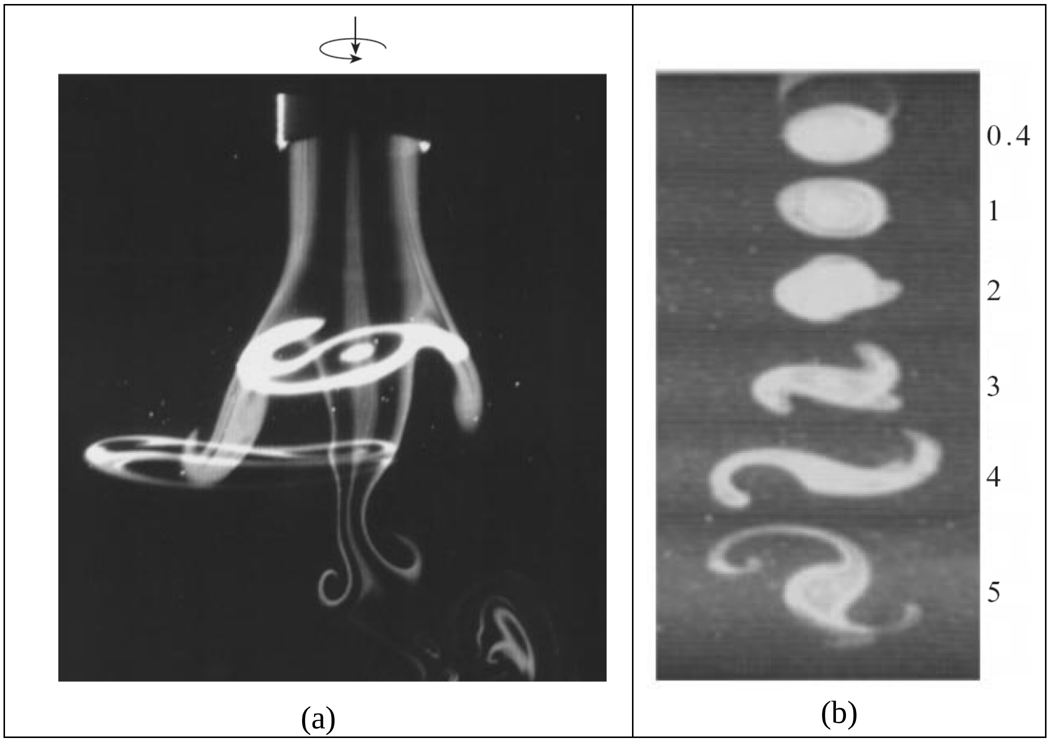

Figure 2.5.5 Helical vortices in a swirling jet at Re = 606 and S = 1.41: (a) vertical and cross-section jet structure, (b) vortex development along the jet axis (locations in diameters) [Billant et al. 1998]

Numerical simulations have also been widely employed to investigate vortex breakdown. Comprehensive reviews of numerical simulations are summarized by Althaus et al. [1995], Lucca Negro and O'Doherty [2001] and Ruith et al. [2003]. While most of these simulations reproduce the bubble mode and the helical mode, Ruith et al. [2003] also captured the double helical mode (figure 2.5.6). In their simulations the winding of the helical vortices was opposite to the main flow, similar to the experimental reports of

Escudier and Zehnder [1982]. The authors did not report counter-rotating flow and they attributed the helical vortices, which were unstable, to amplification of helical disturbances.

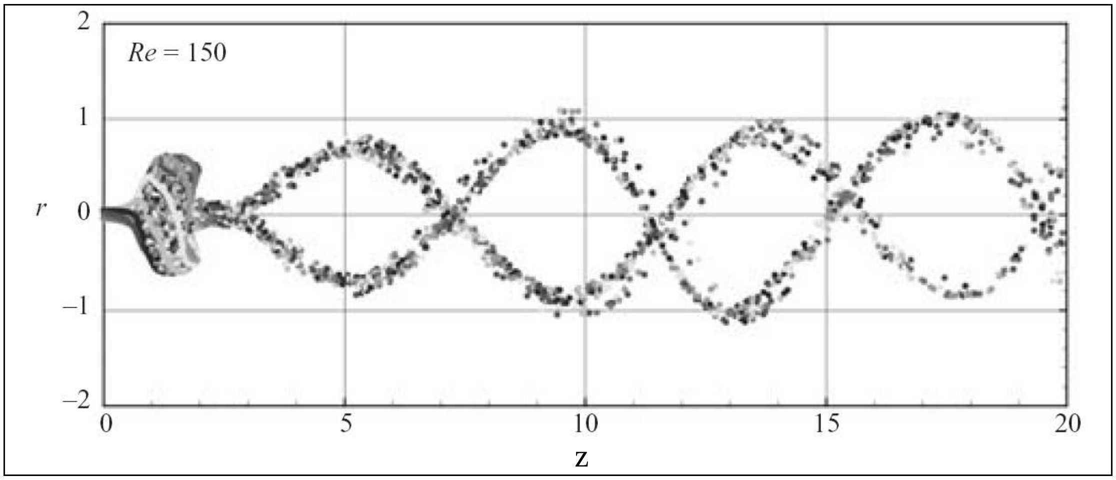

Figure 2.5.6 Particle paths in a numerical simulation of a swirling jet show a double helix structure downstream of a breakdown bubble at Re = 150 [Ruith et al. 2003].

In conclusion the double helical mode in vortex breakdown is an unstable flow regime generally attributed to a centrifugal amplification of helical instabilities. The lack of stability suggests that the helical vortices are weak and no counter-rotating flow have been observed either in flow measurements, visualizations or numerical simulations.

Helical vortices were also reported in the swirling flow created by tangential injection inside a chamber with a closed end [Alekseenko et al. 1999]. The authors created experimentally different types of helical structures by varying the inclination of plates at the bottom of the chamber, the inlet conditions of the injection nozzles and the characteristics of the chamber outlet. One of the helical structures visualized by air bubble injection was a double helix similar to the vortex system discussed in the following chapters (figure 2.5.7). However, the double helix structure was very unstable, unlike the helical vortices identified in the present study. The authors developed a simplified analytical model which they used to calculate the flow field for a given pitch of the helix, radius of the helix, strength of the vortex (circulation) and ratio between the axial and tangential velocity. This approach was continued later by one of the authors to calculate velocity distributions for different combinations of multiple helical vortices [Okulov 2004, Fukumoto and Okulov 2005]. None of these studies reported counter-rotating flow.

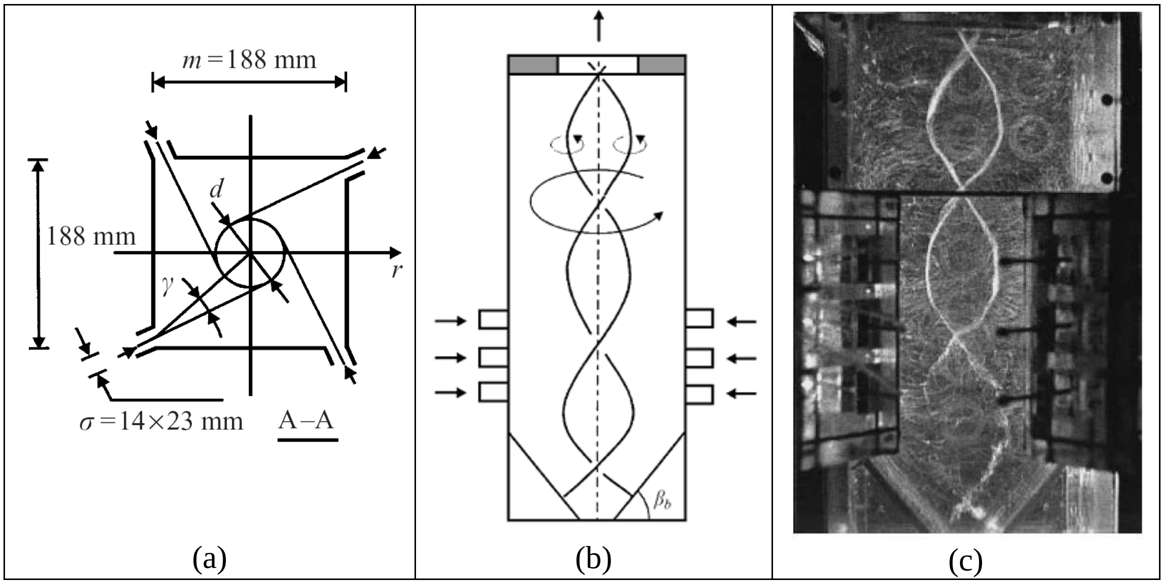

Figure 2.5.7 Helical vortices in the swirling flow induced by centrifugal injection into a rectangular container [Alekseenko et al 1999]: (a) setup top view, (b) setup side view with a sketch of the helical vortices, (c) air bubble visualization.

The articles presented in this section show that helical vortices are not a rare occurrence in nature, but also that in most cases they are unstable and difficult to measure. As the helical vortices observed in the present study are stable, their investigation could help the understanding of the flow structures and their interaction in vortex breakdown and other rotating flows as well, even though specific flows are strongly dependent on the swirl generation system.

CHAPTER 3

EXPERIMENTAL SETUP

3.1 General setup

The experimental setup is designed to allow the investigation of the swirling flow induced by a twisted tape in a circular pipe (Figures 3.1.1 and 3.1.2). It consists of a closed circuit where water from the tanks is pumped by a 0.5 HP magnetic drive centrifugal pump with a frequency controlled motor. The inner diameter of the testing pipe is 1 inch (d = 25.4 mm) and the pipe is made of 1.5 mm thick glass which provides optical access. Seymour [1966] investigated twisted tapes inserts in 1, 2 and 3 inch (25.4, 50.8 and 76.2 mm) diameter pipes and showed that the tube diameter does not influence the structure of the secondary flow. Consequently, in this study only a 1 inch (25.4 mm) diameter pipe is considered. The pump allows tests at Reynolds numbers in the range $10^4 - 10^5$ (Re based on the pipe diameter d). The water tanks 1 and 2 have a maximum combined capacity of approximately 1 cubic meter but usually about half of this capacity is used during tests.

The flow circuit has a calming section immediately upstream of the twisted tape. The calming section is designed to reduce the turbulence level and consists of a coarse screen, a honeycomb, two fine screens and a nozzle as suggested by Farell and Youssef [1996]. The hexagonal cells of the honeycomb have a flat side to flat side dimension of 6.35 mm and wall thickness of 0.25 mm. The coarse screen and the two fine screens have square cells with cell sizes 9.6, 2 and 1 mm.

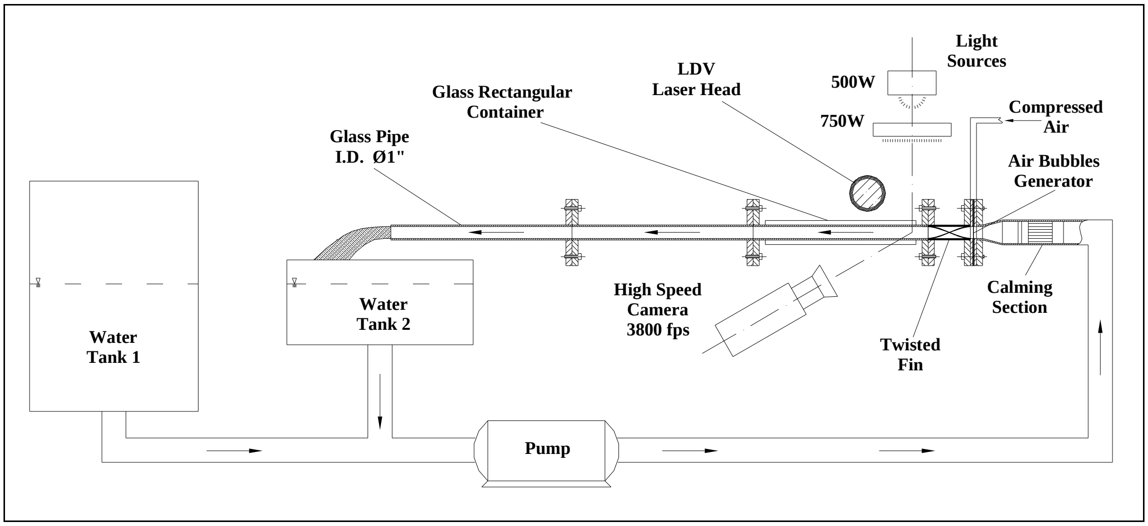

Figure 3.1.1: Setup schematic.

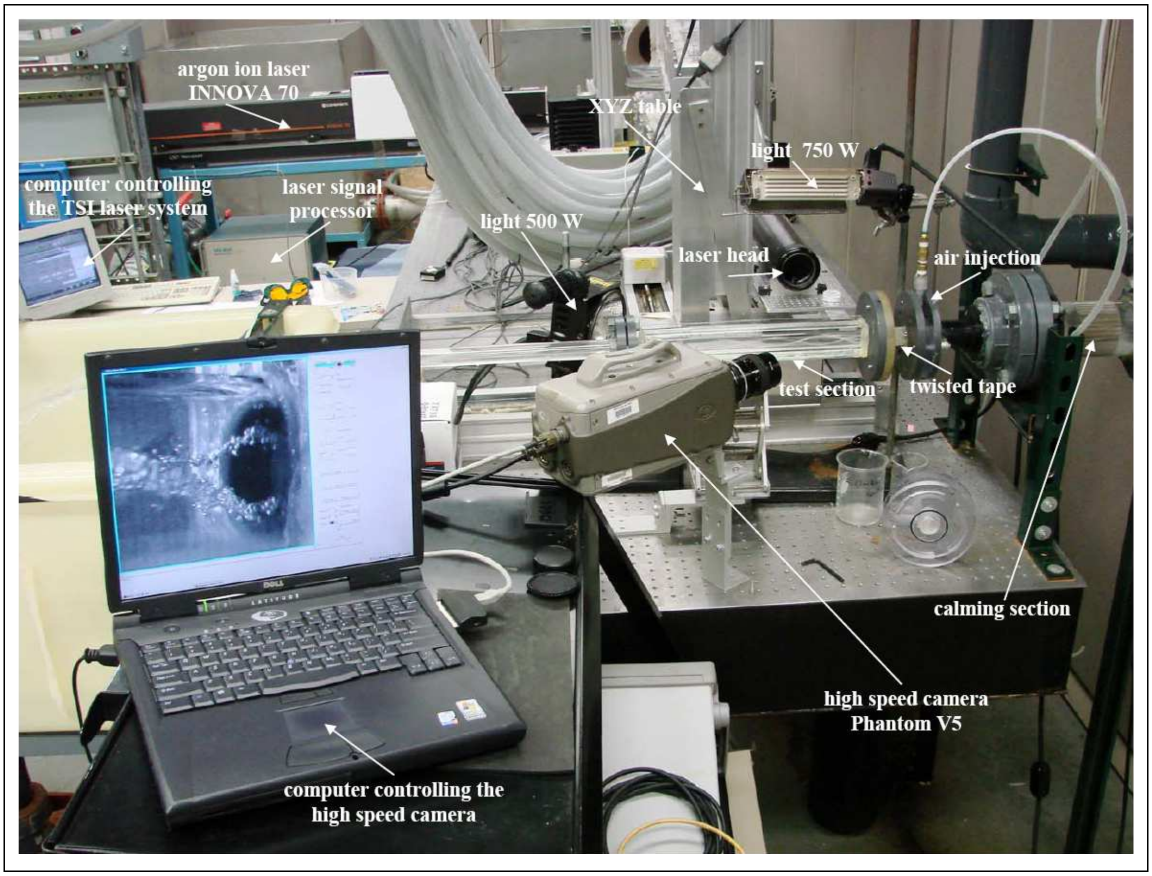

Figure 3.1.2: General view of the experimental setup.

The 140 mm long nozzle is installed 1d (25.4 mm) downstream of the second fine screen and has a 9:1 area contraction ratio. The inlet diameter is 3d (76.2mm) and the outlet diameter is 1d (25.4mm) [Islek 2004]. The system used to straighten the flow is similar to the one used by Seymour [1966]. The flow exits from the nozzle into the twisted tape swirler.

The twisted tapes tested have lengths of 45, 60 and 90 mm and they are twisted 180° (the pitch is equal to the length). The corresponding pitch to diameter ratios are 1.77, 2.36 and 3.54, respectively. The swirlers were manufactured by stereolithography (by Vistatek Inc.) using “Somos Watershed 11120” resin. The twisted tape and the pipe form a single part, so the width of the tape is equal to the inner diameter of the pipe with no gap in between (figure 3.1.3). This design eliminates uncertainties due to any secondary effects of the tape/wall clearance which occur for common twisted tape inserts. The twisted tape has a profiled edge to limit flow separation at the leading edge of the swirler. The tape thickness is 3 mm (0.118d) at the leading edge and 1.5 mm (0.059d) at the trailing edge.

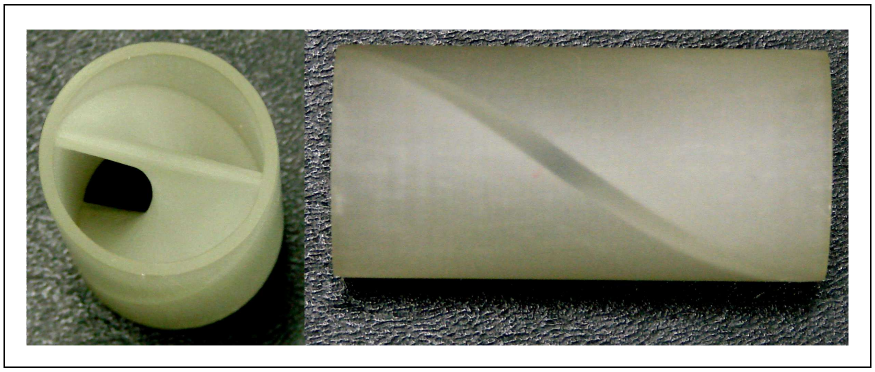

Figure 3.1.3: Twisted tape swirler: pitch H = 60 mm, diameter d = 25.4 mm, pitch to diameter ratio y_r = 2.36.

The flow is investigated using LDV measurements and direct visualization of injected fine air bubbles. The air bubbles generator was built using a spinal needle (a large needle designed to be inserted into the spinal column between the lumbar vertebrae for diagnostic purposes or to administer medication) with a 1.25 mm (0.049d) outer diameter, 0.9 mm (0.035d) inner diameter and with 4 equally spaced holes of 0.45 mm (0.018d) oriented upstream (figure 3.1.4). A thin long plug is used to prevent water infiltration into the air circuit when the air injection is stopped. The needle was inserted into a polycarbonate flange with a 25.4 mm (1d) diameter flow section. The device is installed just upstream of the swirler. The air mass flow is supplied by a compressed air line controlled by a ball valve.

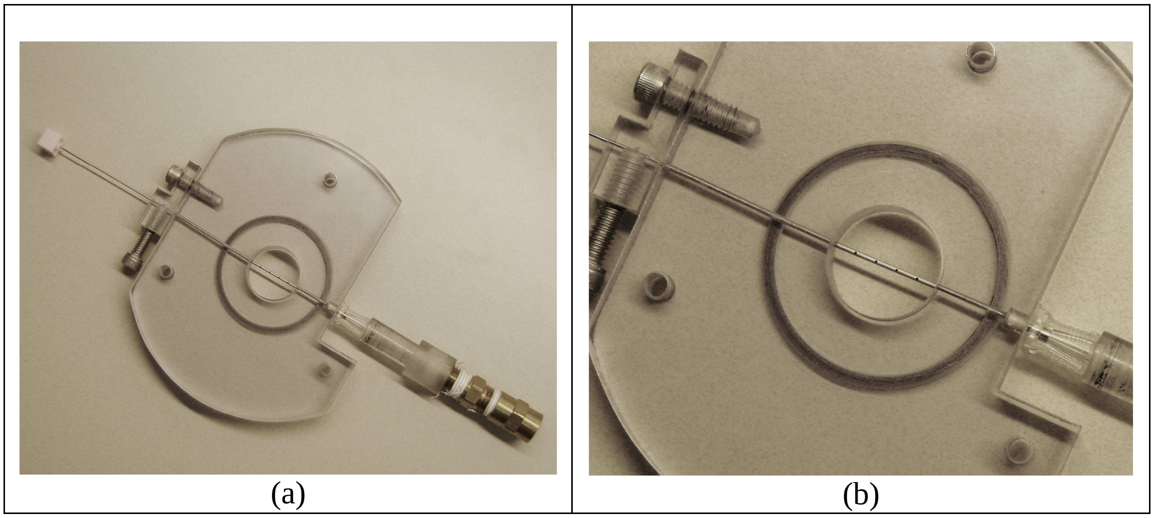
(a) (b)

Figure 3.1.4: Air bubbles injector: (a) general view, (b) close-up of the perforated needle.

The bubbles motion is recorded using a black and white “Phantom V5” high-speed camera capable of 3800 frames per second (fps) for frame sizes of 512x512 pixels or 4200 fps frame sizes of 1024x256 pixels. The camera was fitted with a Nikon “Micro-Nikkor” lens with focal length f = 55 mm for close shots and a Elicar V-HQ Macro lens with focal length f = 90 mm for wider field views. The lighting is provided by two "Lowe" light sources "Omni–Light" of 500 W and "Tota-Light" of 750 W. In addition to the high speed camera some images were also recorded with a regular camera (Sony DSC-H5).

3.2 Setup for Laser Doppler Velocimetry (LDV) measurements

Flow velocities are measured using a two-component LDV system (TSI Inc.) in backscattering mode with an argon-ion laser (Coherent Innova 70 - C3). The laser has a maximum power of 3.4 W. Green light with wavelength $\lambda_n = 514.5\,\mathrm{nm}$ was used for axial velocity measurements while blue light ($\lambda_n = 488\,\mathrm{nm}$) was used for the tangential velocity measurements. One of the blue light beams had a phase shift of 1 MHz to distinguish between the positive and negative velocities. The half angle between the laser beams is $\kappa = 3.97°$.

The head of the laser can be translated in all three directions using a traverse system with three electric motors controlled by a computer. The spatial resolution of the traverse is 10^{-2} mm.

Velocities are calculated from the Doppler signal as $\tilde{V}_i = f_d \cdot d_{fr}$ where $\tilde{V}_i$ is the instantaneous velocity in *i* direction , f_d is the Doppler frequency and d_{fr} is the fringe spacing $d_{fr} = \lambda_n / 2 \cdot \sin\kappa$. Velocity statistics were calculated from batches of 5,000 samples collected at each measurement point.

The high curvature of the pipe walls required special measures to compensate for light refraction. Following previous investigations of the lensing effect of curved glass walls [Glover et al. 1985], a rectangular glass enclosure ($340 \times 40 \times 50$ mm) with 3 mm thick walls was attached to the glass pipe, while the space between the straight walls and the pipe was filled with glycerin which has an index of refraction close to the index of refraction of glass. The velocities were measured only along the horizontal diameter where the vertical component of the velocity measured with the laser is equal to the tangential velocity V_θ. This strategy also minimized the effects of light distortion on the measurements.

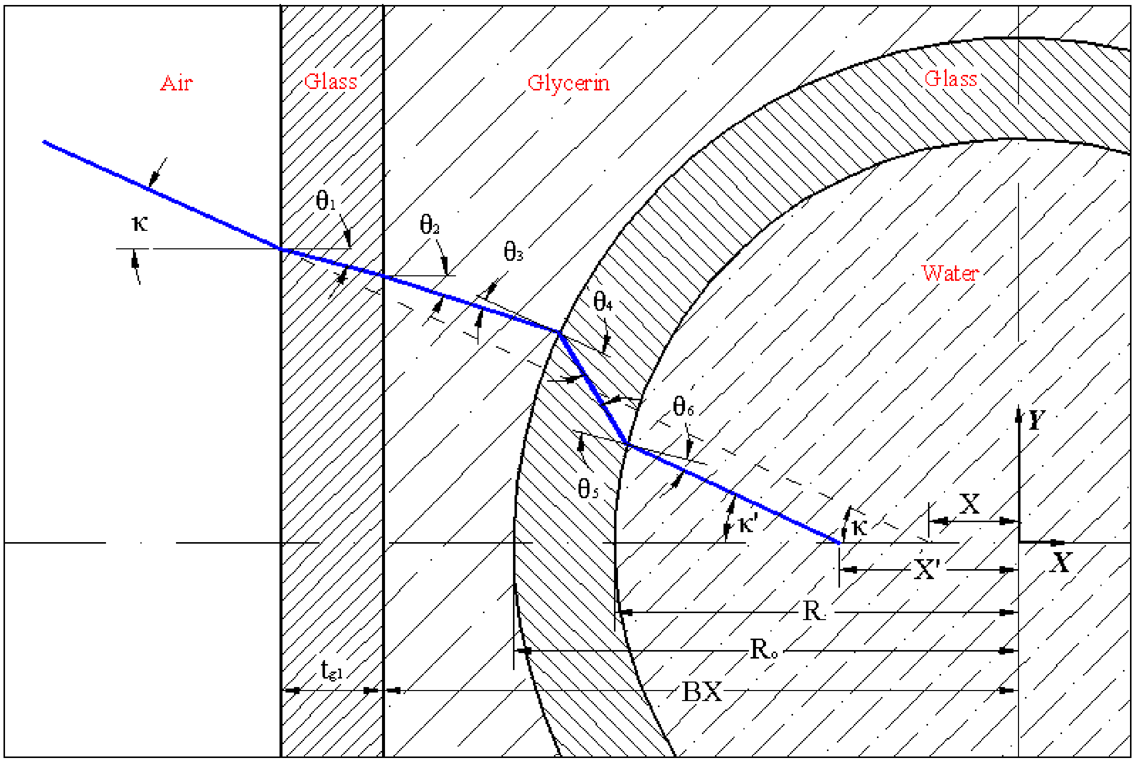

Figure 3.2.1: Light refraction through the different media surrounding the test section for tangential velocity component measurements (not to scale).

The level of light distortion induced by the curved glass walls and medium changes (air/glass/water) is still significant even with the presence of the rectangular container filled with glycerin. While the laser head moves 15 mm toward the pipe, the measuring volume created at the intersection of the light beams actually sweeps 24 mm across the horizontal diameter inside the pipe. Consequently, the actual locations of the measurements are determined from the positions of the laser head after calculating corrections which account for the angle changes of the light due to refraction at the interfaces between different mediums [Glover et al. 1985].

Figure 3.2.1 shows the direction changes for the upper blue light beam used to measure the tangential component of the velocity. X' is the actual position of the measuring volume while X is the position if the refraction is ignored. The beam intersection angle is also modified by refraction from κ to κ'. The lower beam follows an identical path.

The following equations describe the path changes due to refraction for the upper beam and they were solved numerically with MATLAB to provide the compensated positions for the laser head:

$$\begin{cases} \sin\theta_1 = \dfrac{n_a}{n_{g1}} \cdot \sin\kappa \\ \sin\theta_2 = \dfrac{n_{g1}}{n_m} \cdot \sin\theta_1 \\ \sin\theta_3 = \dfrac{\cos\theta_2}{R_0} \cdot \left[BX \cdot (\tan\kappa - \tan\theta_2) + t_{g1} \cdot (\tan\kappa - \tan\theta_1) + X \cdot \tan\kappa\right] \\ \sin\theta_4 = \dfrac{n_m}{n_{g2}} \cdot \sin\theta_3 \\ \sin\theta_5 = \dfrac{R_0}{R} \cdot \sin\theta_4 \\ \sin\theta_6 = \dfrac{n_{g2}}{n_w} \cdot \sin\theta_5 \\ X' = R_0 \cdot \dfrac{n_m}{n_w} \cdot \dfrac{\sin\theta_3}{\sin(\theta_2 + \theta_3 - \theta_4 + \theta_5 - \theta_6)} \end{cases} \tag{3.2.1}$$

The new angle between the beams is calculated from the "Law of Sines" as $\frac{X'}{\sin\theta_6} = \frac{R}{\sin(\pi - k')}$, so the actual angle is given by $\kappa' = \pi - a\sin\left(\frac{R}{X'}\sin\theta_6\right)$. The measured velocities are corrected using κ'.

In the previous equations system, as well as in figure 3.2.1, $\kappa = 3.97°$ is the laser angle, $BX = 17$ mm is the tank half thickness, $t_{g1} = 3$ mm is the container wall thickness, $R = 12.7$ mm is the inner radius of the pipe and $R_o = 14.2$ mm is the outer radius of the pipe. The indices of refraction are $n_a = 1$ for air, $n_{g1} = 1.51$ for the container wall, $n_m = 1.47$ for glycerin, $n_{g2} = 1.47$ for the pipe wall and $n_w = 1.33$ for water (all values are standard values for yellow light at $\lambda = 589$ nm).

This non-linear system of equations describes the actual position inside the pipe for known laser head positions. However, in order to describe the flow field uniformly with equally spaced measurements, the inverse problem was solved, calculating the laser head positions corresponding to specific positions inside the pipe (between -12 and 12 mm with 1 mm spacing). The inverse system was solved by minimizing the error function defined as:

$$err = abs(x_{t\arg et} - x_{calculated})/abs(x_{t\arg et}) \qquad (3.2.2)$$

where $x_{t\arg et} = -12,-11,...-2,-1,0,1,2...11,12$ mm. The maximum error was under 1% (0.83% for $x_{t\arg et} = 2$ mm) and the solutions of the inverse problem are tabulated in table A1 in Appendix 1. The fourth column of the table shows the positions of the traverse after the 0 position of the traverse has been align with the pipe centerline. The fifth column of the table shows the velocity correction corresponding to the change in the beam intersection angle; the measured velocities were multiplied with those coefficients.

The flow was seeded with 3 μm diameter titanium dioxide (TiO_2) particles with density 4.2 g/cm^3 and index of refraction 2.6. Initial measurements for the 90 mm swirler were performed using 0.3 μm diameter alumina particles (Al_2O_3) with density 3.84 g/cm^3 and index of refraction 1.67, but the increase in the diameter and index of refraction greatly improved the signal to noise ratio (SNR) without any loss of sensitivity [Menon and Lai 1991]. As a result, the measurements with TiO_2 particles were collected much faster.

The settling velocity for the TiO_2 particles calculated as $V_s = \frac{\Delta\rho \cdot a^2 \cdot g}{18 \cdot \mu_g}$ is 1.568×10^{-5} m/s, much lower than the velocities measured (in the range 10^{-1} - 10^{1} m/s). In the previous formula $\Delta\rho$ is the difference between the density of the medium and the density of the particles, a is the particle diameter, g the gravitational acceleration and μ_g is the viscosity of water.

The measurements were processed using transit time weighting with statistics calculated as:

average velocity $\overline{V_i} = \frac{\sum \tilde{V}_i \cdot \tau_b}{\sum \tau_b}$

standard deviation $\sigma_v = \sqrt{\left(\frac{\sum \tilde{V}_i^{\,2} \cdot \tau_b}{\sum \tau_b} - \overline{V_i}^{\,2} \right)}$

where τ_b is the total burst time of the signal and $\tilde{V}_i$ is the instantaneous velocity in i direction. The data processing is incorporated in the control software of the laser. No differences were observed between measurements with and without velocity biased correction (without bias correction statistics are calculated considering $\tau_b = 1$).

An extensive investigation of the measurements uncertainty in this experimental setup was performed in a previous study [Islek 2005]. Four types of errors were considered: (1) errors due to factors upstream of the twisted tape (alignment of the flow loop components), (2) errors due to factors downstream of the twisted tape (test section/LDV head alignment), (3) errors in the twisted tape alignment (from vertical) and (4) errors due to variation in LDV sampling. The uncertainty was found to be approximately 3% for average velocities and 10% for turbulent root mean square (rms) fluctuations.

The laser was also used to create a cross section sheet of light after passing a green light beam through a divergent cylindrical lens with a focal length f = -40 mm. The air bubble streams reflect and scatter the laser light, marking the positions of the centers of the secondary vortices as two bright white spots on the green circular cross-section.

CHAPTER 4

EXPERIMENTAL RESULTS AND COMMENTS

4.1 Results of the LDV measurements

Tangential velocities were measured in the swirling flow induced by twisted tape inserts with 45, 60 and 90 mm pitch (1.77, 2.36 and 3.54 twist ratio) at different Re from 10^4 to 10^5. The measurements were collected along the horizontal diameter of the pipe at 5 mm (0.2d) intervals along the pipe axis. Each set of measurements contains 25 radial positions spaced 1 mm (0.039d) apart. The range of optical accessible locations along the pipe axis was from 25 mm to 350 mm (1d to 13.78d) starting from the end of the twisted tape.

Figure 4.1.1 shows a sample of these measurements collected between 150 mm (5.91d) and 230 mm (9.06d) for the 60 mm (y_r = 2.36) swirler at Re = $7.7\text{x}10^4$ (bulk velocity $U_b = 3\,\text{m/s}$). As reported previously by Aidun and Parsheh [2007], the profiles of the tangential velocity V_θ between z = 170 mm (6.69d) and z = 180 mm (7.09d) show an inflection point which eventually leads to asymmetric counter rotating flow near the centerline for z-positions between 185 mm (7.28d) and 205 mm (8.07d) but which returns to the initial typical “S” profile of a simple vortex at z = 230 mm (9.06d). This pattern repeats periodically along the pipe axis for all the 3 swirlers investigated. Positive values of the tangential velocity are marked “+” on the plots and negative values of the tangential velocity are marked “-” on the plots.

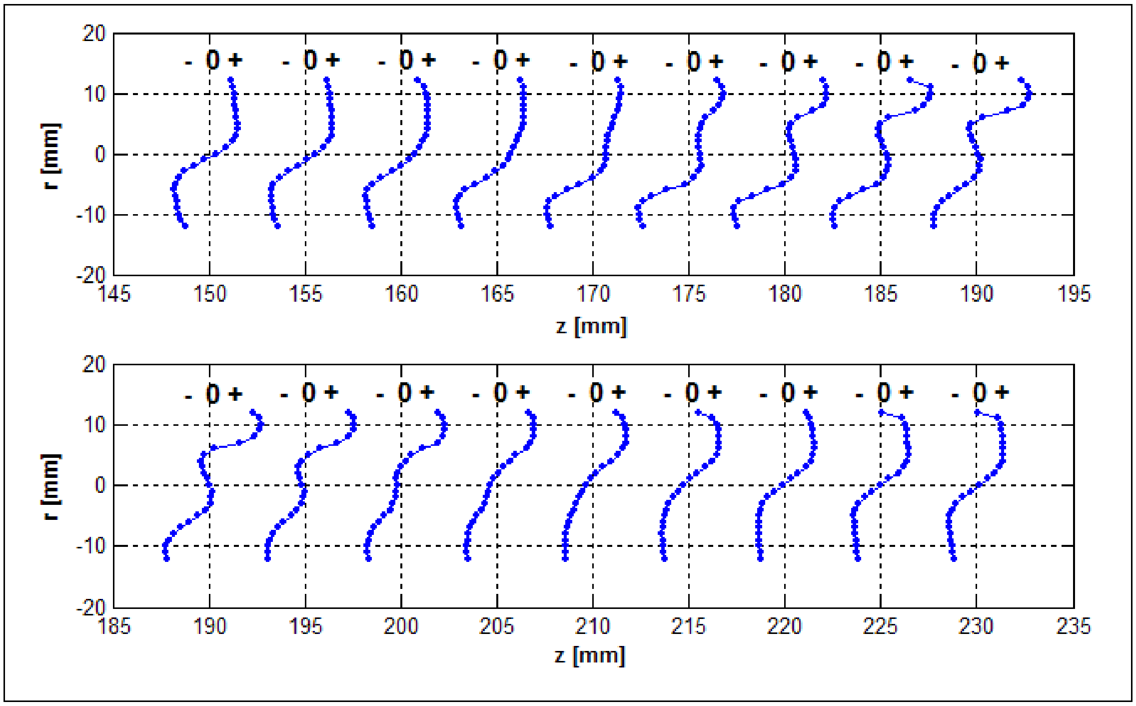

Figure 4.1.1: Variation of the average tangential velocity V_θ along the pipe axis from $z = 150$ mm (5.91d) to $z = 230$ mm (9.06d) for the flow induced by a twisted tape with $H = 60$ mm pitch ($y_r = 2.36$) at $\mathrm{Re} = 7.7\times10^4$.

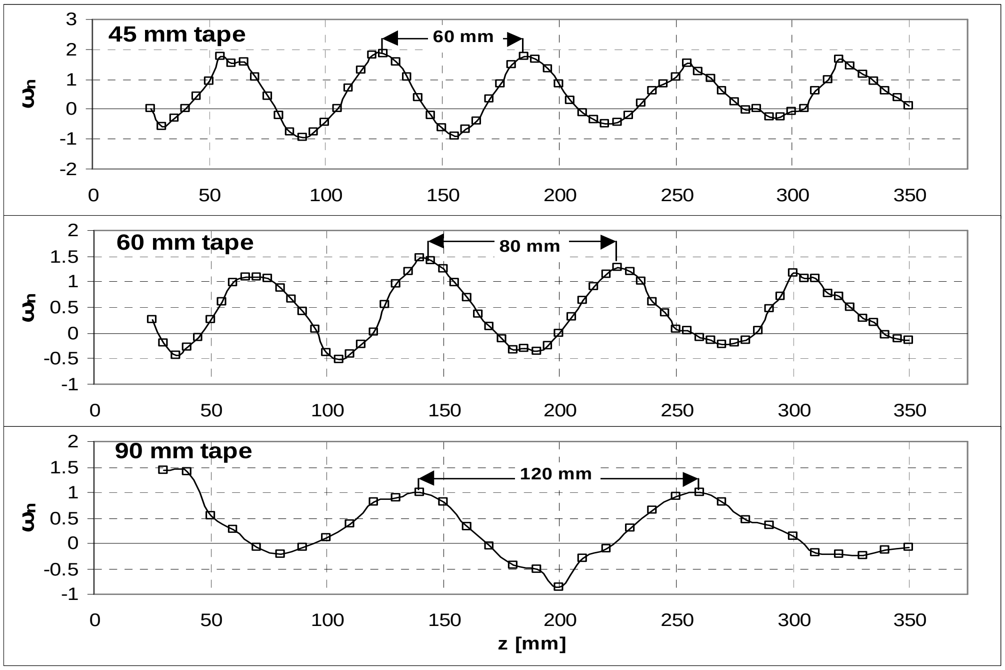

Figure 4.1.2: Variation of the normalized angular velocity ω_n along the pipe axis from 0 to 350 mm (13.78d) from swirler exit for flows induced by twisted tapes with H = 45, 60 and 90 mm pitch (1.77, 2.36 and 3.54 twist ratio) at $\mathrm{Re} = 7.7\times10^4$.

The first profile in figure 4.1.1 is typical for swirling motions. The tangential velocity increases linearly in a core region, reaches a maximum for $r = \pm 5$ mm (± 0.2d) and slowly decays toward the edge of the pipe. When the product $r \cdot V_\theta$ is positive, the flow rotates in the direction of the tape and when the product is negative, the flow rotates against the direction of the tape.

Aidun and Parsheh [2007] proposed using the normalized angular velocity at the pipe centerline ω_n to characterize the periodicity of the flow induced by twisted tapes. The normalized angular velocity at the centerline is defined as:

$$\omega_n = \frac{R \cdot \omega_0}{U_b} \qquad (4.1.1)$$

where R is the pipe inner radius, $\omega_0 = \lim_{r \to 0} \omega = \partial V_\theta / \partial r \big|_{r=0}$ is the centerline angular velocity, V_θ is the average tangential velocity, $U_b = \nu \cdot \mathrm{Re} / (2 \cdot R)$ is the bulk streamwise mean velocity, Re is the Reynolds number and ν is the kinematic viscosity of water.

Figure 4.1.2 shows the variation of the normalized angular velocity at the centerline ω_n along the pipe axis for the three swirlers investigated. The negative values of ω_n represent counter-rotating flow while the positive values show rotation in the direction of the tape. All three profiles clearly show a sinusoidal variation corresponding to a periodic repetition of profiles similar to those shown in figure 4.1.1. The pitch of the sinusoids is approximately 1/3 larger than the corresponding swirler pitch ($H_\omega = (4/3) \times H$). The pitch of the profiles is independent of Reynolds number, as confirmed by the plots of ω_n at five different Re for the 90 mm long swirler ($y_r = 3.54$) (figure 4.1.3).

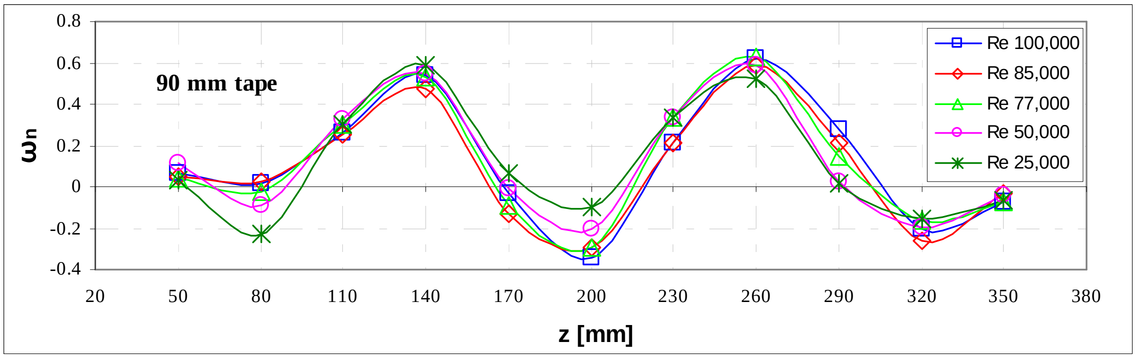

Figure 4.1.3: Variation of the normalized angular velocity ω_n with Reynolds number for the swirler with pitch H = 90 mm (y_r = 3.54) on axial locations from 50 mm (2d) to 350 mm (13.78d) from swirler exit.

The influence of the secondary vortices in the flow induced by a 60 mm long twisted tape (y_r = 2.36) for Re = $7.7\text{x}10^4$ (U_b = 3m/s) on the average axial velocity V_z and the root mean square (rms) fluctuations of the axial velocity v'_z is shown in figure 4.1.4. The influence of the secondary vortices on the average tangential velocity V_θ and the rms of the tangential velocity v'_θ is shown in figure 4.1.5. The fluctuations are normalized by the bulk velocity $U_b = 3\,\text{m/s}$. While the average axial velocity profiles and the rms profiles for both axial and tangential velocities are not as instructive as the average tangential velocity, they still display distinctive features.

Figure 4.1.4 shows the changes in the average axial velocity profiles at three axial locations. The axial velocity profiles are not symmetric because the two secondary vortices are not identical. The increase in the average tangential velocity due to the superposition of the main and the secondary vortices near the wall at $z = 185$ mm (7.28d) significantly decreases the axial velocity (by approximately 30%U_b) while the core region of approximately 10 mm (0.4d) is less affected.

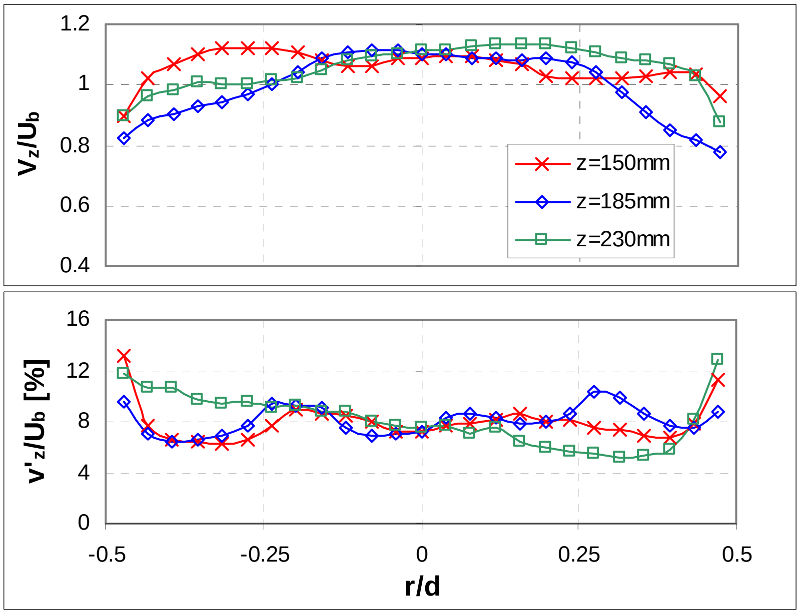

Figure 4.1.4: Measurements of the normalized average axial velocity V_z / U_b (top) and the normalized rms fluctuations of the axial velocity v'_z / U_b (bottom) in the flow induced by a 60 mm long twisted tape (y_r = 2.36) at Re = 7.7×10^4 (U_b = 3m/s) at three axial locations z = 150, 185 and 230 mm (5.9d, 7.28d and 9.06d) downstream of the swirler.

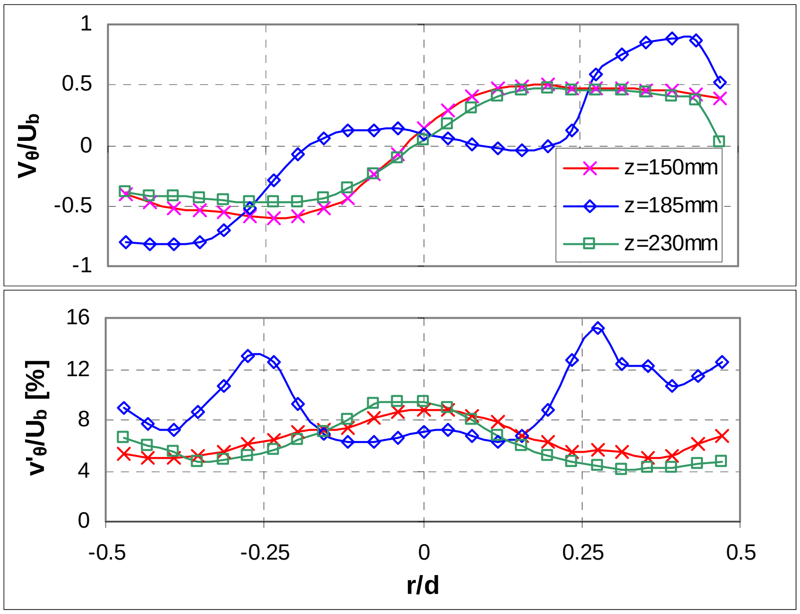

Figure 4.1.5 Measurements of the normalized average tangential velocity V_θ / U_b (top) and the normalized rms fluctuations of the tangential velocity v'_θ / U_b (bottom) in the flow induced by a 60 mm long twisted tape (y_r = 2.36) at Re = 7.7×10^4 (U_b = 3m/s) at three axial locations z = 150, 185 and 230 mm (5.9d, 7.28d and 9.06d) downstream of the swirler.

Both the axial and the tangential velocity fluctuations in Figs. 4.1.4 and 4.1.5 show an increase near the centers of the secondary vortices. These are most likely due to oscillations of the secondary vortices visible in the air bubble visualizations, which are described in the next section.

The impact of the oscillations is slightly stronger on tangential velocities which show maximum fluctuations of approximately 15% while the axial velocity fluctuations have a maximum of approximately 10%. Near the pipe centerline both the axial and tangential velocity fluctuations are approximately 8%. The oscillations seem incoherent as a power spectrum analysis of the axial velocity measurements did not reveal any dominant frequency (figure 4.1.6). The power spectrum was evaluated inside the helical vortex core at the location z = 185 mm (7.28d) and r = -5 mm (-0.2d) from 50,000 axial velocity measurements sampled at 1,000 Hz and processed with Hamming windows on sub-segments of 4096 measurements.

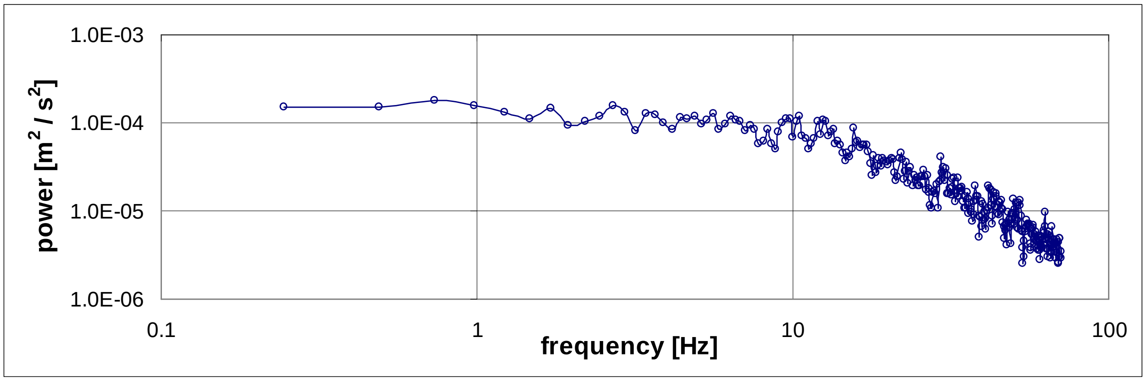

Figure 4.1.6: Power spectrum analysis of the axial velocity V_z inside the helical vortex core at z = 185 mm (7.28d) and r = -5 mm (-0.2d) for the flow induced by a twisted tape with 60 mm pitch (y_r = 2.36) at Re $= 7.7\times10^4$.

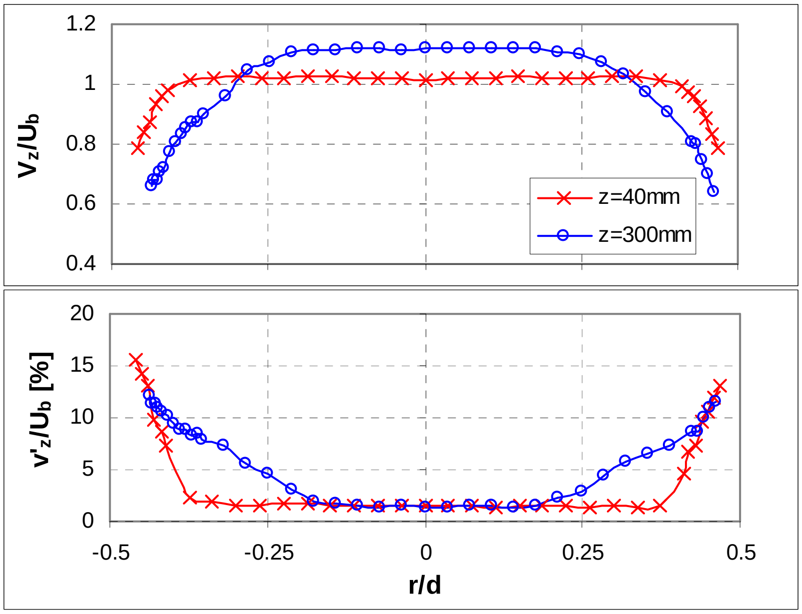

Figure 4.1.7: Normalized average axial velocity V_z/U_b (top) and normalized rms fluctuations of the axial velocity v_z'/U_b (bottom) at $\mathrm{Re}=7.7\times10^4$ (U_b =3m/s) in the absence of the swirler at two axial locations, $z=40$ mm (1.57d) and $z=300$ mm (11.81d) downstream of the contraction end.

Velocity LDV measurements were also collected inside the pipe in the absence of the twisted tape in order to evaluate the flow characteristics at the inlet of the twisted tape swirler. The honeycomb and the 9:1 contraction significantly suppress the velocity fluctuations for all Re investigated. Figure 4.1.7 shows the flow characteristics in the absence of the swirler at two axial locations $z=40$ mm (1.57d) and $z=300$ mm (11.81d), downstream of the contraction end at Re = 7.7x10^4 (bulk velocity $U_b=3$ m/s). At $z=40$ mm (1.57d) the average axial velocity V_z has a flat profile of approximately 101% of U_b while the velocity fluctuations represent approximately 1% of the bulk velocity throughout the pipe except very close to the walls where viscous effects reduce the average velocity while increasing turbulence intensity to approximately 15%. The average axial velocity profile is similar for all Re investigated (in the range 10^4-10^5). The normalized rms fluctuations of the axial velocity v'_z / U_b represent approximately $1 \pm 0.5\%$ of the bulk velocity near the centerline for the whole range of Re investigated. These profiles are used later as inlet boundary conditions for the numerical simulations. The flow development along the axis is slow and at the next location at $z = 300$ mm (11.81d), close to the end of the test section, the viscous effects increase the centerline average axial velocity to 110% of U_b while the decrease in the axial velocity near the walls is accompanied by an increase in fluctuations.

4.2 Air bubble visualization

The air-bubble injection device described in the previous section was installed to visualize the secondary flow. As shown in figure 4.2.1, the air bubbles injected follow stable helical trajectories which do not change throughout the experiments. The air bubble trajectories also do not change with Re, consistent with the LDV measurements. The LDV measurements were done in the absence of the air bubbles, thus avoiding any interference. As the photos in figure 4.2.1 are recorded without the rectangular glass container, the air bubbles appear closer to the wall than they actually are.

Figure 4.2.1 also shows that the pitch of the air bubble streams and the pitch of the measured normalized angular velocity ω_n are identical. This similarity suggests that the sinusoidal variation of ω_n is a result of two helical vortices originating inside the twisted tape swirler and winding with the swirl. The centers of the vortices create low pressure regions which concentrate the air bubbles. These vortices are similar to the double helix described in the investigation of the swirling flow induced in a rectangular chamber by tangential injection [Alekseenko et al. 1999] and shown in figure 2.5.7.

However, as mentioned before, the helical structures created using two plane slopes at the chamber's bottom were very unstable.

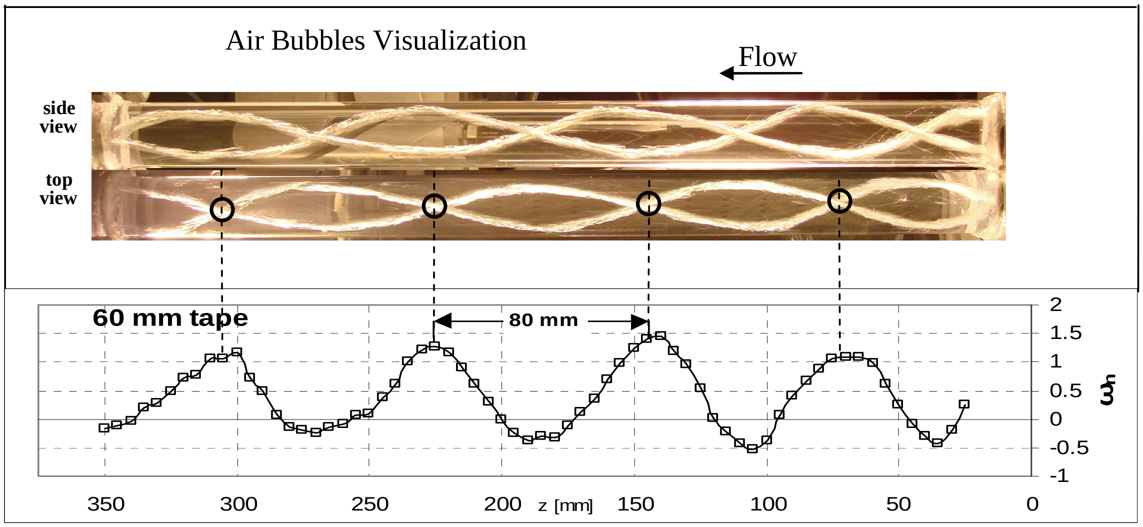

Figure 4.2.1: Side and top views of the air bubble streams showing their helical nature and corresponding centerline angular velocities calculated from LDV measurements for the flow induced by a twisted tape with pitch H = 60 mm (y_r = 2.36) at Re = $7.7\text{x}10^4$ (U_b=3m/s).

The impact of the swirl decay is very limited over the short axial length of the pipe in our investigation as both the measurements (Figures 4.1.1 and 4.1.2) and the visualizations (figure 4.2.1) confirm. This is in agreement with the study preformed by Kreith and Sonju [1965] which showed that the swirl behind a twisted tape decays approximately 20% over the first 10 diameters with slower decay at higher Re and independent of the tape pitch (figure 2.3.1). The focus of this study is within few diameters downstream of the twisted tape.

A thin laser light sheet reveals the location of the centers of the secondary vortices in the pipe cross-section plane (figure 4.2.2a). A movie showing the laser sheet moving along the pipe axis highlights the stability of the helical vortices and confirms that their centers are located about a quarter of a diameter away from the pipe edge, consistent with the measurements.

The secondary vortices are stationary with low amplitude oscillations as they respond to random turbulent fluctuations. The minimum pressure location in the flow field is not at the pipe centerline as in regular swirling flows, but at the center of the secondary vortices, as proved by the air bubble streams. High speed camera recordings show the rotation of individual air bubbles around the secondary vortices 200 times slower than the actual motion (figures 4.2.2 b, c and d). The air bubbles rotating under the influence of the primary vortex are trapped when they pass through the field of the secondary vortices.

Once the bubbles are trapped on the orbit of a secondary vortex, they spiral toward the secondary vortex axis. Within approximately 3 diameters along the pipe axis most bubbles are sucked in the center of the secondary vortices. Downstream the bubbles size increases, restricting good visualization close to the entrance of the straight pipe. The size of the air bubbles increases as Re decreases because the injection holes are facing upstream and the bubble size depends on the dynamic pressure of the incoming fluid (figure 4.2.2d).

A photo of the swirler under intense light proves that the vortices change their pitch compared to the twisted tape while still inside the twisted semicircular channels. The air bubble stream drifts away from the tape toward the center of the channels and it continues smoothly inside the straight pipe (figure 4.2.3). The photo is not very clear as the swirler was not designed to be optically accessible.

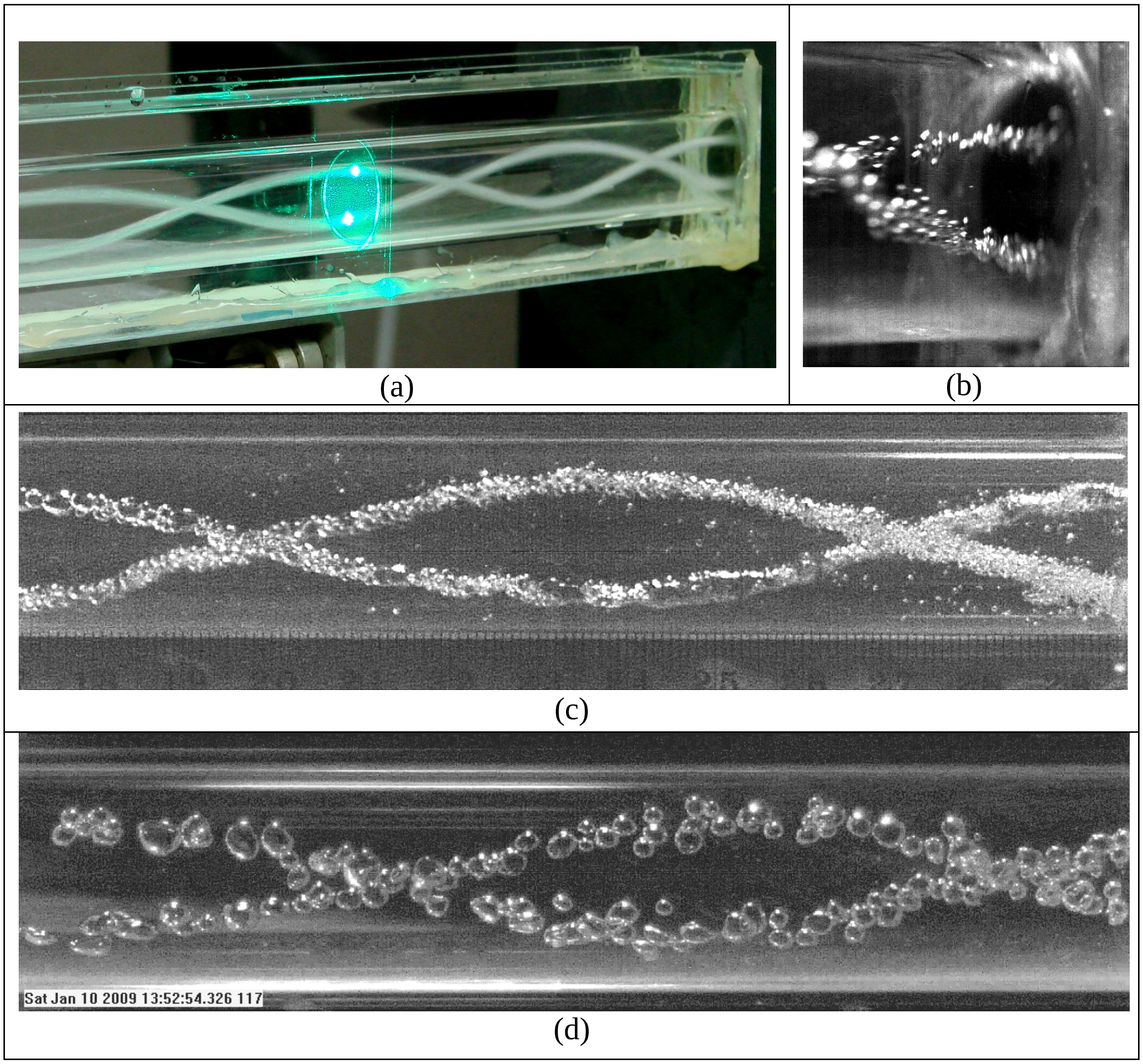

Figure 4.2.2: Air bubble visualizations of the helical vortices for the flow induced by the tape with pitch $H = 60$ mm ($y_r = 2.36$) at Re = $7.7\text{x}10^4$ (the flow is from right to left): (a) general view, (b) high speed camera close-up at the straight pipe entrance, (c) high speed camera side view, d) high speed camera side view at Re = $2.5\text{x}10^4$.

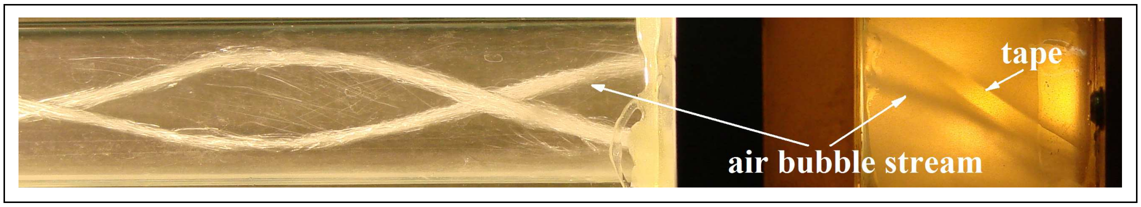

Figure 4.2.3: The air bubble stream drifts away from the twisted tape toward the center of the channel (right) and continues smoothly inside the straight pipe (left) (flow induced by the tape with pitch $H = 60$ mm ($y_r = 2.36$) at Re = $7.7\text{x}10^4$).

The LDV measurements showed that the pitch of the helical vortices did not change with Re. Those measurements are confirmed with high speed camera photos recorded at 4,200 fps (figure 4.2.4) which show how the flow induced by the tape with pitch 45 mm ($y_r = 1.77$) changes with Re in the interval $10^4 – 10^5$.

The pitch does not change even for the flow at Re = $2x10^4$ where the helical vortices are visible only in first half of the test section. In the second half of the test section the bubbles accumulate at the centerline suggesting the flow has become a regular swirling flow. The air bubbles do not identify any helical vortices inside the test section for Re = 10^4 and the main swirl is indicated only in the first half of the test section by the bubbles accumulating at the centerline. Further investigations of the presence of vortices inside the swirler at lower Re are described in Chapter 6.6 using numerical simulations and the λ_2 vortex identification method.

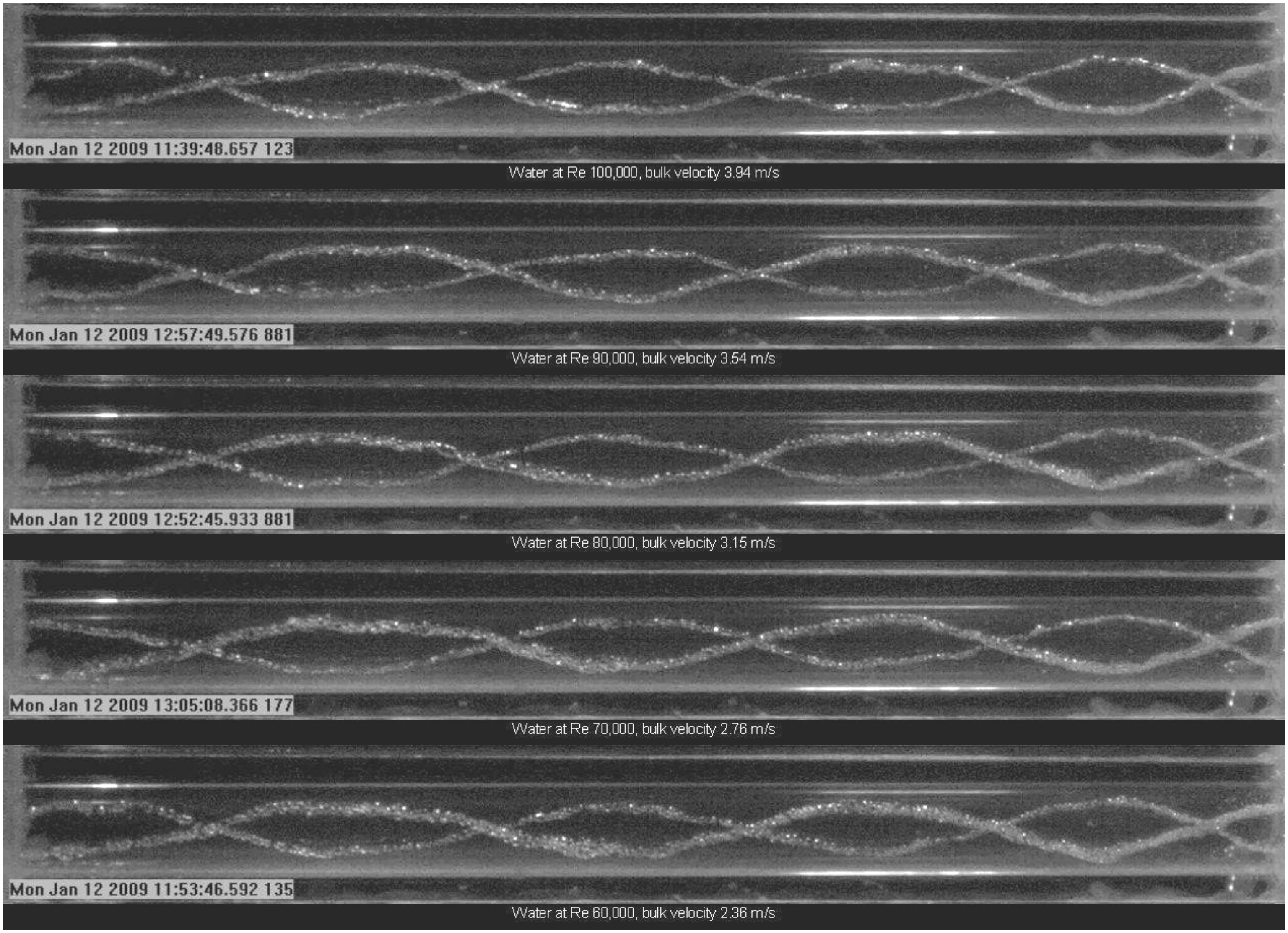

Figure 4.2.4: Helical vortices variation with Re in the range 10^5 to $6x10^4$ (45 mm pitch tape).

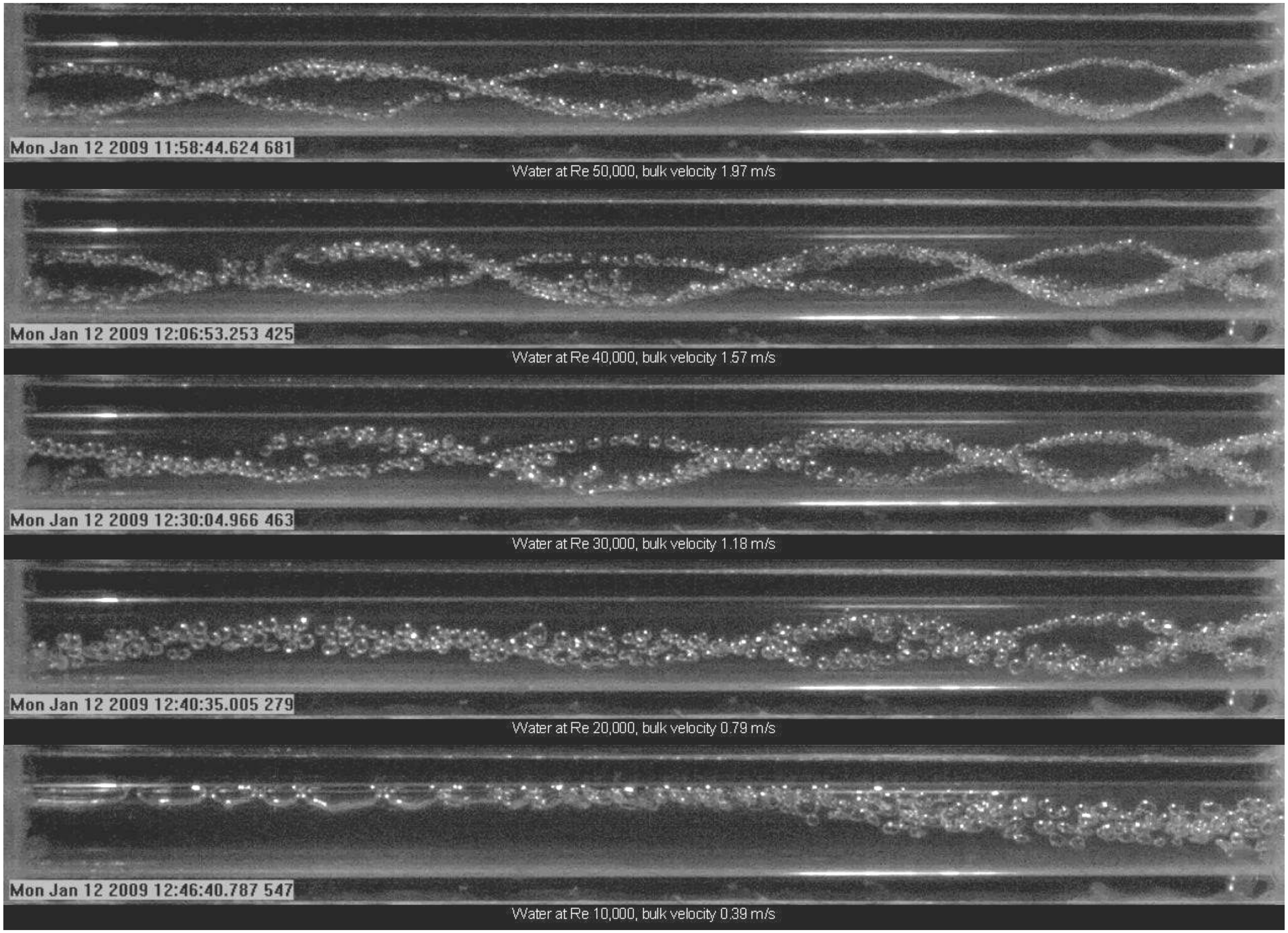

Figure 4.2.4 continued: Helical vortices variation with Re in the range $5x10^4$ to 10^4 (45 mm pitch tape).

The movies show that one of the vortices becomes unstable at the end of the 350 mm (13.78d) test section. In order to investigate if this is an effect of an imperfect connection between the test section and the rest of the pipe, a 1.3 m (51.18d) long continuous pipe section was attached to the 60 mm ($y_r = 2.36$) long twisted tape swirler. Air bubble visualizations in this new setup at $Re = 7.7 \times 10^4$ revealed that the helical vortex becomes unstable approximately 15d downstream from the swirler and confirmed that this effect was not a result of the test section configuration (figure 4.2.5). The flow transitions from a double helix structure to a single helix structure as the weaker vortex merges with the stronger one, which then maintains its helical path until the end of the pipe. As the photo in figure 4.2.5 is recorded without the rectangular glass container, the air bubbles appear closer to the wall than they actually are.

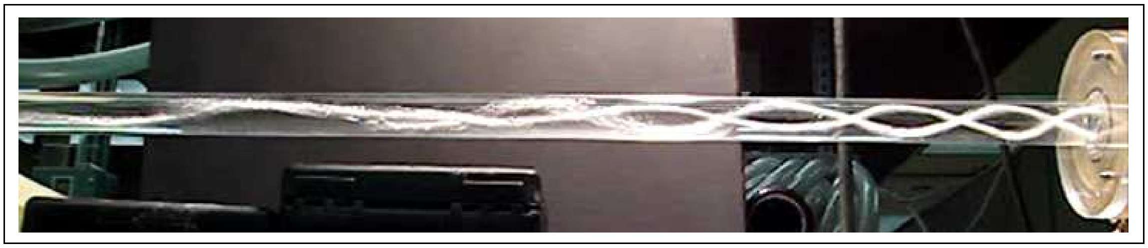

Figure 4.2.5: Vortex development in the flow induced by a 60 mm long twisted tape ($y_r = 2.36$) at $Re = 7.7 \times 10^4$ in a 1.3 m (51.18d) pipe.

Another set of tests was performed using a conventional copper twisted tape inserted into a transparent plexiglass pipe (figure 4.2.6). The new setup, which allows optical access inside the swirler, was designed to confirm the early secondary vortex formation inside the swirler seen in figure 4.2.3. This experiment also confirmed that regular twisted tapes produce helical vortices just like the compact swirler used in the previous experiments. Unfortunately the tape was twisted only to a 110 mm pitch (y_r = 4.33), as the copper failed on attempts to twist it further, so it did not match exactly the compact swirler characteristics described previously. However, even the weaker swirl induced by this long tape created helical vortices as shown in figure 4.2.7. The photo in figure 4.2.7 is also recorded without the rectangular glass container, so the air bubbles appear closer to the wall than they actually are.

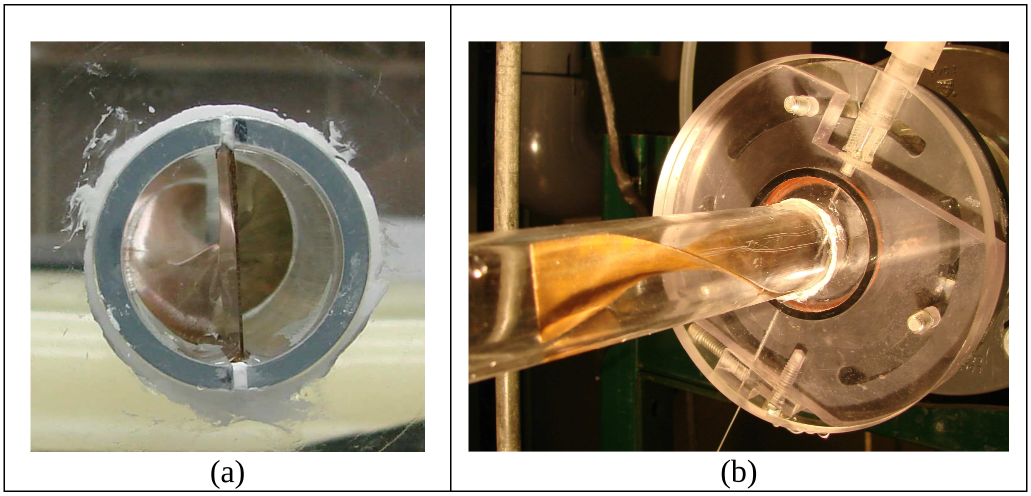
(a) (b)

Figure 4.2.6: Copper twisted tape swirler with 110 mm pitch ($y_r = 4.33$) (a) inlet view, (b) inside the straight pipe.

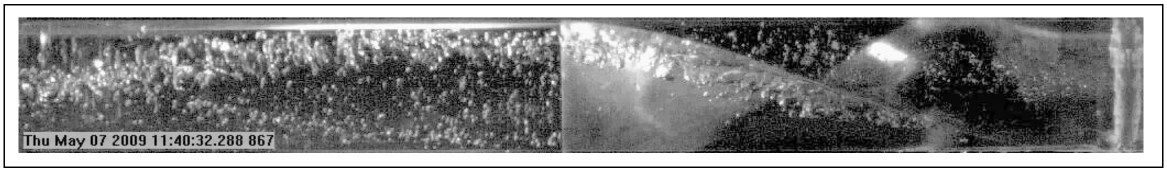

Figure 4.2.7 High-speed camera view of the formation of the helical vortices inside the 110 mm ($y_r = 4.33$) long twisted tape swirler at Re = 7.7×10^4.

4.3 Velocity field reconstruction

The stability of the helical vortices throughout the test section suggests that successive cross sectional flow fields are almost identical, except being rotated relative to each other. As the swirl decay is slow over the helical vortex pitch which spans 80 mm (3.15d) at Re=7.7×10^4 (figure 4.1.1), and considering the periodicity of the flow (figure

4.2.1), an approximation of the flow field is recovered from measurements at several axial locations. The measurements collected across the horizontal diameter at successive axial locations can be considered as measurements at different angles of the same cross-sectional flow field, enabling its reconstruction. The flow field resulted from the combination of all the measurements from figure 4.1.1 with appropriate angular phase shift is shown in figure 4.3.1.

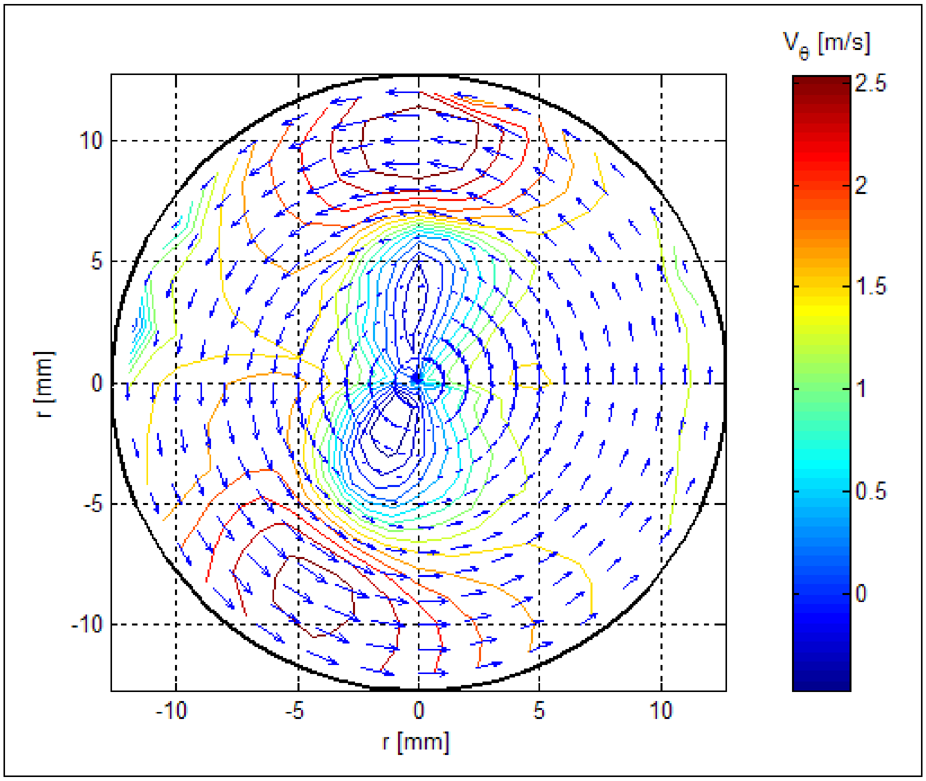

Figure 4.3.1: Reconstructed average tangential velocity field of the swirling flow induced by a twisted tape with pitch $H = 60$ mm (y_r =2.36) at Re = 7.7x10^4 (U_b = 3m/s).

The number of diameters used for the flow field reconstruction depends on the periodicity of the normalized angular velocity. For the 60 mm long swirler (y_r = 2.36) the variation of the angular velocity at the centerline exhibits an 80 mm (3.15d) period. The measurements were collected every 5 mm (0.2d) along the pipe so the cross sectional flow field reconstruction includes $m = 80/5 = 16$ measurement sets. The angle between the measurements was determined assuming equal spacing ($\theta = 180°/16 = 11.25°$). Each measurement set contains 25 radial positions spaced 1 mm (0.039d) apart. As the centerline measurement is repeated in all 16 measurements sets, the cross sectional flow field is characterized by $16 \times 25 - 15 = 385$ independent measurements.

The arrows in figure 4.3.1 show the location of the measurements and the relative magnitude and orientation of the tangential velocity in the cross sectional field. The arrows are not complete velocity vectors as they lack the radial velocity component. The radial velocity components must have the same order of magnitude as the tangential velocities of the secondary vortices to satisfy mass conservation in the regions showing low tangential velocities near the edges of the secondary vortices. To display the arrows, the velocities were projected on the vertical and horizontal axis using the corresponding angle for each measurement diameter ($0°$ for the first one, $11.25°$ for the second, $22.50°$ for the third, etc.).

The cumulative plot in figure 4.3.1 shows a three vortex structure with two secondary vortices superimposed over the main swirling flow created by the twist of the tape. The two secondary vortices have a diameter equal to the pipe radius. They rotate in the same direction as the main flow and have a skewed shape due to its presence.

4.4 Secondary flow recovery

The analysis of the velocity profiles from figure 4.1.1 suggests that the velocity distribution of the tangential velocity field generated by the main swirl is described by the measurements that do not cross the secondary vortices. The measurements least affected by the secondary vortices are collected perpendicular to the line crossing through their centers (figure 4.3.1). In the case of the twisted tape with 60 mm pitch (y_r = 2.36) presented in figure 4.1.1, these measurements are the ones collected at the axial location z = 225 mm (8.86d) for which ω_n exhibits a peak in figure 4.1.2. In order to reveal the effect of the secondary vortices on the total tangential velocity field, the background created by the velocity field of the main vortex was subtracted from all velocities profiles in figure 4.1.1.

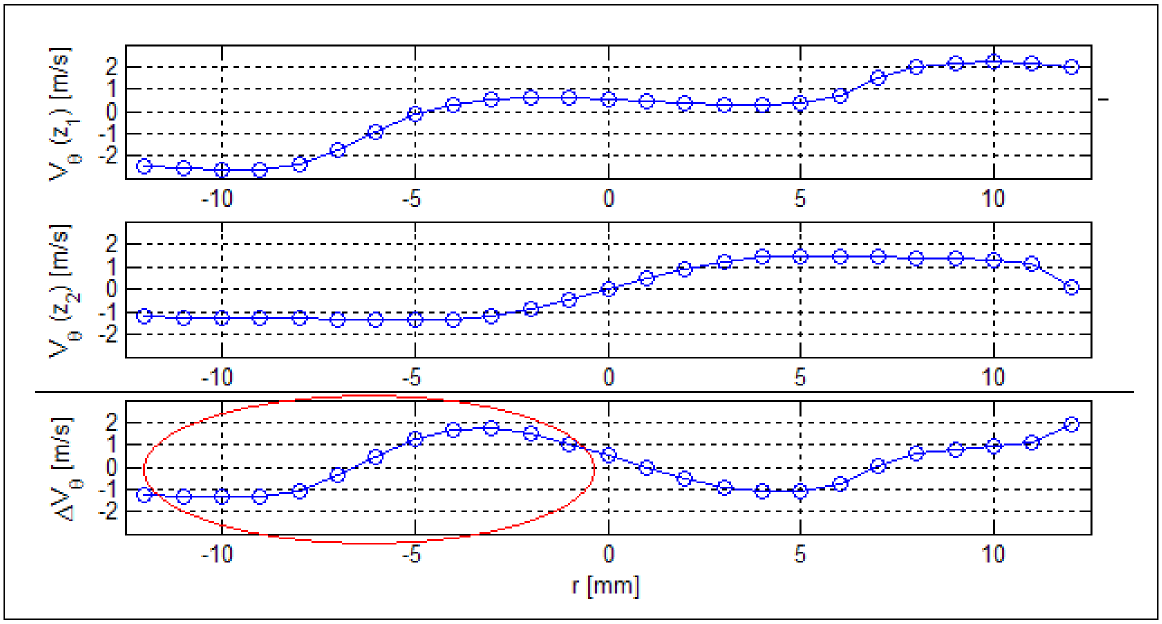

Figure 4.4.1: The actual tangential velocity profile of the lower secondary vortex is highlighted in the plot of $\Delta V_\theta = V_\theta(z_1) - V_\theta(z_2)$ where V_θ(z_1=180mm) are the measurements through the center of the lower vortex and V_θ(z_2=225mm) is the main vortex velocity distribution.

The actual velocity distribution of the secondary vortices can be extracted only from the measurements which cross through their centers. These measurements sets are identified in figure 4.1.1 as the ones showing maximum counter-rotating flow, respectively the measurements at z = 180 mm (7.09d) for the lower vortex (located on the lower side of figure 4.3.1) and z = 190 mm (7.48d) for the upper vortex. The background removal process is shown in figure 4.4.1 for the measurements which cross through the center of the lower vortex.

The total tangential velocity field after subtraction of the velocity field induced by the primary vortex is shown in figure 4.4.2 as seen looking upstream. Compared to the original field, the secondary vortices recovered the round shape and their centers shifted approximately 1.5 mm (0.06d) toward exterior. The arrows show the direction of rotation for both secondary vortices and also for the main field.

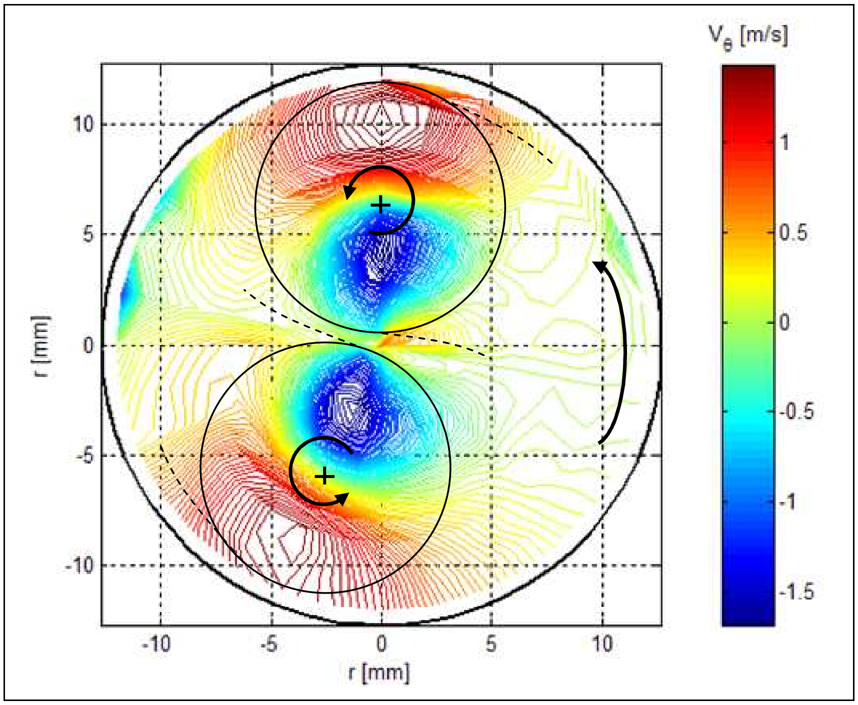

Figure 4.4.2: Average tangential velocity contours of the secondary vortices after removing the main vortex background at Re = 7.7x10^4 (U_b = 3m/s). The circles show the boundaries of the vortices while the arrows show their rotation.

Figure 4.4.3 shows the tangential velocity profiles of all three vortices present in the flow field ignoring the angle difference between the two secondary vortices. These velocity profiles are extracted from the measurements which cross through the center of the secondary vortices, thus showing the actual distance between the center of the pipe and the centers of the vortices and also the actual tangential velocity magnitudes.

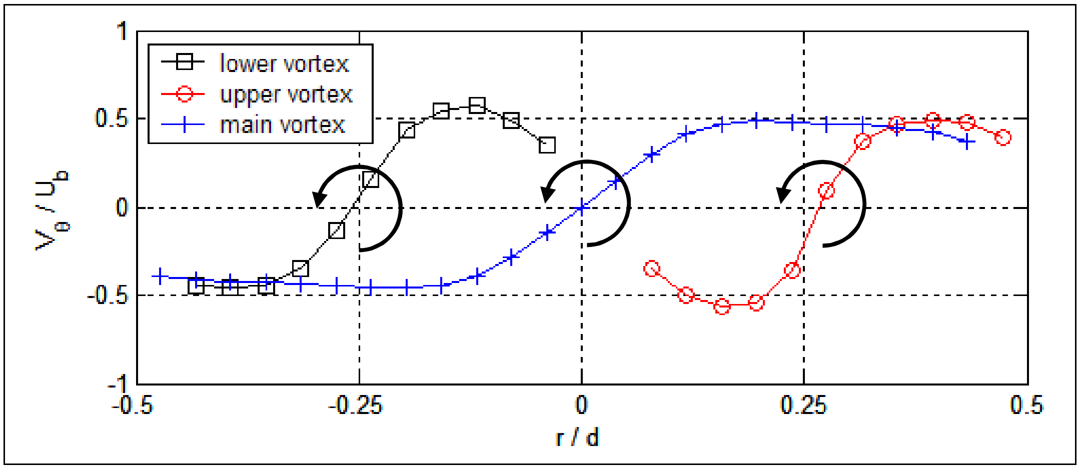

Figure 4.4.3: Average tangential velocity profiles of the three vortices present in the flow induced by a twisted tape with pitch H = 60 mm (y_r = 2.36) at Re = 7.7x10^4 (U_b = 3m/s).

The fact that without the influence of the primary vortex the two secondary vortices recovered their symmetric shape suggests that the overall flow field is the result of a superposition of the fields induced by the secondary vortices on the field generated by the primary vortex, regardless of Reynolds numbers or the turbulence level.

The maximum velocity induced by the secondary vortices is approximately the same as the maximum velocity induced by the primary vortex. Due to space restrictions, the size of the core region of the secondary vortices is only 6 mm (0.24d) compared to the 10 mm (0.39d) for the primary vortex, meaning that the secondary vortices have a higher angular velocity than the primary vortex. In figure 4.4.3 the angular velocities calculated at the centers of the secondary vortices are 135 rot/s for the lower vortex and 175 rot/s for the upper vortex, while the angular velocity of the primary vortex is 71 rot/s.

The distance between the centers of the secondary vortices and the pipe centerline is approximately 0.25d (6.6 - 6.8 mm). The space separating the two secondary vortices is approximately 3 mm (0.12d). The measurements are confirmed by the air bubble visualizations described in section 4.2.

Despite the fact that the swirler is symmetric and the two helical vortices have the same pitch, the angle formed by their centers and the center of the main vortex (which is also the center of the pipe) is 155° instead of 180° angle. The angle observed between the secondary vortices is created as one of the vortices becomes unstable before eventually merging with the second helical vortex (see visualization in figure 4.2.5). The remaining helical vortex oscillates and its pitch increases but it does not disappear until the end of the 1.3m (51.18d) pipe. The oscillations of the helical vortices create the peaks observed in the velocity fluctuations plots near the cores of the helical vortices (figures 4.1.4 and 4.1.5).

4.5 Vortex inception and development

Previous studies of swirling flows induced by twisted tapes inserts suggest that the secondary motion is produced by the centrifugal imbalance caused by the radial velocity distribution coupled with the rotational motion created by the twist of the tape. These studies generally showed two counter-rotating vortices appearing on each side of the twisted tape and changing their size and location in the cross-section along the pipe [Seymour 1966, Kazuhisa et al. 2004, Yerra et al. 2007].

The swirlers investigated here do not allow direct measurements inside them. At the same time, no traces of a counter-rotating vortex were observed either in the air bubble visualizations or in the LDV measurements inside the straight pipe presented in this study.

The experiments presented in this chapter suggest that single co-rotating vortices form on each side of the twisted tape. As the co-rotating vortex strengthens and expands, its core slowly moves away from the twisted tape resulting in the increase of the vortex pitch relative to the twisted tape pitch (as shown in figure 4.1.2). Once the twisted tape ends, the co-rotating secondary vortices preserve their size, helical trajectory and pitch inside the straight pipe.

The same tangential velocity component drives the primary vortex and also accelerates the secondary vortices. As a result all vortices reach approximately the same maximum tangential velocity, as indicated by the measurements. Figure 4.4.3 shows that for the swirling flow induced by the tape with 60 mm (2.36d) pitch at Re = 7.7×10^4 the maximum velocity of all three vortices is approximately half the magnitude of the bulk velocity.

The pitch of the secondary vortices $H_\omega = (4/3) \times H$ is characteristic to 180° twisted tapes and it is not the same for tapes twisted more than 180^o (as it will be shown in the next chapters). The coexistence of the two co-rotating vortices is possible due to the presence of the primary vortex, which reduces the tangential velocity of the two secondary vortices near the pipe centerline, allowing a smooth transition. Further details of the formation of the secondary vortices are presented in the following chapters using numerical simulation.

CHAPTER 5

NUMERICAL SIMULATIONS: MODELS

5.1 Background

While the experimental measurements and the air bubble visualizations clearly answered the main question of the present study, showing that counter-rotating flow is possible as a result of the presence of secondary helical vortices, it also raised the question of how these vortices form and develop inside the swirler. As the setup does not allow non-intrusive measurements inside the swirler, an alternative solution for investigating the inception of the secondary vortices is to model the flow using commercial CFD software. Numerical simulations are capable of providing a complete description of the flow field, including the velocity field and the pressure distribution, thus complementing the experimental observations.

The purpose of the simulation is not to reproduce the flow precisely. The accuracy of the simulation is limited by the computational resources available and the demanding characteristics of the flow (high Re flow, large domain and large 3D gradients). Consequently, the simulation is designed to capture qualitatively the helical vortices observed in the experiments, in order to identify their origin.

Simulations of swirling flows through pipes with twisted tapes inserts at low Re [Date 1974, Kazuhisa et al. 2004, Yerra et al. 2007] and also simulations of flows through static mixers using the software “FLUENT” for Re up to $5x10^3$ [Rahmani 2004, 2005] were described in Chapter 2.3. However, all the previous studies investigated the flow inside the twisted tape, while the present study analyzes the behavior of the secondary flow downstream of a short twisted tape swirler. This explains the absence of any previous reports of helical vortices induced by twisted tapes.

The secondary flow observed in the experiments and presented in the previous chapters is further investigated using numerical models. The models simulate the swirling flow through an 180^o twisted tape swirler with a straight pipe section upstream of the swirler and another straight pipe section downstream from the swirler. Additionally, swirlers with multiple twists and multiple chambers are also investigated. The flow is calculated using the commercial CFD software FLUENT (Fluent Inc., Lebanon, NH) while the various computational grids are created using the grid generator software GAMBIT produced by the same company. The main characteristics of the simulations are described in the following sections.

5.2 Governing equations

The stability of the helical vortices observed during the experiments suggests that the flow is in a quasi-steady state, thus the flow is modeled using the steady state Navier-Stokes equations. A Cartesian coordinates system XYZ was preferred because the flow is not axi-symmetric and the Cartesian system avoids the singularities which the Navier-Stokes equations in cylindrical coordinates have at the centerline from terms containing $1/r$ and $1/r^2$. The working fluid in the model is liquid water (incompressible) at room temperature. The flow field is obtained solving the governing integral equations for the conservation of mass and momentum using a pressure-based solver in which the pressure field is extracted by solving a pressure correction equation.

For a steady incompressible flow, the mass conservation equation in Cartesian coordinates expressed in index notation (where repeated indices imply summation) is:

$$\frac{\partial u_i}{\partial x_i} = 0 \qquad (5.1)$$

where u_i represents the velocity component in the x_i direction. The momentum conservation equation in the absence of external body forces is:

$$\rho \frac{\partial \left(u_i u_j \right)}{\partial x_j} = -\frac{\partial p}{\partial x_i} + \frac{\partial \tau_{ij}}{\partial x_j} + \rho g_i \qquad (5.2)$$

where ρ is the density, p is the pressure and g is the gravitational acceleration in the x_i direction. The stress tensor τ_{ij} for an incompressible flow is given by:

$$\tau_{ij} = \mu \left(\frac{\partial u_i}{\partial x_j} + \frac{\partial u_j}{\partial x_i} \right) \qquad (5.3)$$

where μ is the kinematic viscosity.

The experimental data show that the flow is laminar at the inlet of the swirler for all Re investigated due to the honeycomb and the 9:1 contraction located immediately upstream (figure 4.1.7). The experiments also showed that inside the straight pipe the flow is stable and the behavior of the secondary motion is closer to a laminar regime rather than the turbulent regime expected at the high Re of the experiments. This is unlikely to be a result of relaminarization as previously observed in rotating flows [Humphrey and Webster 1993], because Re is very high. This behavior is most likely caused by the close proximity of the test section to the calming section installed immediately upstream from the swirler. Simulations are run with both laminar and turbulent formulations and compared to the experimental data to determine which effects are dominant.

When turbulence effects are incorporated into the governing equations, the momentum equation becomes:

$$\rho \frac{\partial (u_i u_j)}{\partial x_j} = \frac{\partial}{\partial x_j}\left[\mu\left(\frac{\partial u_i}{\partial x_j} + \frac{\partial u_j}{\partial x_i}\right)\right] - \frac{\partial p}{\partial x_i} + \rho g_i + \frac{\partial}{\partial x_j}\left(-\rho \overline{u_i' u_j'}\right) \qquad (5.4)$$

which is the Reynolds averaged Navier-Stokes equation for a steady, incompressible flow. In equation (5.4) $\rho \overline{u_i' u_j'}$ is the Reynolds stress produced by velocity fluctuations u_i'. The large gradients in the flow and its 3D nature (associated with the presence of the helical vortices) require a fine grid with large numbers of computational cells so Direct Numerical Simulations (DNS) and Large Eddy Simulations (LES) methods are computationally expensive. To reduce the computational requirements the Reynolds stresses $\rho \overline{u_i' u_j'}$ have to be modeled. The “Reynolds Stress Model” (RSM) which solves the transport equation for each component of the Reynolds stress tensor is recommended for swirling flows where the turbulence is anisotropic [Pope 2000].

5.3 Computational domain

The flow is three-dimensional and non-axisymmetric. The numerical model simulates a 1 inch (25.4 mm) diameter cylindrical pipe with a twisted tape insert using finite volumes. The computational domain employs a 3D Cartesian coordinate system XYZ centered on the pipe axis at the end of the swirler with the Z axis orientated along the pipe centerline, in the direction of the flow. The coordinate system was centered at the end of the swirler to match the experimental measurements.

The reference parameters for the simulations are the diameter d = 25.4 mm, the Reynolds number and the atmospheric pressure P_0 = 101,325 Pa. Velocities are normalized with the bulk velocity $U_b = \frac{\nu \cdot \mathrm{Re}}{d}$, where the kinematic viscosity of water at 1 atm. and 15 ^{o}C is $\nu = 10^{-6}$ m^2/s. The following numerical results are expressed in non-dimensional form but some physical dimensions are also provided for comparison with the experiments. Also, when compared to the experimental data, the results of the numerical modeling are converted in cylindrical coordinates where the velocity components are the axial velocity V_z, the tangential velocity V_θ and the radial velocity V_r.

The mesh is unstructured and it consists of tetrahedral cells selected for their capacity to accommodate the complex 3D shape of the twisted tape. Grid independence tests for grids with 0.039, 0.027 and 0.021 average side length cells indicated that the 0.027 cells represent the optimum for these simulations. Grids with 0.039 cells underestimated the pitch of the secondary vortices while 0.027 and 0.021 provide similar results.

The mesh with 0.027 cells contains approximately 4 million tetrahedral cells. The 17.72 long computational domain (equivalent to 450 mm) has three sections: a 1.57 long straight pipe inlet section (40 mm) followed by a pipe section containing an 180^{o} twisted tape insert with twist ratios 1.77, 2.36 or 3.54 (45, 60 or 90 mm pitch) and ending with a straight pipe section corresponding to the experimental test section.

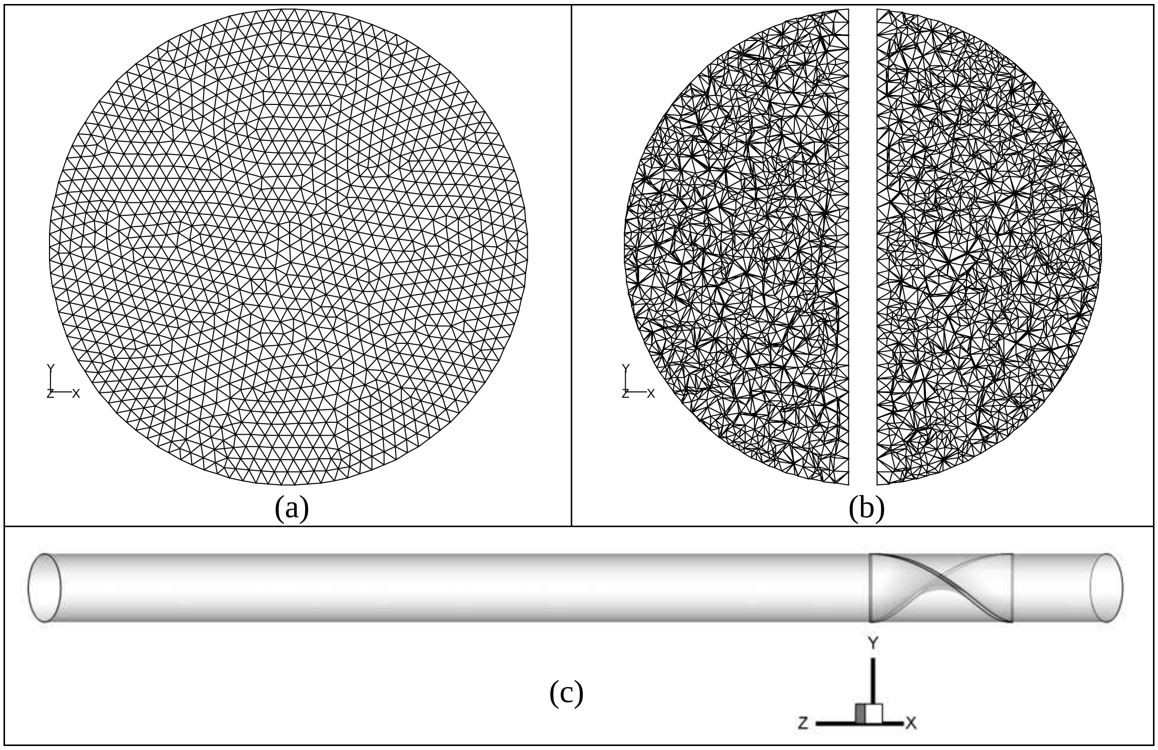

Figure 5.3.1: Computational domain for the twisted tape with $y_r = 2.36$: (a) inlet cross section, (b) cross section showing the inlet of the twisted tape swirler, (c) full 17.72d long computational domain .

In order to correlate the results with the more general case of regular twisted tapes with constant width, the swirlers in the simulations have a constant width equal to the width of the experimental swirlers at the exit 0.059 (1.5 mm). The pitch of the helical vortices is likely to depend on the position of the vortices relative to the tape at the exit of the swirler. As the vortices form inside the swirler, the effect of the larger entrance blockage is considered negligible for the qualitative simulations performed in this study. Figure 5.3.1 shows the grid cross-section at the pipe inlet, the cross-section at the twisted tape inlet and a general view of the entire domain for the twisted tape with $y_r = 2.36$.

5.4 Numerical solver

The steady state flow is solved using the commercial CFD software FLUENT. The solver is 3D, pressure based, segregated and implicit. The gradients are evaluated using the node based Green–Gauss method. A third order MUSCLE scheme is used for discretization. The pressure velocity coupling is implemented using the PISO method and the pressure discretization is implemented using the PRESTO method. Details about the solver are presented in the following paragraphs.

In the pressure-based solver the pressure equation is derived from the mass and momentum conservation equations so the velocity field, corrected by the pressure, satisfies the mass continuity equation. Since the governing equations are nonlinear and coupled to one another, the solution process involves iterations until the solution converges. In this simulation the governing equations are solved sequentially using the "segregated" algorithm in which the individual governing equations for the solution variables are solved one after another. The "segregated" algorithm is memory-efficient as the discretized equations are stored in the memory one at a time. While the solution convergence is relatively slow compared to the "coupled" algorithm which solves the pressure and momentum equations at the same time, the memory requirement is half and allows the use of a finer grid.

The equations are linearized with an implicit formulation in which the unknown value in each cell is computed using a relation that includes both existing and unknown values from neighboring cells. Each unknown appears in more than one equation in the system creating a system of linear equations solved using a Gauss-Seidel algorithm.

The gradients are computed using the “Green-Gauss Node Based” scheme. This scheme reconstructs values at a node from surrounding cell-centered values on arbitrary unstructured meshes by solving a constrained minimization problem and it provides second-order spatial accuracy. The node-based averaging scheme provides better accuracy for unstructured tetrahedral meshes compared with the cell-based scheme [Holmes and Connell 1989, Rauch et al 1991].

The pressure equation is discretized with the PRESTO scheme (PREssure STaggering Option) which uses the discrete continuity balance for a control volume to compute the face pressure. The PRESTO scheme provides improved accuracy for flows with high swirl numbers, high-speed rotating flows, and flows in strongly curved domains compared to the other models available in FLUENT [Fluent Inc. 2006].

The momentum equation is discretized with a third-order MUSCL (Monotone Upstream-Centered Schemes for Conservation Laws) scheme. This scheme was created from the original MUSCL scheme [Van Leer 1979] by combining a central differencing scheme and second-order upwind scheme. The MUSCL scheme is applicable to arbitrary meshes and improves spatial accuracy for all types of meshes by reducing numerical diffusion, particularly for complex three-dimensional flows [Fluent Inc. 2006].

The coupling between pressure and velocity is achieved using PISO scheme (Pressure-Implicit with Splitting of Operators) with skewness correction which provides faster convergence on meshes with a high degree of distortion [Issa 1985]. The PISO coupling scheme is part of the SIMPLE family of algorithms [Patankar 80] and it performs two corrections: “neighbor” correction and “skewness” correction. The “neighbor” correction adds iterations inside the solution stage of the pressure-correction equation in order to satisfy the continuity and momentum equation more closely. The "skewness" correction adds iterations to improve the adjustment of the face mass flux correction according to the normal pressure correction gradient. For meshes with a high degree of skewness the PISO algorithm applies one or more iterations of skewness correction for each separate iteration of neighbor correction. The PISO algorithm takes more CPU time per solver iteration, but it decreases the number of iterations required for convergence [Fluent Inc. 2006].

The flow is solved with both laminar and turbulent simulations. The turbulent flow is modeled using Reynolds Stress Model (RSM) [Launder et al 1975] which is recommended for swirling flows and flows with secondary motion where the turbulence is anisotropic [Pope 2000]. In the turbulent simulation a new set of 7 more equations is solved in addition to the equations solved with the laminar model. These equations are the transport equations for all six components of the Reynolds stress tensor and an additional scale-determining equation for the turbulent dissipation rate. The equations are discretized with a second order scheme.

At the walls, the near-wall Reynolds stresses and the dissipation rate are calculated with the standard wall functions proposed by Launder and Spalding [1974]. The stresses are specified explicitly assuming that equilibrium and the log-law are valid near the walls while convection and diffusion are neglected in the stress transport equations. The addition of the turbulent model approximately doubles the solver run time.

The simulations are run on a computer with dual core processor (Intel 2.13 GHz) and with 4 GB of memory. The solution is considered satisfactory when the convergence criterion $\varepsilon_i < 10^{-3}$ is satisfied where ε_i are the relative errors for the three momentum equations along each coordinate axis and the mass conservation. For turbulent flows the residuals of the six components of the Reynolds stress tensor are monitored in addition to the residuals of mass and momentum. Comparisons with experimental data are also used to asses the quality of the simulation in the case of high residual error. Most laminar simulations require about 3000 iterations to converge at approximately 1 iteration/minute (50 clock hours).

5.5 Boundary conditions

No-slip boundary conditions are applied on solid surfaces (on the wall and twisted tape). The inflow velocity profile was determined experimentally by running a test with a simple pipe, without the swirler. The experiments showed that, despite the large Reynolds number used, the honeycomb flow straightner and the 9:1 contraction maintained the flow laminar at the swirler inlet for the entire velocity range investigated (figure 4.1.7). The experimental inlet profiles used in the simulations are flat as observed in the experiments (figure 4.1.7) with specified axial inlet velocities corresponding to Re in the range 10^2 to 10^5 (between 0.004 m/s and 4 m/s) and 1% turbulence intensity for the turbulent simulations. The mass flow through the inlet is constant. The outflow boundary condition is also constant mass flow.

In addition to the boundary conditions provided for the laminar case, the RSM turbulent model requires inlet boundary conditions for each component of the Reynolds stress and for the dissipation rate. These quantities are calculated using the inlet turbulent intensity and a characteristic length. In these simulations the turbulent intensity is specified to be 1% (determined from experiments) and the characteristic length is the hydraulic diameter equal to the pipe diameter d = 0.0254 m.

CHAPTER 6

NUMERICAL SIMULATIONS: RESULTS AND ANALYSIS

6.1 Numerical model validation

The numerical model is validated by comparing the pitch of the helical vortices and the tangential velocity profiles with the experimental observations (flow visualizations and LDV measurements). Figure 6.1.1 shows numerical results obtained with the laminar simulation for the swirler with $y_r = 2.36$ at $Re = 7.7x10^4$ (bulk velocity 3m/s) side by side with a photo recorded during experimental tests. The helical vortices are identified from the numerical simulation results by isobar surfaces of low pressure which are equivalent to the air bubbles accumulations observed in the experiments. Figure 6.1.2 shows a comparison between the position of the helical vortices in the pipe cross-section as shown by a laser sheet in the experiments and the positions shown by a cross-section plane in the numerical simulation.

Comparing the pitch of the helical vortices and their axial and radial positions inside the pipe, the results of the laminar steady state numerical simulation match qualitatively with the experimental images both in the developing region inside the swirler and in the stable region inside the straight pipe. Inside the straight pipe the pitch of the helical vortices is approximately 3.15 (80 mm) both in the experiments and in the numerical simulation. The reference value of the pressure $p = 1$ for the isobar surfaces used for this case to identify the helical vortices is selected to match approximately the thickness of the bubble streams observed in experiments. The pathlines calculated numerically (figure 6.1.1b) also match well the few short pathlines of small air bubbles visible in the experimental photo as a result of the fast flow motion relative to the exposure time 1/250 seconds (figure 6.1.1a).

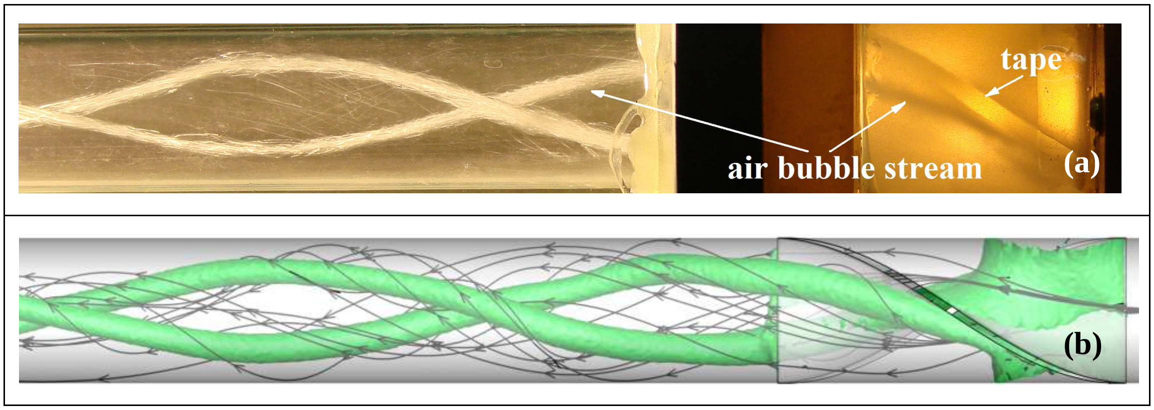

Figure 6.1.1: Experimental and numerical visualizations of the development of the helical vortices for the twisted tape with $y_r = 2.36$ at $Re = 7.7 \times 10^4$: (a) side view photo of air bubbles streams, (b) side view plot of isobar surfaces ($p = 1$) and pathlines calculated with a laminar numerical simulation at steady state.

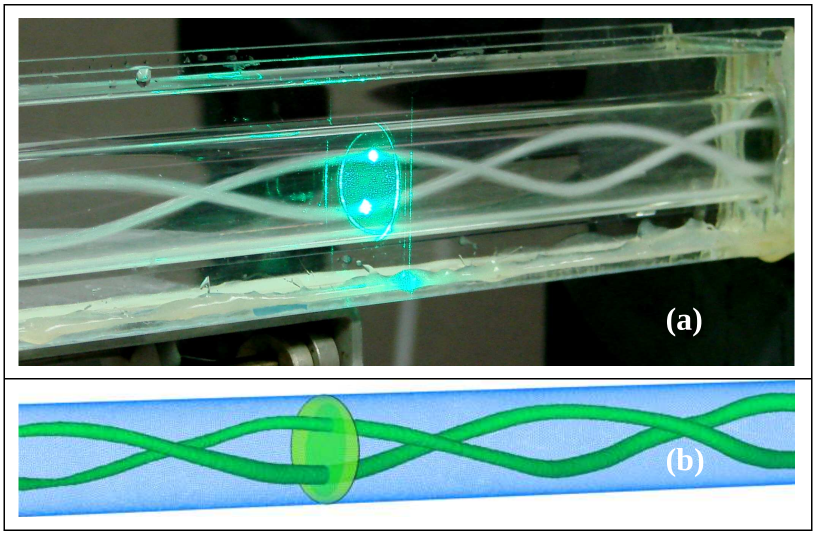

Figure 6.1.2: Relative position in the pipe cross-section of the helical vortices induced by the twisted tape with $y_r = 2.36$ at $Re = 7.7 \times 10^4$: (a) experimental photo, (b) laminar numerical simulation.

Similar comparisons showing the entire experimental test section for the flows induced by all the swirlers available (y_r = 1.77, 2.36 and 3.54) at Re = 7.7x10^4 are shown in figures 6.1.3, 6.1.4 and 6.1.5. The pitch and position of the helical vortices predicted by the laminar steady state numerical simulations are in good agreement with the experiments. For the twisted tapes with y_r = 1.77 and y_r = 2.36, the locations of the helical vortices in the numerical results are slightly shifted toward the exit, but the pitch is approximately the same as observed in the experiments.

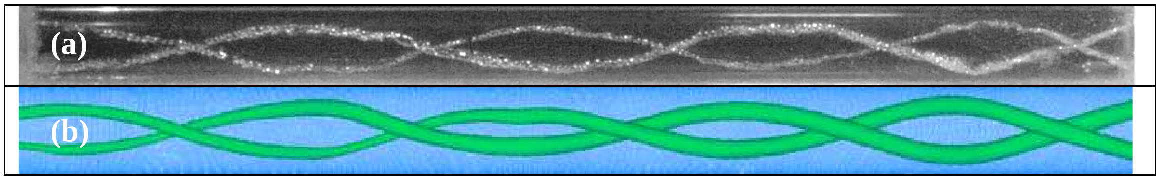

4

Figure 6.1.3: Helical vortices generated by a twisted tape with twist ratio y_r = 1.77 (45 mm pitch) at Re = 7.7x10^4: (a) high speed camera visualization, (b) numerical results.

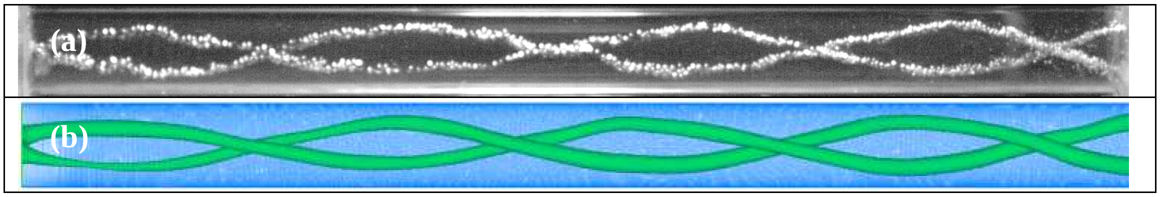

Figure 6.1.4: Helical vortices generated by a twisted tape with twist ratio y_r = 2.36 (60 mm pitch) at Re = 7.7x10^4: (a) high speed camera visualization, (b) numerical results.

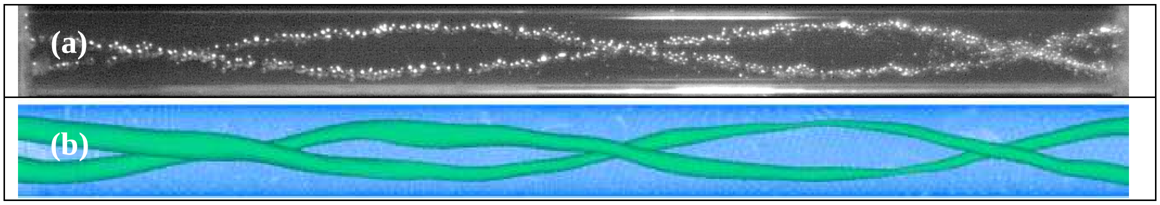

Figure 6.1.5: Helical vortices generated by a twisted tape with twist ratio y_r = 3.54 (90 mm pitch) at Re = 7.7x10^4: (a) high speed camera visualization, (b) numerical results.

The pitch of the helical vortices is approximately 2.36*d* (60±15%mm) for the swirler with y_r = 1.77, 3.15*d* (80±9%mm) for the swirler with y_r = 2.36 and 4.72*d*

(120±6% mm) for the swirler with y_r = 3.54, both in the experiments and in the numerical simulations. The reference values for the isobar surfaces which identify the vortex cores are p = 0.99 for the swirler with y_r = 1.77, p = 1 for the swirler with y_r = 2.36 and p = 1 for the swirler with y_r = 3.54, as the shorter tape generates stronger vortices with larger pressure drop in the core than longer tapes.

Figures 6.1.6 and 6.1.7 allow a comparison between the pitch of the helical vortices induced by twisted tapes with y_r = 1.77 and y_r = 2.36 calculated with both laminar and turbulent simulations. As shown before, the laminar simulation recovers well the characteristics observed in the experiments. The turbulent simulation however shows significant discrepancies with the experiments.

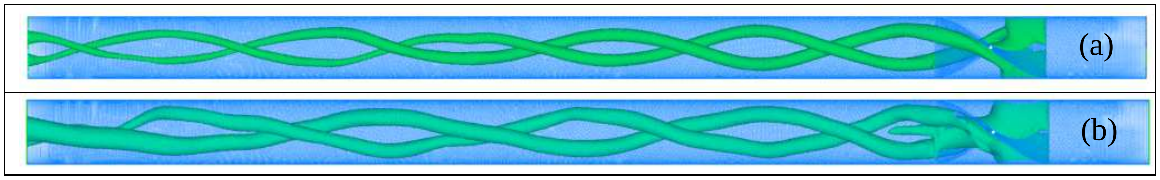

Figure 6.1.6: Helical vortices induced by a swirler with y_r = 1.77 at Re = 7.7×10^4: (a) isobar surfaces of p = 0.99 for the laminar simulation, (b) isobar surfaces of p =1.01 for the turbulent simulation.

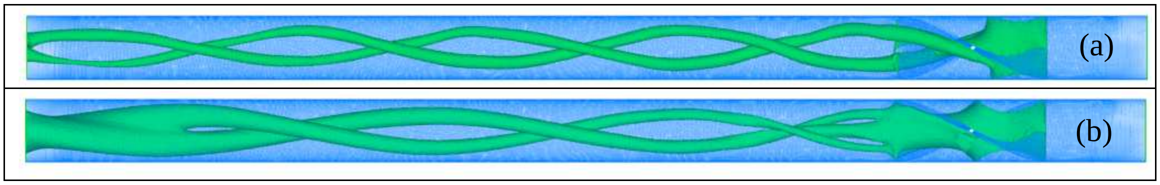

Figure 6.1.7: Helical vortices induced by a swirler with y_r = 2.36 at Re = 7.7×10^4: (a) isobar surfaces of p = 1 for the laminar simulation, (b) isobar surfaces of p = 1.02 for the turbulent simulation.

The pitch determined using the turbulent simulation is approximately 25% longer for both the twisted tape with y_r = 1.77 (75 mm pitch instead of 60 mm measured in experiments) and the twisted tape with y_r = 2.36 (100 mm instead of 80 mm measured in experiments). The vortices are also weaker in the turbulent model as shown by the higher pressure characterizing the vortex core. For the y_r = 1.77 tape the vortex cores calculated with the laminar simulation are identified by the isobar surfaces of p = 0.99 while in the turbulent simulation the core pressure is p = 1.01.

Downstream from the swirler, the pitch of the helical vortices is approximately constant inside the straight pipe for both the laminar and turbulent simulations. This fact, coupled with the experimental observation that the pitch does not vary with Re, suggest that turbulence does not have a major influence inside the test section which extends 14d from the end of the swirler. The discrepancy between the results of the turbulent simulations and the experiments is likely due to a slower vortex development inside the swirler and not to excessive dissipation inside the straight pipe. The flow at the swirler inlet is laminar while the flow inside the straight pipe is turbulent, thus the vortices are generated inside the swirler in a transitional flow.

As the cross-section velocity vectors show (figure 6.1.8), the vortices are closer to the twisted tape at the swirler exit in the results obtained with the turbulent simulation compared to those calculated with laminar simulations. The difference between the positions of the vortices relative to the tape is the cause of the longer pitch in the turbulent simulations. The fact that the results of the laminar simulations are closer to the experimental results than those obtained with the turbulent simulations could be due to a more accurate description of the transitional flow inside the swirler which is involved in the vortex generation.

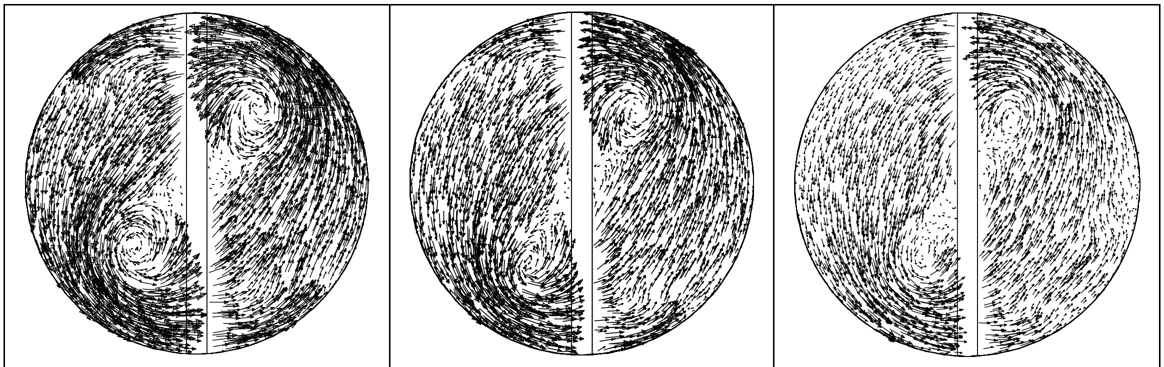

y_r = 1.77, laminar

y_r = 2.36, laminar

y_r = 3.54, laminar

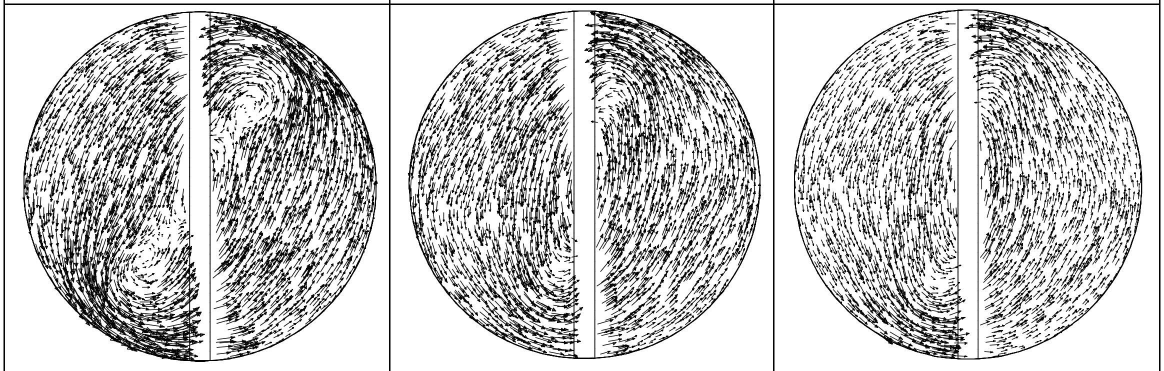

y_r = 1.77, turbulent

y_r = 2.36, turbulent

y_r = 3.54, turbulent

Figure 6.1.8: Cross-section velocity vectors at the end of the swirler (z = 0) for the tapes with y_r = 1.77, 2.36 and 3.54 at Re = $7.7\text{x}10^4$: (top row) laminar simulation, (bottom row) turbulent simulation.

In addition to the experimental photos, the numerical models are also validated against LDV measurements. Figure 6.1.9 shows a comparison between the experimental measurements of the average tangential velocity and tangential velocity profiles calculated with the steady state laminar simulation across the horizontal diameter at two axial locations. Figure 6.1.9a shows the velocity profiles when the helical vortices are in vertical position (z/d = 5.9 in experiments, z/d = 6.57 in the laminar numerical simulation as shown in figure 6.1.4) and the velocities are measured between the helical vortices for the flow induced by a twisted tape with y_r = 2.36 at Re = $7.7\text{x}10^4$. Figure 6.1.9b shows the velocity profiles when the helical vortices are in horizontal position (z/d = 7.48 in experiments, z/d = 8.03 in the numerical simulation as shown in figure 6.1.4) and the velocities are measured through the helical vortices.

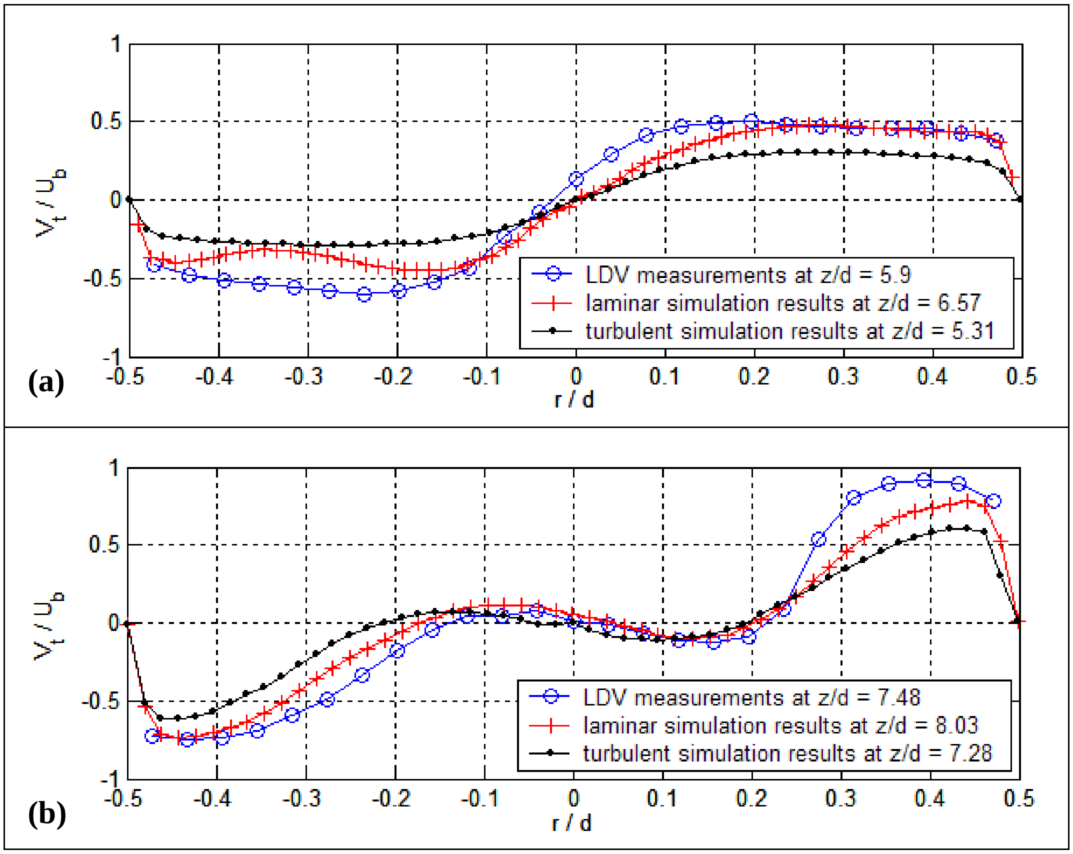

Figure 6.1.9: Comparison between experimental average tangential velocity profiles and calculated tangential velocity profiles from the steady state numerical simulation for the tape with y_r = 2.36 at Re = 7.7×10^4 (U_b = 3 m/s): (a) between the helical vortices, (b) through the helical vortices.

Also shown for comparison are the average tangential velocity profiles calculated with the turbulent simulation at axial locations close to the experimental locations. The profiles between the helical vortices (z/d = 5.31) and through the helical vortices (z/d = 7.28) are measured across the vertical diameters (rotated 90°) as the pitch in the turbulent results does not match the experimental pitch (as shown in figure 6.1.7).

In figure 6.1.9 the tangential velocity profiles calculated using the laminar numerical simulations match qualitatively the trends observed in the experiments. However, as figure 6.1.4 also shows, the helical vortices in the simulation are shifted by a small 0.6d axial displacement relative to the experiments. In figure 6.1.9a the maximum values calculated with the laminar numerical simulation are within 2% of the experimental values on the right side and within 18% on the left side, as the two sides have different amplitudes. In figure 6.1.9b the maximum values calculated with the laminar numerical simulation are within 15% of the experimental values on the right side and within 1% on the left side. The simulation does not capture however the angle between the two helical vortices observed experimentally. The angle did not appear in unsteady simulations either (the results are identical with the steady state results).

While the average tangential velocity profiles calculated with the turbulent model also capture the trends from the experimental measurements, the tangential velocity maxima in figure 6.1.9a are 55% lower than the experimental results on the left side and 40% lower on the right side. In figure 6.1.9b the tangential velocity maxima are 15% lower than the experimental results on the left side and 30% lower on the right side. This effect, just like the longer pitch, is the result of the underestimation of the vortex strength inside the swirler, which could be caused by an overestimation of the turbulence level. The characteristics of the early development of the vortices inside the swirler completely define the behavior of the helical vortices inside the straight pipe.

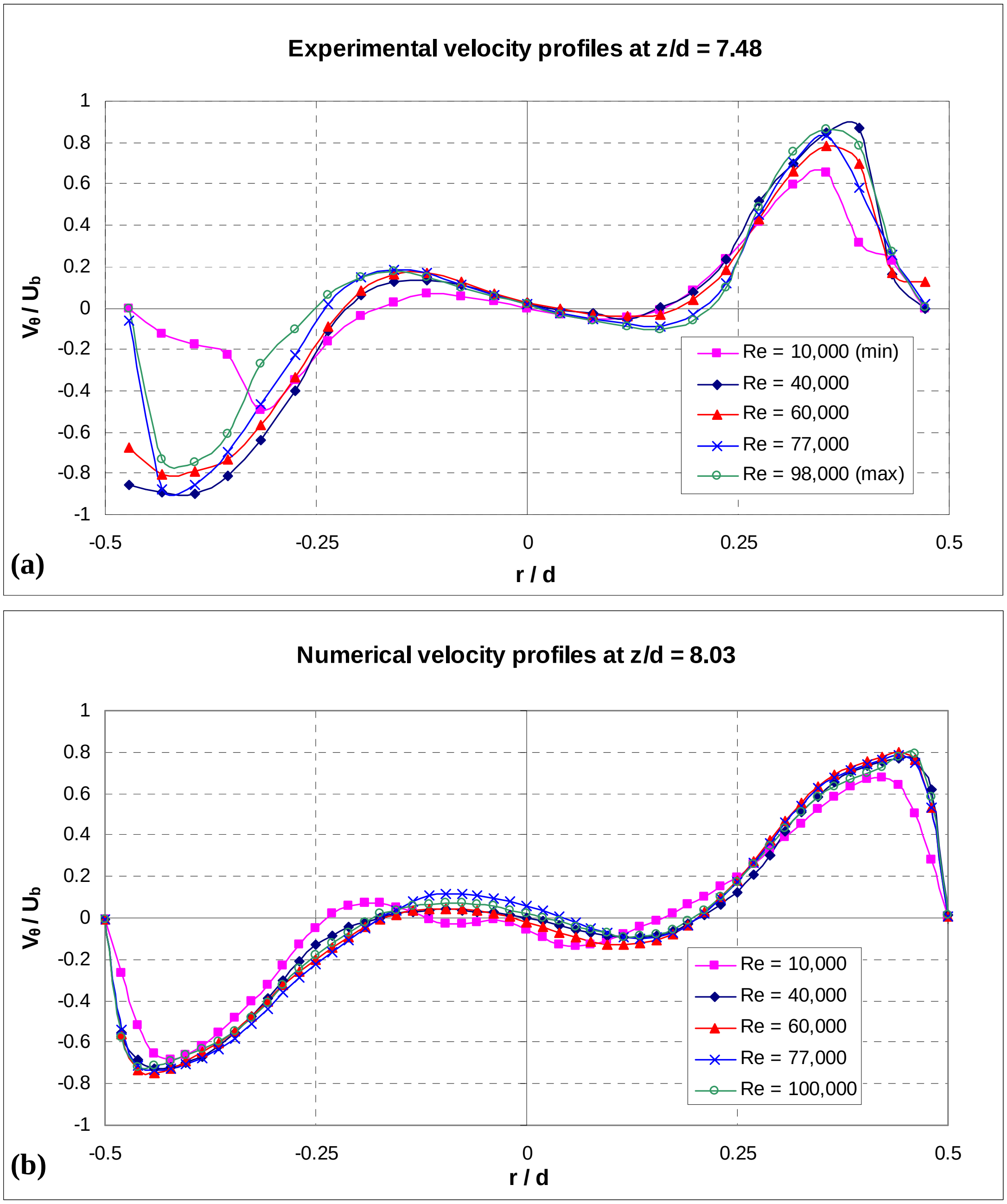

Figure 6.1.10 Variation of the normalized tangential velocity with Re: (a) Experimental profiles at z/d = 7.48, (b) Results of laminar numerical simulations at z/d = 8.03 (the profiles collected through the secondary co-rotating helical vortices display counter-rotating flow).

Figure 6.1.10 shows a comparison between the variation of the normalized tangential velocity with Re for the entire range available in the experiments (Re from 10^4 to 10^5) measured experimentally and the variation calculated with laminar numerical simulations. As mentioned before, the only fluid used in these simulations is water, so different Re represent different inlet velocities. The tangential velocities are normalized with the bulk velocity corresponding to Re. The numerical results at z/d = 8.03 (figure 6.1.10b) match qualitatively the experimental profiles measured at z/d = 7.48 (figure 6.1.10a). The calculated maxima of the tangential velocity profiles are within 20% compared to the maxima measured experimentally for Re between $4\text{x}10^4$ and 10^5. The simulation captures the change in the velocity profile at Re = 10^4 but not its magnitude. The plots also confirm that the pitch of the helical vortices does not change with Re, as the counter-rotating flow is present at the same axial location both in the results of the laminar numerical simulations and in the experimental measurements at all Re.

Using the axial vorticity component and the area integral also allowed the evaluation of the circulation in cross-section planes (using formula 2.1.2), in order to verify the accuracy of the simulations. The area integral of a variable Φ in a cross-section plane is calculated as $\int \Phi \cdot dA = \sum_{i}^{N_c} \Phi_i \cdot A_i$ where A_i is the area of the intersection between the cross-section plane and the tetrahedral cell i, Φ_i is the value of the variable inside the cell i and N_c is the number of cells intersected by the cross-section plane.

For the reference case of a flow through a swirler with y_r = 2.36 at Re = $7.7\text{x}10^4$ the values of the circulation normalized by $U_b \cdot R$ were $-7\text{x}10^{-6}$ at z/d=0, $5.5\text{x}10^{-6}$ at z/d =1, $-7.6\text{x}10^{-7}$ at z/d=5 and $1.2\text{x}10^{-7}$ at z/d=10. These values represent a reasonable approximation for 0 as expected, confirming the accuracy of the simulations.

A test case was run with an inviscid formulation and slip boundary conditions at the walls, in order to investigate if the formation of the helical vortices is an inviscid phenomenon. The results show that without viscosity and wall shear stress there are no helical vortices and the flow becomes a regular swirling flow (figure 6.1.11).

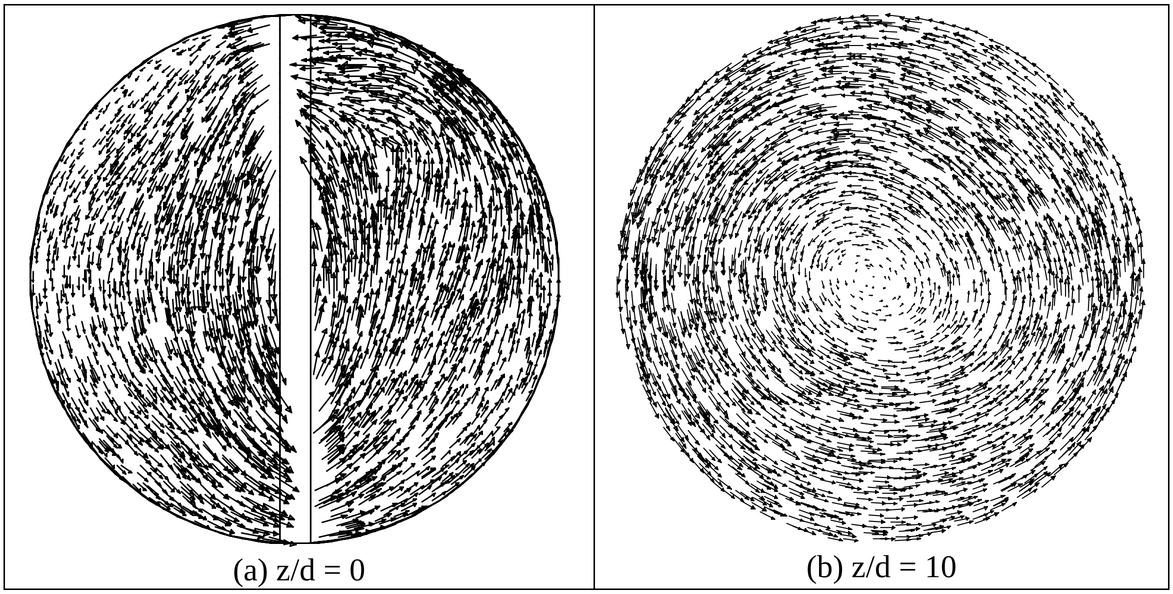
(a) z/d = 0 (b) z/d = 10

Figure 6.1.11 Velocity vectors calculated with an inviscid numerical simulation for the tape with $y_r = 2.36$ at $Re = 7.7x10^4$ at two axial locations: (a) z/d = 0, (b) z/d = 10.

All previous results showed that turbulence is not a major influence for the characteristics of the helical vortices and also that the laminar simulations reproduce the helical vortices more accurate than the turbulent simulations, relative to the experimental data. As a result, laminar numerical simulations are used for the rest of the numerical investigation.

6.2 Vortex identification

In the previous chapters, the helical vortices have been identified in the results from numerical simulations by isobar surfaces of low pressure [Robinson 91], which correspond to the air bubbles accumulations in the experimental flow visualizations. That method is confirmed in this chapter using closed streamlines [Lugt 1979, Robinson 91], vorticity [Hussain and Hayakawa 1987] and the more advanced λ_2 method [Jeong and Hussain 1995] described in Chapter 2.2.

Figure 6.2.1 shows the velocity vectors and the streamlines in the cross-section plane at z/d = 6.57 for the flow induced by a twisted tape with $y_r = 2.36$ at Re = 7.7×10^4. The closed streamlines indicate the presence of the helical vortices and also the main rotation around the pipe centerline.

The primary vortex (or main swirl) is not identified by the low pressure methods because the pressure is the lowest in the cores of the secondary vortices, hiding the primary vortex effect on the pressure field. As the streamlines show, the flow obviously rotates around the pipe centerline in the direction of the tape twist (which was the expected effect from the twisted tape) but the two helical vortices induce motion in opposite direction near the centerline. The entire field can be considered a vortex with large parts of the cross-section flow actually belonging to two vortices.

Figure 6.2.2 shows the vorticity magnitude normalized by U_b/R at z/d = 6.57. Similarly to pressure contours, the vorticity contours identify the secondary vortices but not the primary vortex which is identified only by the streamlines. The plot is dominated by the wall vorticity with a magnitude approximately three times larger than the vorticity magnitude of the secondary vortices.

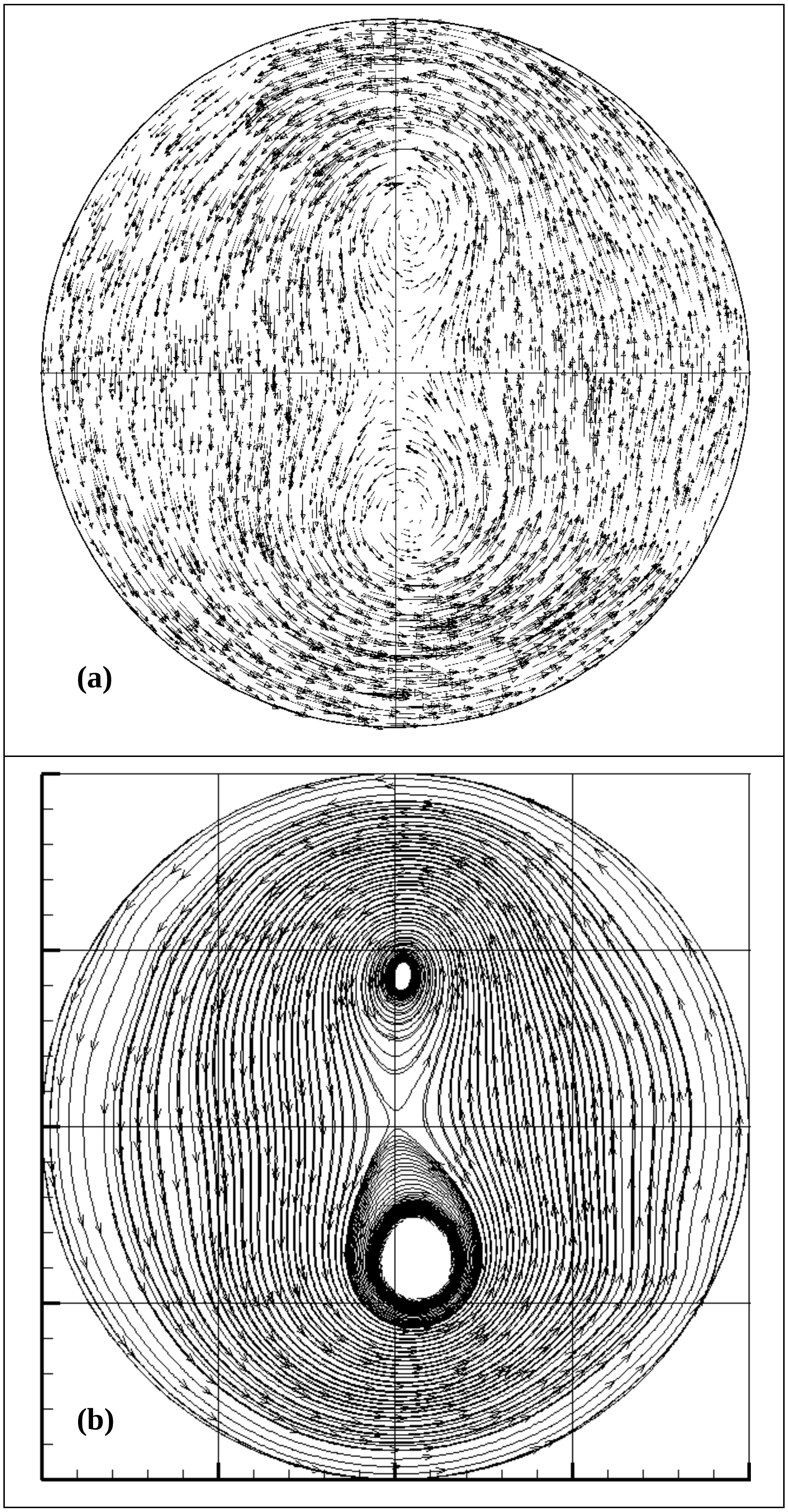

Figure 6.2.1: Visualizations of the velocity field in the cross-section plane at z/d = 6.57 in the flow induced by a twisted tape with $y_r = 2.36$ at Re = $7.7\text{x}10^4$ (a) velocity vectors, (b) stream lines.

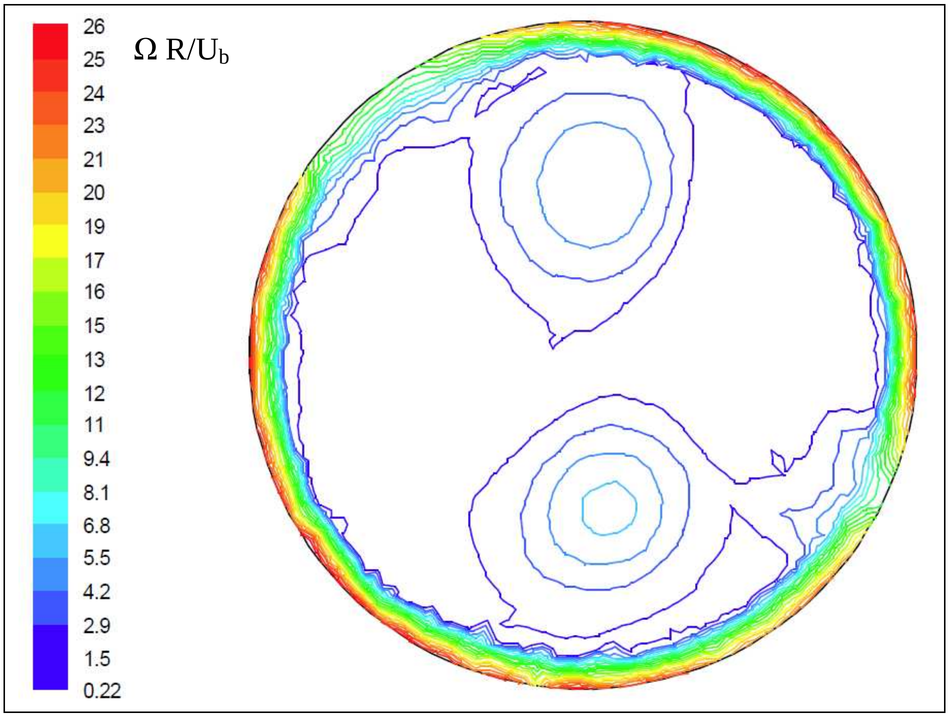

Figure 6.2.2 Normalized vorticity magnitude contours at z/d = 6.57 in the flow induced by a twisted tape with $y_r = 2.36$ at $Re = 7.7x10^4$

In figure 6.2.3 the cores of the secondary vortices are identified by the λ_2 method in addition to the isobar surfaces of low pressure. The λ_2 method is also based on identifying low pressure cores but, as explained in Chapter 2.2, it also removes the viscous effects. Figure 6.2.3 shows the entire computational domain and a swirler close-up where the centers of the connected regions with $\lambda_2 < 0$ are marked by line segments. The plots show the reference case: a laminar simulation of the flow induced by a twisted tape with $y_r = 2.36$ at $Re = 7.7x10^4$. The isobar surfaces are made transparent which allows the λ_2 lines to be visible at the centers of the low pressure isobar surfaces.

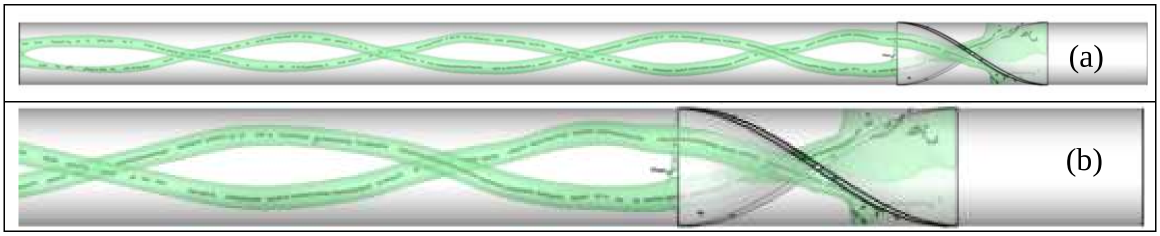

Figure 6.2.3: Comparison between vortex identification with isobar surfaces and λ_2 lines: (a) full domain, (b) close-up view of the swirler.

The plots confirm that the isobar surfaces are reliable in identifying the vortex cores at high Re where the pressure gradients generated by the swirling motion are larger than viscous effects. All the identification methods used confirm that the large, stable structures which intuitively were considered vortices based on the velocity vectors in the cross-section are actually vortices according to generally accepted vortex identification criteria. Thus the presence of the helical vortices in the swirling flow induced by short twisted tapes is confirmed. The isobar surface remains the most convenient method for vortex identification in this investigation as it allows direct comparison between the numerical results and the experimental visualizations. The λ_2 method is useful to identify vortices at low Re where the pressure gradients inside the swirler are lower and viscous effects hide the secondary motion.

6.3 Flow field analysis

As the helical vortices behind twisted tapes have never been observed before, the numerical simulation results will be used next to provide an in depth analysis of their behavior and their interaction with the main swirl. The advantage offered by the numerical simulation compared to the experimental investigation is that it provides all the flow variables at the same moment of time.

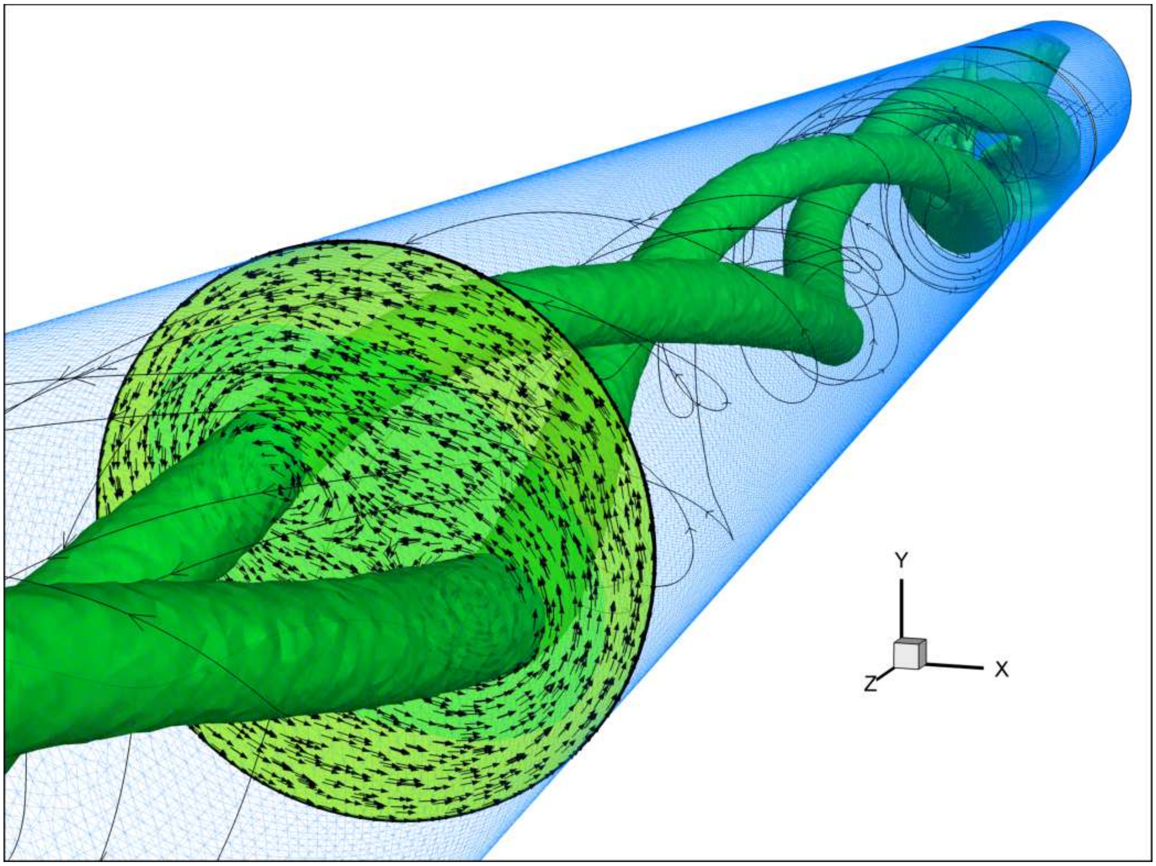

Figure 6.3.1: Isobar surfaces, pathlines and velocity vectors identify helical vortices in the flow field induced by a twisted tape with $y_r = 2.36$ at Re = 7.7×10^4 calculated with a steady state laminar simulation (perspective view).

Figure 6.3.1 shows a perspective view of the flow field induced by a twisted tape with $y_r = 2.36$ inside a straight pipe at Re = 7.7×10^4 calculated with a steady state laminar simulation. The cross-section plane shows the velocity vectors while pathlines originating at the pipe inlet on the horizontal diameter reveal the complex 3D motion created by the interaction of the two helical vortices and the main swirl. The isobar surfaces of p = 1 mark the cores of the helical vortices.

In the experimental part, the presence of the helical vortices inside the swirling flow was indicated by counter-rotating flow encountered in the measurements of the tangential velocity. The flow field was recreated from the experimental velocity plots between and through the helical vortices assuming that the velocity profiles from figure 4.1.1 are similar to the velocity profiles in a cross-section plane at different angles. Figure 6.3.2 shows that the assumption was correct and the velocity field recovered from the LDV measurements (figure 4.3.1) is qualitatively similar to the one calculated with the laminar simulation (figure 6.3.2a).

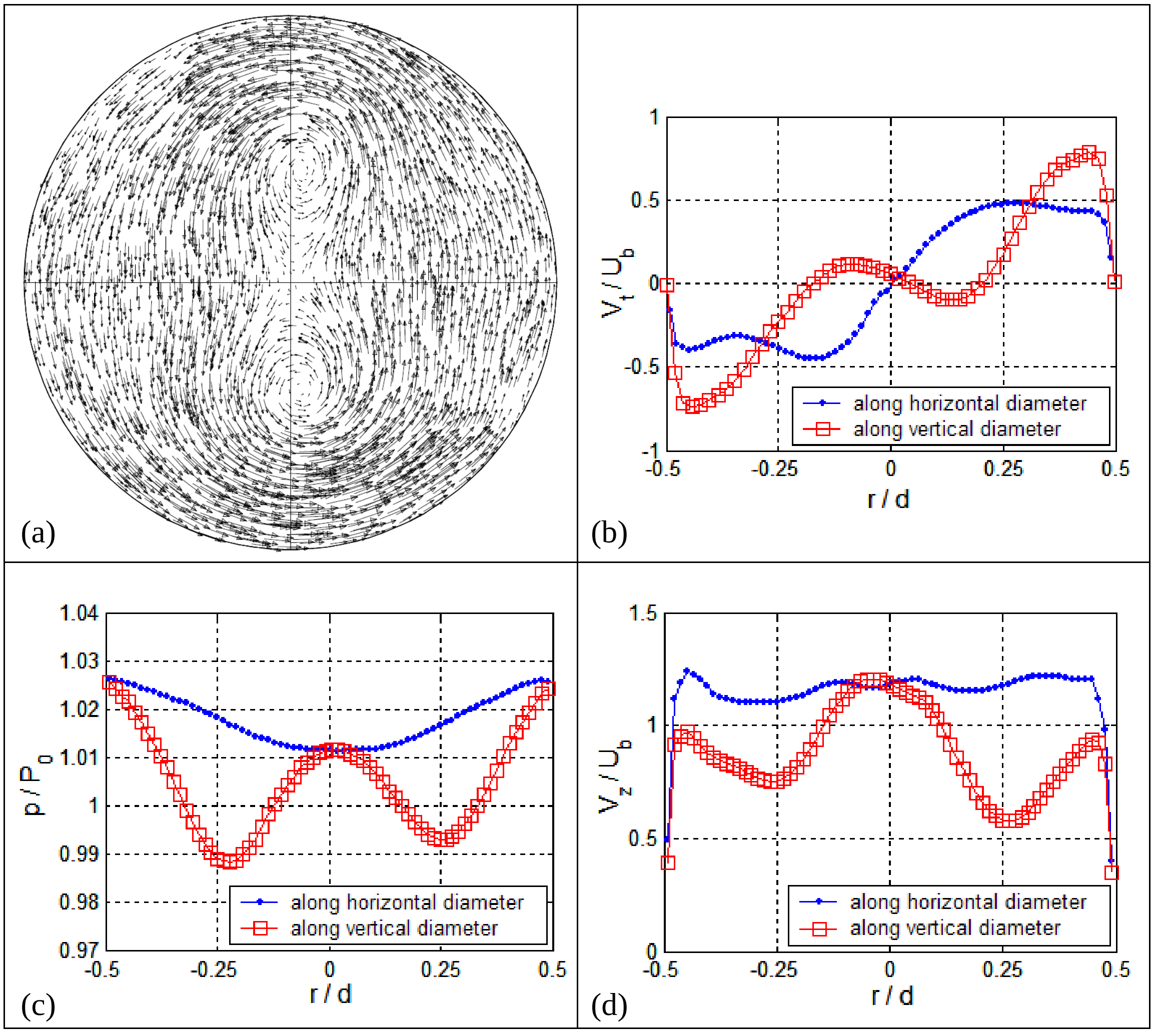

Figure 6.3.2: Variation of the flow parameters between and through the helical vortices (along the horizontal and vertical diameter, respectively) for the flow induced by a twisted tape with y_r = 2.36 at Re = 7.7x10^4 (U_b = 3m/s) in the cross-section plane at z/d = 6.57 downstream of the swirler: (a) velocity vectors, (b) tangential velocity, (c) pressure, (d) axial velocity.

Figures 6.3.2b and 6.3.2d show the tangential and axial velocity distributions which are very similar to the profiles shown in figures 4.1.5 and 4.1.4 respectively. Figure 6.3.2c shows the pressure distribution where the effect of the secondary vortices is clearly visible as a large pressure drop inside the cores of the helical vortices (responsible for the air bubble accumulations in the experimental visualizations). The pressure distribution plot shows that the two vortices have slightly different strengths, possibly as an effect of the twisted tape wake at the exit of the swirler. The main difference between experiments and the results of the numerical model is the absence of the angle observed experimentally between the secondary vortices, which is an unsteady behavior (as explained in Chapter 4.2).

While figure 6.3.2 showed one dimensional plots which confirmed the experimental measurements, figure 6.3.3 shows the full 2D distribution of the flow parameters in the cross-section using colored vectors. As the flow field is not axis-symmetric, only the 2D map of the velocity components and the pressure distribution throughout the domain reveals the actual correlations between these parameters.

The normalized pressure distribution in figure 6.3.3a shows that the helical vortices create much larger pressure gradients than the pressure gradients in the plane perpendicular to the vortices. The presence of the helical vortices reduces the axial velocity which has maxima between the vortices and minima inside the helical vortices (figure 6.3.3c). The plots also show that the radial velocity component at the edges of the helical vortices is of the same order of magnitude as the axial and tangential velocity component, with magnitudes as large as half of the bulk velocity (figure 6.3.3d).

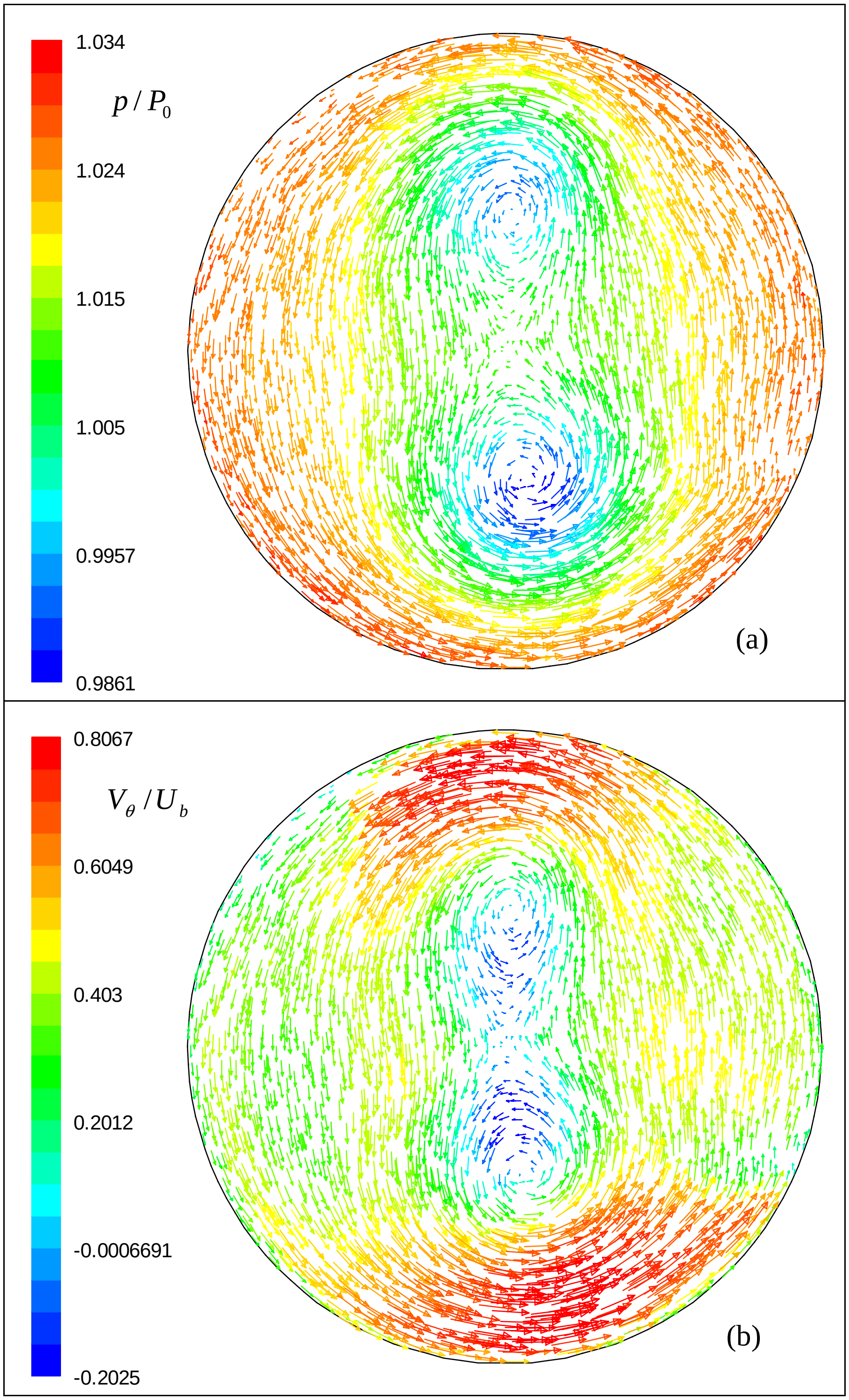

Figure 6.3.3 2D distribution of the flow parameters for the flow induced by a twisted tape with y_r = 2.36 at Re = $7.7\text{x}10^4$ (U_b = 3 m/s) in the cross-section plane at z/d = 6.57 downstream of the swirler: (a) normalized pressure p/P_0, (b) normalized tangential velocity V_θ/U_b,

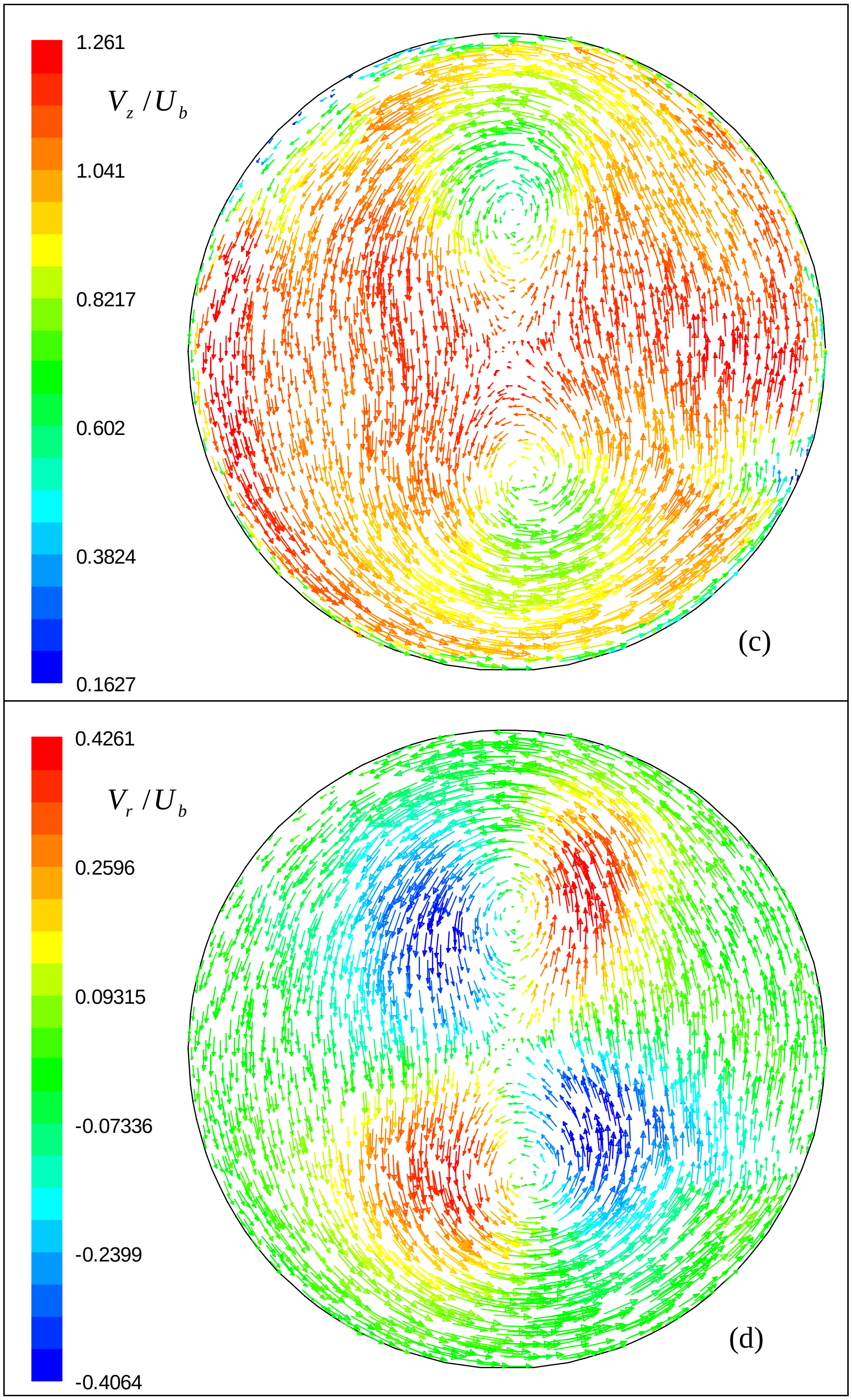

Figure 6.3.3 continued: (c) normalized axial velocity V_z/U_b, (d) normalized radial velocity V_r/U_b.

Figure 6.3.3b shows that the tangential velocity component has maxima where the edges of the secondary vortices reach near the wall and the contributions from the secondary motion and the main swirl overlap and have the same direction. The magnitude of the resulting tangential velocity is double the magnitude of the tangential velocity corresponding to the main swirl which is visible in the plane perpendicular to the secondary vortices. The tangential velocity component induced by the main swirl is small near the pipe centerline, which is also the center of rotation for the main swirl. At the same time the tangential components induced by the helical vortices have their maxima near the pipe centerline because the centers of the two secondary vortices are located in the middle of the pipe radius and their edges reach the wall and the pipe centerline. Near the pipe centerline the larger tangential velocity components induced by the helical vortices rotate in the opposite direction compared to the main swirl and overcome its effect which results in two patches of counter-rotating flow visible in figure 6.3.3b between the two vortices.

Figure 6.3.4 shows the helical vortices for the three main cases investigated (tapes with twist ratio y_r = 1.77, 2.36 and 3.54 at Re = 7.7×10^4), including their development inside the swirler. The pitch calculated with the laminar simulation matches well the pitch of the normalized angular velocity extracted from the LDV measurements (figure 4.1.2). The similar ratio between the helical vortex pitch and the twisted tape pitch in all three cases (approximately 4/3) is likely due to the similar position of the helical vortices at the end of the 180^o twist. The plots show that the ratio between the pitch of the helical vortices and the pitch of the swirler is almost the same for all three swirlers tested for Re in the range 10^4-10^5. As the swirl number plots show, in this range the swirl number is almost constant.

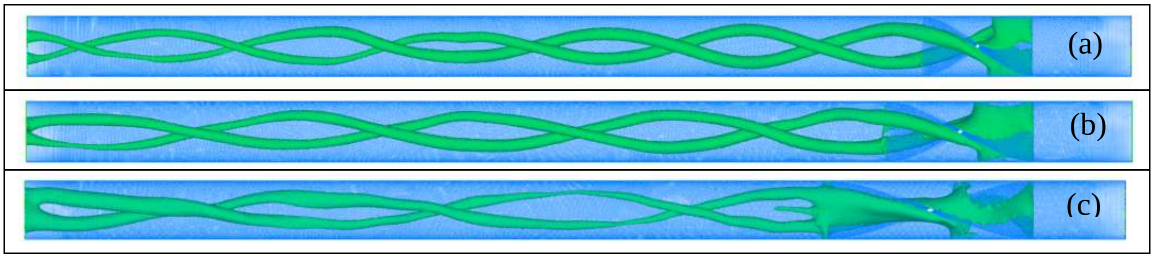

Figure 6.3.4: Helical vortices for the three cases investigated experimentally at Re = $7.7\text{x}10^4$: (a) y_r = 1.77 tape, (b) y_r = 2.36 tape, (c) y_r = 3.54 tape.

Figure 6.3.5 shows the positions of the secondary vortices at the exit of swirler with velocity vectors and streamlines for all three cases investigated. The patterns are very similar even though the shorter tapes induce stronger swirl. The closed streamlines clearly identify in all three cases the presence of a single vortex co-rotating with the main flow on each side of the tape.

Figure 6.3.6 shows the cross-section isobar contours at axial locations where the helical vortices are in vertical and horizontal positions (top and bottom row respectively) for the y_r = 2.36 tape at Re = $7.7\text{x}10^4$. The pitch of the helical vortices is the distance between two consecutive plots with the same vortex orientation. The pitch is slightly uneven as the secondary vortices are not perfect helices and the angle between the vortices is approximately 176^o instead of 180^o. However, the plots show that the characteristics of the flow field change very little along the pipe axis, its periodicity justifying the velocity field reconstruction from the LDV measurements along the axis presented in Chapter 4.3.

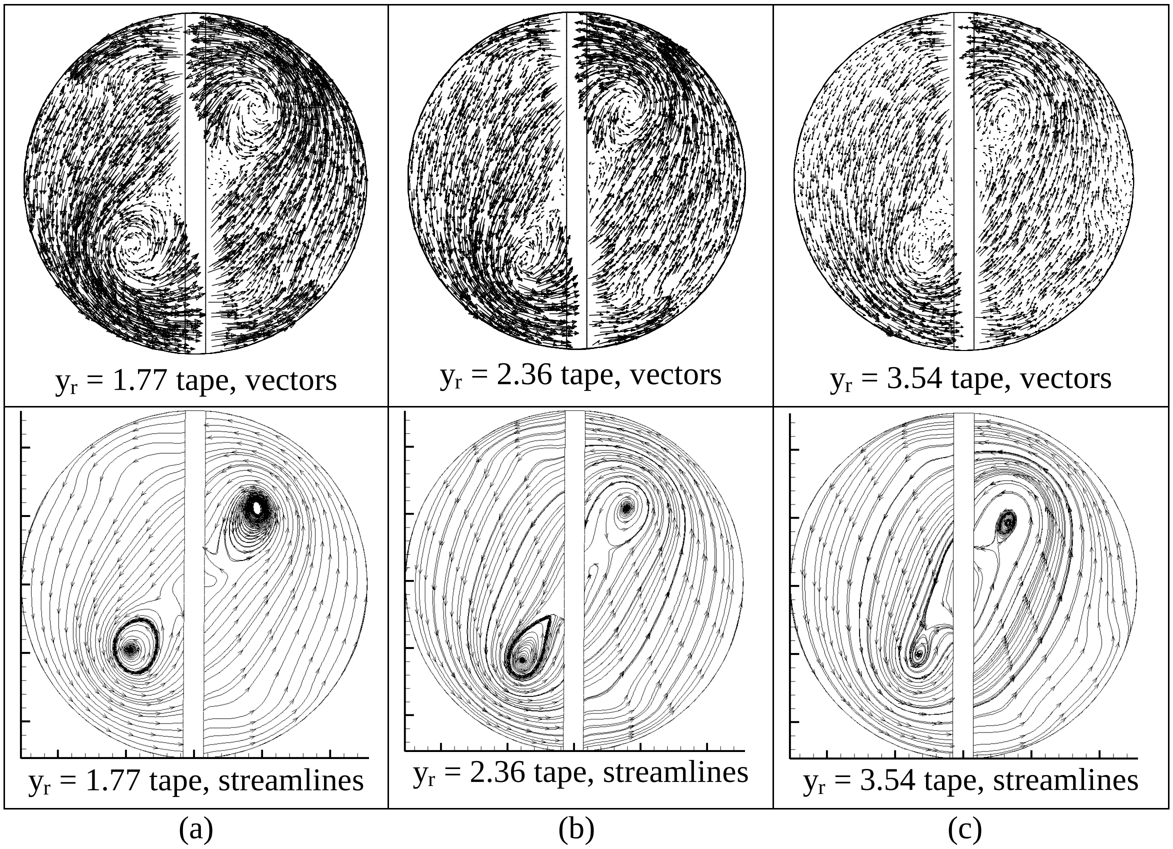
y_r = 1.77 tape, vectors

y_r = 2.36 tape, vectors

y_r = 3.54 tape, vectors

y_r = 1.77 tape, streamlines

y_r = 2.36 tape, streamlines

y_r = 3.54 tape, streamlines

(a) (b) (c)

Figure 6.3.5: The flow field at the swirler exit described by velocity vectors (top row) and streamlines (bottom row) at Re = 7.7×10^4: a) y_r = 1.77 tape, b) y_r = 2.36 tape, c) y_r = 3.54 tape.

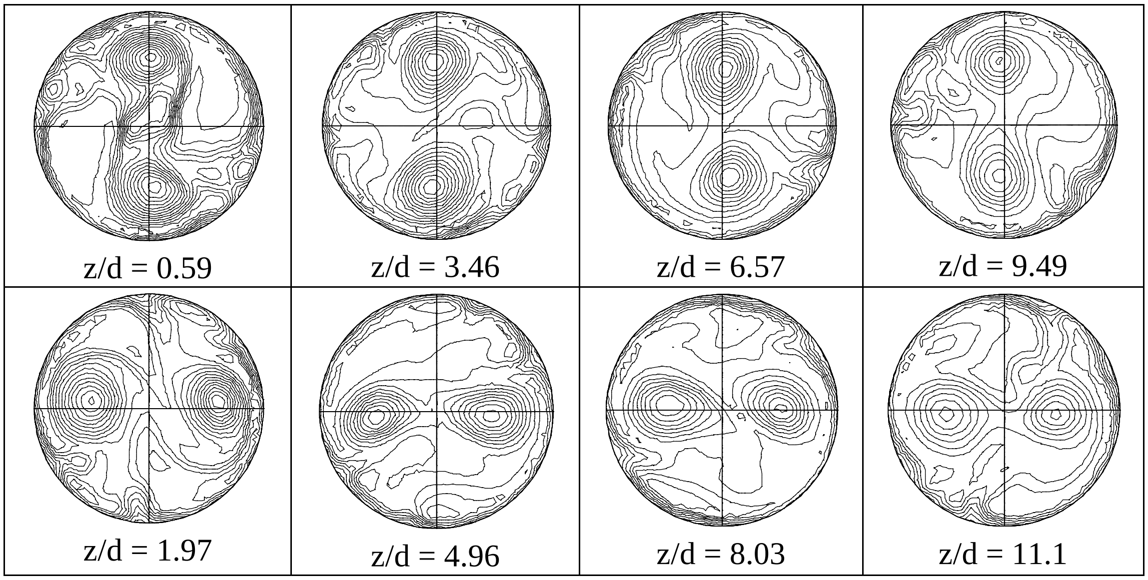
z/d = 0.59

z/d = 3.46

z/d = 6.57

z/d = 9.49

z/d = 1.97

z/d = 4.96

z/d = 8.03

z/d = 11.1

Figure 6.3.6: Pressure contours at axial positions where the helical vortices are in vertical and horizontal positions. The flow is induced by a tape with y_r = 2.36 at Re = 7.7×10^4).

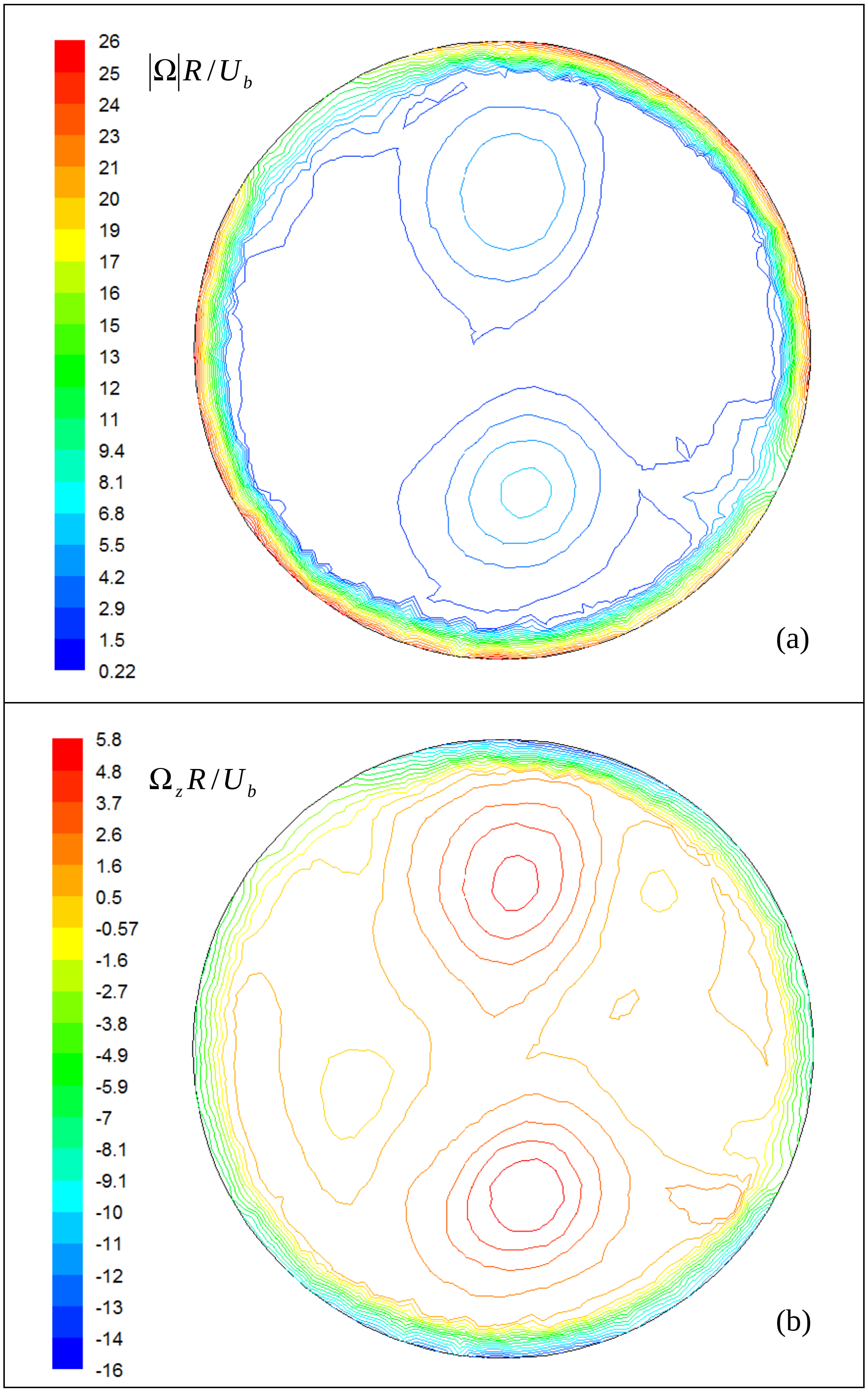

Figure 6.3.7 Vorticity distribution for the flow induced by a twisted tape with twist ratio $y_r = 2.36$ at Re = 7.7x10^4 (U_b = 3 m/s) in the cross section plane at z/d = 7.28: (a) normalized vorticity magnitude, (b) normalized axial vorticity component

The numerical simulation results contain the complete velocity field which allows the calculation of vorticity. Figure 6.3.7a shows the vorticity magnitude and figure 6.3.7b shows the axial vorticity component, both normalized with U_b / R, at z/d = 7.28 for the reference case of a flow through a swirler with $y_r = 2.36$ at Re = 7.7x10^4. As explained in the previous section, vorticity plots are dominated by vorticity produced near the wall, in the boundary layer. In the vorticity magnitude plot the wall vorticity is approximately 4.5 times larger than the vorticity corresponding to the secondary vortices. In figure 6.3.7b the axial vorticity near the wall is approximately 2.5 times larger than the axial vorticity in the secondary vortices and it is oriented in the opposite direction. The λ_2 method and the low-pressure isobar surfaces were preferred for vortex identification in order to avoid the effects of viscosity near the wall.

The swirl downstream of the twisted tape swirler is decaying as shown by Kreith and Sonju [1965] (figure 2.3.1). The swirl decay is quantified by the variation of the swirl number along the pipe axis. The complete flow field calculated with the laminar model allows an accurate estimation of the swirl number in cross-section planes along the pipe axis using formula 2.1.6.

Figure 6.3.8 shows the swirl numbers calculated at axial locations 1, 5 and 10 diameters downstream of the swirler for 180^o twisted tape swirlers with twist ratio 1.77, 2.36 and 3.54 at Re = 7.7x10^4 (bulk velocity 3 m/s). The decay along the first 10 diameters downstream of the swirler, which is the focus of this study, is approximately the same in absolute value for all three cases at 0.03. The decay represents 7.3 % for the swirler with $y_r = 1.77$, 10.3 % for the swirler with $y_r = 2.36$ and 10.8 % for the swirler with $y_r = 3.54$. These results are similar to those of Kreith and Sonju [1965] (figure 2.3.1) and confirm that the decay over 3.15d (80 mm) along the pipe axis from 5.9d to 9.05d for the swirler with twist ratio y_r = 2.36 at Re = 7.7x10^4 is very limited (~3%) which justifies the reconstruction of the flow field from the LDV measurements performed in Chapter 4.3.

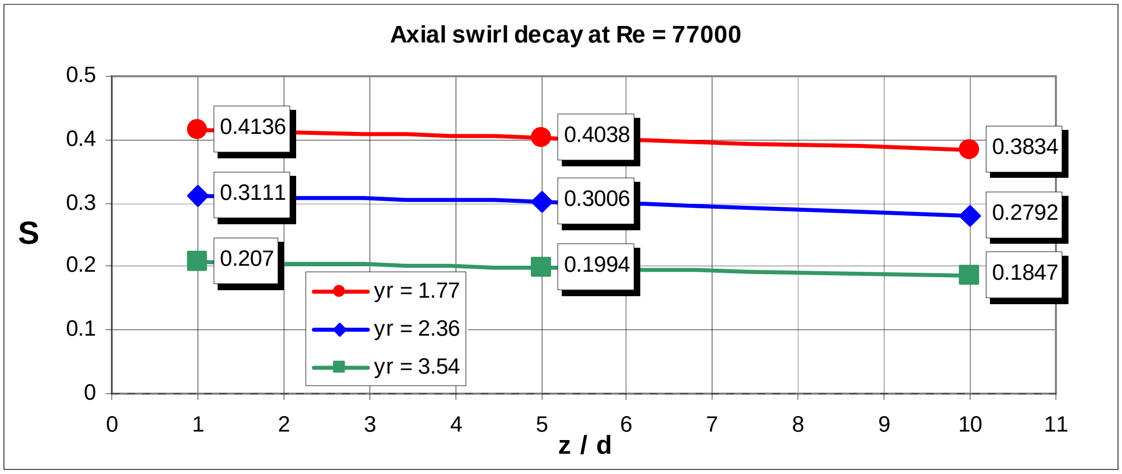

Figure 6.3.8 Swirl decay along the pipe axis as quantified by the variation of the swirl number S for the three swirlers with twist ratios 1.77, 2.36 and 3.54 at Re = 7.7x10^4

Figure 6.3.9 shows on a logarithmic scale how the swirl induced by the tape with twist ratio y_r = 2.36 varies with Re in the range 10^2 to 10^5. As mentioned before, the only fluid used in these simulations is water, so different Re represent different inlet velocities. The swirl is quantified by the swirl number calculated one diameter downstream from the swirler exit. The plot shows that the swirl number increases rapidly with Re from Re = 10^2 to Re = 10^3 and then it reaches asymptotically a level of S = 0.31, almost constant from Re = 10^4 to Re = 10^5 which is the experimental flow range in this study.

The swirl decay also varies with the inlet velocity, expressed in non-dimensional form by Re (for water only). Figure 6.3.10 shows the swirl decay dependency on Re for the tape with twist ratio y_r = 2.36 and Re in the range 10^2 to 10^5. The plot confirms that the swirl decay along the pipe axis decreases with an increase in Re as observed by Kreith and Sonju [1965].

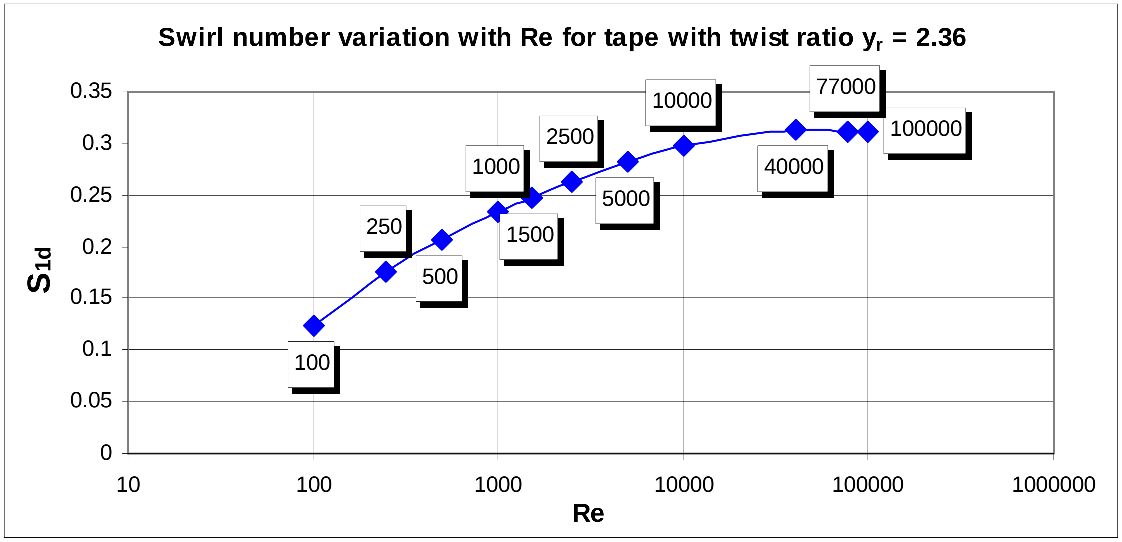

Figure 6.3.9 Swirl number variation with Re. The swirl number S is calculated at z/d = 1 downstream of the swirler with twist ratio y_r = 2.36 (60 mm pitch in the experiments).

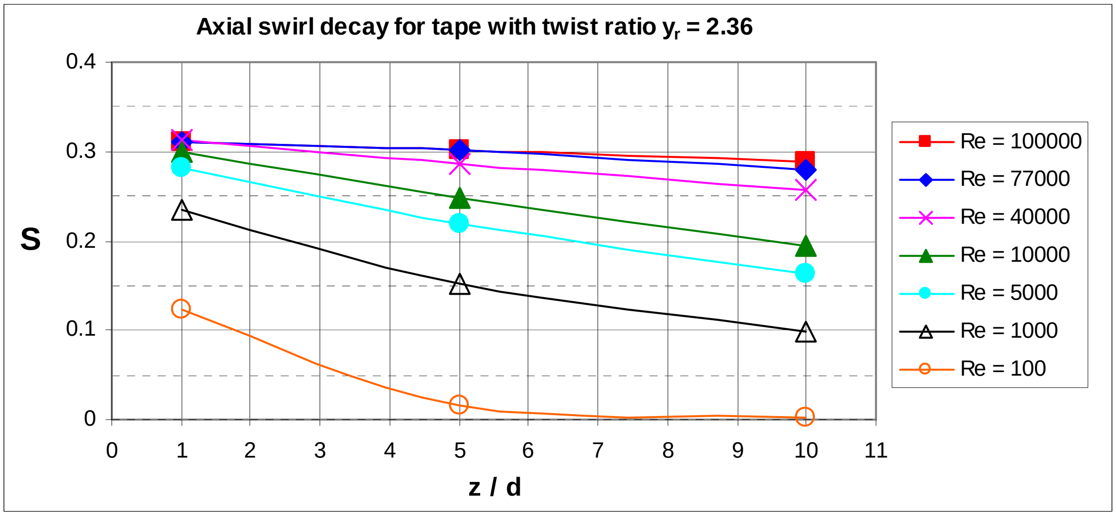

Figure 6.3.10 Swirl decay along the pipe axis as quantified by the variation of the swirl number S for the flow induced by the swirler with twist ratio y_r = 2.36 (60 mm pitch) at Re in the range 10^2 to 10^5.

6.4 Comparison with counter-rotating flow in previous studies

As described in chapter 1.1, the counter-rotating flow has been observed before only in swirling jets generated by rotating pipes, and it was attributed to turbulence. In those reports, the tangential velocity was related to the cross-section Reynolds stress by formula 1.1 which was derived for a fully developed swirling flow inside the rotating pipe, assuming axis-symmetric flow and no axial gradients. However, the formula was used to explain the flow behavior inside the swirling jet, 6.5d downstream from the pipe exit.

An LES simulation of the same flow [Meciel et al. 2008] shows that the swirling jet is expanding (figure 6.4.1a and 6.4.1c) and also that helical vortices are present immediately downstream from the pipe exit (figure 6.4.1b), challenging the axi-symmetric flow and no axial gradients assumptions. The assumption of axi-symmetric flow dismisses a priori the possibility of a non-axi-symmetric rotating flow with a counter-rotating core, similar to the counter-rotating flow region identified in the present study.

The two flow cases share common features as both are swirling flows and contain counter-rotating flow and helical vortices, but also have differences as the jet is unbounded and spreading. Also, the swirl is generated differently which means the helical vortices are generated differently too.

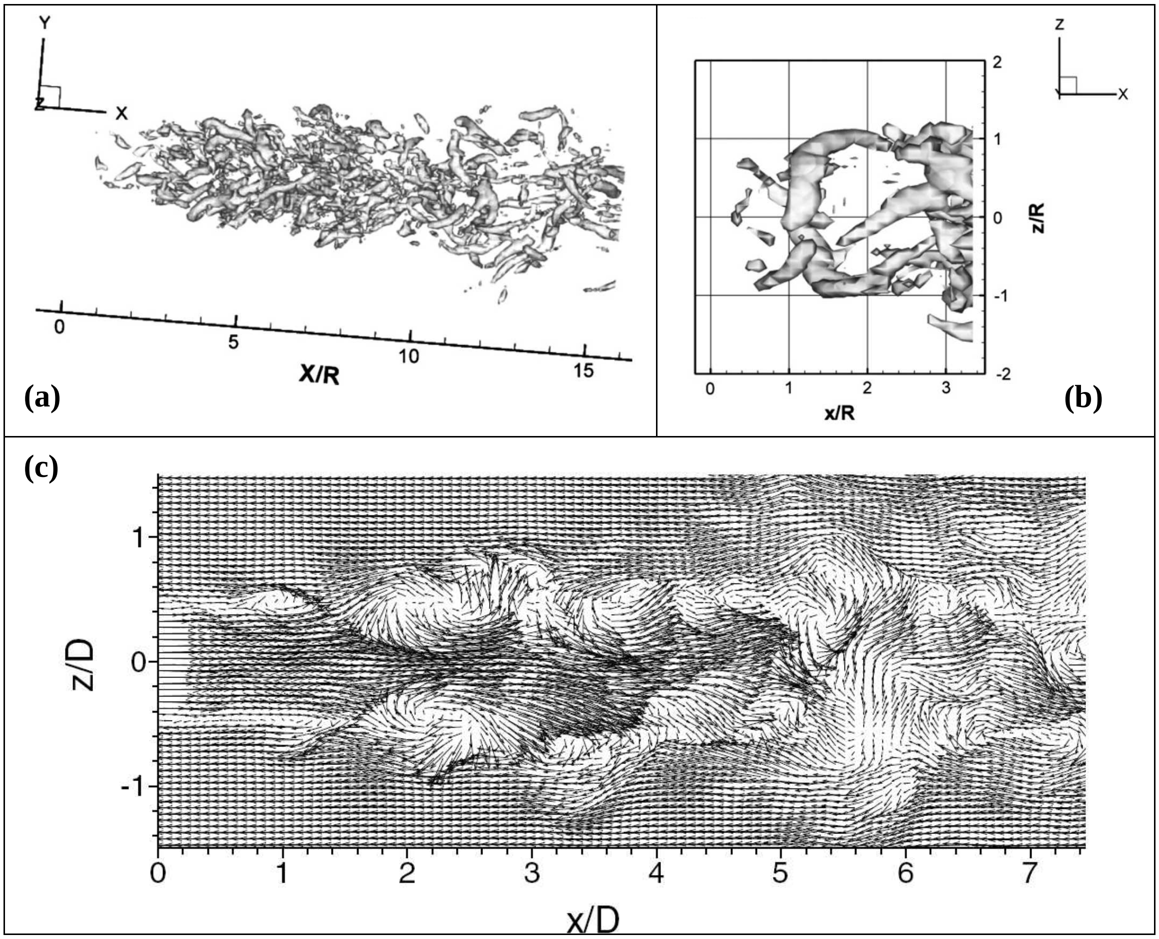

Figure 6.4.1 Flow structures in the swirling jet induced by a rotating pipe [Meciel et al. 2008] (in these plots x is the jet axis): (a) snapshots of instantaneous vortical structures identified with λ_2 iso-surfaces, (b) side-view close-up at the pipe exit, (c) instantaneous velocity field.

Figures 6.4.2 and 6.4.3 show a flow in which the fluid discharges from the swirler with d = 1 (25.4 mm) and y_r = 2.36 into a pipe with a larger cross-section (d2 = 1.4d) and length 7.87d (200 mm). Figure 6.4.2 shows the helical vortices identified by isobar surfaces of $p/P_0 = 1.03$ and vortex cores identified with λ_2 method while figure 6.4.3 shows the cross-section velocity distribution at several axial locations using velocity vectors. While the step is disrupting, the helical vortices are clearly visible in both figures. Figure 6.4.2 and the first plot in figure 6.4.3 at z/d = 0 show that the secondary vortices inside the swirler did not change as a result of the increase in diameter downstream. The flow adjusts to the new cross-section and the helical vortices are present at z/d =4 but they disappear by the end of the 7.87d test section.

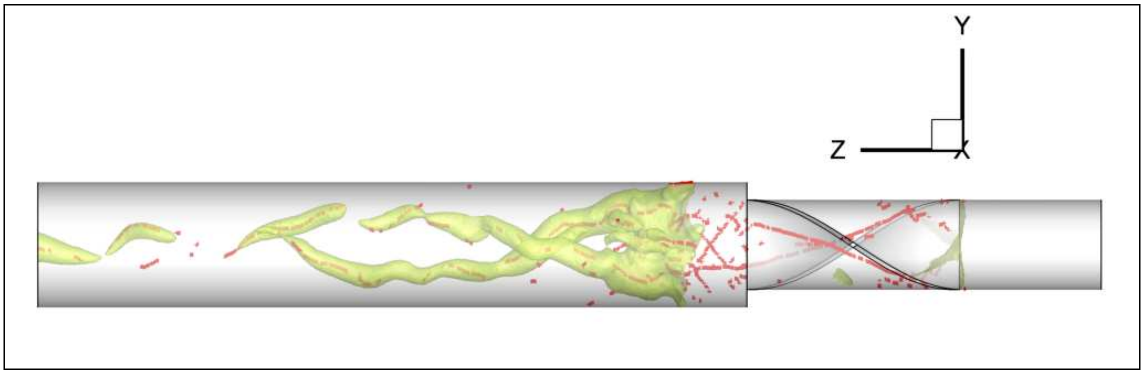

Figure 6.4.2 Helical vortices identified by isobar surfaces of $p/P_0 = 1.03$ and vortex cores identified with λ_2 method in the swirling flow induced by a swirler with d = 25.4mm and $y_r = 2.36$ at Re = 7.7×10^4

Larger increases in cross-section could not be simulated with the available computational resources, while maintaining a test section long enough to observe the behavior of the helical vortices. However, the case tested suggests that helical vortices are likely to survive a cross-section change and could also be the cause of the counter-rotating flow observed in swirling jets.

Further detailed analysis of this topic would require additional resources and rotating pipes are not the focus of this study. As a result, the confirmation of the source of counter-rotating flow in swirling jets induced by rotating pipes is left for future studies.

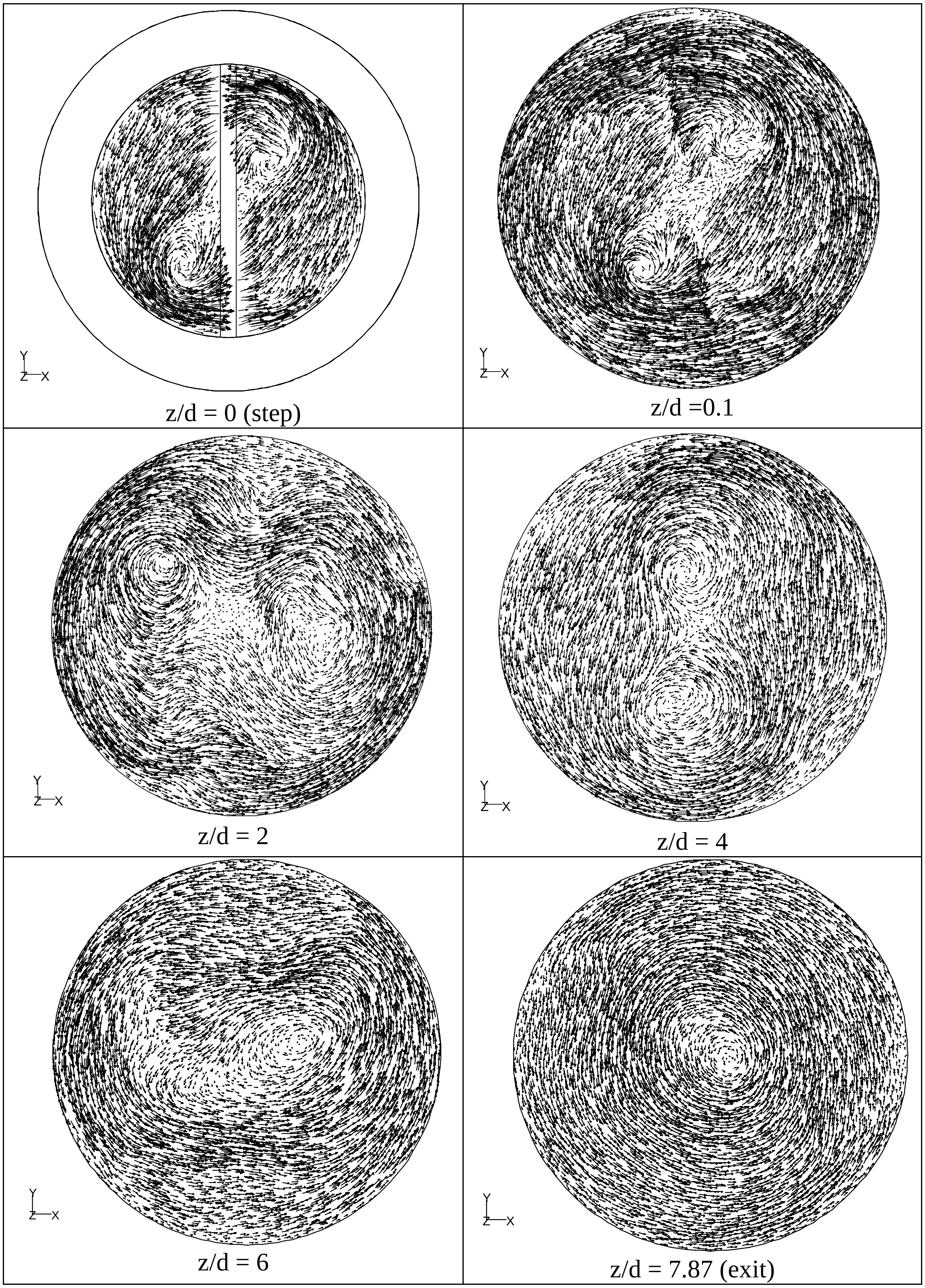

z/d = 0 (step)

z/d =0.1

z/d = 2

z/d = 4

z/d = 6

z/d = 7.87 (exit)

Figure 6.4.3 Velocity vectors at several axial locations following a 40% increase in the pipe diameter downstream from the swirler with y_r =2.36 at Re = $7.7x10^4$

6.5 Vortex inception and development

The main goal of the numerical simulations is to identify the formation process of the helical vortices in order to eliminate them. None of the previous studies presented in chapter 2.3 reported helical vortices. Most of those investigations described secondary flow inside the twisted tape swirlers consisting of two counter-rotating vortices on each side of the tape (figure 2.3.4).

There are also some similarities between the twisted tape swirler and blades in turbomachines. The effect of the twisted tape on the flow could be compared to the effect of two blades extending from the centerline to the pipe wall and spaced 180^o apart. Like blades in turbines and compressors, each half of the twisted tape has a pressure side and a suction side driving the flow. However, the turn angle of the twisted tape is much larger compared to typical blade turns.

In turbomachines secondary flow is created when a shear layer is turned through a duct or cascade. Streamwise vorticity is generated due to the velocity differential between the streamlines and also due to translation of the vorticity vector associated with the shear layer [Squire and Winter 1961, Lakshminarayana 1995].

The high resolution of the velocity field calculated with the numerical model allows a detailed investigation of the vortex formation and also of the characteristics of the helical vortices downstream from the swirler. A description of the vortex formation for the reference case of flow induced by a twisted tape with twist ratio $y_r = 2.36$ (60 mm pitch) at $Re = 7.7x10^4$ (bulk velocity 3 m/s) is presented in the following paragraphs. The positions of the cross-section planes are expressed both as angle of twist and as the corresponding physical distance in mm. Relative to the photo of the swirler in figure 6.5.1a the cross-section planes progress from the far end of the swirler toward the viewer.

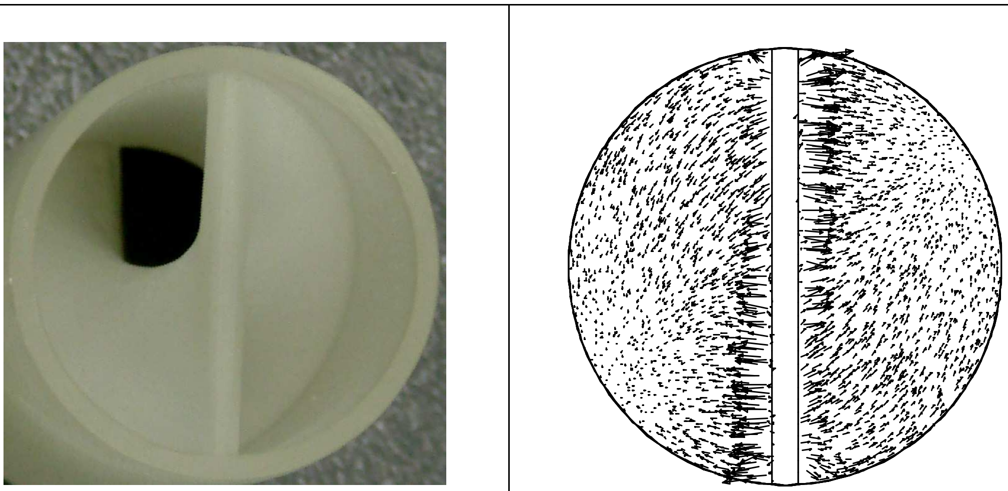

(a) twisted tape swirler exit

(b) 0 twist (inlet)

Figure 6.5.1: Swirler inlet: (a) photo of the swirler, (b) velocity vectors at the inlet (at the far end in figure 6.5.1a)

As the fluid enters the swirler, the twisted tape starts blocking the flow gradually (figure 6.5.1a and 6.5.1b). Figure 6.5.1.b shows velocity vectors in the cross section at the inlet, seen from the end of the tape. The flow at the inlet is axial except for the leading edge effect of the twisted tape splitting the flow.

After the first 5^o of twist (~2 mm in axial direction for the 60 mm pitch tape) the flow hits the twisted tape on half of the semicircular channel and the wall reaction exerts pressure on the fluid pushing the flow in the direction of the tape twist. At the same time the other half of the tape pulls away from the fluid creating a low pressure region (a suction side) (figure 6.5.2 a). Similarly to secondary flow formation in turbomachines, in the case of the twisted tape swirler the secondary flow is initiated by the viscous shear layer formed on the twisted tape surface.

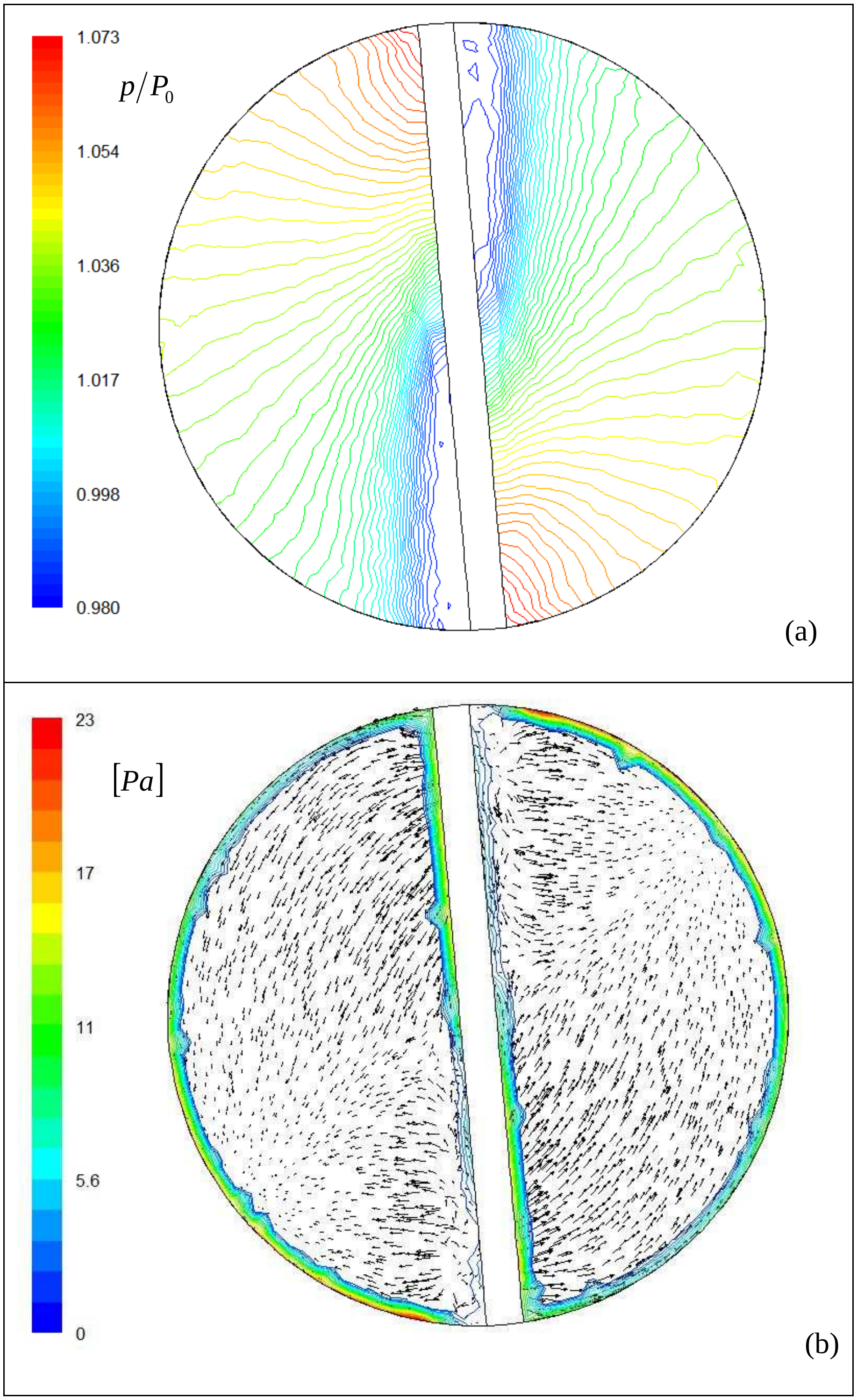

Figure 6.5.2: Flow field inside the swirler after 5^o twist (~2mm): a) static pressure contours after 5^o twist, b) Wall shear stress contours [Pa] and cross-section velocity vectors

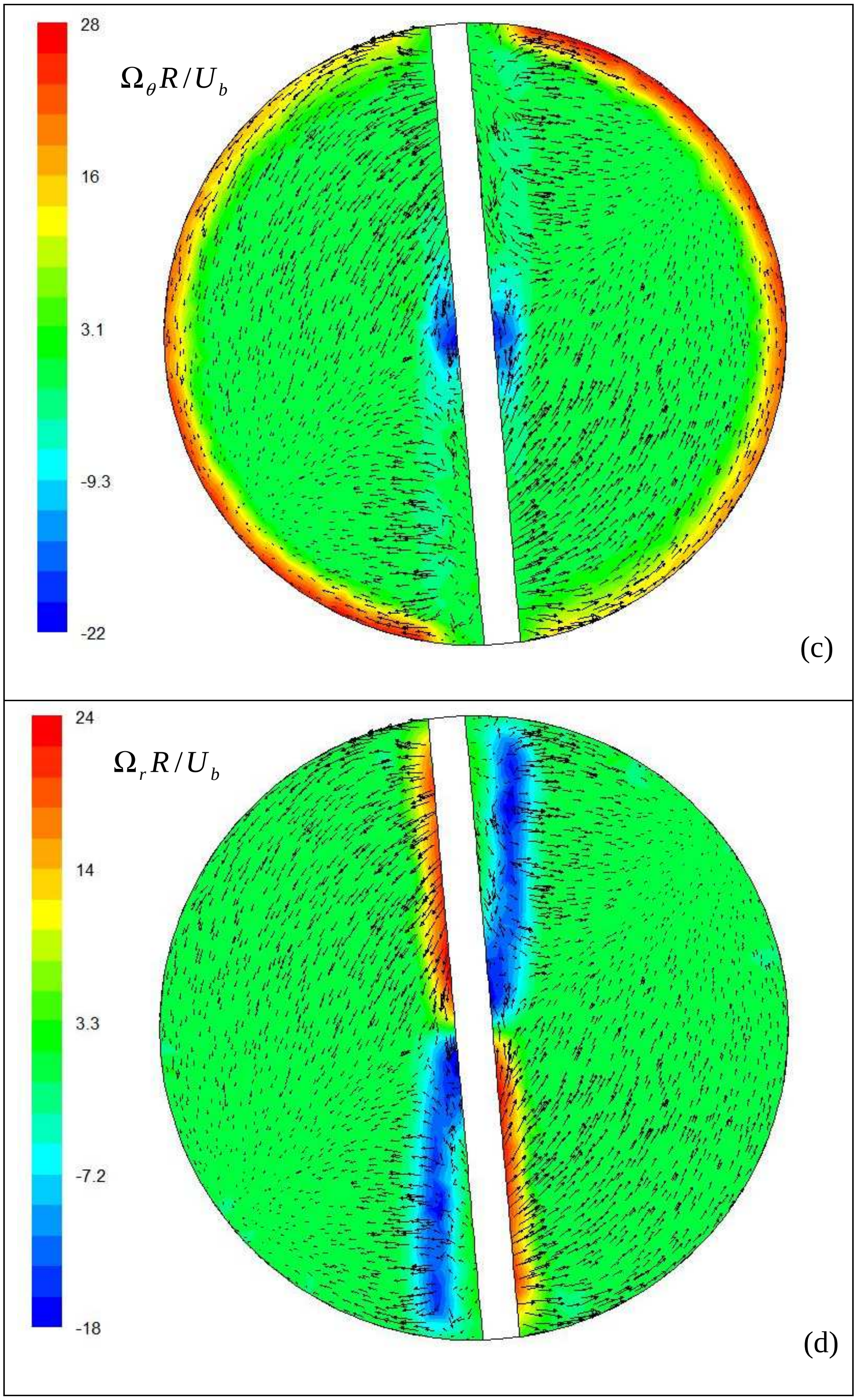

Figure 6.5.2 (cont): Flow field inside the swirler after 5^o twist (~2mm): c) normalized tangential vorticity, d) normalized radial vorticity

On the suction side of the twisted tape, the wall shear stress decreases until it becomes zero, producing flow separation (figure 6.5.2b). At the same time the pressure imbalance creates a flow across the twisted tape surface from the pressure side toward the suction side. At the swirler inlet the dominant vorticity components are tangential and radial formed near the walls (figures 6.5.2c and 6.5.2d) while there is little axial vorticity.

The wall shear stress contours and velocity vectors in figure 6.5.3a show that the region of flow separation increases in size after 30^o twist. After approximately 60^o twist (20 mm), secondary vortices appear on the suction side of the tape from the flow separation region, as shown by velocity vectors and the normalized axial vorticity plots in figure 6.5.3b. The streamlines in figure 6.5.4a show that these vortices become distinct after 75^o twist (25 mm). The axial vorticity inside the secondary vortices reaches maximum after 75^o twist. The flow across the twisted tape generates positive axial vorticity on the tape surface which is convected toward the emerging secondary vortices, as both the flow direction and the gradient of axial vorticity are aligned from the pressure side toward the suction side (figure 6.5.4b). After inception, the secondary vortices development is a result of competing effects from vortex stretching produced by strong tangential and radial vorticity components (figures 6.5.4c and 6.5.4d), viscous diffusion and axial vorticity convection from the surface of the twisted tape (figure 6.5.4b), according to equation 2.1.1. As the flow continues to turn, the small vortex formed in the flow separation region on the suction side of the tape grows in size due to vortex stretching, while the axial vorticity inside the vortex starts to decrease.

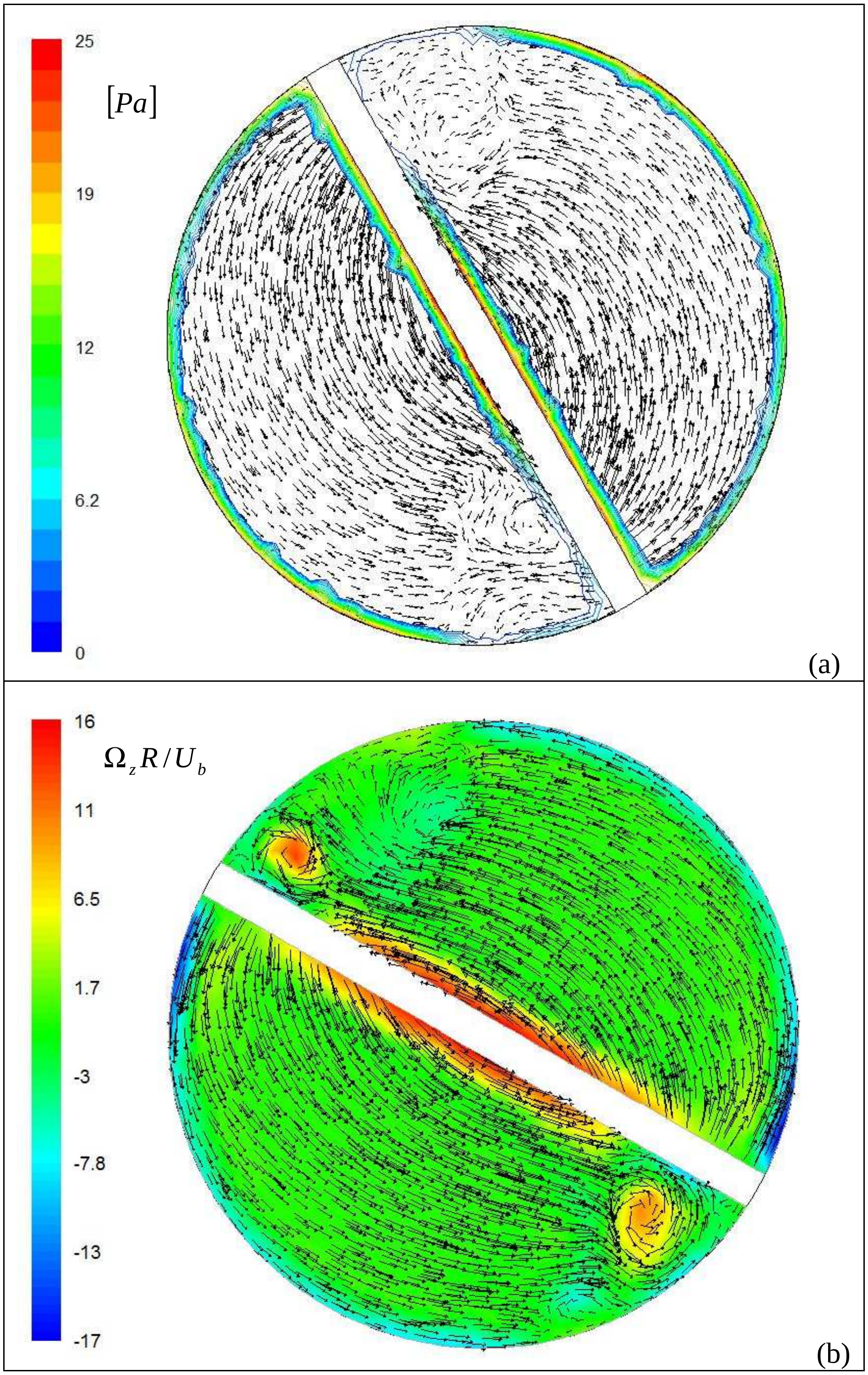

Figure 6.5.3: Secondary vortex development: (a) wall shear stress and velocity vectors after 30^o twist (10 mm), (b) normalized axial vorticity and velocity vectors after 60^o twist (20mm).

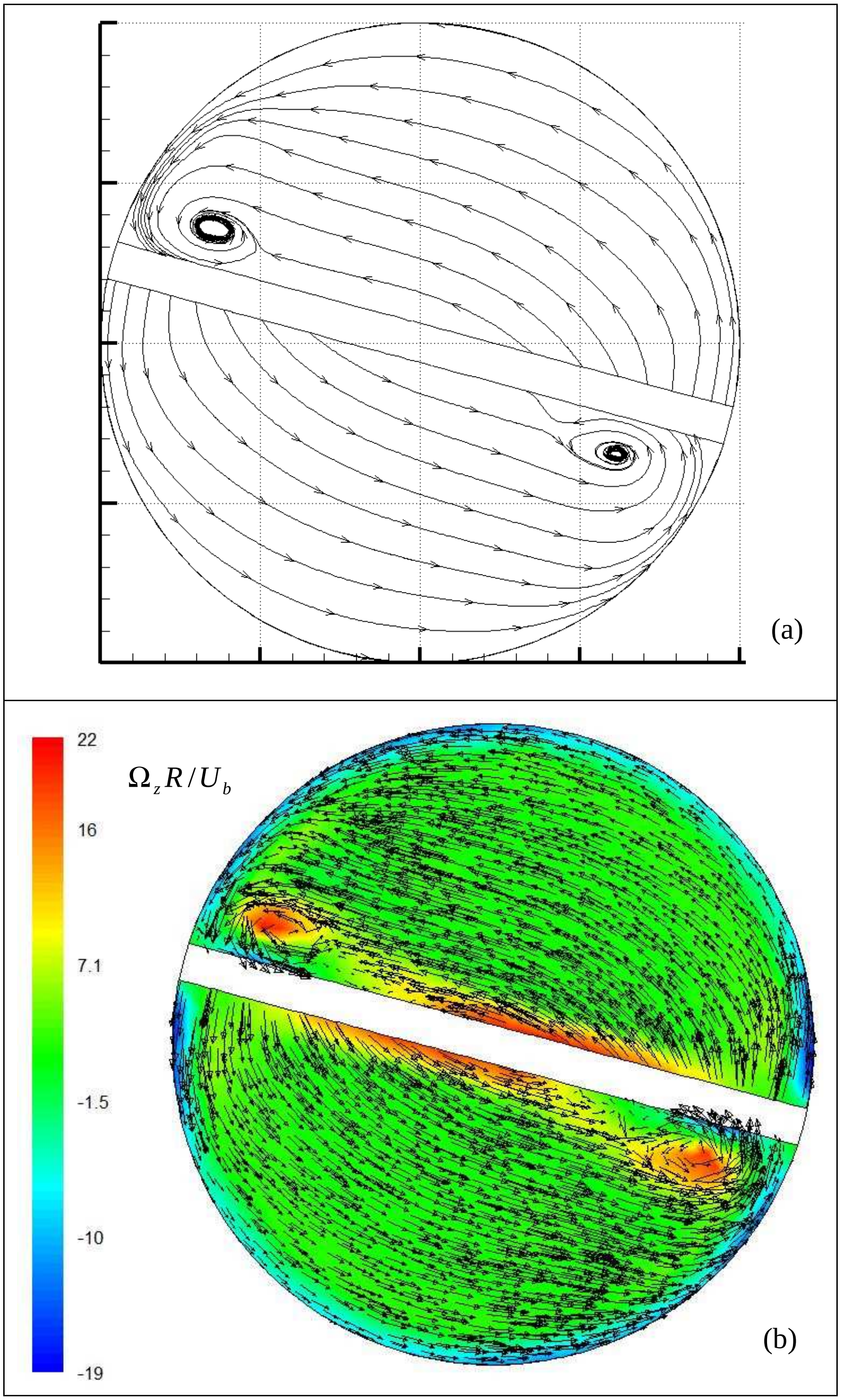

Figure 6.5.4: Flow field inside the swirler after 75^{o} twist (25mm): a) streamlines, b) normalized axial vorticity and velocity vectors,

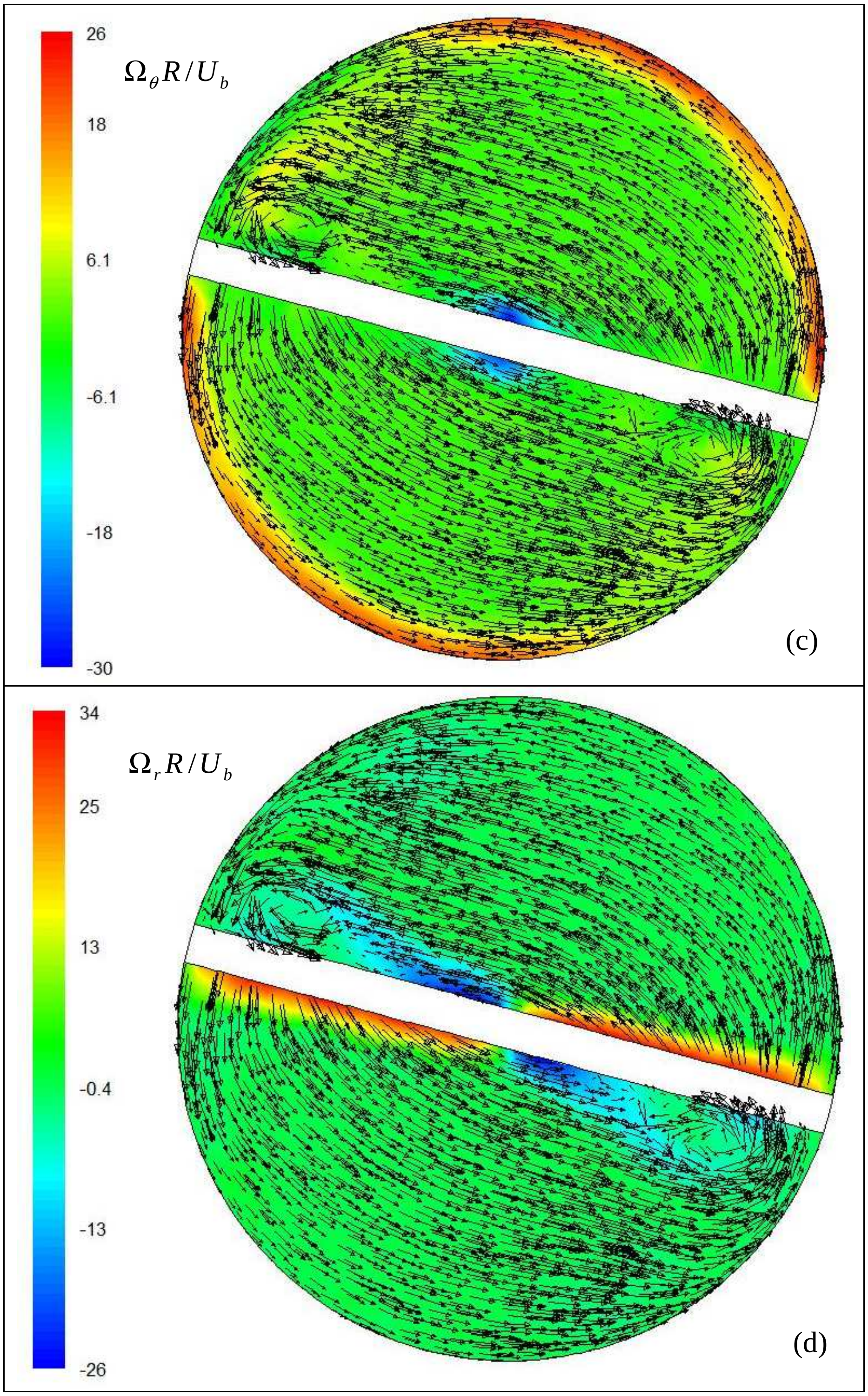

Figure 6.5.4 (cont.): Flow field inside the swirler after 75^o twist (25mm): c) normalized tangential vorticity and velocity vectors, d) normalized radial vorticity and velocity vectors.

As the secondary vortex grows, it changes its position inside the semicircular channel in an apparent move against the flow (figure 6.5.5a and 6.5.5b). This motion against the flow is likely due to conservation of angular momentum as the vortex tends to preserve its rotation axis direction and oppose the change forced by the tape. The vortices do not move against the flow in the semicircular channel, rather the channel moves around the secondary vortices, changing their relative position.

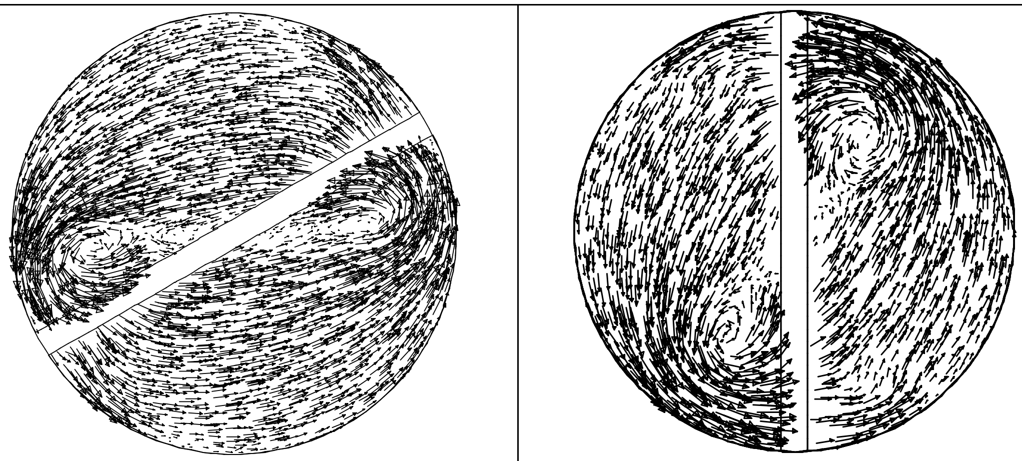

(a) velocity vectors after 120^o twist (40 mm inside the swirler)

(b) velocity vectors after 180^o twist (swirler exit)

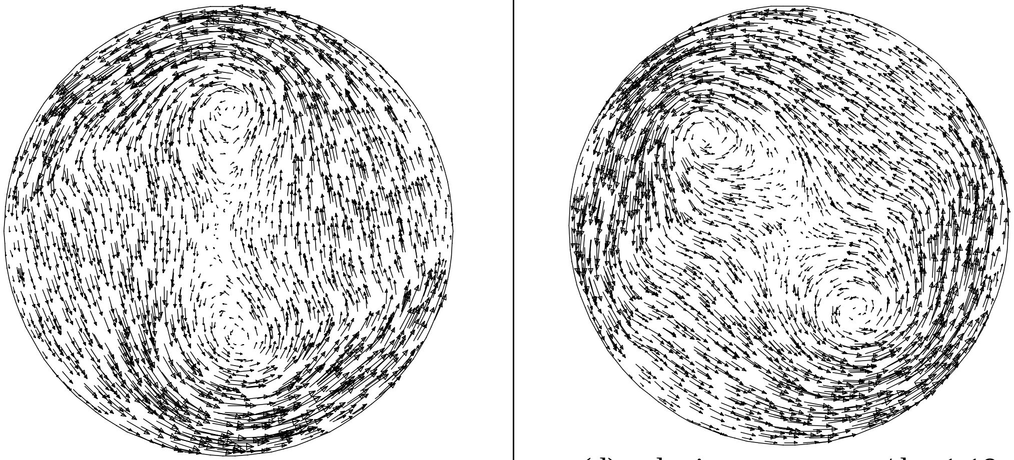

(c) velocity vectors at z/d = 0.59 (15 mm from the end of the tape)

(d) velocity vectors at z/d = 1.18 (30 mm from the end of the tape)

Figure 6.5.5: Vortex formation for a twisted tape with y_r = 2.36 (60 mm pitch) at Re = $7.7\text{x}10^4$.

After the exit, the two vortices maintain their helical shape imposed in the formation stage inside the swirler and continue into the straight pipe (figure 6.5.5c and 6.5.5d). The position of the vortex at the exit determines the pitch of the helical vortices inside the straight pipe.

Figure 6.5.6 shows the evolution of the normalized axial vorticity inside the center of a secondary vortex along the twisted tape, as a function of the twist angle of the tape. After 45^o twist, axial vorticity spots become distinguishable in the flow on the suction side of the twisted tape. The secondary vortex becomes evident in the velocity field and low pressure isobar surfaces after approximately 60^o twist, as the axial vorticity increases very fast. The axial vorticity reaches its peak after 75^o twist, and then the vortex starts growing in size while the axial vorticity decreases fast due to the cumulated effect of vortex stretching and viscous dissipation. After approximately 150^o twist there is a distinct change of slope in the axial vorticity decay, suggesting that the vortices have reach their final size and vortex stretching is not a factor anymore, leaving viscous dissipation as the only cause of decay at a slower rate.

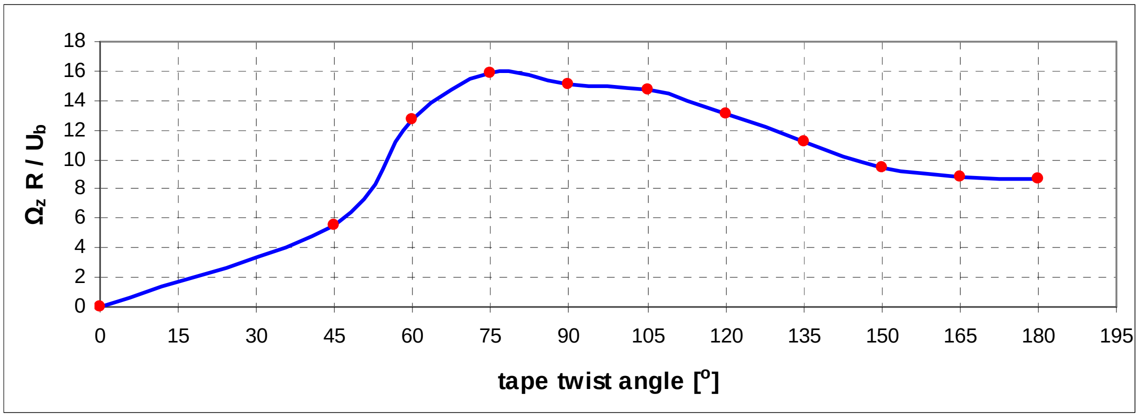

Figure 6.5.6: Variation of the normalized axial vorticity in the center of the secondary vortex along the twisted tape for the flow through an 180^o twisted tape with $y_r = 2.36$ at Re = $7.7x10^4$.

Figure 6.5.7 shows side and front views of the development of the helical vortices inside the swirler with $y_r = 2.36$ at $Re = 7.7 \times 10^4$, giving a better perspective of the actual physical phenomenon. Figure 6.5.7c shows the actual swirler to allow a direct comparison with the numerical results. The secondary vortices are identified with isobar surfaces of $p/P_0 = 1$ while tangential velocity vectors show the local flow direction in cross-section planes.

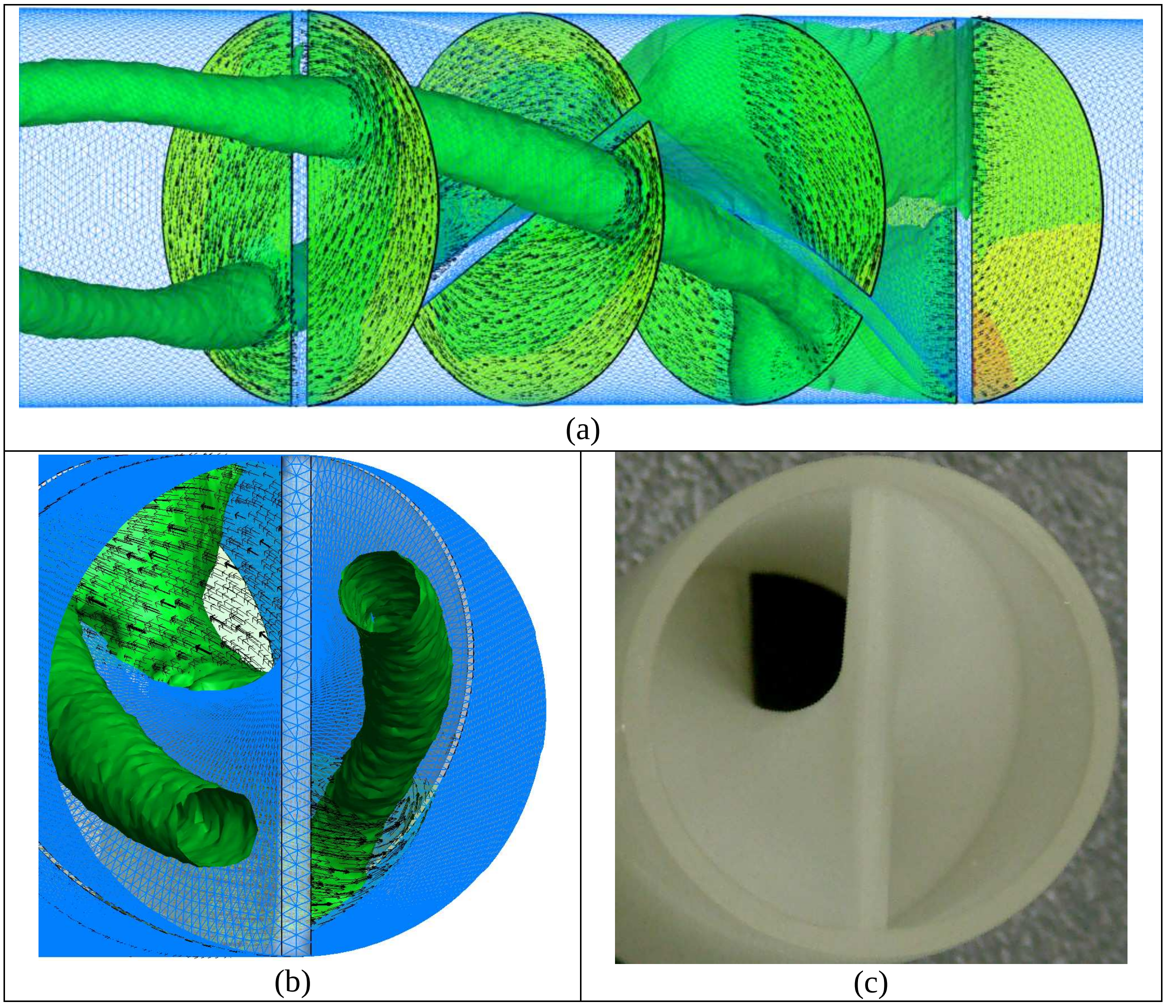
(a)

(b)

(c)

Figure 6.5.7: Formation of the secondary vortices inside the swirler. The plots show isobar surfaces of $p/P_0 = 1$ and cross-section planes with tangential velocity vectors for the tape with $y_r = 2.36$ (60 mm pitch) at $Re = 7.7 \times 10^4$: (a) side view, (b) front view, (c) actual swirler.

In figure 6.5.7a the cross-section planes show the flow at 0^o, 60^o, 120^o and 180^o while in figure 6.5.7b the velocity vectors are shown in a plane after 75^o. Figure 6.5.7a shows that a distinct vortex emerges approximately after 60^o twist (20 mm inside the swirler) matching the experimental observations. Figure 6.5.7b shows that the secondary vortices follow the tape twist and describe helical trajectories relative to the pipe axis which continue inside the straight pipe.

These results are similar to the results showed by Rahmani [2004, 2005] for static mixers and Date [1974] for a short swirler. The present results also match well the swirl decay measurements of Kreith and Sonju [1965]. However, these results differ from the results published by Manglik et al. [1993, 1997], Yerra et al. [2007], Kazuhisa et al. [2004] and the measurements of Seymour [1966], which show counter-rotating vortices inside or at the exit of the twisted tape. The differences could be caused by the fact that Manglik et al. [1997], Yerra et al. [2007] and Kazuhisa et al. [2004] used different numerical models and different grid resolutions to simulate air at low Re and twisted tapes with multiple twists. Little details are given on the numerical method of Manglik et al. [1997] and Yerra et al. [2007] (streamlines and velocity vectors plots are presented in those articles, but the numerical method was not published and it is referenced to an internal lab report TFTPL-7 from the University of Cincinnati , September 2002 which was unavailable for this study). No details are given about the numerical grid used in Kazuhisa et al. [2004] and a low grid resolution and the use of a non-orthogonal coordinate system could significantly impact the results.

One of the reasons previous authors proposed a two counter-rotating vortex structure inside twisted tapes was the fact that axial velocity contours measured [Seymour

1966] or simulated [Date 1974] displayed two peaks. Figure 6.5.8a shows that the axial profile indeed has two peaks in the current simulation but these are created by a single co-rotating vortex as shown by the velocity vectors in figure 6.5.8b.

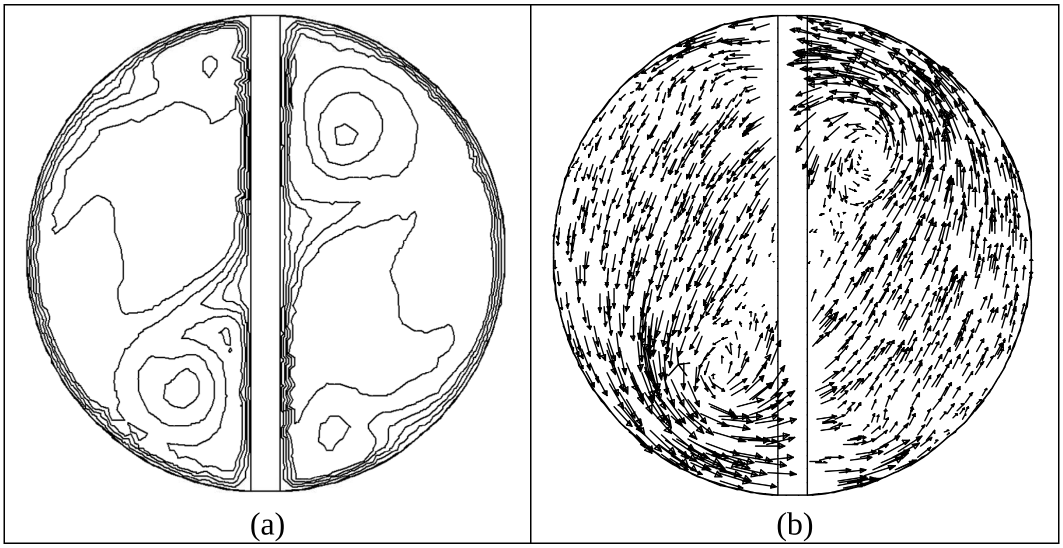

Figure 6.5.8 Axial velocity contours (a) and velocity vectors (b) at the exit of the twisted tape swirler with $y_r = 2.36$ at $Re = 7.7x10^4$.

The measurements of Seymour were done after multiple tape twists with probes inserted directly in the flow which could have altered the flow. Given the close match between experiments and the simulations presented in this study, the vortex formation mechanism described here seems reliable for water flow through 180^o twisted tapes.

For all three swirlers tested, the position of the secondary vortices inside the swirler relative to the twisted tape depends on the angle of the twist. In all three cases the vortices appear after approximately 60^o (1/3 of the swirler) as shown by the isobar-surfaces in figure 6.3.4. The secondary vortices also reach similar positions at the end of the swirler as shown by streamlines in figure 6.3.5. The pitch of the secondary vortices changes continuously inside the swirler as the vortices change their position relative to the twisted tape from the location where they first appear until the end of the twisted tape. While the tape rotates 120^o after the secondary vortices form, the vortices lag behind and rotate approximately 90^o inside the swirler over 2/3 of the twisted tape length, which also represents half of the first 180^o pitch of the helical vortices (figure 6.5.9). After the twisted tape ends, inside the straight pipe the pitch does not change anymore and mirrors the part of the pitch shaped inside the swirler. As such, the pitch of the helical vortices is twice as long as the part of the pitch created inside the swirler, resulting in the 4/3 ratio between the pitch of the helical vortices and the pitch of the twisted tape observed in both experiments and simulations.

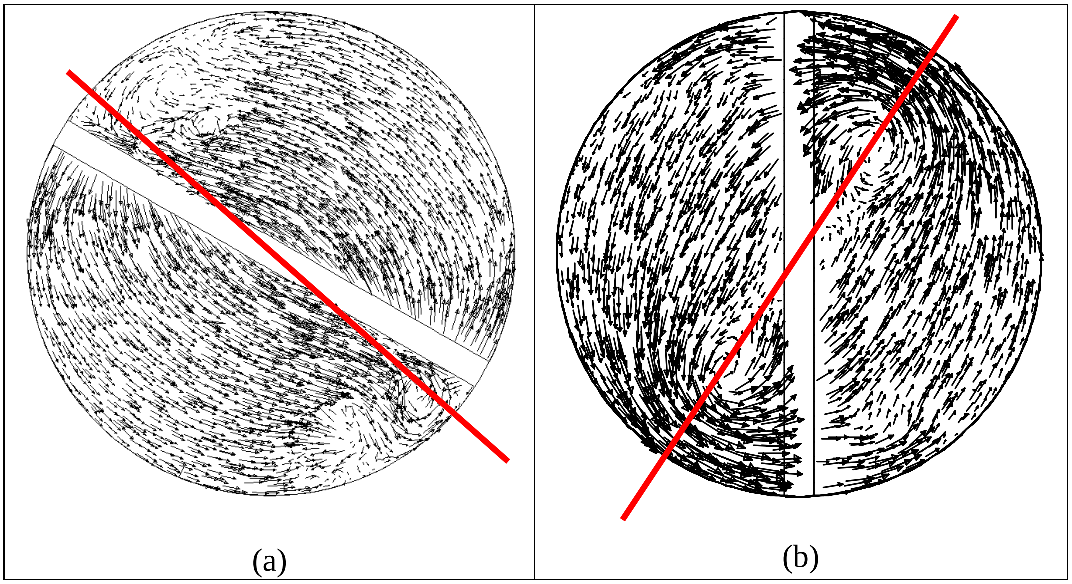

Figure 6.5.9 Change of position for the secondary vortices inside the swirler: (a) the vortices appear first after 60^o twist; (b) secondary vortices at the swirler exit, after 180^o twist. The red lines highlight the fact that the angle between lines passing through the secondary vortices in the two plots is approximately 90^o.

6.6 Multiple twists

As the previous chapter showed, after their inception the vortices keep moving away from their initial position against the main flow. This behavior raised the question how the vortices develop if the tape is twisted more than 180°.

Figure 6.6.1 shows the behavior of the secondary vortices for tapes with twist ratio 2.36 (60 mm pitch) and with twists of 180°, 360°, 720° and 1080° at Re = 7.7×10^4. The tape with the 180° twist is shown as reference. The 360° tape produces helical vortices which spiral toward the centerline where they merge. For the 720° tape helical vortices are still visible but they are weak and unstable. In the last case, the flow downstream of the tape with 1080° twist is a simple swirling flow without any secondary vortices. The swirling flow induced by the tape with 180° twist has the most stable helical vortices. There is no tape-end effect on the position of the secondary vortices. After 180° the position of the secondary vortices in the cross-section is the same either if the tape ends or if more twists are following.

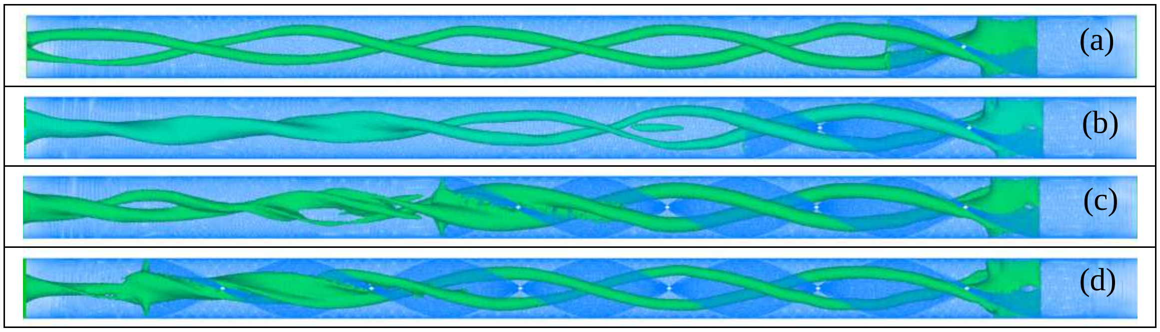

Figure 6.6.1: Effect of multiples twists on the secondary vortices: (a) 180° twist, (b) 360° twist, (c) 720° twist, (d) 1080° twist.

In order to verify the numerical predictions for multiple twists two, 180° twisted tapes with twist ratio $y_r = 2.36$ (60 mm pitch) were installed in succession and the flow was visualized with air bubbles and high speed camera. Figure 6.6.2 shows the comparison between the experiment and the numerical prediction for the flow at Re = 7.7×10^4 including the swirler exit. The experimental visualization confirms both the convergence of the helical vortices toward the centerline and the shorter pitch of the helical vortices (70 mm) compared to the 180^o case (80 mm). The helical vortices however do not merge in the experiments. After the two secondary vortices get close together, the radius of the helix increases back to half a radius and the vortices continue in a stable double helix structure until the end of the 1.14 m (45d) long pipe.

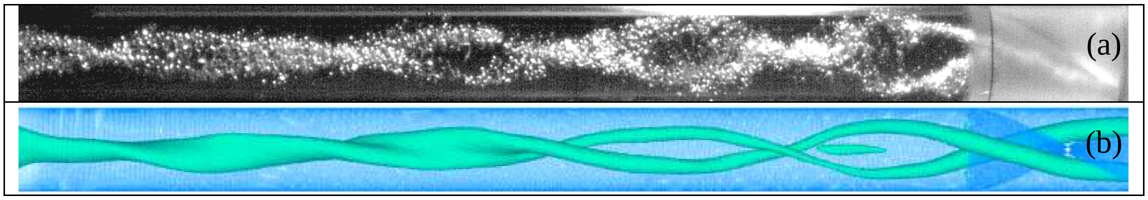

Figure 6.6.2 Helical vortices induced by a 360^o twisted tape with 60 mm pitch (y_r = 2.36) at Re = 7.7×10^4: a) high speed camera visualization, b) numerical simulation.

In order to investigate the behavior of the secondary vortices for tapes with multiple twists, the flow created by a twisted tape with 1080^o twist and twist ratio y_r = 2.36 is sampled with cross-section planes extracted after each 90^o twist. The locations of the cross-section planes are shown in figure 6.6.3 and the plots of the tangential velocity vectors in each cross-section are presented in detail in figure 6.6.4.

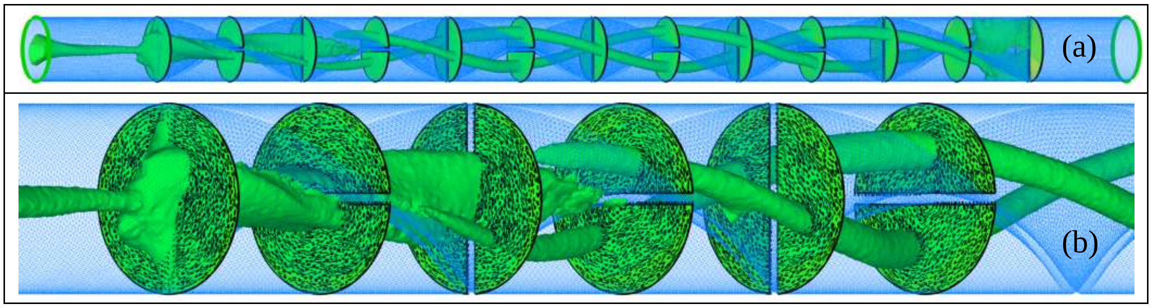

Figure 6.6.3: Cross-section planes on a tape with 1080^o twist: (a) full domain, (b) close-up of the last twists (between 540^o and 1080^o) with isobar surfaces of $p/P_0 = 1$.

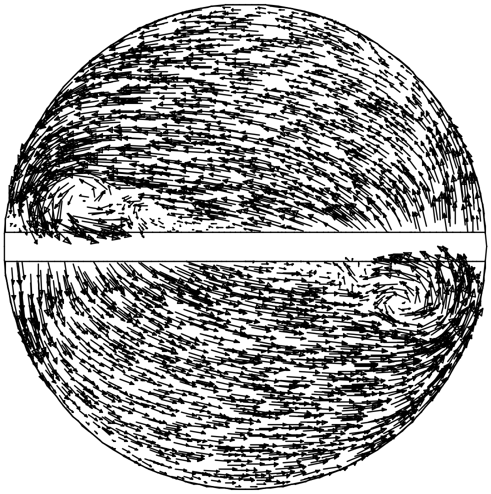

after 90° twist

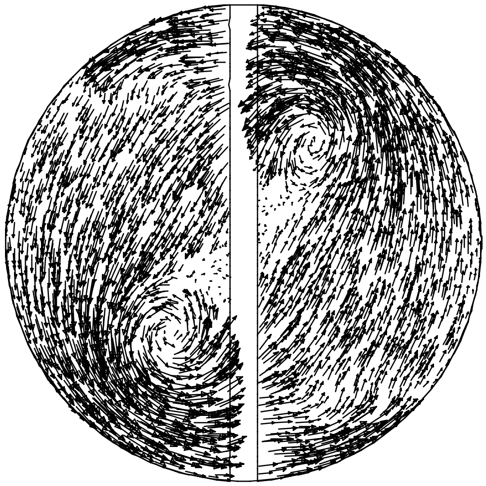

after 180° twist

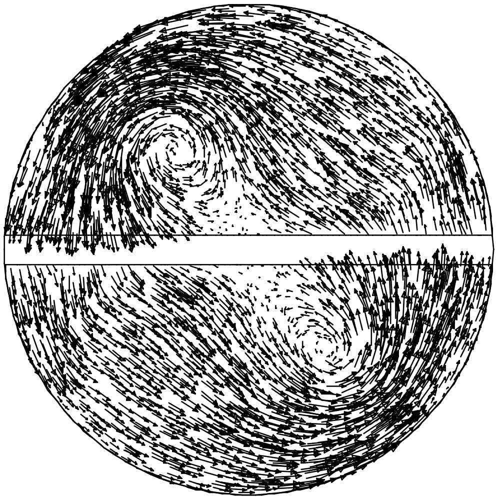

after 270° twist

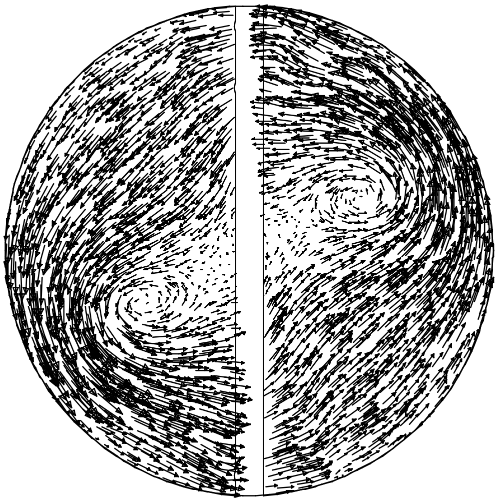

after 360° twist

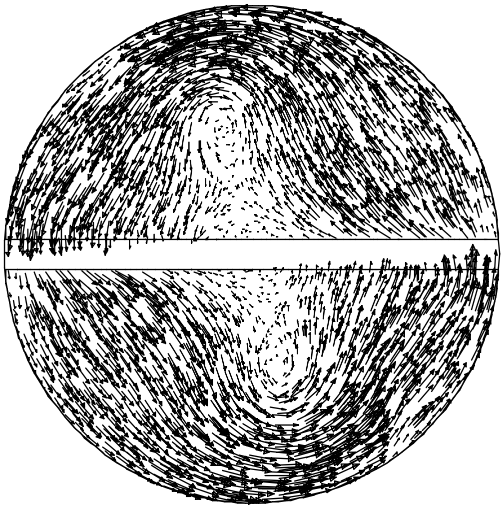

after 450° twist

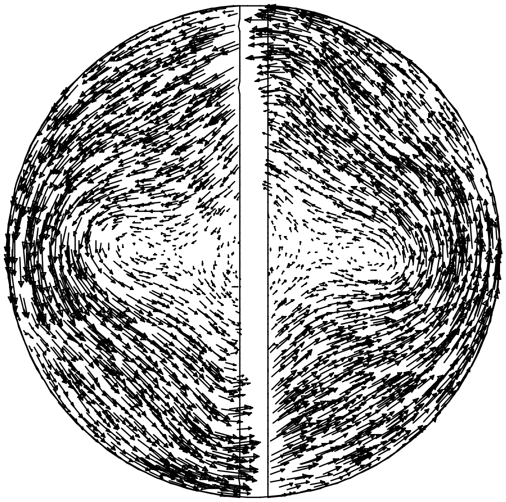

after 540° twist

Figure 6.6.4: Development of the secondary vortices.

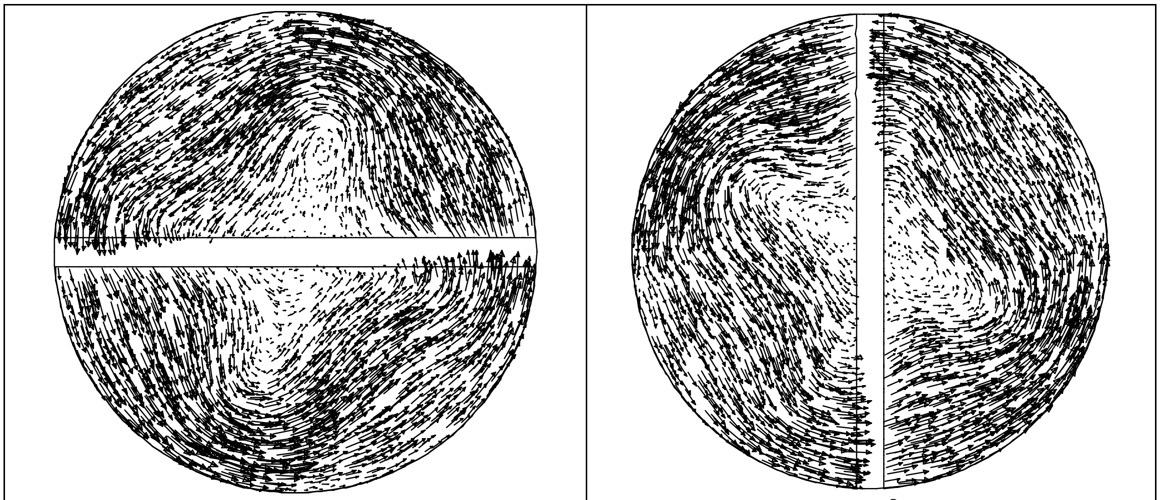

after 630° twist

after 720° twist

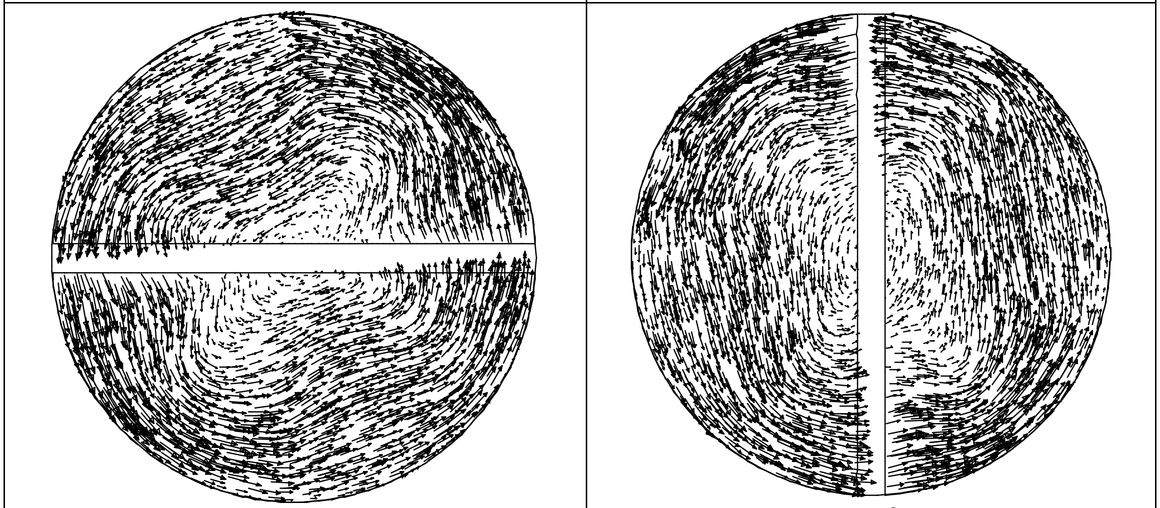

after 810° twist

after 900° twist

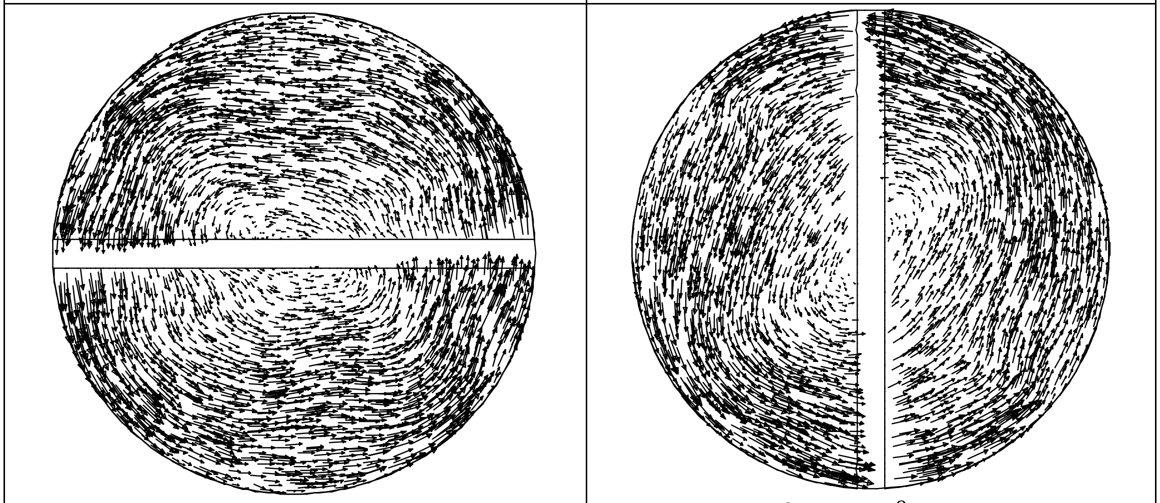

after 990° twist

after 1080° twist

Figure 6.6.4 (continued): Development of the secondary vortices.

Through the first 180^o twist the secondary vortices have exactly the same behavior shown in the previous chapter for a tape with a simple 180^o twist. As the tape continues to twist, the secondary vortices move further against the flow and they reach the middle of the channel after 450^o. The vortices continue to move against the tape rotation but after 720^o twist they weaken. After 900^o twist there are little indications of secondary motion in the velocity vectors and the flow becomes a regular swirling flow with a low pressure region near the centerline.

As explained before, the motion against the flow is likely due to conservation of angular momentum as the helical vortices tend to preserve their rotation axis direction while the channel moves around them, changing their relative position. This lagging is what gives the helical vortices a longer pitch than the pitch of the tape for the 180^o tape.

In the previous section it was shown that after approximately 150^o twist there is a distinct change of slope in the axial vorticity decay, suggesting that the vortices have reach their final size and vortex stretching is not a factor anymore, leaving viscous dissipation as the only cause of vorticity decay at a slower rate. Figure 6.6.5 shows that from 150^o to 1080^o the axial vorticity decreases at a relatively constant rate until it reaches the background level of axial vorticity corresponding to the main swirl. The velocity vectors in figure 6.6.5b show that after 1080^o twist the remnants of the secondary vortices create just a slight disturbance in the swirling flow.

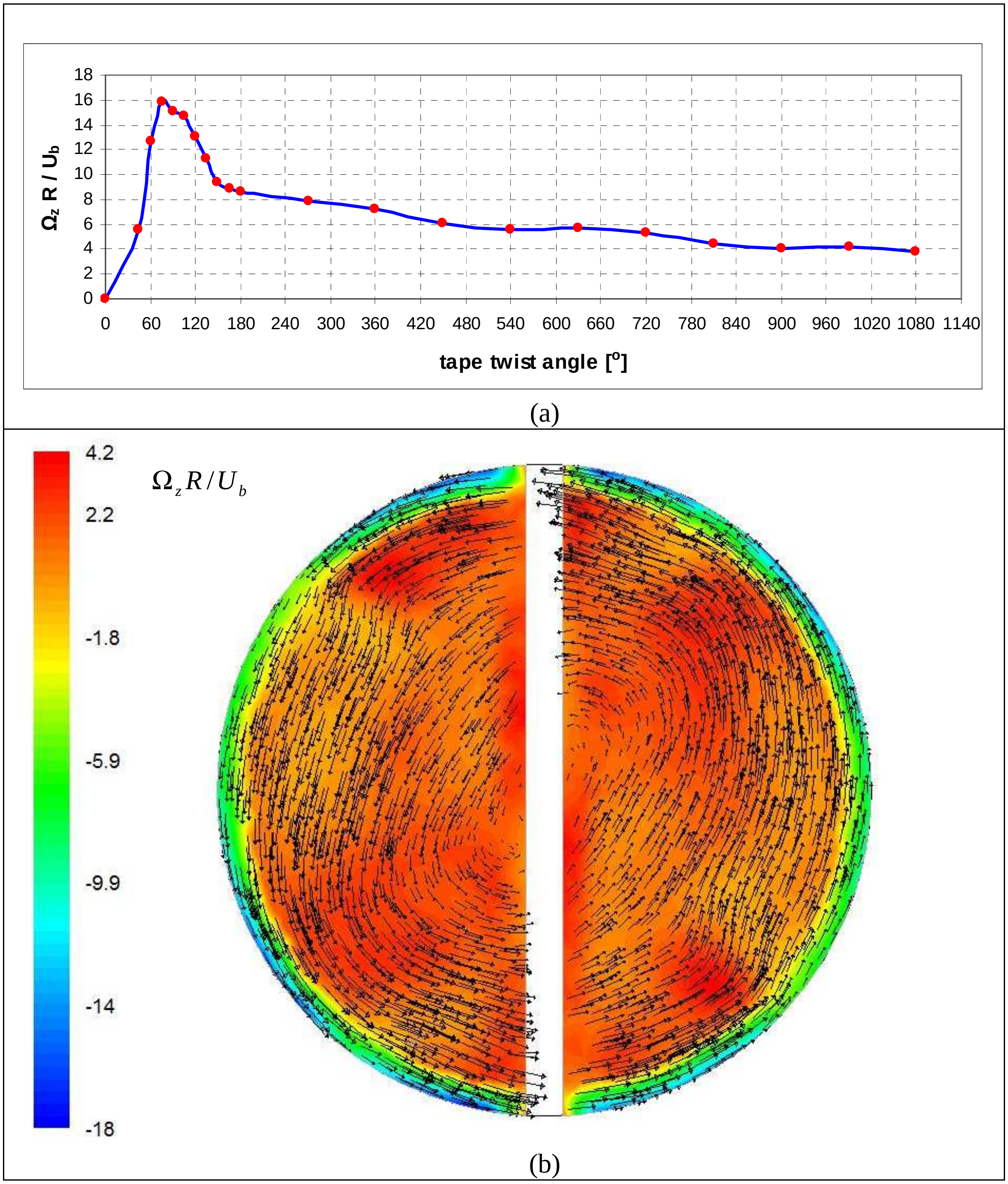

Figure 6.6.5 Normalized axial vorticity inside a twisted tape swirler with y_r =2.36 and multiple twist at Re = 7.7x10^4: a) variation along the swirler, b) cross-section velocity vectors and normalized axial vorticity after 1080° twist.

6.7 Secondary motion at low Re

LDV measurements and high speed camera visualizations showed that the helical vortices induced by twisted tapes have a constant pitch independent of Re in the range $2x10^4$ to 10^5 while for Re = 10^4 there are no visible helical vortices inside the test section, downstream of the swirler. In order to investigate the secondary vortices at lower Re and determine the critical Re at which the secondary vortices appear first inside the twisted tape swirler, numerical simulations are run for Re in the range 100 to 1,500. At low Re the secondary vortices are weak and the pressure gradients are small so the cores cannot be visualized with isobar surfaces as the viscous effects hide them. Instead the vortices are identified using the λ_2 method which removes the viscous effects [Jeong and Hussain 1995].

Figure 6.7.1 shows the velocity vectors at the end of the 180^o twisted tape with y_r = 2.36 (60 mm pitch) and the side views of the twisted tape for Re 100, 250, 500, 750 and 1,000. The vortices are identified with red line segments marking the centers of the regions where $\lambda_2<0$ which correspond to vortex cores.

The velocity vectors show that the flow change is not sudden but rather gradual, so the appearance of the secondary motion is better described by a range of Re rather than a critical value. There are no secondary vortices visible at Re = 100 and Re =250 but the vortex cores are visible at Re = 500, so the secondary vortices appear first in this range (bulk velocities between 10 and 20 mm/s). While secondary vortices form inside the swirler for Re between 500 and $2x10^4$, the experimental visualizations show that the helical vortices are not strong enough to hold the air bubbles outside the swirler.

(a) Velocity vectors	**(b) Vortex cores (λ_2)**
	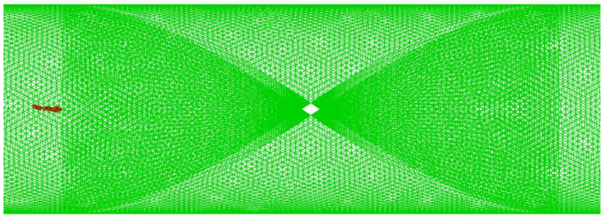
Re = 100 (U_b = 0.004 m/s)	
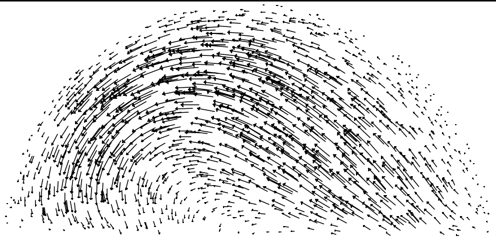	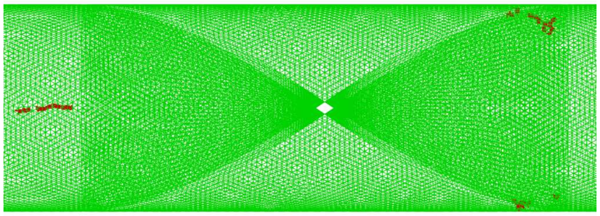
Re = 250 (U_b = 0.01 m/s)	
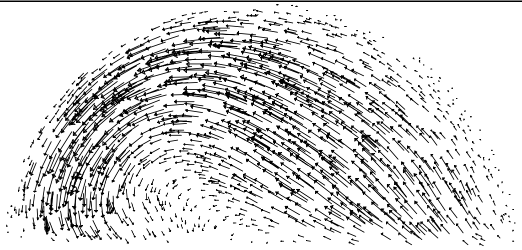	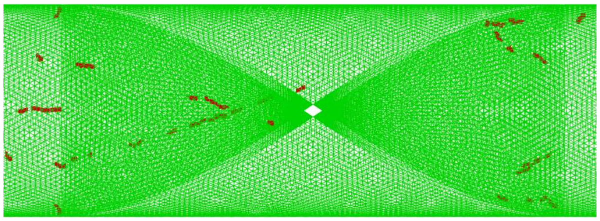
Re = 500 (U_b = 0.02 m/s)	
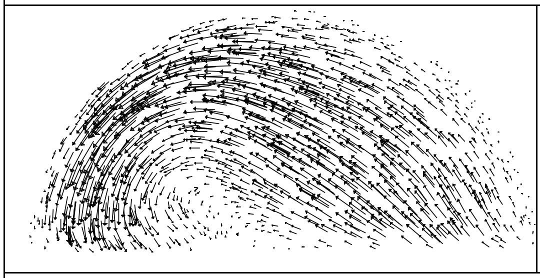	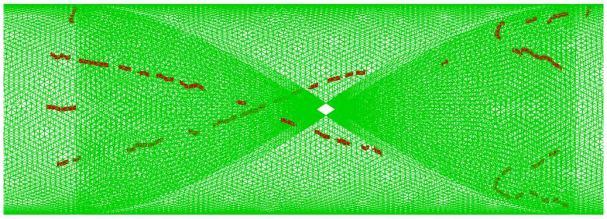
Re = 750 (U_b = 0.03 m/s)	
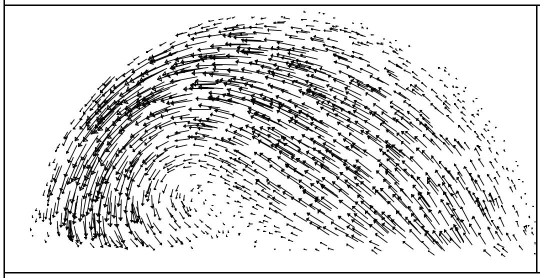	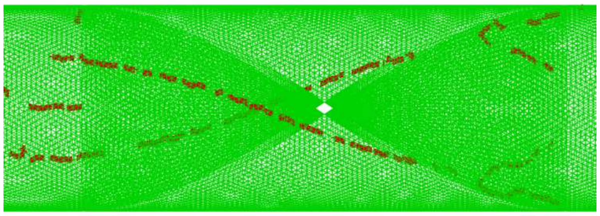
Re = 1000 (U_b = 0.04 m/s)	

Figure 6.7.1: Secondary motion at low Re: (a) velocity vectors at the swirler exit, (b) side views of the swirler with secondary vortices identified by λ_2 method (the flow is from right to left).

As explained in the previous section, at the swirler inlet the leading edge of the twisted tape and the sudden turn create a low pressure region with flow separation where weak vortices form. As the plots in figure 6.7.1 show the inlet vortices disappear within 30^{o} twist (10 mm) from the swirler inlet as the centrifugal forces grow. The plots at Re = 500 and 750 show that the secondary vortices present at the end of the swirler form after the inlet vortices disappear.

As the twisted tape induces flow rotation, the centrifugal force could be a plausible cause for the secondary motion. One of the first investigations on centrifugal stability was published by Rayleigh [1916] who showed that the presence of an inverse stratification along the radius (a negative gradient) of the square of the angular momentum per unit mass $(r \cdot v_{\theta})^{2}$ indicates that the flow is unstable to axi-symmetric disturbances. Rayleigh referred to $r \cdot v_{\theta}$ as the circulation ($2\pi \cdot r \cdot v_{\theta}$ is the circulation round the circle defined by r = constant and z = constant [Drazin and Reid 1981]) which is why the criterion is referred to as the "circulation criterion".

The plots in figure 6.7.2 show the distribution of the square of the circulation $(r \cdot v_{\theta})^{2}$ for Re = 500 where the secondary vortices were first identified by the λ_2 method. The colored vectors plot (figure 6.7.2a) shows that there is an uneven stratification of the squared circulation throughout the domain. Figure 6.7.2b shows the profiles of the circulation squared inside the semicircular channel along the radii at 45^{o} and 135^{o} which are shown in figure 6.7.2a. For the 45^{o} plot the maximum occurs close to the middle of the radius followed by an obvious negative gradient toward the wall, confirming the flow is centrifugally unstable. The inverted stratification in the first half of the domain leads to the appearance of the secondary motion in the second half as the fluid close to the axis is ejected toward the wall. By the 135° plane the circulation is concentrated near the wall.

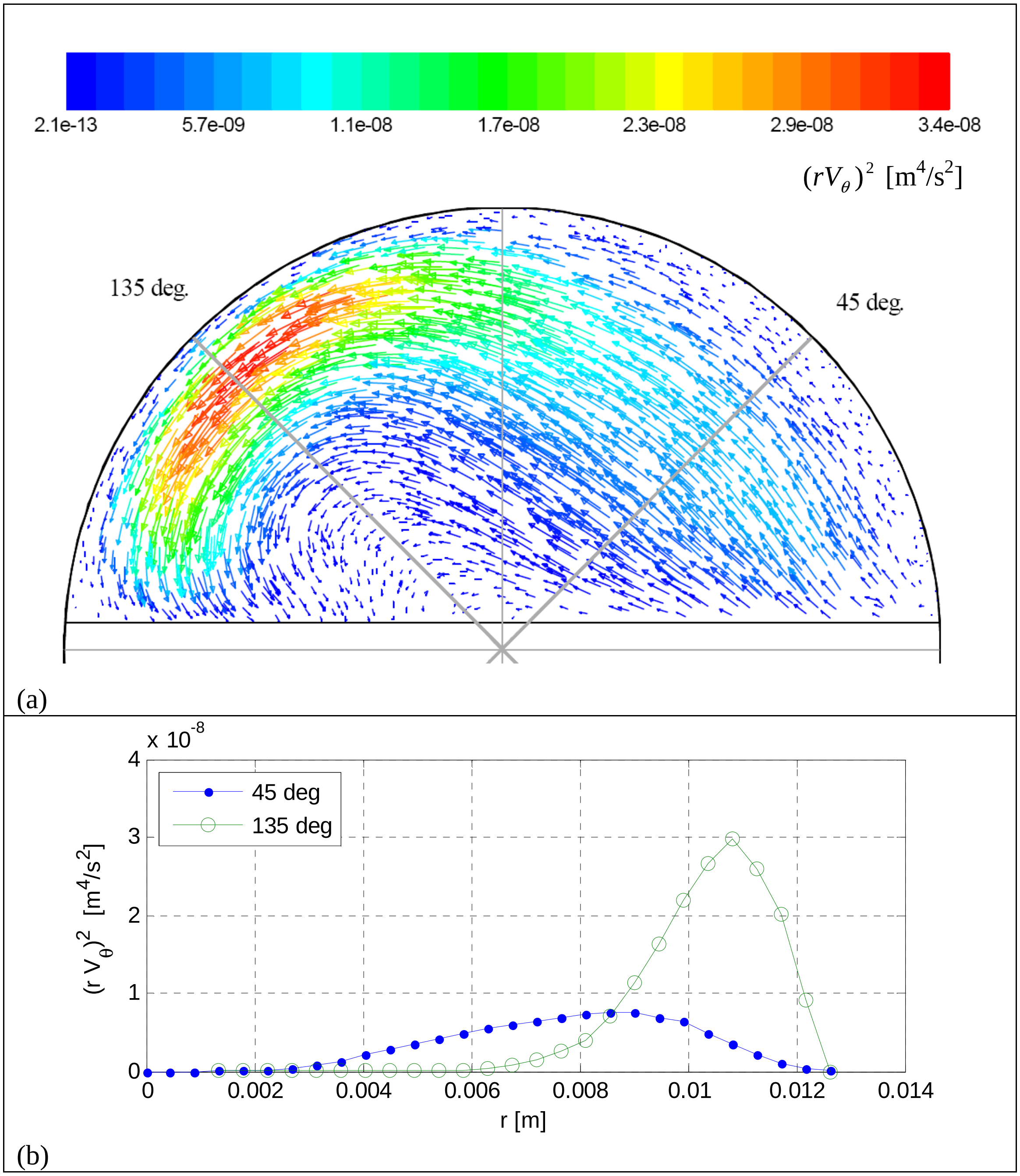

Figure 6.7.2 Squared circulation distribution at the swirler exit for Re = 500 (U_b = 0.02 m/s): (a) colored velocity vectors, (b) radial profiles along the radii (R = 0.0127 m) at 45° and 135° shown in plot (a).

The centrifugal stability criterion determined by Rayleigh was developed based on the flow between coaxial rotating cylinders. That case was an axis-symmetric flow where the occurrence of a centrifugal instability was a 1D problem. In this case the problem is 2D and the effect of the centrifugal forces is to shift the center of rotation of the flow away from the pipe axis, breaking the flow symmetry.

Figure 6.7.3 shows a comparison between the variations of the tangential velocity, the centrifugal force density $F_{cf} = \rho \cdot V_\theta^2 / r$, the total pressure, the circulation squared and the axial vorticity for Re = 100, 250 and 500. The twisted tape creates two semicircular channels inside the pipe which could be considered to have an inlet half and an exit half (see velocity vectors in figure 6.7.2a). The plots show that the centrifugal force distribution (b) and the squared circulation distribution (d) in the first half of the domain have approximately the same spatial distribution for all three Re.

However, as Re increases the centrifugal forces become stronger and the flow symmetry is lost. The location of the maximum tangential velocity (a) shifts from near the inlet toward the second half of the domain and this shift in the tangential velocity distribution is accompanied by an emergence of an off-center low pressure region absent at Re = 100 and very distinct at Re = 500 (c). As Re increases, the axial vorticity plots (e) also show a peak emerging at the same location where the tangential velocity (a) has its maximum. The plots show that the flow patterns do not change suddenly, rather the flow changes as the pressure gradients increase as a result of an increase in Re.

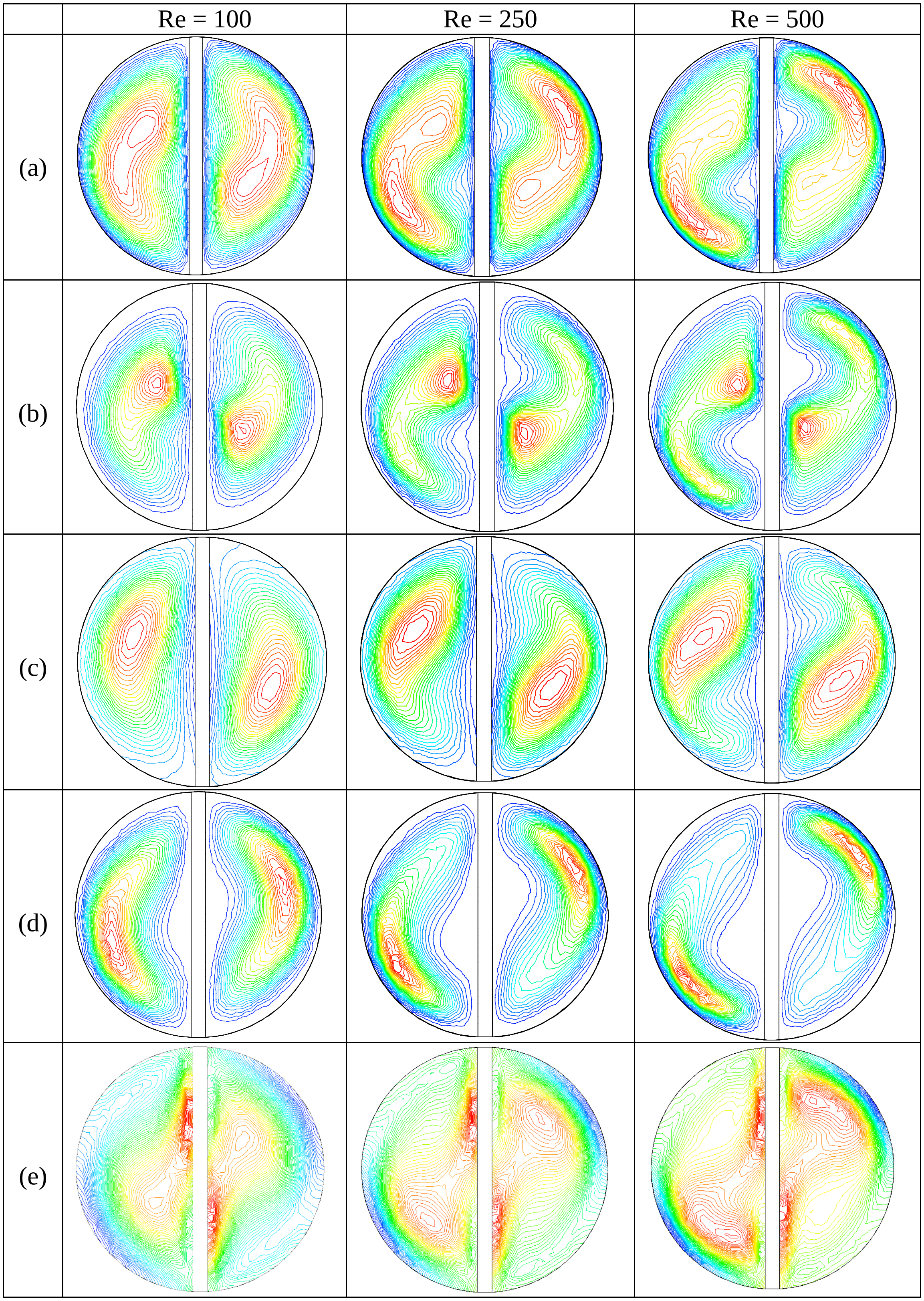

Figure 6.7.3 Flow characteristics at the swirler exit for Re 100, 250 and 500 (bulk velocities 4, 10 and 20 mm/s): (a) tangential velocity, (b) centrifugal force density, (c) total pressure, (d) circulation squared, e) axial vorticity; (red indicates maxima).

Figure 6.7.4 shows the streamlines at the swirler exit for Re 100, 250, 500, 750, 1000 and 1500. The streamlines appear to enter into the tape because the twisted tape is inclined relative to the XYZ coordinate system and the flow parallel to the tape actually has a vertical component.

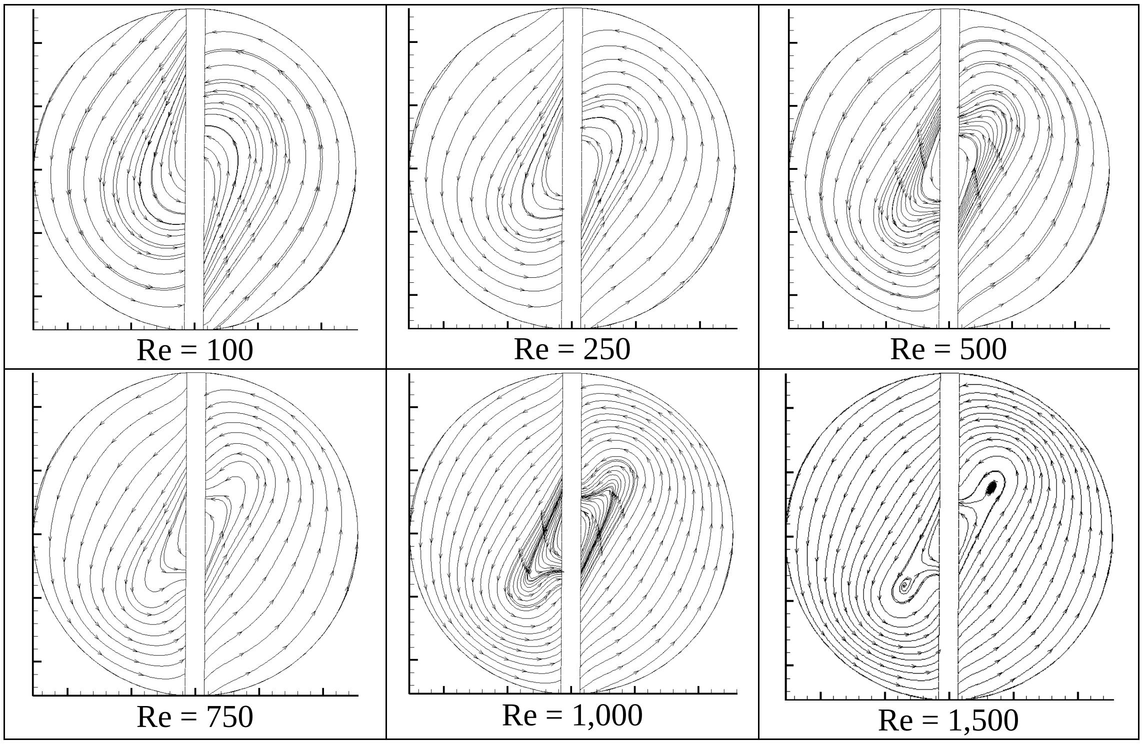
Re = 100
Re = 250
Re = 500
Re = 750
Re = 1,000
Re = 1,500

Figure 6.7.4 Streamlines at the swirler exit at different Re

Comparing the plots in figure 6.7.4, the angle of the streamlines at the swirler exit is approximately the same for all Re as it depends only on the twist of the tape. While the λ_2 method indicates the presence of secondary vortices at Re = 500, the streamlines in figure 6.7.4 do not close until Re = 1,500.

The two distinctive features of a vortex (low pressure and large tangential velocity) are formed separately and they evolve gradually into a vortex as the velocity gradients become larger. The coherent low pressure cores appear at lower Re than closed streamlines. The streamlines exhibit sharp turns near the low pressure region for Re from 500 to 1,000 but whether the low pressure structures identified by the λ_2 method are vortices is questionable. It seems that these structures should rather be considered a precursor of a vortex and that the actual secondary vortices occur when the streamlines close.

The pressure gradients are very small and the vortices very weak and unstable. It seems unlikely that these structures could be investigated experimentally and one has to rely on numerical simulation to obtain some insights into vortex inception.

6.8 Multiple vortices

Numerical simulations were also run to see if the stability of the pair of two helical vortices is maintained in the case of three and four vortices. Swirlers with three and four chambers twisted 180° are employed to investigate the generation and development of multiple vortices (figure 6.8.1). These complex swirlers could be manufactured by stereolitography similarly with the compact swirlers used in the experiments.

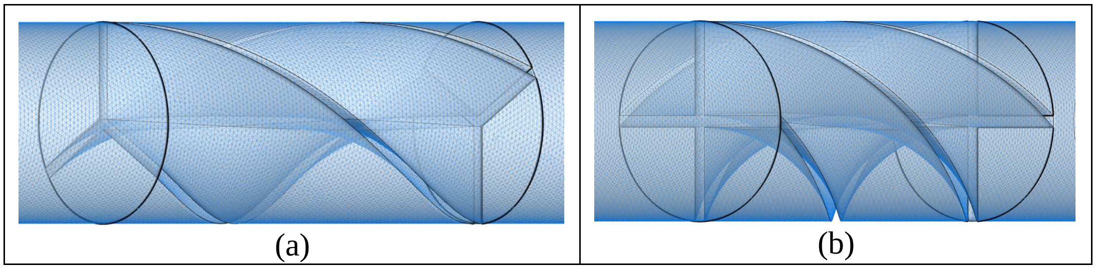
(a)
(b)

Figure 6.8.1: Complex 180° swirlers: (a) three chambers, (b) four chambers.

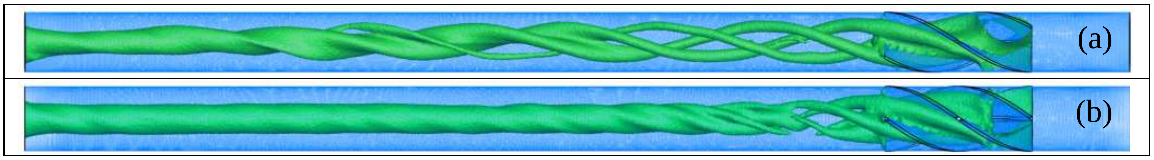

Figure 6.8.2: Secondary vortices in 180°, 60 mm long swirlers (y_r = 2.36) at Re = 7.7×10^4 identified by isobar surfaces $p/P_0 = 1$: (a) three chambers swirler, (b) four chambers swirler.

Figure 6.8.2 shows the secondary motion generated by three and four chambers, 180° swirlers. Just like in the case of the swirler with two chambers, single co-rotating vortices form early inside the swirler near the wall and then drift against the flow. However, the pressure gradients are lower than in the case of the regular twisted tape.

Despite some differences, in both cases the secondary vortices converge toward the centerline and the flow becomes a regular swirling flow. Details of the convergence process are shown for both cases in figure 6.8.3 using streamlines. In the case with three vortices the convergence is slower in approximately 12d while the four vortices converge after approximately 6d. The convergence creates unusual structures such as squared and triangular vortex cores.

This study investigated the twisted tape swirler and the counter-rotating flow because it was detrimental for the pulp mixing in the paper production. The secondary motion was creating preferential alignment of the pulp fibers, resulting in streaks on the final paper. These simulations suggest that multi-chamber swirlers can be used to produce swirling flow without the undesirable secondary motion in paper production.

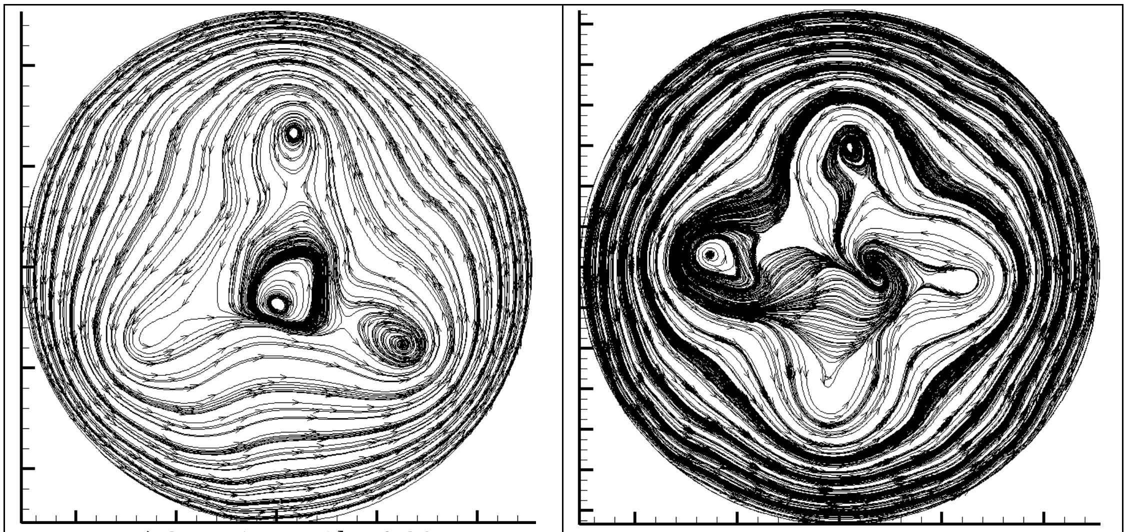

a) 3 vortices, z/d = 0.39

d) 4 vortices, z/d = 0.35

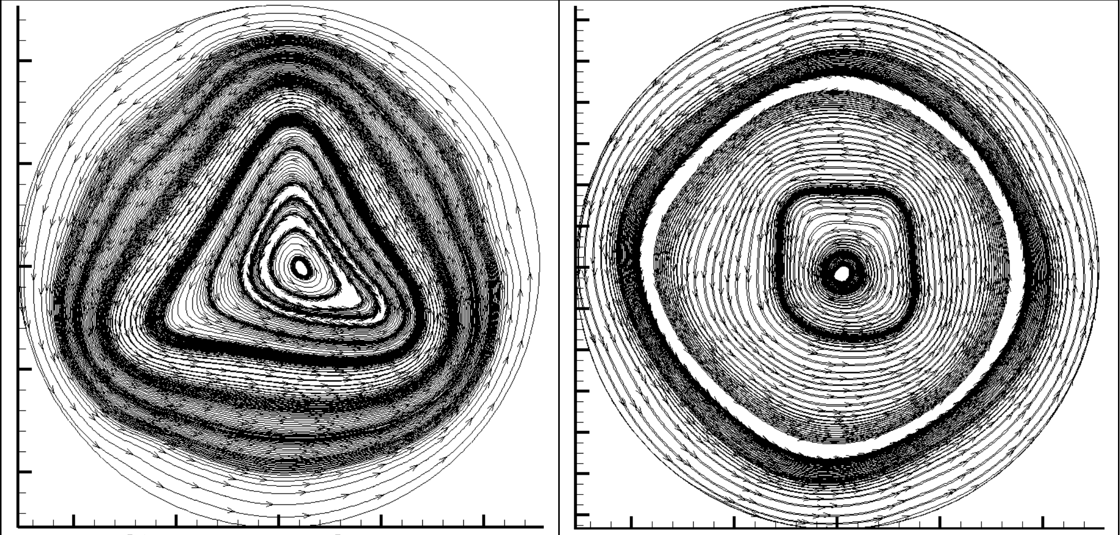

b) 3 vortices, z/d = 5.01

e) 4 vortices, z/d = 3.58 mm

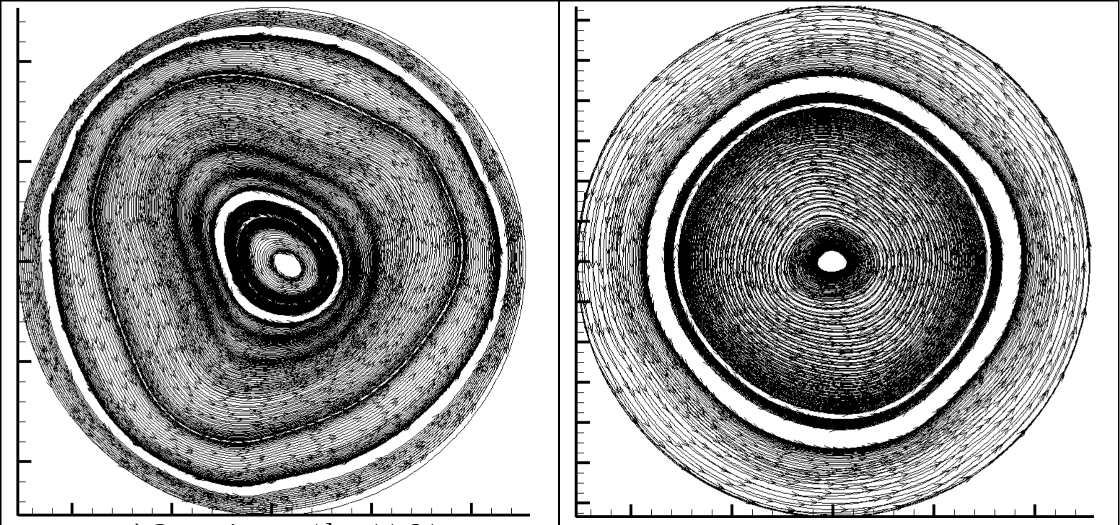

c) 3 vortices, z/d = 11.81

f) 4 vortices, z/d = 5.91

Figure 6.8.3: Streamlines for multiple vortices: a), b), c) 3 vortices; d), e), f) 4 vortices

CHAPTER 7

CONCLUSIONS AND RECOMMENDATIONS

7.1 Conclusions

Summarizing the contributions made by the present study, the main contribution is the identification of the cause of the secondary flow in short twisted tape swirlers. This investigation showed that the counter-rotating flow is produced by helical vortices. A solution to remove the secondary motion in applications where it is undesirable was proposed using multiple chambers swirlers. Removing the secondary flow in paper manufacturing will improve paper quality and it is expected to produce economical and environmental benefits.

Starting from an investigation of the cause of the counter-rotating flow observed downstream of twisted tapes swirlers during experimental tests, the present study identified for the first time the presence of helical vortices in the swirling flow induced by 180^o twisted tapes. The characteristics of this complex flow were investigated using LDV measurements, flow visualizations and numerical simulations. Helical vortices occur often in nature but these are the first stable helical vortices ever observed and they allowed detailed air bubble visualizations of the complex flow field resulting from the interaction between the helical vortices and the main swirl. The newly uncovered characteristics of the flow induced by twisted tapes can be used to design mixers with improved efficiency and calibrate numerical simulations. This study suggests that a short twisted tape (180^o) would create a very strong secondary flow while a long tape (720^o)

would suppress the secondary flow. The results presented here should benefit both the researchers and the industry using twisted tapes for mixing or heat transfer, or affected by helical vortices.

The experimental investigation demonstrated that the counter-rotating flow is produced by two secondary helical vortices superimposed on the main swirl. The two secondary vortices almost double the tangential velocity near the wall. The smaller secondary vortices rotate faster than the main vortex and as a result their centers have the lowest pressure in the cross sectional field as shown by the air bubble streams. The air bubbles provide a good description of the motion associated with the secondary vortices.

Experiments showed that short 180^o twisted tapes produce coherent secondary flow for Re in the range $2x10^4$ to 10^5. The helical vortices generated by the swirler become stronger with Re but the secondary flow structure does not change with Re (the pitch is constant for a given swirler). The tangential field created by the interaction of the three vortices is shown to be well described by superposition of the velocity fields of the secondary vortices on the main vortex velocity field. The characteristic tangential velocity profiles were identified for each vortex for the swirling flow induced by a twisted tape with twist ratio $y_r = 2.36$ (60 mm pitch) at $\mathrm{Re} = 7.7 \times 10^4$.

The helical vortices originate inside the swirler, and their inception and development inside the swirler were investigated using numerical simulations. The numerical simulations using a laminar formulation described well the transitional flow inside the swirler, while simulations using the RSM turbulence model gave only qualitative results that did not match the experiments very well.

The numerical simulations results showed that the secondary vortices appear early inside the swirler as single, small co-rotating vortices in the corner leading the rotation, on the suction side. As the tape continues to twist the co-rotating vortices become stronger and move away from the twisted tape and from the pipe wall. After the exit, the two vortices maintain their helical shape imposed in the formation stage inside the swirler and continue into the straight pipe. These results are similar to results showed by Rahmani [2004, 2005] but do not agree with the results published by Manglik et al. [1993, 1997], Yerra et al. [2007], Kazuhisa et al. [2004] and the measurements of Seymour [1966] which showed counter-rotating vortices inside or at the exit of the twisted tape. The differences in the numerical methods used could explain some of the discrepancies. At the same time, the use of air as medium and heat transfer in those previous numerical studies may also be responsible for some differences. The experimental measurements of Seymour could have been influenced by the intrusive techniques used. The simulations in the present study are validated against the experiments presented in the first part and they agree qualitatively with the experimental data. No counter-rotating vortices were observed downstream from the swirler in the experiments.

The flow downstream of the swirler was comprehensively described with numerical results, which confirmed the experimental tests while providing the pressure and the radial velocity component distributions. The helical vortices were identified using isobar surfaces of low pressure (corresponding to air bubble accumulations in the experiments), closed streamlines, vorticity and the negative eigenvalues of the velocity gradient tensor λ_2. While all the vortex identification methods clearly identify the secondary, helical vortices, the low pressure surfaces and λ_2 methods failed to identify the main swirl with its center on the centerline, which is obvious in the streamlines plots. This is a result of the low pressure regions created by the two helical vortices.

After running numerical simulations at low Re, the secondary motion was shown to appear first for Re between 250 and 500 (bulk velocities between 10 and 20 mm/s). At low Re the pressure gradients are weak and the vortices were better identified by the λ_2 method.

The flow behavior for twists larger than 180^o was also investigated numerically and the results showed that as the tape continues to twist, the secondary vortices move further against the flow and they reach the middle of the channel after 450^o for Re = $7.7x10^4$ (bulk velocity 3 m/s). The vortices continue to move against the tape rotation but after 720^o twist they weaken. After 900^o twist there are no more indications of secondary motion and the flow becomes a regular swirling flow with a low pressure region near the centerline. A plot of the variation of the axial vorticity along the twisted tape showed that the vorticity inside the secondary vortices increases fast at the beginning of their formation followed by a fast decrease as the size of the vortices increases due to vortex stretching. Once the size of the vortices stops changing, the axial vorticity intensity decreases at a slower, steady rate due to viscous dissipation. For twisted tapes with multiple twists, the viscous dissipation reduces the intensity of the secondary vortices until they disappear.

The motion against the flow is likely created by the tendency of the helical vortices to preserve their rotation axis direction and oppose the change forced by the tape. The vortices do not move against the flow in the semicircular channel, rather the channel moves around the secondary vortices, changing their relative position. This lagging is what gives the helical vortices a longer pitch than the pitch of the tape for the 180^o tape.

The helical vortices could also be the cause of the counter-rotating flow in swirling jets generated by rotating pipes which was reported by Facciolo and Alfredsson [2004]. Their explanation based on a dominant effect of the cross-section Reynolds stress was derived assuming axis-symmetric flow and no axial gradients. The LES simulation published by the same research group [Maciel et al. 2008] showed the presence of two helical vortices in the swirling jet immediately downstream of the rotating pipe. Their presence suggests that the mechanism responsible for the presence of the counter-rotating flow in the swirling jet could also be the same as the one presented in this study for twisted tape.

7.2 Recommendations for future work

While the present investigation answered how the secondary flow occurs and how to eliminate it, it also raised new questions. This study was focused on the vortex behavior which is not significantly affected by turbulence (no Re sensitivity), and calculating the detailed structure of the turbulent flow was not a present goal. At the same time the computational resources available were not sufficient for a rigorous Direct Numerical Simulation (DNS) of the flow. However, if sufficient computational resources would become available, a future DNS study of the flow could provide a valuable insight into how the multiple vortices affect turbulence compared to a regular pipe flow, while ensuring that the flow transition inside the swirler is computed accurately.

Multiple twists and multi-chambers swirlers could be manufactured to confirm the numerical findings presented in this study with measurements and visualizations downstream from the swirlers. While challenging, a setup allowing non-intrusive measurements inside a twisted tape with multiple twists would provide a valuable confirmation for the corresponding numerical results. The existing setup could be further used to investigate the vortex/air bubbles interaction in two-phase flows and flow stability.

Further research could also be performed on the secondary flow in jets induced by rotating pipes, in order to clarify if there is a connection between helical vortices and the observed counter-rotating flow. LDV measurements could be used to determine if the counter - rotating flow is axi-symmetric or not.

Numerical simulations could also be developed to investigate flows of different fluids through twisted tapes, such as air or pulp (pulp is a two-phase flow consisting of water, chemicals and wood fibers). Another research topic with economic potential would be an investigation of the potential of helical vortices behind twisted tapes to improve heat transfer in air and water flows.

REFERENCES

Abu-Khader M.M. (2006), Further Understanding of Twisted Tape Effects as Tube Insert for Heat Transfer Enhancement, *Heat and Mass Transfer*, Vol. 43, pp. 123-134;

Aidun C.K. (1995), Formation Hydrodynamics and Effects on Paper Physics, *Proceedings of the International Paper Physics Conference*, pp. 1-4;

Aidun C.K (1998), Method and Apparatus to Enhance Paper and Board Forming Qualities, *U.S. Patent 5,792,321*;

Aidun C.K (1999), Method and Apparatus to Enhance Paper and Board Forming Qualities, *U.S. Patent 5,876,564*;

Aidun C.K (2000), Method and Apparatus to Enhance Paper and Board Forming Qualities, *U.S. Patent 6,153,057*;

Aidun C.K (2002), Method and Apparatus to Enhance Paper and Board Forming Qualities, *U.S. Patent 6,368,460*;

Aidun C.K. and Parsheh M. (2007) Spatially Periodic Reversing Core in a Twisted-Fin Generated Swirling Pipe Flow, *Physics of Fluids*, Vol. 19, No. 6, p 061704;

Alekseenko S.V., Kuibin P.A., Okulov V.L. and Shtork S.I. (1999), Helical Vortices in Swirl Flow, *Journal of Fluid Mechanics*, Vol. 382, pp. 195-243;

Algifri A.H., Bhardwaj R.K. and Rao Y.V.N. (1987), Prediction of the Decay Process in Turbulent Swirl Flow, *Proceeding of the Institution of Mechanical Engineers*, Vol. 201, pp. 279-283;

Althaus W., Brucker C. and Weimer M. (1995), Breakdown of Slender Vortices, in Green S.I. editor, *Fluid Vortices – Fluid Mechanics and its Applications*, Vol. 30, Dordrecht: Kluwer Academic, pp. 373-426 (ISBN 0-7923-3376-4);

Anwer M. and So R.M.C. (1989), Rotation Effects on a Fully-Developed Turbulent Pipe Flow, *Experiments in Fluids*, Vol. 8, pp. 33-40;

Baker D.W. and Sayre C.L. Jr. (**1974),** Decay of Swirling Turbulent Flow of Incompressible Fluids in Long Pipes, *Flow: its measurement and control in science and industry*, Vol.1, pp. 301-312;

Batchelor G.K. (**1964),** Axial Flow in Trailing Line Vortices, *Journal of Fluid Mechanics*, Vol. 20, pp. 645-658;

Billant P., Chomaz J.M. and Huerre P (1998), Experimental Study of Vortex Breakdown in Swirling Jets, *Journal of Fluid Mechanics*, Vol. 376, pp. 183-219;

Burgers J.M. **(1948)**, A Mathematical Model Illustrating the Theory of Turbulence, *Advances in Applied Mechanics,* Vol. 1, pp. 171-199;

Cazan R. and Aidun C.K. (2009), Experimental Investigation of the Swirling Flow and the Helical Vortices Induced by a Twisted Tape Inside a Circular Pipe, *Physics of Fluids*, Vol. 21, no.3, pp. 037102;

Chakraborty P., Balachandar S. and Adrian R.J. (2005), On the Relationships between Local Vortex Identification Schemes, *Journal of Fluid Mechanics,* Vol. 535, pp. 189–214;

Cheng K.C., Inaba T. and Akiyama M. (1987) Flow Visualization Studies of Secondary Flow Patterns and Centrifugal Instability in Curved Circular and Semicircular Pipes, *Proceedings of the 3rd International Symposium of Flow Visualization,* Ann Arbor, MI, pp. 531-536;

Chong, M.S., Perry, A.E. and Cantwell, B.J. (1990), A General Classification of Three-Dimensional Flow Fields, *Physics of Fluids* A**2 (5)**, pp. 765–777;

Date A.W. (1974), Prediction of Fully-Developed Flow in a Tube Containing a Twisted-Tape, *International Journal of Heat Mass Transfer,* Vol. 17, pp. 845-859;

Dean W.R. (1927), Note on the Motion of Fluid in a Curved Pipe, *The London, Edinburgh and Dublin Philosophical Magazine and Journal of Science*, Series 7, Vol. 4, No. 20, pp. 208-223;

Dean W.R. **(1928),** Fluid Motion in a Curved Channel, *Proceedings of the Royal Society of London*, Series A, Vol. 121, No.787, pp. 402-420;

Dewan A., Mahanta P., Raju K. S. and Kumar P. S. (2004), Review of Passive Heat Transfer Augmentation Techniques, *Proceedings of the Institution of Mechanical Engineers, Part A: Journal of Power and Energy*, Vol. 218, No. 7, pp. 509-527;

Drazin P.G. and Reid W.H. (1981), *Hydrodynamic Stability*, Cambridge University Press, London;

Escudier M.P. (1988), Vortex Breakdown: Observations and Explanations, *Progress in Aerospace Science*, Vol. 25, pp. 189-229;

Escudier M.P. and Zehnder N. (1982), Vortex-Flow Regimes, *Journal of Fluid Mechanics*, Vol. 115, pp. 105-121;

Eustice J. (1911), Experiments on Stream-line Motion in Curved Pipes, *Proceedings of the Royal Society of London*, Series A, Vol. 85, No. 576, pp. 119-131;

Facciolo L. and Alfredsson P. H. (2004), The Counter-Rotating Core of a Swirling Turbulent Jet Issued from a Rotating Pipe Flow, *Physics of Fluids*, Vol. 16, No. 9, pp. L71-L73;

Facciolo L., Tillmark N., Talamelli A. and Alfredsson P. H. (2007), A Study of Swirling Turbulent Pipe and Jet Flows, *Physics of Fluids*, Vol. 19, No. 3, p 035105;

Farell C. and Youssef S (1996), Experiments on Turbulence Management Using Screens and Honeycombs, *Journal of Fluids Engineering*, Vol. 118, pp. 26-32;

Fluent Inc. (2006), *FLUENT 6.3 User's Guide*, Lebanon, NH;

Fukumoto Y. and Okulov V.L. (2005), *The Velocity Field Induced by a Helical Vortex Tube,* Physics of Fluids, Vol. 17, pp. 107101;

Germano M. (1982), On the Effect of Torsion on a Helical Pipe Flow, *Journal of Fluid Mechanics*, Vol. 125, pp. 1-8;

Glover J., Bullen P.R. and Cheeseman D.J. (1985), The Effects of Refraction on the Measurement of Velocity of Water Flow in a Circular Pipe Using a Three Beam Laser Doppler Anemometer System, *Proceedings of the Developments in Measurements and Instrumentation in Engineering*, Durham, England, pp. 59-72;

Gupta A.K., Lilley D.G. and Syred N. (1984), *Swirl Flow*, Abacus Press, Great Britain;

Holmes D.G. and Connell S.D. (1989), Solution of the 2D Navier-Stokes Equations on Unstructured Adaptive Grids, *Presented at the AIAA 9th Computational Fluid Dynamics Conference, Buffalo NY, June, 1989*;

Humphrey J.A.C. and Webster D.R. (1993), Questions in Fluid Mechanics - Reverse Transition Phenomena in Helically Coiled Pipes, *Transactions of the ASME*: *Journal of Fluids Engineering*, Vol. 115, pp. 191-192;

Hunt J.C.R., Wray A.A. and Moin P. (1988), Eddies, Stream, and Convergence Zones in Turbulent Flows, *Center for Turbulence Research Report CTR-S88*, pp. 193–208;

Hussain A.K.M.F. and Hayakawa M. (1987), Eduction of Large-Scale Organized Structures in a Turbulent Plane Wake. *Journal of Fluid Mechanics,* Vol. 180**,** pp. 193;

Imao S., Itoh M. and Harada T. (1996), Turbulent Characteristics of the Flow in an Axially Rotating Pipe, *International Journal of Heat and Fluid Flow*, Vol. 17, pp. 444-451;

Islek A.A. (2004), The Impact of Swirl in Turbulent Pipe Flow, *M.S. Thesis*, Georgia Institute of Technology;

Issa R.I. (1985), Solution of the Implicitly Discretized Fluid Flow Equations by Operator-Splitting, *Journal of Computational Physics*, Vol. 62, pp. 40-65;

Jeong J. and Hussain F. (1995), On the Identification of a Vortex, *Journal of Fluid Mechanics*, Vol. 285, pp. 69–94;

Kao H.C. (1987), Torsion Effect on Fully Developed Flow in a Helical Pipe, *Journal of Fluid Mechanics*, Vol. 184, pp. 335-356;

Kazuhisa Y., Hidetoshi H., Saburo T. and Chikahiro S. (2004), Numerical Simulation on Heat Transfer Enhancement in Twisted-Tape-Inserted Tubes, *Journal of Enhanced Heat Transfer*, Vol. 11, No. 4, pp.379-389;

Kitoh O. (1991), Experimental Study of Turbulent Swirling Flow in a Straight Pipe, *Journal of Fluid Mechanics*, Vol. 225, pp. 445-479;

Klepper O. H. (1972), Heat Transfer Performance of Short Twisted Tape, *American Institute of Chemical Engineers Papers,* Vol. 35, pp. 1-24;

Kobayashi T. and Yoda M. (1987), Modified $k-\varepsilon$ Model for Turbulent Swirling Flow in a straight Pipe, *JSME International Journal*, Vol. 30, No. 259, pp. 66-71;

Kreith F. and Sonju O.K. (1965), The Decay of a Turbulent Swirl in a Pipe, *Journal of Fluid Mechanics*, Vol. 22, pp. 257-271;

Lakshminarayana B. (1995), *Fluid Dynamics and Heat Transfer of Turbomachinery,* Wiley-Interscience, New York;

Lambourne N.C. and Bryer D.W. (1961), The Bursting of Leading-Edge Vortices-Some Observations and Discussion of the Phenomenon, *Aeronautical Research Council Report R & M 3282;*

Launder B.E., Reece G.J. and Rodi W. (1975), Progress in the Development of a Reynolds-Stress Turbulence Closure, *Journal of Fluid Mechanics*, Vol. 68, No.3, pp. 537-566;

Launder B.E. and Spalding D.B. (1974), The Numerical Computation of Turbulent Flows, *Computer Methods in Applied Mechanics and Engineering*, Vol. 3, pp. 269-289;

Leibovich S. (1978), The Structure of Vortex Breakdown, *Annual Review of Fluid Mechanics*, Vol. 10, pp. 22-246;

Leibovich S. (1984), Vortex Stability and Breakdown: Survey and Extension, *AIAA Journal*, Vol. 22, pp. 1192-1206;

Lessen M., Singh P.J. and Paillet F. (1974), The Stability of a Trailing Line Vortex Part 1. Inviscid Theory, *Journal of Fluid Mechanics*, Vol. 63, pp. 753-763;

Liu S. and Masliyah J.H. (1993), Axially Invariant Laminar Flow in Helical Pipes with Finite Pitch, *Journal of Fluid Mechanics*, Vol. 251, pp. 315-353;

Loiseleux T., Chomaz J.M. and Huerre P. (1998), The Effect of Swirl in Jets and Wakes: Linear Instability of the Rankine Vortex with Axial Flow, *Physics of Fluids*, Vol. 10, No. 5, pp. 1120-1134;

Lucca-Negro O. and O'Doherty T. (2001), Vortex Breakdown: A Review, *Progress in Energy and Combustion Science*, Vol. 27, pp. 431-481;

Lugt, H.J. (1979), The Dilemma of Defining a Vortex, *Recent Developments in Theoretical and Experimental Fluid Mechanics*, Springer, pp. 309–321;

Maciel Y., Facciolo L., Duwig C., Fuchs L. and Alfredsson P.H. (2008), Near-Field Dynamics of a Turbulent Round Jet with Moderate Swirl, *International Journal of Heat and Fluid Flow*, Vol. **29**, pp. 675-686;

Manglik R.M. and Bergles A.E. (1993), Heat Transfer and Pressure Drop Correlations for Twisted-Tape Inserts in Isothermal Tubes: Part I – Laminar Flows, *Journal of Heat Transfer*, Vol. 115, No. 4, pp. 881-889;

Manglik R.M., Maramaju S. and Bergles A.E. (2001), The Scaling and Correlation of Low Reynolds Number Swirl Flows and Friction Factors in Circular Tubes with Twisted-Tape Inserts, *Journal of Enhanced Heat Transfer*, Vol. 8, No. 6, pp. 383-395;

Manglik R.M. and Ranganathan C. (1997), Visualization of Swirl Flows Generated by Twisted-Tape Insert in Circular Pipes, *Proceedings of the 4th World Conference on Experimental Heat Transfer, Fluid Mechanics and Thermodynamics*, pp. 1631-1636;

Menon R. and Lai W.T. (1991), Key Considerations in the Selection of Seed Particles for LDV Measurements, *Presented at the 4th International Conference on Laser Anemometry,* Cleveland, Ohio, August;

Nishibori K., Kikuyama K. and Murakami M. (1987), Laminarization of Turbulent Flow in the Inlet Region of an Axially Rotating Pipe, *JSME International Journal*, Vol. 30, No. 260, pp. 255-262;

Okulov V.L. (2004), On the Stability of Multiple Helical Vortices, *Journal of Fluid Mechanics*, Vol. 521, pp. 319-342;

Orlandi P. and Fatica M. (1997), Direct Simulations of Turbulent Flow in a Pipe Rotating About Its Axis, *Journal of Fluid Mechanics*, Vol. 343, pp. 43-72;

Parchen R.R. and Steenbergen W. (1998), An Experimental and Numerical Study of Turbulent Swirling Pipe Flows, *Journal of Fluids Engineering*, Vol. 120, pp. 54-61;

Pashtrapanska M., Jovanović J., Lienhart H. and Durst F. (2006), Turbulence Measurements in a Swirling Pipe Flow, *Experiments in Fluids*, Vol. 41, pp. 813-827;

Patankar S.V. (1980), *Numerical Heat Transfer and Fluid Flow*, Hemisphere, Washington, DC;

Peckham D.H. and Atkinson S.A. (1957), Preliminary Results of Low Speed Wind Tunnel Tests on a Gothic Wing with Aspect Ratio 1.0, *Aeronautical Research Council Report CP 508*;

Pope S. (2000), *Turbulent Flows*, Cambridge Press, Cambridge;

Rahmani R.K. (2004), Three-Dimensional Numerical Simulation and Performance Study of an Industrial Helical Static Mixer, *Ph.D. thesis*, University of Toledo;

Rahmani R.K., Keith T.G. and Ayasoufi A. (2005), Three-Dimensional Numerical Simulation and Performance Study of an Industrial Helical Static Mixer, *Journal of Fluids Engineering*, Vol. 127, pp. 467-483;

Rankine W.J.M. (1888), *A Manual of Applied Mechanics*, 12th edition, London;

Rauch R.D., Batira J.T. and Yang N.T.Y. (1991), Spatial Adaption Procedures on Unstructured Meshes for Accurate Unsteady Aerodynamic Flow Computations, *Technical Report AIAA-91-1106*;

Rayleigh, Lord (1916), On the Dynamics of Revolving Fluids, *Proceedings of the Royal Society of London, Series A*, Vol. 93, No. 648, pp. 148-154;

Robinson S.K. (1991), Coherent Motions in the Turbulent Boundary Layer, *Annual Revue of Fluid Mechanics*, Vol. 23, pp. 601-639;

Rocklage-Marliani G., Schmidts M. and Vasanta R.V.I. (2003), Three-Dimensional Laser-Doppler Velocimeter Measurements in Swirling Turbulent Pipe Flow, *Flow, Turbulence and Combustion*, Vol. 70, pp. 43-67;

Ruith M.R., Chen P., Meiburg E. and Maxworthy T. (2003), Three-Dimensional Vortex Breakdown in Swirling Jets and Wakes: Direct Numerical Simulation, *Journal of Fluid Mechanics*, Vol. 486, pp. 331-378;

Saha S. K., Dutta A. and Dahl S. K. (2001), Friction and Heat Transfer Characteristics of Laminar Swirl Flow through a Circular Tube Fitted with Regularly Spaced Twisted-Tape Elements, *International Journal of Heat and Mass Transfer*, Vol. 44, pp. 4211-4223;

Sarpkaya T. (1971), On Stationary and Travelling Vortex Breakdowns, *Journal of Fluid Mechanics*, Vol. 45, pp. 545-559;

Seymour E.V. (1966), Fluid Flow through Tubes Containing Twisted Tapes, *The Engineer*, Vol. 222, pp. 634-642;

Smithberg E. and Landis F. (1964), Friction and Forced Convection Heat Transfer Characteristics in Tubes with Twisted Tape Swirl Generators, *Journal of Heat Transfer*, Vol. 86, pp. 39-49;

Squire H.B. and Winter K.G. (1951), Secondary Flow in Cascade of Airfoils in Non-uniform Stream, *Journal of the Aeronautical Sciences*, vol. 18, no 4, p271-277;

Tiwari P., Antal S.P. and Podowski M.Z. (2006), Three-Dimensional Fluid Mechanics of Particulate Two-Phases Flows in U-Bend and Helical Conduits, *Physics of Fluids*, Vol. 18, 043304;

Ujhidy A., Nemeth J. and Szepvolgyi J. (2003), Fluid Flow in Tubes with Helical Elements, *Chemical Engineering and Processing*, Vol. 42, pp. 1-7;

Van Leer B. (1979), Toward the Ultimate Conservative Difference Scheme. A Second Order Sequel to Godunov's Method, *Journal of Computational Physics,* Vol. 32, pp 101-136;

Widnall S.E. (1975), The Structure and Dynamics of Vortex Filaments, *Annual Reviews of Fluid Mechanics,* Vol. 7, pp. 141-165;

Yamamoto K., Aribowo A., Hayamizu Y., Hirose T. and Kawahara K. (2002), Visualization of the Flow in a Helical Pipe, *Fluid Dynamic Research,* Vol. 30, pp. 251-267;

Yerra K. K., Manglik R. M. and Jog M. A. (2007), Optimization of Heat Transfer Enhancement in Single-Phase Tubeside Flows with Twisted-Tape Inserts, *International Journal of Heat Exchangers*, Vol. 8, No. 1, pp. 117-138;

Zhou J., Adrian R.J., Balachandar S. and Kendall, T.M. (1999), Mechanisms for Generating Coherent Packets of Hairpin Vortices, *Journal of Fluid Mechanics*, Vol. 387, pp. 353–396;

APPENDIX 1

Table A1 Tangential Velocity Corrections

Measurements Index	Pipe Position [mm]	Traverse Position [mm]	Centered Traverse Position [mm]	Velocity Correction
1	-12	-15.54	-8.10	1.3378
2	-11	-14.81	-7.37	1.3488
3	-10	-14.08	-6.64	1.3599
4	-9	-13.37	-5.93	1.3709
5	-8	-12.67	-5.23	1.3819
6	-7	-11.98	-4.54	1.3929
7	-6	-11.30	-3.86	1.4040
8	-5	-10.63	-3.19	1.4150
9	-4	-9.97	-2.53	1.4260
10	-3	-9.32	-1.88	1.4371
11	-2	-8.68	-1.24	1.4481
12	-1	-8.06	-0.62	1.4590
13	0	-7.44	0	1.4700
14	1	-6.83	0.61	1.4810
15	2	-6.22	1.22	1.4922
16	3	-5.63	1.81	1.5032
17	4	-5.05	2.39	1.5141
18	5	-4.47	2.97	1.5252
19	6	-3.91	3.53	1.5361
20	7	-3.35	4.09	1.5472
21	8	-2.80	4.64	1.5582
22	9	-2.25	5.19	1.5693
23	10	-1.72	5.72	1.5802
24	11	-1.19	6.25	1.5913
25	12	-0.67	6.77	1.6023